



# Diffraction inverse par des inclusions minces et des fissures

Won-Kwang Park

## ► To cite this version:

Won-Kwang Park. Diffraction inverse par des inclusions minces et des fissures. Mathématiques [math]. Ecole Polytechnique X, 2009. Français. NNT : . pastel-00004834

**HAL Id: pastel-00004834**

**<https://pastel.archives-ouvertes.fr/pastel-00004834>**

Submitted on 4 Mar 2009

**HAL** is a multi-disciplinary open access archive for the deposit and dissemination of scientific research documents, whether they are published or not. The documents may come from teaching and research institutions in France or abroad, or from public or private research centers.

L'archive ouverte pluridisciplinaire **HAL**, est destinée au dépôt et à la diffusion de documents scientifiques de niveau recherche, publiés ou non, émanant des établissements d'enseignement et de recherche français ou étrangers, des laboratoires publics ou privés.



# THÈSE

Présentée pour obtenir

LE GRADE DE DOCTEUR EN SCIENCES  
DE L'ÉCOLE POLYTECHNIQUE

Spécialité : Mathématiques Appliquées

par

Won-Kwang Park

## Diffraction Inverse par des Inclusions Minces et des Fissures

Soutenue le 24 février 2009 devant la commission d'examen formée de :

M.	Habib Ammari	Directeur de thèse
M.	Dominique Lesselier	Co-directeur de thèse
Mme.	Elena Beretta	Rapporteur
M.	Oliver Dorn	Rapporteur
M.	François Jouve	Président
M.	Roman Novikov	Examineur
M.	Knut Solna	Examineur



**Thèse préparée au**  
Centre de Mathématiques Appliquées  
CNRS UMR 7641  
École Polytechnique  
91128 Palaiseau CEDEX

## Résumé

Le contrôle non destructif de défauts du type fissures pénétrables ou impénétrables constitue un problème inverse très intéressant parmi ceux de la physique, de l'ingénierie des matériaux et structures, des sciences médicales, etc., et en soi est donc un sujet d'importance sociétale certaine.

Le but de cette thèse est de développer des méthodes de reconstruction efficaces afin de les appliquer à une variété de problèmes de fissures. Premièrement, nous proposons un algorithme non-itératif afin de déterminer les extrémités de fissures conductrices, algorithme basé sur une formulation asymptotique appropriée et une méthode d'identification de pôles simples et de résidus d'une fonction méromorphe. Puis un algorithme non-itératif de type MUSIC(MULTiple SIGNAL Classification) est considéré afin d'imager une fissure pénétrable ou impénétrable à partir du champ qu'elle diffracte, ce champ pouvant être représenté grâce à une formulation asymptotique rigoureuse. Une technique d'ensembles de niveaux est alors proposée afin de reconstruire une fissure pénétrable, deux fonctions d'ensemble de niveaux étant utilisées pour la décrire puisqu'une méthode traditionnelle d'ensembles de niveaux ne le permet pas de par sa petite épaisseur. Finalement, cette thèse traite de la reconstruction des fissures courtes et étendues avec des conditions limites de Dirichlet. Nous développons alors un algorithme de type MUSIC pour reconstruire les petites fissures et un algorithme d'optimisation pour les fissures longues basé sur la formulation asymptotique. Des simulations numériques nombreuses illustrent les performances des méthodes de reconstruction proposées.

**Mots-clefs** : contrôle non destructif, fissures pénétrables ou impénétrables, problème inverse, formulation asymptotique, MUSIC(MULTiple SIGNAL Classification), technique d'ensembles de niveaux, algorithme d'optimisation, simulations numériques.

---

## INVERSE SCATTERING FROM TWO-DIMENSIONAL THIN INCLUSIONS AND CRACKS

### Abstract

Non-Destructive testing to retrieve a penetrable or impenetrable crack appears to be one of the interesting inverse problems which is arising in physics, medical science, material engineering, and so on, highly related with human life.

The aim of this thesis is to develop suitable reconstruction methods in order to apply them to various kinds of crack problems. First, we propose a non-iterative algorithm for retrieving the end points of conducting cracks based on an appropriate asymptotic formula and an identification method for simple poles and residues of a meromorphic function. Second, a non-iterative MUSIC(MULTiple SIGNAL Classification)-type algorithm is considered to image a penetrable or impenetrable crack from scattered field data which can be represented via a rigorous asymptotic formulation. Third, a level-set technique is proposed to reconstruct a penetrable crack. Two level-set functions are used to express the crack because it cannot be easily described by traditional level-set methods due to the small thickness. Finally, this thesis deals with the reconstruction of small and extended cracks with Dirichlet boundary conditions. Based on the asymptotic expansion formula, we develop a MUSIC-type algorithm for retrieving small cracks and an optimization algorithm for reconstructing extended cracks. Comprehensive numerical simulations illustrate the performances of the proposed reconstruction methods.

**Keywords** : non-destructive testing, penetrable or impenetrable crack, inverse problem, asymptotic formula, MUSIC(MULTiple SIGNAL Classification), level set technique, optimization algorithm, numerical simulations.



*À mes parents, mon frère et ma sœur*



# Remerciements

I would like thank to Prof. Habib Ammari, my supervisor, for his kindness, many suggestions and constant support during this research. He developed my mathematical inspirations and helped me to overcome many difficult problems. I am also express my gratitude to Prof. Dominique Lesselier for his careful consideration, great guidance and advices during my PhD course. Under his assistance, I can developed my scientific techniques and it make me a better scientist.

I would particularly like to thank Prof. Elena Beretta and Oliver Dorn for their attention in my work and I am also have grateful feeling for their investment to careful reading. And I appreciate kindness of thesis committee member Prof. François Jouve, Roman Novikov and Knut Solna for their compliance. They provided me with a great convenience in order that I can submit my thesis successfully.

I had the pleasure of meeting all members of CMAP (Centre de Mathématiques APpliquées) in École Polytechnique and LSS (Laboratoire des Signaux et Systèmes) in Supélec (L'École Supérieure d'Électricité). They are wonderful people and their enormous encouragement makes me complete this thesis satisfactory.

I want to thank all of my former/nowadays teachers and colleagues in South Korea. Especially I am obliged to Prof. Jin Keun Seo, Hyeonbae Kang, Eunjoo Kim, Hyundae Lee and Mikyoung Lim. Their suggestions and encouragements helped me in all the time of research and writing of this thesis.

Finally, I am grateful to my family for their patience and love. Without them, this work would never have come into existence.

Supélec, Gif-sur-Yvette  
February 10, 2009

Won-Kwang Park



# Table des matières

<b>Introduction</b>	<b>11</b>
<b>I Reconstruction of Penetrable Cracks</b>	<b>14</b>
<b>1 Reconstructing End-Points of Thin Conductivity Inclusions</b>	<b>16</b>
1.1 Introduction . . . . .	16
1.2 Mathematical formulation for the conductivity problem . . . . .	16
1.3 Asymptotic formula for the steady state voltage potential . . . . .	17
1.4 Reconstruction algorithm for identifying the end-points of single thin inclusion . . . . .	19
1.5 Numerical examples . . . . .	20
1.6 Reconstruction algorithm for identifying the end-points of multiple thin inclusions . . . . .	24
1.7 Numerical examples . . . . .	28
1.8 Conclusion . . . . .	36
<b>2 Imaging of Thin Penetrable Inclusions by a MUSIC-Type Algorithm</b>	<b>37</b>
2.1 Introduction . . . . .	37
2.2 Maxwell's equations and the direct scattering problem . . . . .	39
2.3 The direct scattering problem and the asymptotic formulation of the scattering amplitude . . . . .	40
2.4 MUSIC type algorithm for imaging a thin inclusion and estimating its length . . . . .	42
2.5 Numerical examples . . . . .	47
2.6 Conclusion . . . . .	75
<b>3 Reconstruction of Thin Electromagnetic Inclusions by a Level Set Method</b>	<b>76</b>
3.1 Introduction . . . . .	76
3.2 Representing thin inclusion with two level set functions . . . . .	78
3.3 Shape deformation by calculus of variations . . . . .	79
3.4 Evolution of level set functions $\varphi$ and $\psi$ . . . . .	85
3.5 Reconstruction algorithm . . . . .	85
3.6 Numerical Examples . . . . .	86

3.7	Conclusion . . . . .	97
<b>II</b>	<b>Reconstruction of Impenetrable Cracks</b>	<b>100</b>
<b>4</b>	<b>Reconstruction of Perfectly Conducting Cracks</b>	<b>101</b>
4.1	Introduction . . . . .	101
4.2	Helmholtz equation and direct scattering problem . . . . .	101
4.3	MUSIC type algorithm for imaging of screens . . . . .	105
4.4	Numerical examples : Dirichlet boundary condition case . . . . .	106
4.5	Numerical examples : Neumann boundary condition case . . . . .	119
4.6	Conclusion . . . . .	131
<b>5</b>	<b>Asymptotic Imaging of Perfectly Conducting Cracks</b>	<b>132</b>
5.1	Introduction and problem formulations . . . . .	132
5.2	Preliminary results . . . . .	133
5.3	Asymptotic expansion . . . . .	135
5.4	MUSIC-type imaging . . . . .	137
5.5	Numerical simulations for imaging of small cracks . . . . .	139
5.6	Deformation of an extended crack . . . . .	146
5.7	Initial guess for an extended crack . . . . .	150
5.8	Numerical simulations for imaging extended cracks . . . . .	152
5.9	An optimization approach for extended cracks . . . . .	157
5.10	Conclusion . . . . .	158
<b>III</b>	<b>Conclusion and Appendix</b>	<b>159</b>
	<b>Conclusion and perspective</b>	<b>160</b>
<b>A</b>	<b>Appendix</b>	<b>162</b>
A.1	Neumann function . . . . .	162
A.2	Identification of simple poles . . . . .	162
A.3	The Moore–Penrose generalized inverse . . . . .	164
A.4	The singular value decomposition . . . . .	164
A.5	Bessel functions . . . . .	165

A.6	Linear system for numerical simulation . . . . .	166
A.7	Uniqueness result . . . . .	171
<b>Références</b>		<b>174</b>

## Introduction

From a point of view, an inverse problem is the problem of determining unknown characteristics of an object (shape, internal constitution, etc.) from measured data. A challenging inverse problem of fundamental importance in non-destructive testing is to retrieve the shape of a unknown crack (inhomogeneity with small thickness) or a screen (with Dirichlet/Neumann type boundary condition). Throughout the literature, various algorithms for reconstructing an unknown object have been suggested, most based on Newton-type iteration schemes. Yet, for successful application of these schemes, one needs a good initial guess, close enough to the unknown object. Without, one might suffer from large computational costs. Moreover, iterative schemes often require regularization terms that depend on the specific problem at hand. So, many authors have suggested non-iterative reconstruction algorithms, which at least could provide good initial guesses. Related works can be found in [4, 5, 12, 11, 45, 46, 48, 51, 54, 68].

This thesis considers the reconstruction of two-dimensional curve-like penetrable thin inhomogeneities and perfectly conducting cracks from the measured boundary data or scattered field. We are concerned with the following items :

1. Location search algorithm of thin conductivity inclusions from boundary data
2. Non-iterative MUSIC-type imaging of cracks or screens from scattered field data
3. Reconstruction of crack by a level set method via the electromagnetic boundary measurement.

In chapter 1, a location search algorithm for finding the end-points of thin conductivity inclusions which occurs in the Electrical Impedance Tomography (EIT) is handled. Based on the asymptotic formula for steady state voltage potentials in the presence of thin inclusions [25], a reconstruction algorithm was established in [4, 5] for the single and multiple case, respectively. In these articles, the authors proved that the thin inclusion can be uniquely determined from the boundary measurements of the first-order correction term in the asymptotic formula. Unfortunately, there was no numerical simulation to support their algorithm, which in addition can be applied only to the thin rectangular inclusions.

Motivated from such an analysis, in this chapter, we consider the following : first, the numerical simulation for reconstructing thin conductivity inclusion introduced in [4], next, for the improvement of algorithm in [5], we develop a new reconstruction algorithm for retrieving the end points of multiple thin inclusions. Although this new algorithm is still restricted in theory to the thin rectangular inclusion, we can say that it can be applied to the non-rectangular one as is shown by the numerical simulations.

The imaging of a thin curve-like penetrable electromagnetic inclusion from the measured scattered field (an inverse scattering problem) is considered in chapter 2. A non-iterative MUSIC(MUltiple SIgnal Classification) algorithm which is generally used in signal processing problems as a method for estimating the individual frequencies of multiple harmonic signals [77] is employed in order to find the location of small volumetric inclusions. This algorithm makes use of a singular value decomposition of the so-called Multi-Static Response (MSR) matrix. Applied works can be found in several references, refer to [8, 10, 12, 11, 13, 32].

Borrowing from previous works carried out for volumetric inclusions, a non-iterative

MUSIC-type algorithm based on an appropriate asymptotic formula of the scattering amplitude is proposed to find the location and or/shape of the thin inclusion, with dielectric and or/magnetic contrast with respect to the embedding homogeneous space. From the several numerical results, this algorithm can be applied to not only single but also multiple thin inclusions.

Through the various results from the reconstruction algorithm introduced in chapter 1 and 2, we can say that, at least, a good initial guess is obtained at low computational cost, to be improved upon by an appropriate iterative algorithm, refer to the level set method. Starting out from the original binary approach of Santosa for solving the shape reconstruction problem [73], various techniques which use a level set representation of shapes for solving inverse problems have been successfully developed, refer to [2, 38, 55, 71, 72].

In chapter 3, we develop a technique which uses the level set method for reconstructing a thin inclusion, with purely dielectric permittivity or magnetic permeability contrast with respect to the embedding homogeneous medium. Opposite to the reconstruction of volumetric objects, a thin inclusion cannot be represented by a single level set function. Therefore, at least, this representation must be provided by using two or more level set functions. In this chapter we adopt two level set functions to do the work : the first one includes the location and shape of crack and the second one enables to cut the curve at crack tips, based on the investigation of [2, 38]. For a successful evolution, we rigorously derive the gradient direction via Fréchet derivative by solving the adjoint problem and illustrate the analysis by several numerical simulations.

In chapter 4, we consider the reconstruction of a perfectly conducting crack (screen) from the far-field pattern for the scattering of time-harmonic electromagnetic plane waves. A Newton-type method to reconstruct a screen with Dirichlet boundary condition is presented for the first time probably in [52] and this method is extended to the Neumann boundary condition in [59]. Unfortunately, this method requires a large computational cost (against a non-iterative algorithm) to calculate the complex Fréchet derivative, an optimized regularization procedure, and a good initial guess. Moreover, it is limited to a single screen, and cannot applied to the multiple screens.

The linear sampling method based on a characterization of the range of the scattering operator for the far-field pattern for a screen with Dirichlet boundary condition is proposed in [29, 30, 35]. This is a non-iterative reconstruction algorithm that has some similarities to the MUSIC algorithm but Tikhonov regularization is required for a successful reconstruction. The relationship between the MUSIC and the linear sampling method is studied in [32].

In this chapter, similarly with the chapter 2, a non-iterative MUSIC-type imaging algorithm is proposed to retrieve the screen with Dirichlet/Neumann boundary condition. This is based on the factorization of the measured Multi-Static Response matrix. Through the several numerical simulations, it is shown to be a suitable algorithm for imaging single or multiple screens.

In chapter 5, we consider the imaging of narrow and extended crack with Dirichlet boundary conditions. First, similarly with the chapter 4, a MUSIC-type imaging algorithm for locating a set of narrow cracks is developed from the fact that the collected Multi-Static Response (MSR) matrix data can be modeled via a rigorous asymptotic

formulation. Next, reconstruction of extended crack from boundary measurements is discussed. This is based on the asymptotic expansion for the boundary perturbations due to a shape deformation of the crack. Numerical experiments demonstrating the performance of the proposed imaging algorithm are presented

In concluding this introduction, in this thesis, although we worked only on a two-dimensional crack and screen problem, yet the mathematical treatment of asymptotic formula, Fréchet derivative, etc. can be developed for the three dimensional problem as well. Hence, we expect all such results herein to be a starting point of a forthcoming implementation of the three-dimensional problem.

Results from this thesis can be found in contributions [15, 54, 66, 67, 68, 69].

## Première partie

# Reconstruction of Penetrable Cracks

## Sommaire

<b>1</b>	<b>Reconstructing End-Points of Thin Conductivity Inclusions</b>	<b>16</b>
1.1	Introduction . . . . .	16
1.2	Mathematical formulation for the conductivity problem . . . . .	16
1.3	Asymptotic formula for the steady state voltage potential . . . . .	17
1.4	Reconstruction algorithm for identifying the end-points of single thin inclusion . . . . .	19
1.5	Numerical examples . . . . .	20
1.6	Reconstruction algorithm for identifying the end-points of multiple thin inclusions . . . . .	24
1.7	Numerical examples . . . . .	28
1.8	Conclusion . . . . .	36
<b>2</b>	<b>Imaging of Thin Penetrable Inclusions by a MUSIC-Type Algorithm</b>	<b>37</b>
2.1	Introduction . . . . .	37
2.2	Maxwell's equations and the direct scattering problem . . . . .	39
2.2.1	Maxwell's equation and mathematical formulation . . . . .	39
2.3	The direct scattering problem and the asymptotic formulation of the scattering amplitude . . . . .	40
2.4	MUSIC type algorithm for imaging a thin inclusion and estimating its length . . . . .	42
2.4.1	Contrast of permittivity : $\gamma = \gamma_0, \varepsilon \neq \varepsilon_0$ . . . . .	43
2.4.2	Contrast of permeability : $\gamma \neq \gamma_0, \varepsilon = \varepsilon_0$ . . . . .	45
2.4.3	Contrast of permittivity and permeability : $\gamma \neq \gamma_0, \varepsilon \neq \varepsilon_0$ . . . . .	46
2.5	Numerical examples . . . . .	47
2.5.1	Common features . . . . .	47
2.5.2	Permittivity contrast only ( $\mu = \mu_0, \varepsilon \neq \varepsilon_0$ ) . . . . .	48
2.5.3	Preliminary results . . . . .	48
2.5.4	On inverse crime and the use of other datasets . . . . .	55
2.5.5	Robustness with respect to noise . . . . .	57
2.5.6	Permeability contrast only ( $\mu \neq \mu_0, \varepsilon = \varepsilon_0$ ) . . . . .	63
2.5.7	Estimation of the best $b$ . . . . .	63
2.5.8	Further examples . . . . .	65
2.5.9	Permittivity and permeability contrasts ( $\mu \neq \mu_0, \varepsilon \neq \varepsilon_0$ ) . . . . .	65
2.5.10	Extension to multiple inclusions . . . . .	71
2.6	Conclusion . . . . .	75
<b>3</b>	<b>Reconstruction of Thin Electromagnetic Inclusions by a Level Set Method</b>	<b>76</b>
3.1	Introduction . . . . .	76

---

3.2	Representing thin inclusion with two level set functions . . . . .	78
3.3	Shape deformation by calculus of variations . . . . .	79
3.3.1	Gradient directions . . . . .	79
3.3.2	Calculation of $\delta b$ due to shape deformation . . . . .	80
3.3.3	Calculation of the gradient direction . . . . .	82
3.4	Evolution of level set functions $\varphi$ and $\psi$ . . . . .	85
3.5	Reconstruction algorithm . . . . .	85
3.6	Numerical Examples . . . . .	86
3.6.1	Permittivity contrast only ( $\mu = \mu_0, \varepsilon \neq \varepsilon_0$ ) . . . . .	87
3.6.2	Permeability contrast only ( $\mu \neq \mu_0, \varepsilon = \varepsilon_0$ ) . . . . .	93
3.7	Conclusion . . . . .	97

---



# 1 Reconstructing End-Points of Thin Conductivity Inclusions

In this chapter we propose an algorithm for retrieving the end points of thin rectangular inhomogeneities of finite conductivity in a homogeneous medium. It is based on an appropriate asymptotic formula for steady state voltage potentials in the presence of thin inhomogeneities. Various numerical experiments exhibit that the proposed algorithm is fast and effective.

## 1.1 Introduction

We consider an inverse problem for reconstructing end-points of thin conductivity inclusion which occurs in the Electrical Impedance Tomography (EIT). Based on the two-dimensional real-time location search algorithm [18] and asymptotic formula for steady state voltage potentials in the presence of thin inhomogeneities [25], an algorithm for finding the end-points of thin inclusions of discontinuous electrical conductivity by two-different current-voltage measurements has been suggested in [4, 5] for single and multiple case respectively.

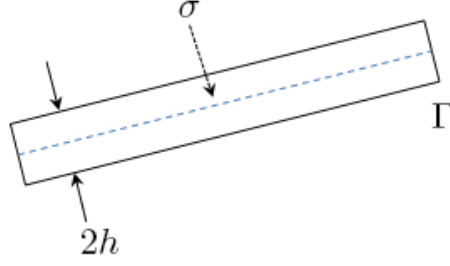
In this chapter, from the idea introduced originally in [4], we present some numerical examples for estimating the end-points for the single thin inclusion. Furthermore, we develop a fast and effective algorithm for retrieving end points of multiple inclusions based on an appropriate asymptotic formula for steady state voltage potentials. The main point of this algorithm is to solve the problem of identifying simple poles and residues of a meromorphic function from measured data on the boundary, the simple poles being the end-points of inclusions and the residues indicating the directions of inclusions for joining end-points.

This chapter is structured as follows. In the second section, following this introduction, the mathematical formulation for conductivity problem is introduced. In section 1.3, the representation formula for the steady state voltage potential in terms of the thickness of inhomogeneities is proposed. In section 1.4, the algorithm for estimating the end-points of the single thin inclusion is sketched. Then, in section 1.5, some numerical examples for estimating the end-points for the single thin inclusion are presented. In section 1.6, the design of an algorithm for identifying the end-points of the multiple thin inclusions is investigated. In section 1.7, numerical experiments demonstrating the performance of the proposed algorithm are presented. A short conclusion follows in the last section.

## 1.2 Mathematical formulation for the conductivity problem

Let  $\Omega \subset \mathbb{R}^n$ ,  $n \geq 2$ , be a homogeneous, electrically conducting domain with smooth boundary  $\partial\Omega$  and  $\mathbf{x}$  be a position vector in  $\mathbb{R}^n$ . By dropping out the time dependence  $e^{-i\omega t}$  and taking the real part of all quantities, the time-harmonic electric field  $\mathbf{E}$  and magnetic field  $\mathbf{H}$  satisfy Maxwell's equations

$$\nabla \times \mathbf{E}(\mathbf{x}) = i\omega\mu(\mathbf{x})\mathbf{H}(\mathbf{x}) \quad \text{and} \quad \nabla \times \mathbf{H}(\mathbf{x}) = (\gamma(\mathbf{x}) - i\omega\varepsilon(\mathbf{x}))\mathbf{E}(\mathbf{x}). \quad (1.1)$$

FIG. 1.1 – Sketch of the thin inclusion  $\Gamma$ .

Here  $\omega > 0$  denotes the given frequency,  $\gamma(\mathbf{x})$  is the conductivity,  $\varepsilon(\mathbf{x})$  is the permittivity, and  $\mu(\mathbf{x})$  is the magnetic permeability at  $\mathbf{x}$ .

Since  $\nabla \cdot \nabla \times \mathbf{H}(\mathbf{x}) = 0$ , a direct calculation yields

$$\nabla \cdot (\gamma(\mathbf{x}) - i\omega\varepsilon(\mathbf{x}))\mathbf{E}(\mathbf{x}) = 0.$$

Notice that at a low enough frequency  $\omega$ , we can set  $\nabla \times \mathbf{E}(\mathbf{x}) = 0$  and the term  $-i\omega\varepsilon(\mathbf{x})$  can be negligible. Then from the above identities, we can define the steady state voltage potential  $u$  in  $\Omega$  which satisfies

$$\nabla u(\mathbf{x}) = \mathbf{E}(\mathbf{x}).$$

Hence, we can formulate the following conductivity problem :

$$\nabla \cdot (\gamma(\mathbf{x})\nabla u(\mathbf{x})) = 0 \quad \text{for } \mathbf{x} \in \Omega.$$

### 1.3 Asymptotic formula for the steady state voltage potential

Let us assume that two-dimensional homogeneous domain  $\Omega$  contains a rectangular thin inclusion denoted as  $\Gamma$  which is localized in the neighborhood of a straight curve. To be more precise, we consider an inclusion of the form

$$\Gamma = \{x + \eta n(x) : x \in \sigma, \eta \in (-h, h)\}, \quad (1.2)$$

where  $\sigma$  is a straight line segment contained in  $\Omega$ , with strictly positive distance from the boundary  $\partial\Omega$ ,  $n(x)$  is a unit normal to  $\sigma$  at  $x$ , and  $h$  is a positive small constant which specifies the thickness of the inclusion (see Fig. 1.1).

Let  $0 < \gamma_0 < +\infty$  and  $0 < \gamma < +\infty$  denote the conductivity of the domain  $\Omega$  and  $\Gamma$ , respectively. Throughout this chapter, we assume that these are strictly positive constants. By using this notation, we adopt the piecewise constant conductivity

$$\gamma(x) = \begin{cases} \gamma_0 & \text{for } x \in \Omega \setminus \bar{\Gamma} \\ \gamma & \text{for } x \in \Gamma \end{cases}. \quad (1.3)$$

If there is no inclusion, i.e., in the homogeneous domain, the function  $\gamma(x)$  is equal to  $\gamma_0$ . For the sake of simplicity, we set  $\gamma_0$  equal to 1.

Let  $u$  be the steady state voltage potential in the presence of the inclusion  $\Gamma$ , that is, the unique solution to

$$\nabla \cdot (\gamma(x)\nabla u(x)) = 0 \quad \text{for } x \in \Omega$$

with the Neumann boundary condition

$$\gamma_0 \frac{\partial u(x)}{\partial \nu(x)} = g(x) \quad \text{for } x \in \partial\Omega$$

and the compatibility condition

$$\int_{\partial\Omega} u(x) dS(x) = 0.$$

Here  $\nu(x)$  denote the unit outer normal to  $\partial\Omega$  at  $x$  and the function  $g \in H^{-\frac{1}{2}}(\partial\Omega)$  represents the applied boundary current satisfies the normalization condition to restore uniqueness

$$\int_{\partial\Omega} g(x) dS(x) = 0.$$

Let us denote  $u_0$  be the potential induced by the current  $g$  in the domain  $\Omega$  without  $\Gamma$ , that is, the unique solution to

$$\gamma_0 \Delta u_0(x) = 0 \quad \text{for } x \in \Omega$$

with the Neumann boundary condition

$$\gamma_0 \frac{\partial u_0(x)}{\partial \nu(x)} = g(x) \quad \text{for } x \in \partial\Omega$$

and the normalization condition

$$\int_{\partial\Omega} u_0(x) dS(x) = 0.$$

In order to introduce the asymptotic expansion of  $u$ , we define a symmetric matrix  $A(x)$  in appropriate manner as follows.

**Definition 1.1** *For every  $x \in \sigma$ , let  $\tau(x)$  and  $n(x)$  be unit vectors that are respectively tangent with and normal to  $\sigma$  at  $x$ . The symmetric matrix  $A(x)$  is as such [25] :*

1.  $A(x)$  has eigenvectors  $\tau(x)$  and  $n(x)$
2. The eigenvalue corresponding to  $\tau(x)$  is  $2(\gamma - \gamma_0)$
3. The eigenvalue corresponding to  $n(x)$  is  $2(\gamma - \gamma_0) \frac{\gamma_0}{\gamma}$ .

In this chapter, we set  $\gamma_0$  equal to 1 for the sake of simplicity.

Based on the Definition 1.1, the following result has been introduced in [4] (see [25] for a rigorous error analysis) :

$$u(y) = u_0(y) + hu_\sigma(y) + o(h), \quad y \in \partial\Omega, \quad (1.4)$$

where the correction term  $u_\sigma$  is given by

$$u_\sigma(y) = - \int_{\sigma} \nabla u_0(x) A(x) \nabla_x N(x, y) d\sigma(x), \quad y \in \bar{\Omega} \setminus \sigma.$$

Here  $N(x, y)$  is the Neumann function related to the domain  $\Omega$ . Let us denote  $\Phi(x, y)$  be the free-space fundamental solution for the Laplace equation

$$\Phi(x, y) = -\frac{1}{2\pi} \ln |x - y|.$$

Since the function  $N(x, y) - \Phi(x, y)$  is smooth, we can write the correction term  $u_\sigma$  as

$$u_\sigma(y) = - \int_{\sigma} \nabla u_0(x) A(x) \nabla_x \Phi(x, y) d\sigma(x) + w_\sigma(y), \quad y \in \bar{\Omega} \setminus \sigma$$

where

$$w_\sigma(y) = - \int_{\sigma} \nabla u_0(x) A(x) \nabla_x (N(x, y) - \Phi(x, y)) d\sigma(x)$$

is the harmonic function in  $\Omega$  and has normal derivative such that

$$\frac{\partial u_\sigma(x)}{\partial \nu(x)} = 0, \quad x \in \partial\Omega$$

and

$$\int_{\partial\Omega} u_\sigma(x) dS(x) = 0.$$

## 1.4 Reconstruction algorithm for identifying the end-points of single thin inclusion

In this section, we present an algorithm for reconstructing a thin inclusion from the boundary measurements. This algorithm is limited to a straight supporting curve  $\sigma$  and is not valid anymore for arbitrary curves, refer to Fig. 1.4. For the detailed description, we refer to the main reference [4].

For any unit vector  $a \in \mathbb{R}^2$ , let us denote  $u_\sigma^a(x)$  be the correction term corresponds to the linear background solution

$$u_\sigma^a(x) = a \cdot x - \frac{1}{|\partial\Omega|} \int_{\partial\Omega} a \cdot y dS(y),$$

i.e., to the Neumann data  $g(x) = a \cdot \nu(x)$ .

We first note that, if we denote by  $e_1$  and  $e_2$  the unit vectors  $(1, 0)$  and  $(0, 1)$ , for any unit vector  $a$ , we have

$$u_\sigma^a = (a \cdot e_1) u_\sigma^{e_1} + (a \cdot e_2) u_\sigma^{e_2} \quad (1.5)$$

so, the knowledge of  $u_\sigma^{a_1}$  and  $u_\sigma^{a_2}$  for any two orthogonal vectors  $a_1$  and  $a_2$  corresponds to the knowledge of  $u_\sigma^{e_j}$  for  $j = 1, 2$ .

Let us to be  $P$  and  $Q$  as the end-points of  $\sigma$ . In the case of a straight line segment, the matrix  $A$  in definition 1.1 is constant along  $\sigma$ . Let  $\tilde{e}_1 = \frac{\overrightarrow{PQ}}{|\overrightarrow{PQ}|}$  and  $\tilde{e}_2$  a unit vector orthogonal to  $\tilde{e}_1$ .

Let us denote  $\mathcal{D}_\Omega v(x)$  the double layer potential of the density function  $v$ , defined by

$$\mathcal{D}_\Omega v(x) = \int_{\partial\Omega} v(y) \frac{\partial \Phi(x, y)}{\partial \nu(y)} dS(y)$$

for any  $x \in \mathbb{R}^2 \setminus \partial\Omega$ . Then the following lemma holds [4].

**Lemma 1.2** *Let  $S$  be an open domain with  $C^2$  boundary  $\partial S$  containing  $\overline{\Omega}$ . For any pair of unit vectors  $a$  and  $a^*$ , we have*

$$\int_{\partial S} \frac{\partial \mathcal{D}_\Omega(u_\sigma^a|_{\partial\Omega})(y)}{\partial \nu(y)} a^* \cdot y dS(y) - \int_{\partial S} \partial \mathcal{D}_\Omega(u_\sigma^a|_{\partial\Omega})(y) a^* \cdot \nu(y) dS(y) = |\sigma| a^* \cdot A \cdot a$$

where  $\nu$  denotes the unit normal to  $\partial S$  pointing outside  $S$ .

From the above lemma, the components of matrix  $A$  in the basis  $(e_1, e_2)$  are given by

$$A_{jl} = \frac{1}{|\sigma|} \int_{\partial S} \frac{\partial \mathcal{D}_\Omega(u_\sigma^{e_j}|_{\partial\Omega})(y)}{\partial \nu(y)} e_l \cdot y dS(y) - \int_{\partial S} \partial \mathcal{D}_\Omega(u_\sigma^{e_j}|_{\partial\Omega})(y) e_l \cdot \nu(y) dS(y).$$

Notice that in order to distinguish between  $\tilde{e}_1$  and  $\tilde{e}_2$  (which one is tangent and which one is orthogonal to  $\sigma$ ) it is not necessary to know the exact value of  $\gamma$  and  $|\sigma|$ . The sign of the eigenvalues of  $A_{jl}$  tells us if  $\gamma$  is larger or smaller than 1 : if the eigenvalues are positive, then  $\gamma > 1$  and  $\tilde{e}_1$  corresponds to the largest eigenvalue. If the eigenvalues are negative, then  $\gamma < 1$ , and  $\tilde{e}_1$  corresponds to the eigenvalue with smaller absolute value.

Now, let us express everything in the coordinate system  $(\tilde{e}_1, \tilde{e}_2)$ . In this way,  $P = (p_1, \zeta)$  and  $Q = (q_1, \zeta)$ . Straightforwardly, one can see that

$$\mathcal{D}_\Omega u_\sigma^{\tilde{e}_2}(0, y_2) = -\frac{1}{\pi} \left(1 - \frac{1}{\gamma}\right) (\zeta - y_2) \int_\sigma \frac{1}{|x - (0, y_2)|} dS(x). \quad (1.6)$$

Notice that, once  $\tilde{e}_2$  is known,  $u_\sigma^{\tilde{e}_2}|_{\partial\Omega}$  is obtained from  $u_\sigma^{e_1}|_{\partial\Omega}$  and  $u_\sigma^{e_2}|_{\partial\Omega}$  according to (1.5). Hence, the left-hand side of (1.6) is known in  $\mathbb{R}^2 \setminus \overline{\Omega}$  and  $\zeta$  can be identified as the value where it changes sign.

Finally, assuming  $p_1 < q_1$  then we can determine  $p_1$  and  $q_1$  by

$$\mathcal{D}_\Omega u_\sigma^{\tilde{e}_1}(y_1, \zeta) = -\frac{1}{\pi} (\gamma - 1) \ln \left( \frac{y_1 - q_1}{y_1 - p_1} \right)$$

for any  $y_1 < p_1$  or  $y_1 > q_1$ .

## 1.5 Numerical examples

In this section, the results of numerical simulations for reconstructing end-points of a thin inclusion are given. To that effect, we use the numerical algorithm introduced in [4]. With reference to Fig. 1.2 for an illustration of the configuration, we consider the domain  $\Omega$  as an unit disk centered at  $(-2, 0)$  in  $\mathbb{R}^2$  and  $S$  as a disk centered at  $(-2, 0)$  with radius 3. We set the parameters  $\gamma$  and  $\gamma_0$  to 5 (see remark 1.3) and 1, respectively.

As for the numerical calculation of the matrix  $A$  defined in 1.1, it is carried out by using  $M = 128$  equidistant points on  $S$ ,

$$\left( 3 \cos \frac{(j-1)\pi}{M} - 2, 3 \sin \frac{(j-1)\pi}{M} \right) \text{ for } j = 1, 2, \dots, M.$$

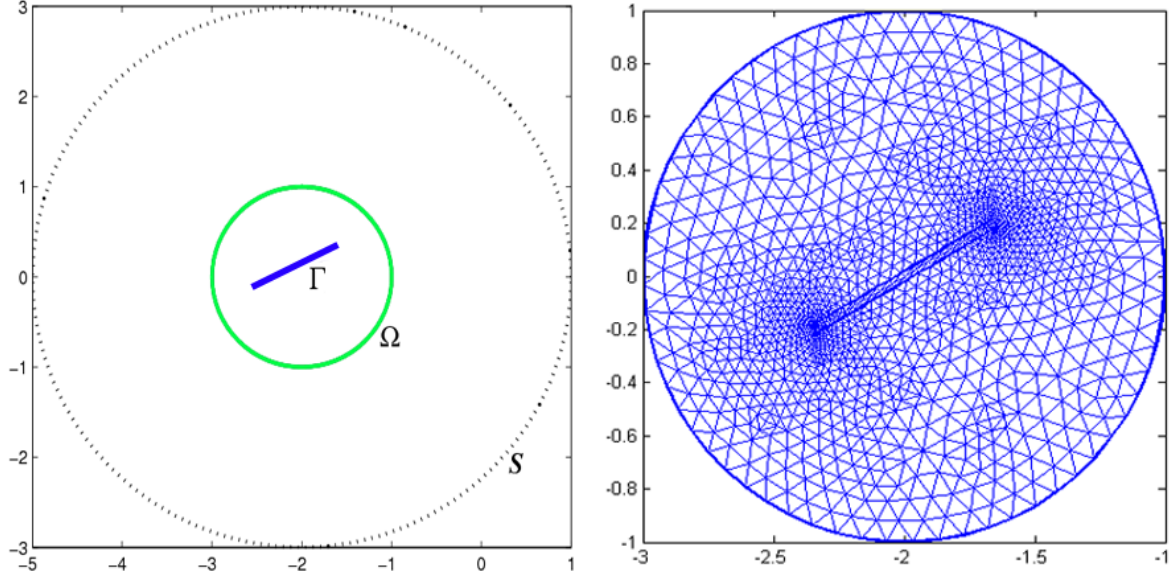


FIG. 1.2 – Left : Description of the configuration in section 1.5. Right : Triangular mesh generated by the package ‘pdetool’ in Matlab for computing the forward solutions  $u$  and  $u_0$  for  $\Gamma_3$ .

At this stage, according to the asymptotic formula (1.4), the forward solutions  $u$  and  $u_0$  are computed by using the FEM method and the meshes have been generated by the package ‘pdetool’ in Matlab for each example —in Fig. 1.2, we exhibit the triangular mesh specialized to the  $\Gamma_3$  considered below. For every example, results with a white Gaussian noise added to the data (so as the signal-to-noise (SNR) ratio is 20 dB) are displayed in addition to noiseless cases.

**Remark 1.3** *In these numerical simulations, several values of  $\gamma$  as 0.1, 0.5, 3, 5, 7 and 10 have been chosen. With all such values of  $\gamma$  we have observed that the results obtained when searching for the end-points of the thin inclusion remain almost the same. We also observed that the eigenvalue corresponding to  $\tau$  is positive when the value  $\gamma$  is greater than 1 and is negative when the value  $\gamma$  lies between 0 and 1 (see [4]).*

Four  $\sigma_j$  characteristic of the thin inclusion  $\Gamma_j$  are chosen :

$$\begin{aligned}\sigma_1 &= \{(z, 0) : z \in (-2.4, 1.6)\} \\ \sigma_2 &= \{(z, 0.3) : z \in (-2.4, 1.6)\} \\ \sigma_3 &= \left\{ \begin{pmatrix} \cos \theta & \sin \theta \\ -\sin \theta & \cos \theta \end{pmatrix} (z, 0)^T : z \in (-2.4, 1.6), \theta = \frac{\pi}{6} \right\} \\ \sigma_4 &= \{(z, (z+2)^2) : z \in (-2.4, 1.6)\}\end{aligned}$$

and the thickness  $h$  of  $\Gamma_j$  is fixed 0.015. Notice that  $\Gamma_2$  is translated from  $\Gamma_1$  and  $\Gamma_3$  is rotated from  $\Gamma_1$ .

Retrieved eigenvectors  $\tau(x)$  and  $n(x)$  from matrix  $A(x)$  and two end-points  $P, Q$  are shown in Table 1.1. Next, we add the aforementioned 20dB noise and computed values are shown in Tab. 1.2. Imaging results are displayed in Figs. 1.3 and 1.4.

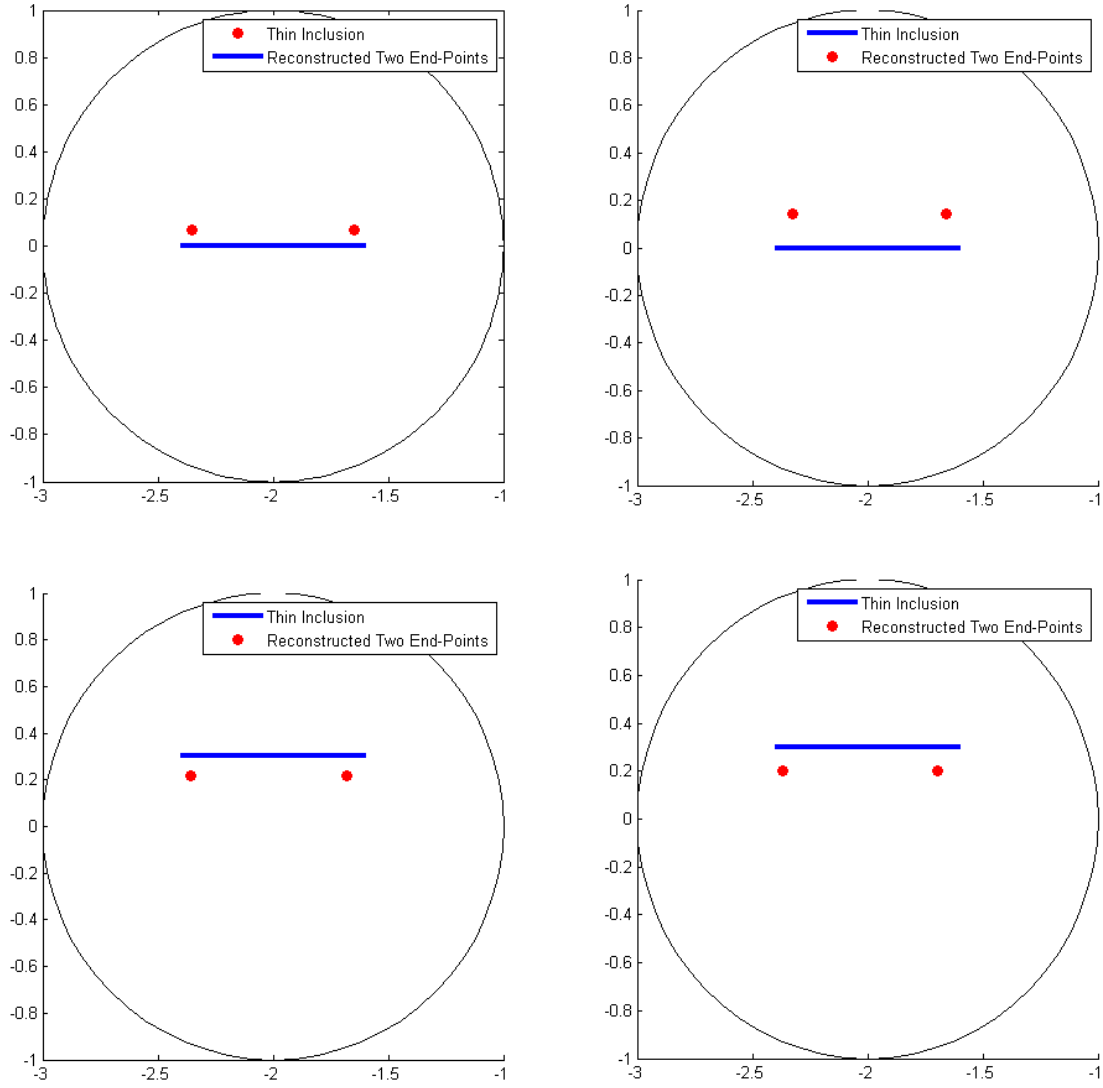


FIG. 1.3 – Illustration of the retrieval of the two end-points of  $\Gamma_1$  (top row) and  $\Gamma_2$  (bottom row) without noise (left column) and with 20dB noise (right column).

	$\tau(x) = \tilde{e}_1$	$n(x) = \tilde{e}_2$	point $P$	point $Q$
$\Gamma_1$	$(1.0000, -0.0098)^T$	$(0.0100, 1.0000)^T$	$(-2.3520, 0.0667)$	$(-1.6499, 0.0667)$
$\Gamma_2$	$(0.9995, 0.0302)^T$	$(-0.0140, 0.9999)^T$	$(-2.3583, 0.2157)$	$(-1.6777, 0.2157)$
$\Gamma_3$	$(0.8714, 0.4905)^T$	$(-0.4958, 0.8684)^T$	$(-2.3398, -0.1147)$	$(-1.7280, 0.2296)$
$\Gamma_4$	$(0.9986, -0.0530)^T$	$(0.0537, 0.9986)^T$	$(-2.5053, 0.0945)$	$(-1.5487, 0.0945)$

TAB. 1.1 – Computed eigenvectors  $\tau(x)$ ,  $n(x)$  and two end-points  $P$ ,  $Q$ .

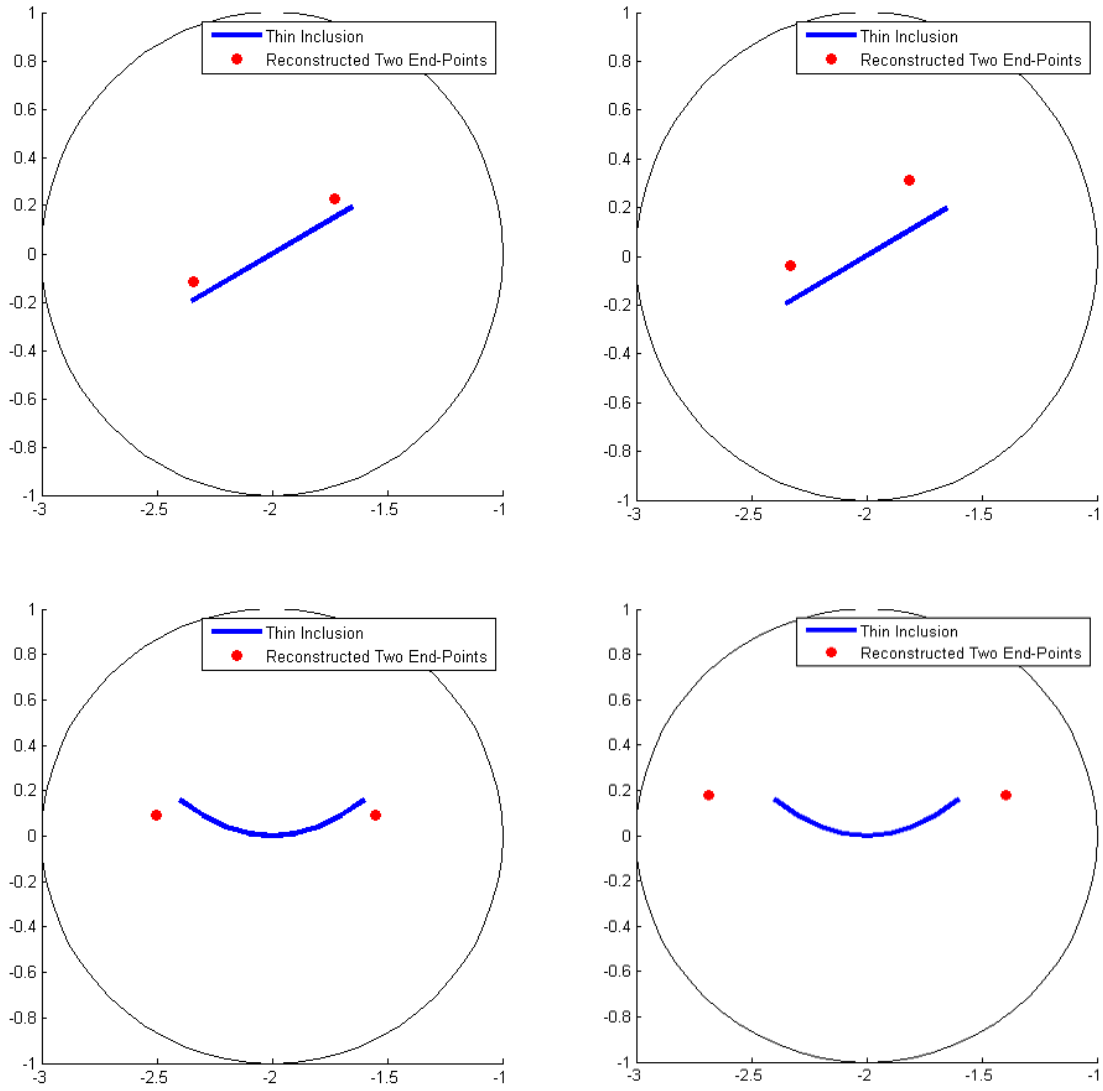


FIG. 1.4 – Illustration of the retrieval of the two end-points of  $\Gamma_3$  (top row) and  $\Gamma_4$  (bottom row) without noise (left column) and with 20dB noise (right column).

From the results for  $\Gamma_1$ ,  $\Gamma_2$  and  $\Gamma_3$ , the imaging algorithm appears useful for the translated and rotated cases. Moreover, we can easily notice that the measured eigenvectors are not sensitive to the observation noise but the measured end-points are. From the results for  $\Gamma_4$ , we can observe that the shape significantly affects the reconstruction. The main reason is that the numerical algorithm is established under the assumption that  $\sigma$  is a straight line, i.e., the thin-inclusion  $\Gamma$  is of rectangular shape.

Now, we end up this section with the following remark.

**Remark 1.4** *With the same choice of  $\sigma_2$ , we adopt the rectangular domain  $\Omega$  instead of the unit circle domain. We set the edges of  $\Omega$  as  $(-3, 1)$ ,  $(-3, -1)$ ,  $(-1, -1)$  and  $(-1, 1)$ . Using the same reconstruction algorithm, we obtain the following results*

$$\tau(x) = (0.9997, 0.0236)^T, \quad n(x) = (-0.0092, 1.0000)^T.$$



	$\tau(x) = \tilde{e}_1$	$n(x) = \tilde{e}_2$	point $P$	point $Q$
$\Gamma_1$	$(1.0000, -0.0079)^T$	$(0.0469, 0.9989)^T$	$(-2.3228, 0.1451)$	$(-1.6592, 0.1451)$
$\Gamma_2$	$(0.9999, 0.0141)^T$	$(-0.0245, 0.9997)^T$	$(-2.3665, 0.2000)$	$(-1.6944, 0.2000)$
$\Gamma_3$	$(0.8061, -0.5779)^T$	$(0.5894, 0.8078)^T$	$(-2.3332, -0.0363)$	$(-1.8150, 0.3122)$
$\Gamma_4$	$(0.9967, -0.8090)^T$	$(0.0888, 0.9960)^T$	$(-2.6866, 0.1811)$	$(-1.3959, 0.1811)$

TAB. 1.2 – Computed eigenvectors  $\tau(x)$ ,  $n(x)$  and two end-points  $P$ ,  $Q$  with 20dB noise.

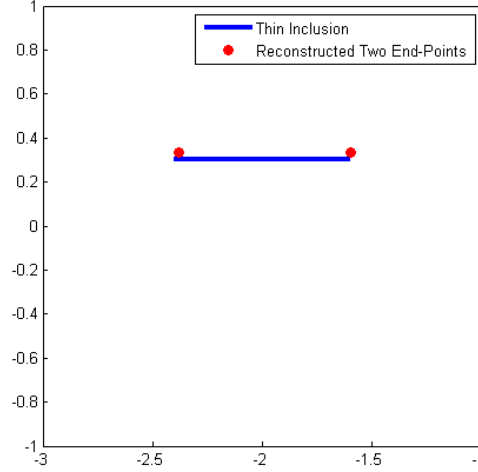


FIG. 1.5 – Illustration of reconstructed two end-points of thin inclusion  $\Gamma_2$  for the rectangular domain case example (compare with Fig. 1.3).

With this result, we can set  $\tilde{e}_1 = (1, 0)$  and  $\tilde{e}_2 = (0, 1)$ . With this coordinate system  $(\tilde{e}_1, \tilde{e}_2)$ , we obtain the following two end-points;

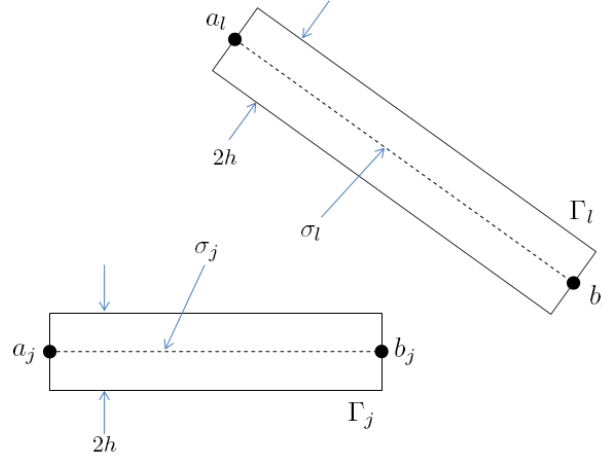
$$P = (-2.3787, 0.3333), \quad Q = (-1.5940, 0.3333).$$

Let us compare this result with another one for  $\Gamma_2$ . The only difference between the second example and this one is the shape of the domain  $\Omega$ . In brief, we observe that we can more accurately estimate the end-points of the thin inclusion when using the rectangular domain. Then, though the reconstruction algorithm is generated on the assumption that the domain remains smooth, we believe that it can be extended to a domain with Lipschitz boundary.

## 1.6 Reconstruction algorithm for identifying the end-points of multiple thin inclusions

Let  $\Omega \subset \mathbb{R}^2$  be a smooth, bounded domain that represents a homogeneous medium. We assume that this medium contains a set of  $N$  well-separated thin inclusions denoted as

$$\Gamma = \bigcup_{j=1}^N \Gamma_j$$

FIG. 1.6 – Sketch of set of thin inclusions  $\Gamma_j$ .

where each  $\Gamma_j$  are apart from  $\partial\Omega$  and localized in the neighborhood of a curve, say  $\sigma_j$ , that is

$$\Gamma_j = \{x + \eta n_j(x) : x \in \sigma_j, \eta \in (-h, h)\},$$

where the supporting  $\sigma_j$  is a straight line in  $\Omega$  (with strictly positive distance from its boundary  $\partial\Omega$ , if there were any at finite distance),  $n_j(x)$  is the unit normal to  $\sigma_j$  at  $x$ , and  $h$  is a positive constant which specifies the thickness of the inclusion (see Fig. 1.6).

Let  $0 < \gamma_0 < +\infty$  and  $0 < \gamma_j < +\infty$  denote the conductivity of the domain  $\Omega$  and  $\Gamma_j$ , respectively. For the sake of simplicity, we set  $\gamma_0$  equal to 1.

Then the asymptotic expansion of steady state voltage potential  $u(x)$  can be represented in terms of the thickness  $h$  (compare to formula (1.4)),

$$\begin{aligned} u(y) &= u_0(y) + hu_\sigma(y) \\ &= u_0(y) - h \sum_{j=1}^N \int_{\sigma_j} \nabla u_0(x) \mathcal{A}^j(x) \nabla_x N(x, y) d\sigma_j(x) + o(h), \quad y \in \partial\Omega. \end{aligned} \quad (1.7)$$

Here  $N(x, y)$  is the Neumann function for the domain  $\Omega$  and  $\mathcal{A}^j = (A_{kl}^j)_{k,l=1,2}$  is the symmetric matrix defined in the same manner as in definition 1.1.

Let us denote  $a_j, b_j, j = 1, \dots, N$ , be the complex numbers representing the end points of thin inclusions of thin inclusions, and let us define

$$H_\sigma(x) := \int_{\partial\Omega} \frac{\partial u_\sigma(y)}{\partial \nu(y)} \Phi(x, y) dS(y) - \int_{\partial\Omega} u_\sigma(y) \frac{\Phi(x, y)}{\partial \nu(y)} dS(y)$$

Here,  $\Phi(x, y)$  is the two-dimensional fundamental solution for the Laplace equation

$$\Phi(x, y) = -\frac{1}{2\pi} \ln |x - y|.$$

Then, the following theorem holds [5] :

**Theorem 1.5** *Let  $x = (x_1, x_2) = x_1 + ix_2$ . For the end-points of thin inclusions  $a_j, b_j$ ,  $j = 1, \dots, N$ ,*

$$V_\sigma(x) := \frac{\partial H_\sigma}{\partial x_1} - i \frac{\partial H_\sigma}{\partial x_2} = \sum_{j=1}^N r_{\sigma,j} \left( \frac{1}{x - b_j} - \frac{1}{x - a_j} \right). \quad (1.8)$$

*Here, the residue of  $V_\sigma$  at one end-point gives information about the direction of the segment*

$$\text{Res}(V_\sigma(x), b_j) = r_{\sigma,j} = -\text{Res}(V_\sigma(x), a_j).$$

From theorem 1.5, in order to find the end-points of the thin inclusions, authors in [5] considered the problem for identifying the number  $N$ , the residues  $r_{\sigma,j}$  and the locations  $a_j, b_j$  of the poles from the meromorphic function (1.8)

$$V_\sigma(x) = \sum_{j=1}^N r_{\sigma,j} \left( \frac{1}{x - b_j} - \frac{1}{x - a_j} \right) = \sum_{j=1}^N \frac{\beta_j}{x - \alpha_j}$$

on a domain  $\Omega$  which encloses all poles  $\alpha_j$ .

The identifying algorithm has been already presented in [48]. The underlying idea comes from the following Cauchy integral formula

$$\frac{1}{2\pi i} \int_C x^n V_\sigma(x) dx = \sum_{j=1}^N \beta_j \alpha_j^n$$

for a simple closed curve  $C$ . Identification of simple poles is based on the following :

**Lemma 1.6** *Suppose that the sequence  $\{c_n\}$  takes the form*

$$c_n = \sum_{j=1}^k \beta_j \alpha_j^n$$

*for  $n = 0, 1, \dots$ . If  $l_1, \dots, l_k$  satisfies the generating equation*

$$c_{n+k} + l_1 c_{n+k-1} + \dots + l_k c_n = 0 \quad \text{for } n = 0, 1, \dots, k-1 \quad (1.9)$$

*then  $\alpha_1, \alpha_2, \dots, \alpha_k$  are solutions of*

$$z^k + l_1 z^{k-1} + \dots + l_k = 0. \quad (1.10)$$

*The converse is also true. Furthermore, if (1.9) holds, then it holds for all  $n$ .*

The proof can be found in [48]. For convenience, we state the proof in appendix. This idea leads to the following formulation.

Let  $u_k$  be the solution with Neumann boundary condition  $g_k$  for  $g = (g_1, g_2)$ , normal vector to the boundary  $\partial\Omega$ , and introduce  $v(x) = (x_1 + ix_2)^n$  where  $x = (x_1, x_2) \in \overline{\Omega}$ .

Then we have

$$\begin{aligned}
\int_{\partial\Omega} (u_k(y) - y_k) \frac{\partial v(y)}{\partial \nu(y)} dS(y) &= h \sum_{j=1}^N \int_{\partial\Omega} \int_{\gamma_j} (A_{k1}^j, A_{k2}^j) \nabla_x N(x, y) d\gamma_j(x) \frac{\partial v(y)}{\partial \nu(y)} dS(y) + o(h) \\
&= h \sum_{j=1}^N \int_{\gamma_j} (A_{k1}^j, A_{k2}^j) \nabla v(x) d\gamma_j(x) + o(h) \\
&= h \sum_{j=1}^N (A_{k1}^j + i A_{k2}^j) \frac{|b_j - a_j|}{b_j - a_j} (b_j^n - a_j^n) + o(h).
\end{aligned}$$

In order to apply Lemma 1.6, it appears that we need two different boundary measurements  $u_1$  and  $u_2$ , applying two different Neumann boundary conditions  $g_1$  and  $g_2$  respectively. By using two different boundary measurements  $u_1$  and  $u_2$ , we can obtain

$$\begin{aligned}
&\int_{\partial\Omega} [u_1(y) - y_1 - i(u_2(y) - y_2)] \frac{\partial}{\partial \nu(y)} (y_1 + iy_2)^n dS(y) \\
&= h \sum_{j=1}^N \text{trace}(\mathcal{A}^j) \frac{\overline{b_j - a_j}}{|b_j - a_j|} (b_j^n - a_j^n) + o(h).
\end{aligned} \tag{1.11}$$

Here,  $\text{trace}(\mathcal{A}^j)$  is the trace of matrix  $\mathcal{A}^j$  for  $j = 1, 2, \dots, N$ . Combining (1.11), lemma 1.6 with the simple pole algorithm [48], we can obtain the following reconstruction algorithm.

**Step 1.** Set  $c_0 = 0$ . For sufficiently large  $M$ , let us calculate the complex numbers  $c_n$  for  $n = 1, 2, \dots, 2M - 1$ , by

$$c_n := \int_{\partial\Omega} [u_1(y) - y_1 - i(u_2(y) - y_2)] \frac{\partial}{\partial \nu(y)} (y_1 + iy_2)^n d\sigma(y). \tag{1.12}$$

**Step 2.** Solve for  $l_1, l_2, \dots, l_M$  the system of linear equations

$$\begin{pmatrix} c_0 & c_1 & \cdots & c_{M-1} \\ c_1 & c_2 & \cdots & c_M \\ \vdots & \vdots & & \vdots \\ c_{M-1} & c_M & \cdots & c_{2M-2} \end{pmatrix} \begin{pmatrix} l_M \\ l_{M-1} \\ \vdots \\ l_1 \end{pmatrix} = \begin{pmatrix} -c_M \\ -c_{M+1} \\ \vdots \\ -c_{2M-1} \end{pmatrix}. \tag{1.13}$$

**Step 3.** (Determination of end-points) Find the zeros  $\alpha_1, \dots, \alpha_M$  of the polynomial equation  $z^M + l_1 z^{M-1} + \dots + l_M = 0$ .

**Step 4.** (Determination of residue for joining end-points) Solve the equation

$$\begin{pmatrix} 1 & 1 & \cdots & 1 \\ \alpha_1 & \alpha_2 & \cdots & \alpha_N \\ \vdots & \vdots & & \vdots \\ \alpha_1^{M-1} & \alpha_2^{M-1} & \cdots & \alpha_M^{M-1} \end{pmatrix} \begin{pmatrix} \beta_1 \\ \beta_2 \\ \vdots \\ \beta_M \end{pmatrix} = \begin{pmatrix} c_0 \\ c_1 \\ \vdots \\ c_{M-1} \end{pmatrix}$$

to find  $\beta_1, \dots, \beta_M$ .

**Step 5.** Finally, discard  $\alpha_j$  if  $|\beta_j|$  is reasonably small. To find the line segments, join the remaining  $\alpha_j$ 's with the same corresponding  $\beta$ 's up to sign. If it is not enough, then consider also the directions of  $\beta$ 's.

$ \beta_j $	$\beta_j$	$\alpha_j$	End-Points
0.0000	$-0.0000 - 0.0000i$	$-0.0296 - 1.6380i$	No
0.0000	$-0.0000 - 0.0000i$	$1.5328 - 0.0336i$	No
0.0000	$-0.0000 - 0.0000i$	$0.7049 + 1.4487i$	No
0.0000	$-0.0000 - 0.0000i$	$-0.3909 + 1.2754i$	No
0.0000	$-0.0000 - 0.0000i$	$-1.2169 + 0.2539i$	No
0.1836	$0.1809 - 0.0314i$	$-0.3701 - 0.4040i$	Yes
0.0935	$0.0822 - 0.0447i$	$-0.3719 - 0.1834i$	Yes
0.1636	$-0.1611 - 0.0285i$	$0.2900 - 0.4165i$	Yes
0.1685	$-0.1505 + 0.0759i$	$0.3423 + 0.1913i$	Yes
0.0563	$0.0484 + 0.0287i$	$0.1821 - 0.0272i$	No

TAB. 1.3 – Computed values of  $\alpha_j$ ,  $\beta_j$  and  $|\beta_j|$  for the first example without noise.

## 1.7 Numerical examples

In this section, the numerical simulations for identifying end-points of multiple thin inclusions are considered, according to the algorithm introduced in the previous section 1.6. The domain  $\Omega$  is chosen as a unit disk centered at  $(0, 0)$  in  $\mathbb{R}^2$  and the thickness  $h$  of all thin inclusions  $\Gamma_j$  is 0.02.

As we mentioned in section 1.6, we first adopt a rectangular shape of the thin inclusions due to the stability of algorithm. For the first example, we consider the case of two thin inclusions parametrized as

$$\Gamma_j = \{x + \eta n_j(x) : x \in \sigma_j, \eta \in (-h, h)\},$$

where

$$\begin{aligned} \sigma_1 &= \left\{ \left( z, \frac{0.2(z - 0.3464)}{0.3464} + 0.2 \right) : z \in (-0.3464, 0.3464) \right\} \\ \sigma_2 &= \{(z, -0.4) : z \in (-0.4, 0.3)\} \end{aligned}$$

and the parameter  $\gamma_j$  is chosen as 5 for  $j = 1, 2$ . Notice that the end-points of  $\Gamma_1$  are

$$a_1 = (0.3464, 0.2000) \quad \text{and} \quad b_1 = (-0.3464, -0.2000)$$

and the end-points of  $\Gamma_2$  are

$$a_2 = (0.3000, -0.4000) \quad \text{and} \quad b_2 = (-0.4000, -0.4000).$$

In order to find the end-points of those two thin inclusions, we have performed the reconstruction presented in previous section with the value of  $M = 10$ . Obtained values of  $\alpha_j$ ,  $\beta_j$  and  $|\beta_j|$  are illustrated in Table 1.3. From this information, we discard  $\alpha_j$  when the associated value of  $|\beta_j|$  is too small and we find four end-points of two thin inclusions.

Let us assume that some noise is added to the measured boundary data, i.e., for  $x \in \partial\Omega$

$$u_{\text{noise}}(x) = u(x) + \xi \times \text{rnd}(-1, 1)$$

$ \beta_j $	$\beta_j$	$\alpha_j$	End-Points
0.0000	$-0.0000 - 0.0000i$	$1.6858 + 0.3455i$	No
0.0000	$-0.0000 - 0.0000i$	$-0.5717 - 1.4782i$	No
0.0000	$-0.0000 + 0.0000i$	$0.1228 + 1.0485i$	No
0.0000	$0.0000 - 0.0000i$	$-0.5925 + 0.9217i$	No
0.0000	$0.0000 - 0.0000i$	$-1.0739 + 0.1080i$	No
0.1607	$-0.1348 + 0.0874i$	$0.3373 + 0.2012i$	Yes
0.0586	$-0.0584 + 0.0040i$	$0.3546 - 0.3604i$	No
0.0891	$-0.0888 - 0.0074i$	$0.2940 - 0.4526i$	Yes
0.1398	$0.1398 + 0.0003i$	$-0.3879 - 0.4139i$	Yes
0.1653	$0.1422 - 0.0843i$	$-0.3364 - 0.2337i$	Yes

TAB. 1.4 – Computed values of  $\alpha_j$ ,  $\beta_j$  and  $|\beta_j|$  for the first example with  $\xi = 10^{-5}$ .

where  $\text{rnd}(-1, 1)$  is a arbitrary real value between  $-1$  and  $1$ . Tab. 1.4, for the case  $\xi = 10^{-5}$ , shows that the algorithm detects end-points and residues accurately. Notice that higher noise level (greater than  $\xi = 10^{-5}$ ) leads to poor results (we observe that the value of  $\alpha_j$  is poor). We recommend [48] for a more detailed discussion.

In Fig. 1.7, we illustrate the results. From them, we can conclude that we retrieve the expected end-points of thin inclusions.

Next, we consider the case of three thin inclusions parametrized as

$$\Gamma_j = \{x + \eta n_j(x) : x \in \sigma_j, \eta \in (-h, h)\},$$

where

$$\begin{aligned} \sigma_1 &= \left\{ \left( z, -\frac{0.5656(z - 0.6822)}{0.5650} - 0.2828 \right) : z \in (0.1172, 0.6822) \right\} \\ \sigma_2 &= \{(z, -0.5) : z \in (-0.6, 0.2)\} \\ \sigma_3 &= \left\{ \left( z, -\frac{0.7608(z + 0.5236)}{0.2472} + 0.0196 \right) : z \in (-0.5236, -0.2764) \right\} \end{aligned}$$

and the parameter  $\gamma_j$  is chosen as 5 for  $j = 1, 2, 3$ . Notice that the end-points of  $\Gamma_1$

$$a_1 = (0.1172, 0.2828) \quad \text{and} \quad b_1 = (0.6822, -0.2828)$$

the end-points of  $\Gamma_2$

$$a_2 = (-0.6000, -0.5000) \quad \text{and} \quad b_2 = (0.2000, -0.5000)$$

and the end-points of  $\Gamma_3$

$$a_3 = (-0.5236, 0.0196) \quad \text{and} \quad b_3 = (-0.2764, 0.7804).$$

The reconstruction algorithm with the value of  $M = 10$  yields values of  $\alpha_j$ ,  $\beta_j$  and  $|\beta_j|$  illustrated in Tab. 1.5. Again, we discard  $\alpha_j$  when the associated value of  $|\beta_j|$  is small and we find six end-points of three thin inclusions.

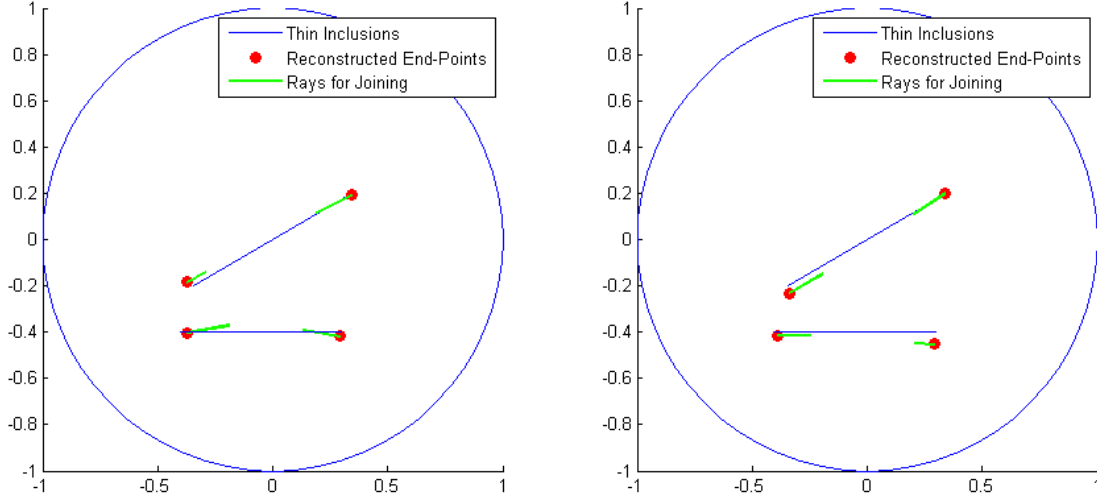


FIG. 1.7 – Reconstructions of two thin inclusions.  $\sigma_j$ 's are given blue lines. Red circles and green rays starting from them represent  $\alpha_j$  and  $\overline{\beta_j}$  without noise (left) and some noise  $\xi = 10^{-5}$ .

$ \beta_j $	$\beta_j$	$\alpha_j$	End-Points
0.0000	$-0.0000 - 0.0000i$	$3.8899 - 3.0467i$	No
0.0000	$-0.0000 - 0.0000i$	$1.4003 + 1.1729i$	No
0.0002	$-0.0000 - 0.0002i$	$-0.4983 - 0.8912i$	No
0.1638	$-0.1168 - 0.1148i$	$0.6850 - 0.2789i$	Yes
0.1830	$0.1830 - 0.0046i$	$-0.5917 - 0.5000i$	Yes
0.1354	$-0.1352 + 0.0086i$	$0.2146 - 0.5150i$	Yes
0.0212	$0.0156 - 0.0144i$	$-0.3873 + 0.7603i$	No
0.1810	$-0.0739 + 0.1652i$	$-0.2789 + 0.7669i$	Yes
0.2170	$0.0565 - 0.2095i$	$-0.4898 + 0.0250i$	Yes
0.1839	$0.0708 + 0.1698i$	$0.1654 + 0.2345i$	Yes

TAB. 1.5 – Computed values of  $\alpha_j$ ,  $\beta_j$  and  $|\beta_j|$  for the second example without noise.

$ \beta_j $	$\beta_j$	$\alpha_j$	End-Points
0.0000	$0.0000 - 0.0000i$	$0.6439 + 1.4667i$	No
0.0003	$0.0003 - 0.0000i$	$-0.1765 + 1.0658i$	No
0.0017	$0.0016 - 0.0005i$	$0.6953 - 0.5859i$	No
0.1459	$-0.1080 - 0.0981i$	$0.6953 - 0.2751i$	Yes
0.1530	$-0.0507 + 0.1444i$	$-0.2767 + 0.7864i$	Yes
0.0922	$-0.0887 - 0.0252i$	$0.1764 - 0.5697i$	Yes
0.2028	$0.2028 - 0.0049i$	$-0.5851 - 0.4936i$	Yes
0.0124	$0.0036 - 0.0119i$	$-0.6685 + 0.2048i$	No
0.2327	$0.0067 - 0.2326i$	$-0.4883 - 0.0521i$	Yes
0.2311	$0.0324 + 0.2288i$	$0.1888 + 0.1661i$	Yes

TAB. 1.6 – Computed values of  $\alpha_j$ ,  $\beta_j$  and  $|\beta_j|$  for the second example with  $\xi = 10^{-4}$ .

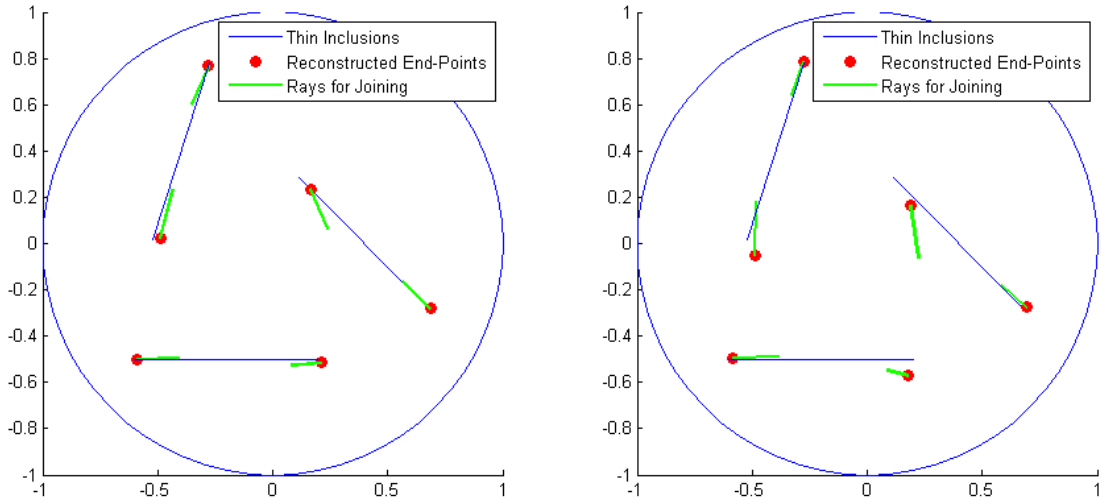


FIG. 1.8 – (All  $\gamma_j$  are the same) Reconstructions of three thin inclusions.  $\sigma_j$ 's are given blue lines. Red circles and green rays starting from them represent  $\alpha_j$  and  $\bar{\beta}_j$  without noise (left) and some noise  $\xi = 10^{-4}$ .

In contrast with the previous example, Tab. 1.6, for the case  $\xi = 10^{-4}$ , shows that the algorithm detects end-points and residues accurately.

In Fig. 1.8, we illustrate the results. We can say that we have obtained the expected end-points of the thin inclusions.

Let us examine the effect of the value  $\gamma_j$ 's. To observe it, we have performed the numerical simulations under the same condition as the one of the second example except  $\gamma_j$ 's. The parameter  $\gamma_j$  is chosen as  $\gamma_1 = 10$ ,  $\gamma_2 = 5$ , and  $\gamma_3 = 20$ .

The reconstruction algorithm is applied with the value of  $M = 10$ . The obtained values of  $\alpha_j$ ,  $\beta_j$  and  $|\beta_j|$  are shown in Tab. 1.7. We still discard  $\alpha_j$  when the associated value of  $|\beta_j|$  is small and we find the six end-points of the three thin inclusions.

$ \beta_j $	$\beta_j$	$\alpha_j$	End-Points
0.0000	$-0.0000 - 0.0000i$	$1.1281 + 0.8499i$	No
0.0000	$-0.0000 - 0.0000i$	$-0.0730 - 1.2244i$	No
0.2622	$-0.1816 - 0.1892i$	$0.6808 - 0.2786i$	Yes
0.0002	$-0.0001 - 0.0000i$	$-0.9143 - 0.4280i$	No
0.1081	$-0.1065 - 0.0186i$	$0.1960 - 0.5422i$	Yes
0.1940	$0.1940 - 0.0018i$	$-0.5865 - 0.4953i$	Yes
0.4325	$-0.1154 + 0.4168i$	$-0.2888 + 0.7606i$	Yes
0.0469	$-0.0279 - 0.0377i$	$-0.4103 + 0.7103i$	No
0.5314	$0.1125 - 0.5194i$	$-0.4791 + 0.0255i$	Yes
0.3717	$0.1251 + 0.3500i$	$0.1608 + 0.1875i$	Yes

TAB. 1.7 – Computed values of  $\alpha_j$ ,  $\beta_j$  and  $|\beta_j|$  for the third example without noise.



$ \beta_j $	$\beta_j$	$\alpha_j$	End-Points
0.0000	$0.0000 + 0.0000i$	$0.5984 - 1.1642i$	No
0.0002	$0.0001 + 0.0002i$	$0.6639 + 0.6711i$	No
0.2613	$-0.1821 - 0.1874i$	$0.6810 - 0.2778i$	Yes
0.1011	$-0.1007 - 0.0094i$	$0.2054 - 0.5468i$	Yes
0.1870	$0.1870 + 0.0048i$	$-0.5916 - 0.4962i$	Yes
0.0001	$-0.0000 - 0.0001i$	$-0.9788 + 0.1254i$	No
0.0150	$-0.0037 - 0.0145i$	$-0.4584 + 0.7498i$	No
0.4052	$-0.1359 + 0.3817i$	$-0.2826 + 0.7621i$	Yes
0.5505	$0.1683 - 0.5241i$	$-0.4697 + 0.0393i$	Yes
0.3553	$0.0671 + 0.3490i$	$0.1805 + 0.1636i$	Yes

TAB. 1.8 – Computed values of  $\alpha_j$ ,  $\beta_j$  and  $|\beta_j|$  for the third example with  $\xi = 10^{-4}$ .

From the results illustrated in Fig. 1.9, we can easily observe that the algorithm is not sensitive to the values of  $\gamma_j$ , neither to translation and rotation of the thin inclusions. Moreover, the rays starting from the estimated end-points are getting long whenever  $\gamma_j$  is large (and getting short for small  $\gamma_j$ ), i.e., we can easily join the end-points.

Now, we apply the algorithm to the non-rectangular thin inclusions. For the fourth example, we consider the case of two thin inclusions parametrized as

$$\Gamma_j = \{x + \eta n_j(x) : x \in \sigma_j, \eta \in (-h, h)\},$$

where

$$\begin{aligned}\sigma_1 &= \{(z, (z + 0.2)^2 + 0.3), z \in (-0.7, 0.3)\} \\ \sigma_2 &= \{(z, -(z - 0.2)^2 - 0.3), z \in (-0.3, 0.7)\}\end{aligned}$$

and the parameter  $\gamma_j$  is chosen as 5 for  $j = 1, 2$ . Notice that the end-points of  $\Gamma_1$  are

$$a_1 = (-0.7000, 0.5500) \quad \text{and} \quad b_1 = (0.3000, 0.5500)$$

and the end-points of  $\Gamma_2$  are

$$a_2 = (-0.3000, -0.5500) \quad \text{and} \quad b_2 = (0.7000, -0.5500).$$

Typical results are in Tables 1.9, 1.10 and in Fig. 1.10 with the value of  $M = 10$  and  $\xi = 5 \times 10^{-4}$ . At this stage, to retrieve the end-points, we must join the  $\alpha$ 's with the same corresponding  $\beta$ 's up to sign of real part, i.e., choose  $\beta_j$  and  $\beta_l$  that satisfy  $\beta_j \approx -\bar{\beta}_l$ .

As a last example, we consider the case of two thin inclusions parametrized as

$$\Gamma_j = \{x + \eta n_j(x) : x \in \sigma_j, \eta \in (-h, h)\},$$

where

$$\begin{aligned}\sigma_1 &= \{(z, -0.5(z - 0.2)^2 + 0.5) : z \in (-0.7, 0.3)\} \\ \sigma_2 &= \{(z, (z - 0.2)^3 + (z - 0.2)^2) - 0.4 : z \in (-0.3, 0.7)\}\end{aligned}$$

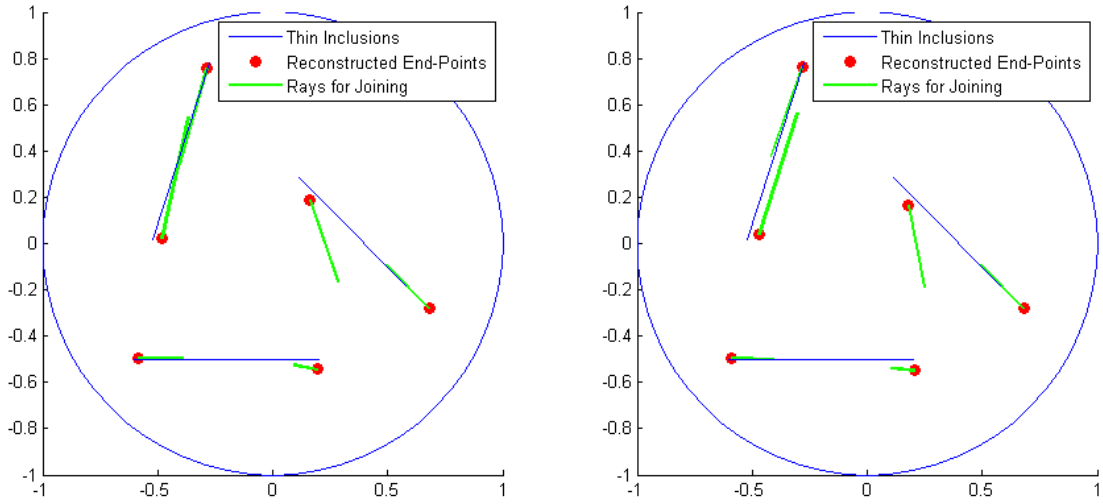


FIG. 1.9 – (All  $\gamma_j$  are different) Reconstructions of three thin inclusions.  $\sigma_j$ 's are given blue lines. Red circles and green rays starting from them represent  $\alpha_j$  and  $\bar{\beta}_j$  without noise (left) and some noise  $\xi = 10^{-4}$ .

$ \beta_j $	$\beta_j$	$\alpha_j$	End-Points
0.0000	$0.0000 + 0.0000i$	$-0.8850 - 1.3360i$	No
0.0000	$-0.0000 - 0.0000i$	$0.5600 + 0.8748i$	No
0.1269	$-0.0981 - 0.0804i$	$0.7038 - 0.5544i$	Yes
0.1341	$-0.1190 + 0.0617i$	$0.3082 + 0.5307i$	Yes
0.1253	$0.0953 + 0.0814i$	$-0.6682 + 0.5271i$	Yes
0.0571	$0.0462 - 0.0336i$	$-0.5671 + 0.3783i$	No
0.1309	$0.1142 - 0.0641i$	$-0.2906 - 0.5200i$	Yes
0.0847	$-0.0655 + 0.0538i$	$0.5206 - 0.3426i$	No
0.0841	$0.0618 + 0.0571i$	$0.2073 - 0.3395i$	No
0.0834	$-0.0347 - 0.0758i$	$-0.2507 + 0.1599i$	No

TAB. 1.9 – Computed values of  $\alpha_j$ ,  $\beta_j$  and  $|\beta_j|$  for the fourth example without noise.

$ \beta_j $	$\beta_j$	$\alpha_j$	End-Points
0.0000	$-0.0000 + 0.0000i$	$1.2877 + 0.7279i$	No
0.0000	$-0.0000 - 0.0000i$	$-1.1314 - 0.4502i$	No
0.0885	$-0.0769 - 0.0438i$	$0.7226 - 0.5681i$	Yes
0.0512	$-0.0510 - 0.0042i$	$0.7210 - 0.4121i$	No
0.0072	$0.0034 - 0.0064i$	$-0.1419 - 0.8116i$	No
0.0694	$0.0655 - 0.0230i$	$-0.3880 - 0.5647i$	Yes
0.1007	$-0.0955 + 0.0318i$	$0.3505 + 0.5516i$	Yes
0.0005	$-0.0005 + 0.0001i$	$-0.9437 + 0.4924i$	No
0.1488	$0.1362 + 0.0600i$	$-0.6774 + 0.5015i$	Yes
0.0238	$0.0188 - 0.0145i$	$-0.2383 + 0.5702i$	No

TAB. 1.10 – Computed values of  $\alpha_j$ ,  $\beta_j$  and  $|\beta_j|$  for the fourth example with  $\xi = 5 \times 10^{-4}$ .

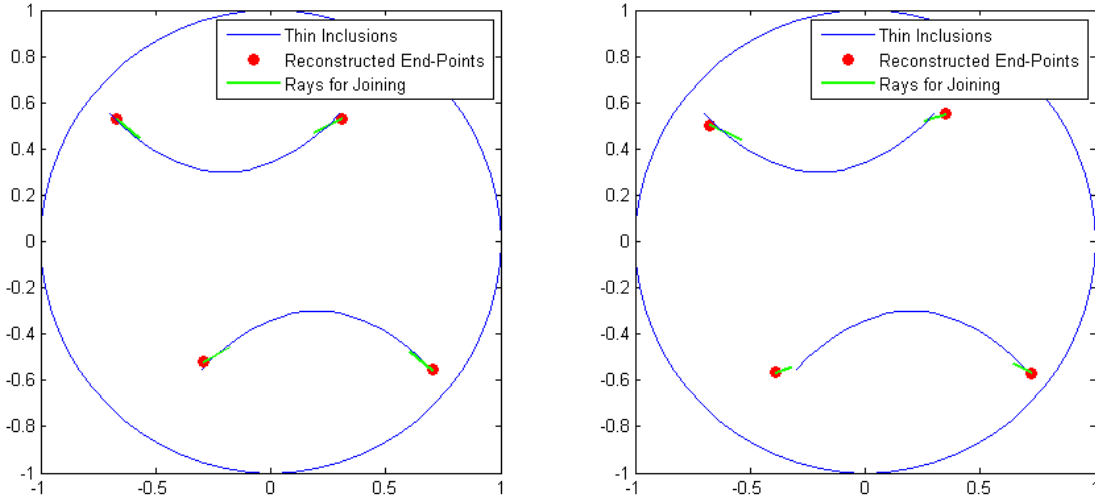


FIG. 1.10 – Reconstructions of two thin inclusions.  $\sigma_j$ 's are given blue lines. Red circles and green rays starting from them represent  $\alpha_j$  and  $\overline{\beta_j}$  without noise (left) and some noise  $\xi = 5 \times 10^{-4}$  (right).

and the parameter  $\gamma_j$  is chosen as 10 and 5 for  $j = 1$  and 2 respectively. Notice that the end-points of  $\Gamma_1$  are

$$a_1 = (-0.7000, 0.3750) \quad \text{and} \quad b_1 = (0.3000, 0.3750)$$

and the end-points of  $\Gamma_2$  are

$$a_2 = (-0.3000, -0.2750) \quad \text{and} \quad b_2 = (0.7000, -0.0250).$$

We exhibit the results in Tables 1.11, 1.12 and in Fig. 1.11 with the value of  $M = 10$  and  $\xi = 10^{-4}$ .

$ \beta_j $	$\beta_j$	$\alpha_j$	End-Points
0.0000	$-0.0000 - 0.0000i$	$0.4213 + 1.5638i$	No
0.0000	$0.0000 + 0.0000i$	$0.6548 - 1.1992i$	No
0.0000	$-0.0000 + 0.0000i$	$-0.9071 - 0.9568i$	No
0.0013	$-0.0013 + 0.0003i$	$-0.7794 + 0.5024i$	No
0.3108	$0.2997 - 0.0823i$	$-0.6715 + 0.3952i$	Yes
0.1080	$-0.0384 + 0.1010i$	$0.6892 - 0.0122i$	Yes
0.1093	$0.0958 + 0.0526i$	$-0.3267 - 0.2862i$	Yes
0.3343	$-0.1562 - 0.2956i$	$0.2587 - 0.2873i$	No
0.2597	$-0.2167 - 0.1432i$	$0.3112 + 0.3776i$	Yes
0.3677	$0.0170 + 0.3673i$	$-0.1222 + 0.2703i$	No

TAB. 1.11 – Computed values of  $\alpha_j$ ,  $\beta_j$  and  $|\beta_j|$  for the last example without noise.

$ \beta_j $	$\beta_j$	$\alpha_j$	End-Points
0.0000	$0.0000 + 0.0000i$	$-1.4783 - 0.3837i$	No
0.0000	$0.0000 + 0.0000i$	$-0.3574 + 1.1247i$	No
0.0001	$0.0001 - 0.0000i$	$0.9674 + 0.4505i$	No
0.0001	$-0.0001 + 0.0000i$	$0.4970 - 0.8952i$	No
0.3132	$0.2994 - 0.0921i$	$-0.6713 + 0.3913i$	Yes
0.0941	$-0.0360 + 0.0869i$	$0.7011 - 0.0155i$	Yes
0.2972	$-0.2384 - 0.1774i$	$0.3053 + 0.3721i$	Yes
0.0748	$0.0547 + 0.0511i$	$-0.3701 - 0.3052i$	Yes
0.3844	$-0.2338 - 0.3051i$	$0.2732 - 0.2638i$	No
0.4631	$0.1543 + 0.4366i$	$-0.1578 + 0.1843i$	No

TAB. 1.12 – Computed values of  $\alpha_j$ ,  $\beta_j$  and  $|\beta_j|$  for the last example with  $\xi = 10^{-4}$ .

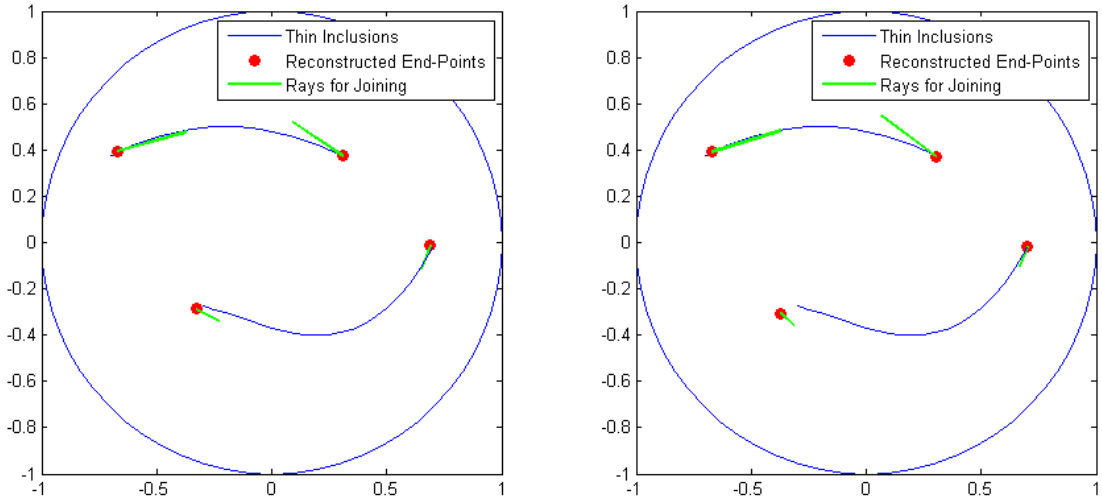


FIG. 1.11 – (All  $\gamma_j$  are different) Reconstructions of two thin inclusions.  $\sigma_j$ 's are given blue lines. Red circles and green rays starting from them represent  $\alpha_j$  and  $\overline{\beta_j}$  without noise (left) and some noise  $\xi = 10^{-4}$  (right).

## 1.8 Conclusion

In this chapter, we have proposed an algorithm to retrieve the end-points of multiple thin rectangular inclusions. This algorithm is based on the detection of simple poles of a meromorphic function in terms of measured boundary values. Then we have performed a large amount of numerical simulations and it turns out that the proposed algorithm identifies the number and the location of end-points of such thin inclusions accurately.

For the case of a curved single thin inclusion, the results based on the algorithm introduced in [4] are not so good as is seen in Fig. 1.4. But our new algorithm still offers useful information and we can say that a good initial guess is obtained at low computational cost, to be improved upon by an appropriate iterative algorithm for example, a level-set evolution, refer to chapter 3 and [2, 38].

It is still desirable to have an efficient and fast method for imaging of arbitrary shaped thin inclusions using finitely many measurements. In the next chapter, we suggest an imaging method at fixed non-zero high frequency for thin inclusions based on the MUSIC (Multiple Signal Classification)-type algorithm.

## 2 Imaging of Thin Penetrable Inclusions by a MUSIC-Type Algorithm

The imaging of a thin inclusion, with dielectric and or/magnetic contrast with respect to the embedding homogeneous medium is investigated. A MUSIC-type algorithm operated at a single time-harmonic frequency is developed in order to map the inclusion (that is, to retrieve its supporting curve) from scattered field data collected within the Multi-Static Response (MSR) matrix. Numerical experiments carried out for several types of inclusions (dielectric and/or magnetic ones, straight or curved ones), mostly single inclusions but also two of them close-by as a straightforward extension, illustrate the pros and cons of the proposed imaging method.

### 2.1 Introduction

In the present chapter, we are investigating the electromagnetic imaging of a single, thin homogeneous inclusion inside a homogeneous (free) space, the inclusion domain (it is localized within the neighborhood of a smooth curve  $\sigma$ , see section 2.3 for the full definition) being characterized either by a contrast of dielectric permittivity with respect to the exterior space, or by a contrast of magnetic permeability, or by both contrasts. The inclusion is both of unknown supporting curve  $\sigma$  and unknown electromagnetic contrast. Its lateral extent (its thickness)  $h$  is small with respect to the wavelength in the exterior space but is not otherwise specified.

The above configuration is two-dimensional, and is associated to a scalar scattering problem for a  $E$ -polarized (Transverse Magnetic) field —the  $H$ -polarized (Transverse Electric) case could be dealt with per duality. The data consist of the Multi-Static Response (MSR) matrix at a single, non-zero operation frequency. This matrix results from illuminating the thin (screen-like) inclusion by a finite number  $N$  of plane waves, then collecting on some prescribed encircling contour, for each given illumination, the corresponding complex-valued scattering amplitude at a finite number of directions (in practice, those  $N$  ones of the incident waves).

The solution method proposed goes as follows. First, a singular value decomposition of the  $N \times N$  MSR matrix is carried out via some standard numerical solver. This enables us to discriminate between a number,  $M$ , of non-zero singular values (in practice, higher than some prescribed threshold in link with the noise level and other inaccuracies of the dataset) and a number  $N - M$  zero ones (better said, below than this threshold). Consequently, singular vectors in the signal subspace from those in the noise subspace are discriminated as well. Second, an appropriate Multiple Signal Classification (MUSIC) estimator is introduced and computed over a very fine mesh within a prescribed search box in the embedding space. This estimator peaks at a finite number of discrete locations along the supporting curve, the number of such peaks being related to  $M$  —the relationship itself depending upon the type of electromagnetic contrast of the inclusion. Numerical experimentations exemplify that the above imaging method works quite well and that the conclusions drawn in terms of curve reproduction.

The starting point is the fact that the  $N \times N$  MSR matrix can be modeled from a rigorous asymptotic field formulation. Indeed, from previous investigations, and starting

from the Helmholtz equation which the field satisfies in the present case, it can be shown that the scattered field due to the inclusion can be expanded into a power series vs.  $h$ , the leading-order term (power 1 in  $h$ ) of which being a line integral along  $\sigma$ ; in terms of scattering, it means also that multiple scattering matters only at higher orders than the one kept in view of the small thickness of the inclusion with respect to the wavelength at the frequency of operation. Thereupon, if the elements of the MSR matrix are further approximated as a finite sum of  $M$  terms ( $M$  being appropriately smaller than  $N$ , one will come back to this aspect in the next sections), each one corresponding to the contribution of a small enough straight segment into which  $\sigma$  is divided, it suffices to proceed with the singular value decomposition of the MSR matrix as just constructed, peaks of a corresponding MUSIC estimator being located along  $\sigma$ .

Regarding the numerical simulations, inverse crime is alleviated for the most part. Indeed, if most images shown are indeed made from first-order data, those are computed via an exact calculation of the line integral, no further hypothesis being made about its discretization, and noise being introduced to test the solution method thoroughly further. Also, though the theoretical analysis is developed for far field scattering amplitudes, almost near fields (one to a few wavelengths away from the center of the search box) are considered here. Furthermore, images from data computed from an alternative asymptotic formulation [61] involving the solution of a second-kind Fredholm integral equation along the supporting curve to compute the MSR matrix are almost indistinguishable from those obtained from our first-order data. This is true as well with images from scattered field data computed by a brute-force Method-of-Moments (MoM) solution algorithm [72] applied to a domain integral formulation in the case of a supporting straight segment, whatever be the assumed thickness  $h$  input into the solution algorithm—the main challenge of the MoM is to cover the inclusion with pixels small enough with respect both to the wavelength and to the inclusion thickness, and not too numerous overall.

Let us emphasize that the extension of the above situation wherein a single thin inclusion is imaged to the case in which several thin inclusions are imaged (again, the theoretical model of the MSR matrix is at first-order, i.e., the inclusions do not couple electromagnetically to one another in the model) is available. But for simplicity, its mathematical derivation is not elaborated upon herein, only a few numerical results for two inclusions being shown to illustrate both the interest of the extension and some of its practical limitations with regards to respective contrasts.

As for the situation of a perfectly impenetrable inclusion (denoted usually as a perfect screen), corresponding to either Dirichlet or Neumann boundary conditions, it is not investigated presently; it will be discussed elsewhere, insisting on the fact that the end-points of such a screen pose quite a challenge in terms of the asymptotic formulation (refer to [31]).

The approach discussed thereafter, in addition to the introduction of the asymptotic field formulation, the derivation of which is sketched from an exact one [25], makes ample use of material already available about MUSIC-type algorithms in electromagnetics in both static and propagative regimes, e.g., [8, 13], with as initial reading [32, 77] about MUSIC in the signal processing community. One could also refer to the textbook [12] for results both on asymptotic approaches (for volumetric inclusions) and inversions carried out from MSR matrices, the case of a thin curve-like inclusion being at least in part an

extension of the case of volumetric inclusions.

About the case of zero-frequency and thin inclusions (with magnetic contrasts only mattering), it is already considered in [4] (single inclusion) and [5, 54] (multiple inclusion) and is leading to a non-iterative retrieval of the end-points of the supporting curve(s). Though the present work is based on a closely connected mathematical formulation of the direct problem, one will not dwell onto it since the choice made is to operate well within the wave propagation regime at a non-zero frequency, with a dedicated, MUSIC-type imaging algorithm.

Let us signal in addition that, once the supporting curve is mapped, one could evolve it. This evolution is enabling in particular to account for possible discrepancies between approximate model (the one which one uses) and exact or experimental ones, and to retrieve a better shape (if there remains a discrepancy between the data and the field scattered by the retrieved inclusion) once an appropriate cost functional is chosen — this could be carried out also from an arbitrary initial choice of the supporting curve— following in that matter reference [2] in the context of controlled evolution of level sets and the optimization of topologies [38].

Finally, let us mention more traditional approaches of the retrieval of screens by a well-chosen succession of small optimal displacements [30], among many references along the same line of thought.

This chapter is organized as follows. In section 2.2, the direct scattering problem is briefly discussed. In section 2.3, the asymptotic formulation of the scattering amplitude is sketched. In section 2.4, the analysis of the MSR matrix is carried out and the MUSIC algorithm is summarized. In section 2.5, a set of numerical results is proposed, spectra of MSR matrices, images of inclusions, mostly single ones but also sets of two at least for an inclusion of single contrast. A short conclusion (section 2.6) follows.

## 2.2 Maxwell's equations and the direct scattering problem

In this section, we introduce the direct scattering problem. A more detailed description of this material can be found in [38, 60].

### 2.2.1 Maxwell's equation and mathematical formulation

Let  $\mathbf{x}$  be a position vector in  $\mathbb{R}^3$ . By dropping out the time dependence  $e^{-i\omega t}$  and taking the real part of all quantities, the time-harmonic electric field  $\mathbf{E} = (E_1, E_2, E_3)$  and magnetic field  $\mathbf{H} = (H_1, H_2, H_3)$  satisfy Maxwell's equations

$$\nabla \times \mathbf{E}(\mathbf{x}) = i\omega\mu(\mathbf{x})\mathbf{H}(\mathbf{x}) \quad \text{and} \quad \nabla \times \mathbf{H}(\mathbf{x}) = -i\omega\epsilon(\mathbf{x})\mathbf{E}(\mathbf{x}). \quad (2.1)$$

Here  $\omega > 0$  denotes the given frequency,  $\epsilon(\mathbf{x})$  the permittivity, and  $\mu(\mathbf{x})$  the magnetic permeability at  $\mathbf{x}$ . Throughout this chapter, we assume that these parameters are locally constant.

Let us consider the scatterer to be a perfectly conducting cylinder with the generator parallel to the  $z$ -axis and contained in a homogeneous and isotropic space. When the



incoming plane wave is parallel to the  $xy$ -plane, by a simple computation, Maxwell's equation (2.1) becomes

$$\frac{\partial E_3}{\partial y} = i\omega\mu H_1, \quad \frac{\partial E_3}{\partial x} = -i\omega\mu H_2, \quad \frac{\partial H_2}{\partial x} - \frac{\partial H_1}{\partial y} = -i\omega\varepsilon E_3 \quad (2.2)$$

and

$$\frac{\partial H_3}{\partial y} = -i\omega\varepsilon E_1, \quad \frac{\partial H_3}{\partial x} = i\omega\varepsilon E_2, \quad \frac{\partial E_2}{\partial x} - \frac{\partial E_1}{\partial y} = i\omega\mu H_3. \quad (2.3)$$

From (2.2) and (2.3), we can easily observe that Maxwell's equations can be split into the two sets of independent equations [38]. One is called  $E$ -polarization

$$\mathbf{E} = (0, 0, E_3), \quad \mathbf{H} = (H_1, H_2, 0) \quad (2.4)$$

and the other,  $H$ -polarization

$$\mathbf{E} = (E_1, E_2, 0), \quad \mathbf{H} = (0, 0, H_3). \quad (2.5)$$

Notice that the set of equations in (2.4) and (2.5) are associated with the terminology : transverse electric waves (TE-waves) and transverse magnetic waves (TM-waves), respectively.

### 2.3 The direct scattering problem and the asymptotic formulation of the scattering amplitude

Let us consider two-dimensional electromagnetic scattering from a thin, curve-like homogeneous inclusion within a homogeneous space  $\mathbb{R}^2$ . This space contains an inclusion denoted as  $\Gamma$  which is localized in the neighborhood of a curve  $\sigma$ . That is,

$$\Gamma = \{x + \eta n(x) : x \in \sigma, \eta \in (-h, h)\}, \quad (2.6)$$

where the supporting  $\sigma$  is a simple, smooth curve in  $\mathbb{R}^2$ ,  $n(x)$  is the unit normal to  $\sigma$  at  $x$ , and  $h$  is a strictly positive constant which specifies the thickness of the inclusion (small with respect to the wavelength, see next), refer to Fig. 2.1.

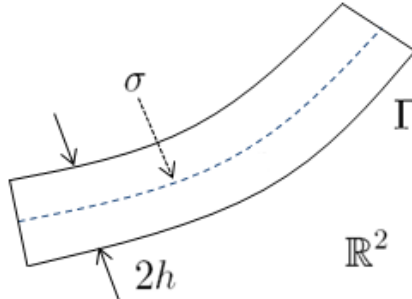


FIG. 2.1 – Sketch of the thin inclusion  $\Gamma$

Constitutive materials are fully characterized by their dielectric permittivity and magnetic permeability at a given frequency. Let  $0 < \varepsilon_0 < +\infty$  and  $0 < \mu_0 < +\infty$  denote the permittivity and permeability of the embedding space  $\mathbb{R}^2$ , and  $0 < \varepsilon < +\infty$

and  $0 < \mu < +\infty$  the ones of the inclusion  $\Gamma$ . Then, one has the piecewise constant dielectric permittivity

$$\varepsilon(x) = \begin{cases} \varepsilon_0 & \text{for } x \in \mathbb{R}^2 \setminus \bar{\Gamma} \\ \varepsilon & \text{for } x \in \Gamma \end{cases} \quad (2.7)$$

and magnetic permeability

$$\mu(x) = \begin{cases} \mu_0 & \text{for } x \in \mathbb{R}^2 \setminus \bar{\Gamma} \\ \mu & \text{for } x \in \Gamma \end{cases} \quad (2.8)$$

If there is no inclusion, i.e., in the homogeneous space,  $\mu(x)$  and  $\varepsilon(x)$  are equal to  $\mu_0$  and  $\varepsilon_0$  respectively. For convenience, one also defines  $\gamma(x) = \frac{1}{\mu(x)}$ . For the sake of simplicity, we set  $\mu_0$  and  $\varepsilon_0$  are equal to 1.

At strictly positive operation frequency  $\omega$  (wavenumber  $k_0 = \omega\sqrt{\mu_0\varepsilon_0}$ ), let  $u(x)$  be the time-harmonic total field which satisfies the Helmholtz equation

$$\nabla \cdot \left( \frac{1}{\mu} \nabla u \right) + \omega^2 \varepsilon u = 0 \quad \text{in } \mathbb{R}^2 \quad (2.9)$$

where  $\theta = (\theta_x, \theta_y)$  is a two-dimensional vector on the unit circle  $S^1$  in  $\mathbb{R}^2$ , i.e.,  $\theta$  satisfies  $\theta \cdot \theta = 1$ . Similarly, the incident field  $u_0(x)$  satisfies the homogeneous Helmholtz equation

$$\nabla \cdot \left( \frac{1}{\mu_0} \nabla u_0 \right) + \omega^2 \varepsilon_0 u_0 = 0 \quad \text{in } \mathbb{R}^2.$$

As is usual, the total field  $u$  divides itself into the incident field  $u_0$  and the scattered field  $u_s$ ,  $u = u_0 + u_s$ . Notice that this unknown scattered field  $u_s(x)$  satisfies the Sommerfeld radiation condition

$$\lim_{|x| \rightarrow \infty} \sqrt{|x|} \left( \frac{\partial u_s(x)}{\partial |x|} - ik_0 u_s(x) \right) = 0$$

uniformly in all directions  $\hat{x} = \frac{x}{|x|}$ .

The following expressions are needed to derive the asymptotic expansion as done next.

**Definition 2.1** For every  $x \in \sigma$ , let  $\tau(x)$  and  $n(x)$  be unit vectors that are respectively tangent with and normal to  $\sigma$  at  $x$ . The symmetric matrix  $A(x)$  is as such [24] :

1.  $A(x)$  has eigenvectors  $\tau(x)$  and  $n(x)$
2. The eigenvalue corresponding to  $\tau(x)$  is  $2(\gamma - \gamma_0)$
3. The eigenvalue corresponding to  $n(x)$  is  $2(\gamma - \gamma_0)\frac{\gamma_0}{\gamma}$ .

So, by combining the results of [12, 25, 78], one is able to obtain the following asymptotic expansion (see [31, formula (8)] also) :

**Proposition 2.2** For  $y \in \mathbb{R}^2 \setminus \bar{\Gamma}$ ,  $u(y)$  can be written

$$u(y) = u_0(y) + u_s(y) = u_0(y) + hu_\sigma(y) + o(h) \quad (2.10)$$

where the correction term  $u_\sigma$  is given by

$$u_\sigma(y) = \int_{\sigma} A(x) \nabla u_0(x) \nabla_x \Phi(x, y) d\sigma(x) + \omega^2 (\varepsilon - \varepsilon_0) \int_{\sigma} u_0(x) \Phi(x, y) d\sigma(x)$$

and

$$\Phi(x, y) = -\mu_0 \frac{i}{4} H_0^1(k_0 |x - y|)$$

is the two-dimensional fundamental solution (or Green function) for the Helmholtz equation.

Now, let us specialize the above to incident plane waves and far fields in free space. Let  $\{\hat{y}_j\}_{j=1}^N \subset S^1$  be a discrete finite set of observation directions and  $\{\theta_l\}_{l=1}^N \subset S^1$  be the same number of incident directions. Let us remember that  $S^1$  indicates the unit circle in  $\mathbb{R}^2$ , i.e., every element  $\xi \in \{\hat{y}_j\}_{j=1}^N$  or  $\{\theta_l\}_{l=1}^N$ .

The scattering amplitude is defined as a function  $K(\hat{y}, \theta)$  which satisfies

$$u(y) - u_0(y) = \frac{e^{ik_0|y|}}{\sqrt{|y|}} K(\hat{y}, \theta) + o\left(\frac{1}{\sqrt{|y|}}\right)$$

as  $|y| \rightarrow \infty$  uniformly on  $\hat{y} = \frac{y}{|y|}$  and  $\theta \in S^1$ . From the asymptotic behavior of the Hankel function [34] and a simple calculation, one easily derives :

$$\Phi(x, y) = \frac{1+i}{4\sqrt{k_0\pi}} \frac{e^{ik_0|y|}}{\sqrt{|y|}} e^{-ik_0 \frac{y}{|y|} \cdot x} + o\left(\frac{1}{\sqrt{|y|}}\right) \quad (2.11)$$

$$\nabla_x \Phi(x, y) = \frac{1+i}{4\sqrt{k_0\pi}} \frac{e^{ik_0|y|}}{\sqrt{|y|}} \left(-ik_0 \frac{y}{|y|}\right) e^{-ik_0 \frac{y}{|y|} \cdot x} + o\left(\frac{1}{\sqrt{|y|}}\right) \quad (2.12)$$

as  $|y| \rightarrow \infty$ . By combining with (2.10), (2.11) and (2.12), the asymptotic formula for the scattering amplitude follows as

$$K(\hat{y}, \theta) = h \frac{k_0^2(1+i)}{4\sqrt{k_0\pi}} \left\{ \int_{\sigma} \{(-\hat{y}) \cdot A(x) \cdot \theta + (\varepsilon - \varepsilon_0)\} e^{ik_0(\theta - \hat{y}) \cdot x} d\sigma(x) \right\} + o(h). \quad (2.13)$$

Let us exclude the asymptotic term  $o(h)$  and constant  $h \frac{k_0^2(1+i)}{4\sqrt{k_0\pi}}$  from formula (2.13). The result, denoted as  $\hat{K}$ , is such that

$$\begin{aligned} \hat{K}(\hat{y}, \theta) &= \int_{\sigma} \{(-\hat{y}) \cdot A(x) \cdot \theta + (\varepsilon - \varepsilon_0)\} e^{ik_0(\theta - \hat{y}) \cdot x} d\sigma(x) \\ &= \int_{\sigma} (-\hat{y}) \cdot A(x) \cdot \theta e^{ik_0(\theta - \hat{y}) \cdot x} d\sigma(x) + \int_{\sigma} (\varepsilon - \varepsilon_0) e^{ik_0(\theta - \hat{y}) \cdot x} d\sigma(x). \end{aligned} \quad (2.14)$$

## 2.4 MUSIC type algorithm for imaging a thin inclusion and estimating its length

In this section, one applies the asymptotic formula (2.14) in order to build up a MUSIC-type algorithm [77], for non-iterative imaging of the thin inclusion, with no prior information save that it is of small thickness (the exact value of  $h$  is not needed however), and that the supporting curve  $\sigma$  is smooth. Here, one makes use of the eigenvalue structure of the Multi-Static Response (MSR) matrix  $K = (K_{jl})$ , where element  $K_{jl}$  is the amplitude collected in the direction of observation numbered  $j$  for an impinging incident wave numbered  $l$ .

To properly exploit that MSR matrix, one will start from the assumption that  $\sigma$  can be partitioned by the set of points  $\{x_1, x_2, \dots, x_M\}$ , the length of interval  $[x_j, x_{j+1}]$  being  $\frac{|\sigma|}{M}$  for  $j = 1, 2, \dots, M-1$ . The analysis is then led in succession for three cases from the most simple to the most complicated : dielectric contrast only ( $\gamma = \gamma_0, \varepsilon \neq \varepsilon_0$ ), magnetic contrast only ( $\gamma \neq \gamma_0, \varepsilon = \varepsilon_0$ ), and both contrasts ( $\gamma \neq \gamma_0, \varepsilon \neq \varepsilon_0$ ).

### 2.4.1 Contrast of permittivity : $\gamma = \gamma_0, \varepsilon \neq \varepsilon_0$

The MSR matrix reads as  $K = (K_{jl})_{j,l=1}^N \in \mathbb{C}^{N \times N}$  :

$$\begin{aligned} K_{jl} &= \hat{K}(\hat{y}_j, \theta_l) \Big|_{\hat{y}_j = -\theta_j} = \int_{\sigma} (\varepsilon - \varepsilon_0) e^{ik_0(\theta_l - \hat{y}_j) \cdot x} d\sigma(x) \Big|_{\hat{y}_j = -\theta_j} \\ &= \int_{\sigma} (\varepsilon - \varepsilon_0) e^{ik_0(\theta_j + \theta_l) \cdot x} d\sigma(x) \approx (\varepsilon - \varepsilon_0) \frac{|\sigma|}{M} \sum_{m=1}^M e^{ik_0(\theta_j + \theta_l) \cdot x_m}. \end{aligned} \quad (2.15)$$

Next, the matrices  $E \in \mathbb{R}^{M \times M}$  and  $F = [F_1 \ F_2 \ \dots \ F_M] \in \mathbb{C}^{N \times M}$  are introduced as  $E = (\varepsilon - \varepsilon_0) \frac{|\sigma|}{M} I_M$  and  $F_j = (e^{ik_0\theta_1 \cdot x_j}, e^{ik_0\theta_2 \cdot x_j}, \dots, e^{ik_0\theta_N \cdot x_j})$  for  $j = 1, 2, \dots, M$ , letting  $I_M$  be the  $M \times M$  identity matrix. With this,  $K$  can be decomposed as

$$K = FEF^T. \quad (2.16)$$

Here,  $F^T \in \mathbb{C}^{M \times N}$  is the transpose matrix of  $F$ . With this decomposition, we observe that  $K$  is symmetric but is not Hermitian —an Hermitian matrix could be formed as  $\tilde{K} = K\bar{K}$ .

Let us emphasize at this stage that  $\bar{K}$  is the frequency-domain version of a time-reversed MSR matrix;  $\tilde{K}$  corresponds to performing a measurement, time-reversing the received signals, and using them as input for a second experiment, and so on [12, 32].

In the above and next,  $N$  should be strictly higher than  $M$  —adverse effects of a  $N$  chosen too close to  $M$  will be illustrated by numerical simulations. Let  $a \in \mathbb{R} \setminus \{0\}$ ; for any point  $z \in \Omega$ , one defines the vector  $g_{z,a} \in \mathbb{C}^N$  as

$$g_{z,a} = (ae^{ik_0\theta_1 \cdot z}, ae^{ik_0\theta_2 \cdot z}, \dots, ae^{ik_0\theta_N \cdot z})^T. \quad (2.17)$$

It can be shown that there exists  $n_0 \in \mathbb{N}$  such that for any  $N \geq n_0$  the following statement holds [8, 12, 50] :

$$g_{z,a} \in \text{Range}(\tilde{K}) \text{ if and only if } z \in \{x_1, x_2, \dots, x_M\}. \quad (2.18)$$

The imaging algorithm follows. Let the singular value decomposition of the matrix  $K$  be  $K = VSW^T$ , where  $V, W \in \mathbb{C}^{N \times N}$  are unitary matrices and where  $S$  is a real nonnegative diagonal matrix with components  $\lambda_1, \lambda_2, \dots, \lambda_N$  which satisfies

$$\lambda_1 \geq \lambda_2 \geq \dots \geq \lambda_M > 0 \quad \text{and} \quad \lambda_j = 0 \text{ for } j = M+1, M+2, \dots, N.$$

Alternatively,  $\lambda_j$ , for  $j = M+1, M+2, \dots, N$ , could merely be very small, below the noise level of the system represented by  $K$ . The numbers  $\{\lambda_j\}$  are the nonnegative

square roots of the eigenvalues of  $K\bar{K}^T = K\bar{K}$ . The columns of  $V$  are the eigenvectors of  $K\bar{K}$  and those of  $W$  are the eigenvectors of  $\bar{K}K$  (arranged in the same order as the corresponding eigenvalues  $\lambda_j^2$ ). The singular value decomposition of  $K$  can be written in the form  $K = VSV^T$  (this holds for symmetric matrices in which  $V = \bar{W}$ ). The first  $M$  columns of the matrix  $V$ ,  $\{v_1, v_2, \dots, v_M\}$ , provide an orthonormal basis for  $K$  and the rest of the matrix  $V$ ,  $\{v_{M+1}, v_{M+2}, \dots, v_N\}$ , provides a basis for the null (or noise) space of  $K$ . So, one can form the projection onto the null (or noise) subspace : this projection is given explicitly by

$$P_{\text{noise}}(f) = \sum_{j>M} v_j \bar{v}_j^T f. \quad (2.19)$$

From (2.18), a point  $z \in \{x_1, x_2, \dots, x_M\}$  if and only if  $g_{z,a} \in \text{Range}(\tilde{K})$ , i.e., equivalently  $\|P_{\text{noise}}(g_{z,a})\| = 0$ . Thus, an image of  $x_j$ ,  $j = 1, 2, \dots, M$ , follows from computing

$$W_a(z) = \frac{1}{\|P_{\text{noise}}(g_{z,a})\|}. \quad (2.20)$$

The resulting plot of this estimator is expected to exhibit large peaks at the sought  $x_j$ .

In good numerical practice, and as it has been already insisted upon in the Introduction, the effective value of  $M$  should be extracted from the distribution of the singular values of  $K$ , which is obtained with a standard Matlab routine of singular value decomposition, the elements  $K_{jl}$  in that  $K$  being computed not from their finite sum representation involving only  $M$  samples (2.15) but from their full asymptotic integral representation (2.10), the integrand involved in it being finely sampled until convergence. Here, by fine sampling, it is understood, e.g., one-tenth of the wavelength or much less, depending upon the convergence rate.

**Remark 2.3** *Assume that asymptotically (with respect to the number  $N$  of  $\theta$ ) we have*

$$(\varepsilon - \varepsilon_0) \frac{|\sigma|}{M} \sum_{m=1}^M e^{ik(\theta+\theta') \cdot x_m}$$

*for any  $\theta$  and  $\theta'$  on the unit sphere. But from the far-field behavior of the Green function (fundamental solution), and by an analytical continuation argument, we can get*

$$(\varepsilon - \varepsilon_0) \frac{|\sigma|}{M} \sum_{m=1}^M \Phi(x, x_m) \bar{\Phi}(x, x_m)$$

*for  $|x|$  large enough. Therefore, we have in hand all the  $\Phi(x, x_m)$  for  $m = 1, 2, \dots, M$  theoretically.*

*But, from [6, Section 2], we can only distinguish between two  $\Phi(x, x_m)$  and  $\Phi(x, x_{m'})$  if the distance between  $x_m$  and  $x_{m'}$  is larger than the first zero of the function  $J_0(0\text{-th Bessel function of the first kind})$  in the two-dimensional case and  $\lambda/2$  in three dimensions. The same arguments can be applied for the other cases.*

Otherwise, it is true that the asymptotic formulation is accurate to first-order only ; one might argue that the inverse crime is only partly alleviated when that formulation

is used to produce the data. Yet, neglecting higher orders should not matter in view of the small thickness of the inclusion.

Let us underscore in addition that using data computed by another asymptotic approach now involving a second-kind boundary integral equation [61] for the field in the same TM-polarization case, refer to equation (1) in this reference, yields closely resembling images, and this holds true as well when applying a method-of-moments to a second-kind domain integral formulation of the field involving covering the domain by small square pixels [72]. Examples will be given in the numerical section.

The dual case of TE-polarization which would correspond to magnetic contrasts has not been considered by us at this stage.

#### 2.4.2 Contrast of permeability : $\gamma \neq \gamma_0$ , $\varepsilon = \varepsilon_0$

The main lines of the analysis are similar with those of the previous case. Still, a number of changes result from the different scattering behavior, so the approach is detailed below as is deemed necessary.

The MSR matrix  $K = (K_{jl})_{j,l=1}^N \in \mathbb{C}^{N \times N}$  is defined as

$$\begin{aligned} K_{jl} &= \hat{K}(\hat{y}_j, \theta_l) \Big|_{\hat{y}_j = -\theta_j} = \int_{\sigma} (-\hat{y}_j) \cdot A(x) \cdot \theta_l e^{ik_0(\theta_l - \hat{y}_j) \cdot x} d\sigma(x) \Big|_{\hat{y}_j = -\theta_j} \\ &= \int_{\sigma} \theta_j \cdot A(x) \cdot \theta_l e^{ik_0(\theta_j + \theta_l) \cdot x} d\sigma(x) \\ &\approx \frac{|\sigma|}{M} \sum_{m=1}^M \left[ 2(\gamma - \gamma_0) \theta_j \cdot \tau(x_m) \theta_l \cdot \tau(x_m) \right. \\ &\quad \left. + 2 \left( 1 - \frac{\gamma_0}{\gamma} \right) \theta_j \cdot n(x_m) \theta_l \cdot n(x_m) \right] e^{ik_0(\theta_j + \theta_l) \cdot x_m} \end{aligned} \quad (2.21)$$

for  $j, l = 1, 2, \dots, N$ . Now, upon the definition of matrices  $C \in \mathbb{R}^{2M \times 2M}$  and  $D = [D_1 \ D_2 \ \dots \ D_{2M}] \in \mathbb{C}^{N \times 2M}$  such as

$$\begin{aligned} C &= \text{diagonal matrix with components } A \frac{|\sigma|}{M} \\ D_{2(j-1)+s} &= (d_s(x_j) \cdot \theta_1 e^{ik_0 \theta_1 \cdot x_j}, d_s(x_j) \cdot \theta_2 e^{ik_0 \theta_2 \cdot x_j}, \dots, d_s(x_j) \cdot \theta_N e^{ik_0 \theta_N \cdot x_j}) \end{aligned} \quad (2.22)$$

for  $j = 1, 2, \dots, M$  and

$$d_s(x_j) = \begin{cases} \tau(x_j) & \text{if } s = 1 \\ n(x_j) & \text{if } s = 2 \end{cases}.$$

Then, one concludes that  $K$  can be expressed by the following decomposition :

$$K = DCD^T. \quad (2.23)$$

Let us observe that  $K$  is symmetric but not Hermitian (one is formed as  $\tilde{K} = K\bar{K}$ ).

One has to assume again that  $N$  is large enough, that is, at least  $N > 2M$ , like in the purely dielectric case, yet with the need of twice more data for the same supporting

curve. Then, let  $b = d_s(z) \in \mathbb{R}^2 \setminus \{0\}$ . For any point  $z \in \Omega$  one defines the vector  $g_{z,b} \in \mathbb{C}^N$  by

$$g_{z,b} = (b \cdot \theta_1 e^{ik_0 \theta_1 \cdot z}, b \cdot \theta_2 e^{ik_0 \theta_2 \cdot z}, \dots, b \cdot \theta_N e^{ik_0 \theta_N \cdot z})^T. \quad (2.24)$$

As already said, it can be shown that there exists  $n_0 \in \mathbb{N}$  such that for any  $N \geq n_0$  the following statement holds [8, 12, 50] :

$$g_{z,b} \in \text{Range}(\tilde{K}) \text{ if and only if } z \in \{x_1, x_2, \dots, x_M\}. \quad (2.25)$$

Now, let the singular value decomposition of matrix  $K$  be defined by  $K = V S \bar{W}^T$ . Since the rank of  $K$  is  $2M$ , the first  $2M$  columns of  $V$ ,  $\{v_1, v_2, \dots, v_{2M}\}$ , provide an orthonormal basis for  $K$  and the rest of the matrix  $V$ ,  $\{v_{2M+1}, v_{2M+2}, \dots, v_N\}$ , provides a basis for the null (or the noise) space of  $K$ . So, one can form the projection onto the null (or noise) subspace : this projection is given explicitly by

$$P_{\text{noise}}(f) = \sum_{j>M} v_j \bar{v}_j^T f. \quad (2.26)$$

From (2.25), a point  $z \in \{x_1, x_2, \dots, x_M\}$  if and only if  $g_{z,b} \in \text{Range}(\tilde{K})$ , i.e., equivalently  $\|P_{\text{noise}}(g_{z,b})\| = 0$ . Hence, an image of  $x_j$  for  $j = 1, 2, \dots, M$ , follows from computing

$$W_b(z) = \frac{1}{\|P_{\text{noise}}(g_{z,b})\|}. \quad (2.27)$$

The resulting plot should have large peaks at the sought  $x_j$ , as in the previously considered purely dielectric case. Otherwise, the comments on the accuracy of the first-order representation of the field and on the fact that  $M$  is a unknown from which everything proceeds in the imaging remain the same as well.

### 2.4.3 Contrast of permittivity and permeability : $\gamma \neq \gamma_0, \varepsilon \neq \varepsilon_0$

This case encompasses both previous ones, but it is slightly more complex and should deserve some exposition.

The MSR matrix  $K = (K_{jl})_{j,l=1}^N \in \mathbb{C}^{N \times N}$  is defined as

$$\begin{aligned} K_{jl} &= \hat{K}(\hat{y}_j, \theta_l) \Big|_{\hat{y}_j = -\theta_j} \\ &= \int_{\sigma} \{(\varepsilon - \varepsilon_0) + (-\hat{y}_j) \cdot A(x) \cdot \theta_l\} e^{ik_0(\theta_l - \hat{y}_j) \cdot x} d\sigma(x) \Big|_{\hat{y}_j = -\theta_j} \\ &= \int_{\sigma} \{(\varepsilon - \varepsilon_0) + \theta_j \cdot A(x) \cdot \theta_l\} e^{ik_0(\theta_j + \theta_l) \cdot x} d\sigma(x) \\ &\approx \frac{|\sigma|}{M} \sum_{m=1}^M \left[ (\varepsilon - \varepsilon_0) + 2(\gamma - \gamma_0) \theta_j \cdot \tau(x_m) \theta_l \cdot \tau(x_m) \right. \\ &\quad \left. + 2 \left( 1 - \frac{\gamma_0}{\gamma} \right) \theta_j \cdot n(x_m) \theta_l \cdot n(x_m) \right] e^{ik_0(\theta_j + \theta_l) \cdot x_m} \end{aligned} \quad (2.28)$$

for  $j, l = 1, 2, \dots, N$ . In accord with (2.16) and (2.23),  $K$  can be decomposed as

$$K = F E F^T + D C D^T = H B H^T$$

where  $H = (F_1 \ F_2 \ \cdots \ F_M \ D_1 \ D_2 \ \cdots \ D_{2M}) \in \mathbb{C}^{N \times 3M}$  and  $B \in \mathbb{R}^{3M \times 3M}$  is a diagonal matrix with component  $\begin{pmatrix} E & 0 \\ 0 & C \end{pmatrix}$ .  $K$  is symmetric but is not Hermitian (it would be  $\tilde{K} = K\bar{K}$ ).

Similarly with the two previous cases, one has to assume a large enough  $N$ , at least  $N > 3M$ . Let  $c = (a, b) = (a, d_s(z)) \in \mathbb{R}^3 \setminus \{0\}$ . For any point  $z \in \Omega$  one defines the vector  $g_{z,c} \in \mathbb{C}^N$  by

$$g_{z,c} = (c \cdot (1, \theta_1)^T e^{ik_0 \theta_1 \cdot z}, c \cdot (1, \theta_2)^T e^{ik_0 \theta_2 \cdot z}, \dots, c \cdot (1, \theta_N)^T e^{ik_0 \theta_N \cdot z})^T. \quad (2.29)$$

Then, it can be shown that there exists  $n_0 \in \mathbb{N}$  such that for any  $N \geq n_0$  the following statement holds [8, 12, 50] :

$$g_{z,c} \in \text{Range}(\tilde{K}) \text{ if and only if } z \in \{x_1, x_2, \dots, x_M\}. \quad (2.30)$$

Now, let the singular value decomposition of the matrix  $K$  be defined by  $K = V S \bar{W}^T$ . As before, since the rank of  $K$  is  $3M$ , the first  $3M$  columns of  $V$ ,  $\{v_1, v_2, \dots, v_{3M}\}$ , provide an orthonormal basis for  $K$  and the rest of the matrix  $V$ ,  $\{v_{3M+1}, v_{3M+2}, \dots, v_N\}$ , provides a basis for the null (or the noise) space of  $K$ . So, one can form the projection onto the null (or noise) subspace : this projection is given explicitly by

$$P_{\text{noise}}(f) = \sum_{j>M} v_j \bar{v}_j^T f.$$

From (2.30), a point  $z \in \{x_1, x_2, \dots, x_M\}$  if and only if  $g_{z,c} \in \text{Range}(\tilde{K})$ , i.e., equivalently  $\|P_{\text{noise}}(g_{z,c})\| = 0$ . Hence, an image of  $x_j$  for  $j = 1, 2, \dots, M$  follows by computing

$$W_c(z) = \frac{1}{\|P_{\text{noise}}(g_{z,c})\|}. \quad (2.31)$$

The resulting plot will show large peaks at the sought  $x_j$  as previously single-contrast cases. In addition to comments already made, and not repeated here, let us notice that any brute-force calculation of fields should now become quite complicated whereas alternative asymptotic formulations in the line of [61] seem not available.

## 2.5 Numerical examples

### 2.5.1 Common features

In this section, a number of numerical examples is shown, with no claim to exhaustivity however. The main attention is put onto the purely dielectric case, with complementary examples given in the other cases, and on the one-inclusion case, a few illustrations of a two-inclusion case being added also.

Throughout, the scattered field is collected on the unit circle (radius 1). The search domain  $\tilde{\Omega}$  is defined as  $\tilde{\Omega} = [-1, 1] \times [-1, 1]$ . The thickness  $h$  of the thin inclusion  $\Gamma$  (see next) is set to 0.015 and parameters  $\mu(= \frac{1}{\gamma})$ ,  $\mu_0(= \frac{1}{\gamma_0})$ ,  $\varepsilon$  and  $\varepsilon_0$  are chosen as 5, 1, 5 and 1, respectively. Since  $\gamma_0$  and  $\varepsilon_0$  are set to unity, the applied frequency reads as  $\omega = \frac{2\pi}{\lambda}$



at wavelength  $\lambda$ , which will be varied in the examples between the low-frequency one of  $\lambda = 1$  and the high-frequency one of  $\lambda = 0.1$ .

Several  $\Gamma$  are chosen for illustration :

$$\Gamma_1 = \{x + \eta n(x) : x \in \sigma_1, \eta \in (-h, h)\}, \quad (2.32)$$

with 0.8-long straight  $\sigma_1 = \{(z, 0.2) : z \in (-0.4, 0.4)\}$ ;

$$\Gamma_2 = \{x + \eta n(x) : x \in \sigma_2, \eta \in (-h, h)\}, \quad (2.33)$$

with 1.04-long  $\sigma_2 = \left\{ \left( z, 0.2 + \frac{(z-0.2)^2}{2} \right) : z \in (-0.3, 0.7) \right\}$  of constant curvature;

$$\Gamma_3 = \{x + \eta n(x) : x \in \sigma_3, \eta \in (-h, h)\}, \quad (2.34)$$

with 1.19-long  $\sigma_3 = \{(z, (z-0.2)^3 + (z-0.2)^2) - 0.3 : z \in (-0.3, 0.7)\}$  of linearly increasing curvature. As for the illumination and observation directions  $\theta_l$ , they are selected as

$$\theta_l = \left( \cos \frac{2\pi(l-1)}{N}, \sin \frac{2\pi(l-1)}{N} \right) \quad \text{for } l = 1, 2, \dots, N.$$

It is worth mentioning again that, unless otherwise indicated, the scattered field dataset (the MSR matrix) is generated from the first-order formulation (2.10), with no far-field assumption, using a very fine sampling along the supporting curve. After computing this dataset, the singular value decomposition of  $K$  is performed thanks to a Matlab subroutine. Once the singular values obtained, they are, save exception (see next), normalized with respect to the one of maximum amplitude.

For each  $z \in \tilde{\Omega}$ , values of scalar  $a$  and vectors  $b$ , and/or  $c$  have to be selected. The choice of  $a = 1$  is obviously as good as another one, the other two are to be appraised from numerical experimentation. As for the step size of  $z$ , it is taken of the order of 0.02.

### 2.5.2 Permittivity contrast only ( $\mu = \mu_0, \varepsilon \neq \varepsilon_0$ )

### 2.5.3 Preliminary results

As pre-condition to efficacy of the imaging, it is necessary to discriminate the singular values that are significant of the signal subspace (and vectors spanning it) from those that are associated to the noise subspace (and vectors spanning it), via a careful thresholding. Let us work on that matter with  $\Gamma_1$ ,  $K$  being collected for  $N = 10$  and  $N = 20$ , and the wavelengths of operation  $\lambda = 0.8$  and  $\lambda = 0.2$ , respectively. Distributions of the normalized singular values of  $K$  and maps of  $W_a(z)$  are displayed in Fig. 2.2.

Each time, a small finite number of singular values (3 at  $\lambda = 0.8$ , 9 at  $\lambda = 0.2$ ) emerges from the remaining, much smaller ones, whilst images thereupon produced by projection onto singular vectors beyond the first 3 or 9 ones appear excellent, a small number of peaks being obtained, each peak being observed to be  $\lambda/2$  away from the next one, the supporting curve passing very closely through their line of crests. No problem of discrimination is faced, and this in effect remains true whenever a straight curve is

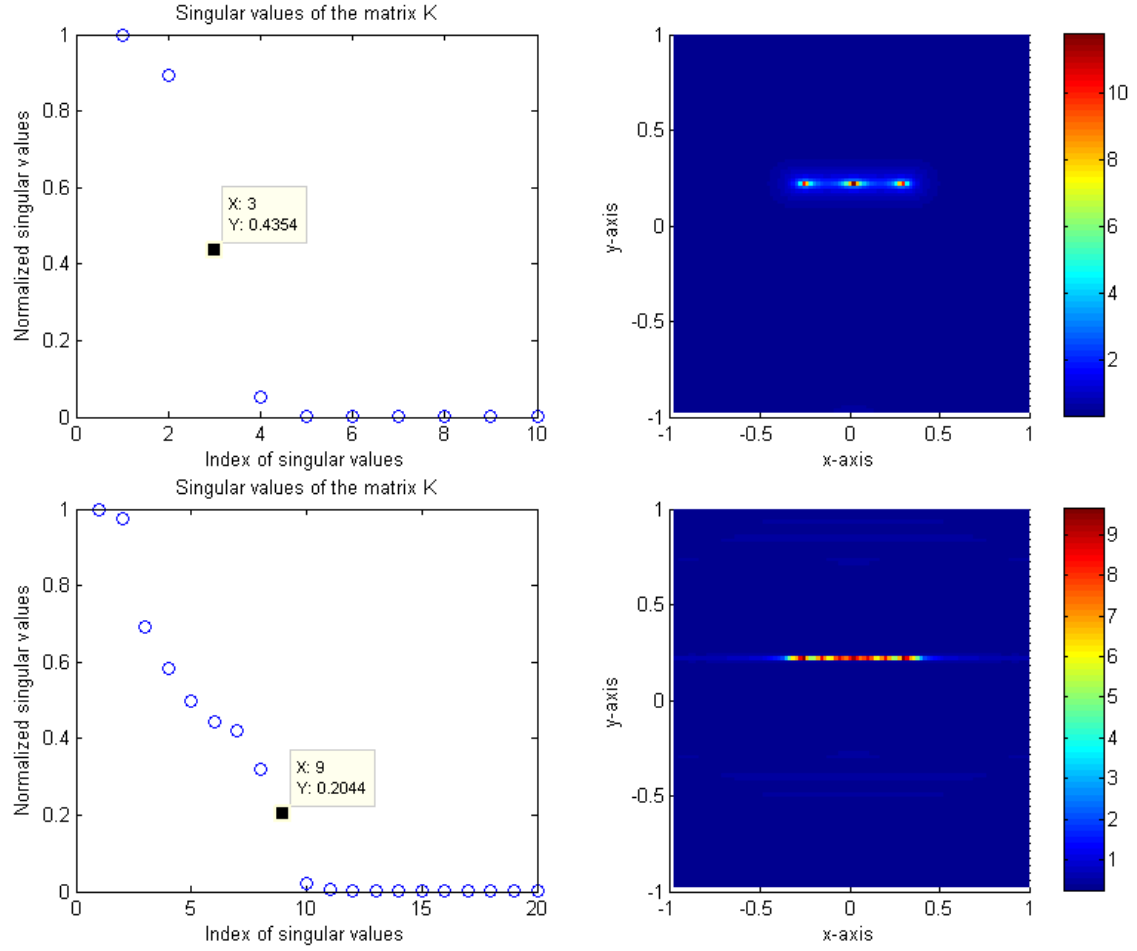


FIG. 2.2 – Distributions of normalized singular values of matrix  $K$  (left column) and maps of  $W_a(z)$ ,  $z \in \tilde{\Omega}$ ,  $a = 1$  (right column), for  $N = 10$  incidences and  $\lambda = 0.8$  wavelength (top line), for  $N = 20$  and  $\lambda = 0.2$  (bottom line), when the inclusion is  $\Gamma_1$ , with dielectric contrast of 5.

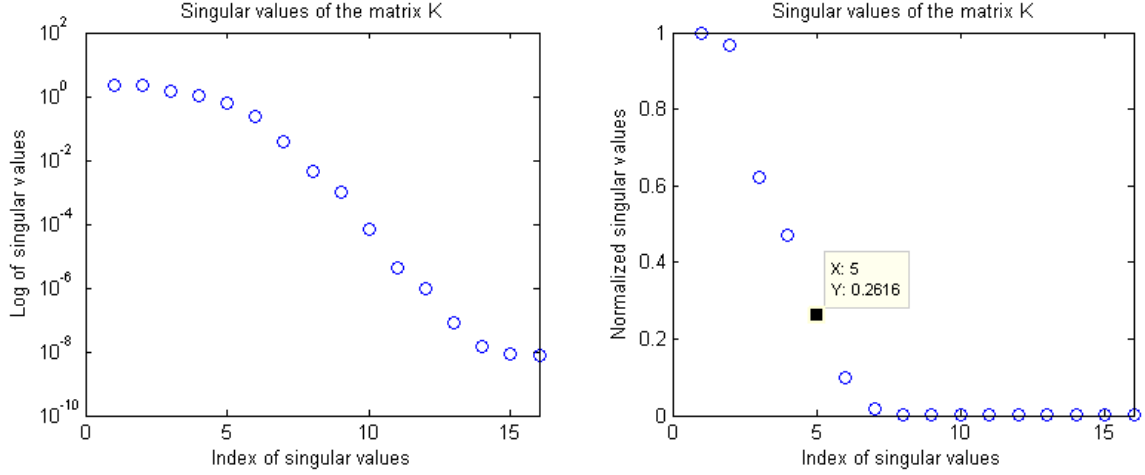


FIG. 2.3 – Distribution of log-scaled (left) and normalized (right) singular values of matrix  $K$  for  $N = 16$  incidences and  $\lambda = 0.6$  wave length, when the inclusion is  $\Gamma_3$ , with dielectric contrast of 5.

to be imaged, whatever be its type of contrast and the conditions of illumination (if the ratio  $N/M$  is kept properly large).

When  $\sigma$  is not anymore a straight segment, the discrimination becomes less obvious. As an example, let us image  $\Gamma_3$ , here using  $N = 16$  incident directions and a wavelength of 0.6, refer to Fig. 2.3. The log-scale distribution of the singular values in this case is certainly not amenable to easy thresholding —this phenomenon is also in contrast with most results on singular value decomposition presented in [8]. The normalized distribution seems however easier to deal with, and keeping only the values  $\lambda_j$  such that  $\frac{\lambda_j}{\lambda_1} \geq 0.1$ , here 5 of them, leads to acceptable imaging. This is further illustrated by Fig. 2.4, where images of  $\Gamma_3$  are displayed for several thresholds, assuming, in consequence, that at least 3 and up to 8 singular values might characterize the signal subspace.

In conclusion, too small a number of singular values (or too high a threshold) leads to a blurred image, whereas too high a number of singular values (or too small a threshold) to a perturbed one, the choice of 5 (and the 0.1 threshold) providing 5 well-defined peaks that are regularly spanning the supporting curve.

Henceforth, the 0.1 threshold is adopted, being acknowledged that this should be in practice tuned to the effectively observed distribution, whereas a change of threshold, and a number of singular values increased or decreased per one unity, might still have not much impact on the final results. Maps of other inclusions are then successfully obtained.

This is illustrated by the case of  $\Gamma_2$ ,  $K$  being collected for  $N = 15$  and  $N = 20$ , and the wavelengths of operation being  $\lambda = 0.5$  and  $\lambda = 0.3$ , respectively. Distributions of the normalized singular values of  $K$  and maps of  $W_a(z)$  are displayed in figure 2.5.

One point is worthwhile to observe at this stage. With reference to figures 2.6 and 2.7, where  $\Gamma_2$  is imaged, with either  $N = 10$  or  $N = 20$  illuminations, at fixed 0.7 wavelength, it appears that too small a  $N$  might be source of inaccuracy, since an isolated high peak is emerging at  $N = 10$ , and is absent at  $N = 20$ , though the thresholding seems efficient

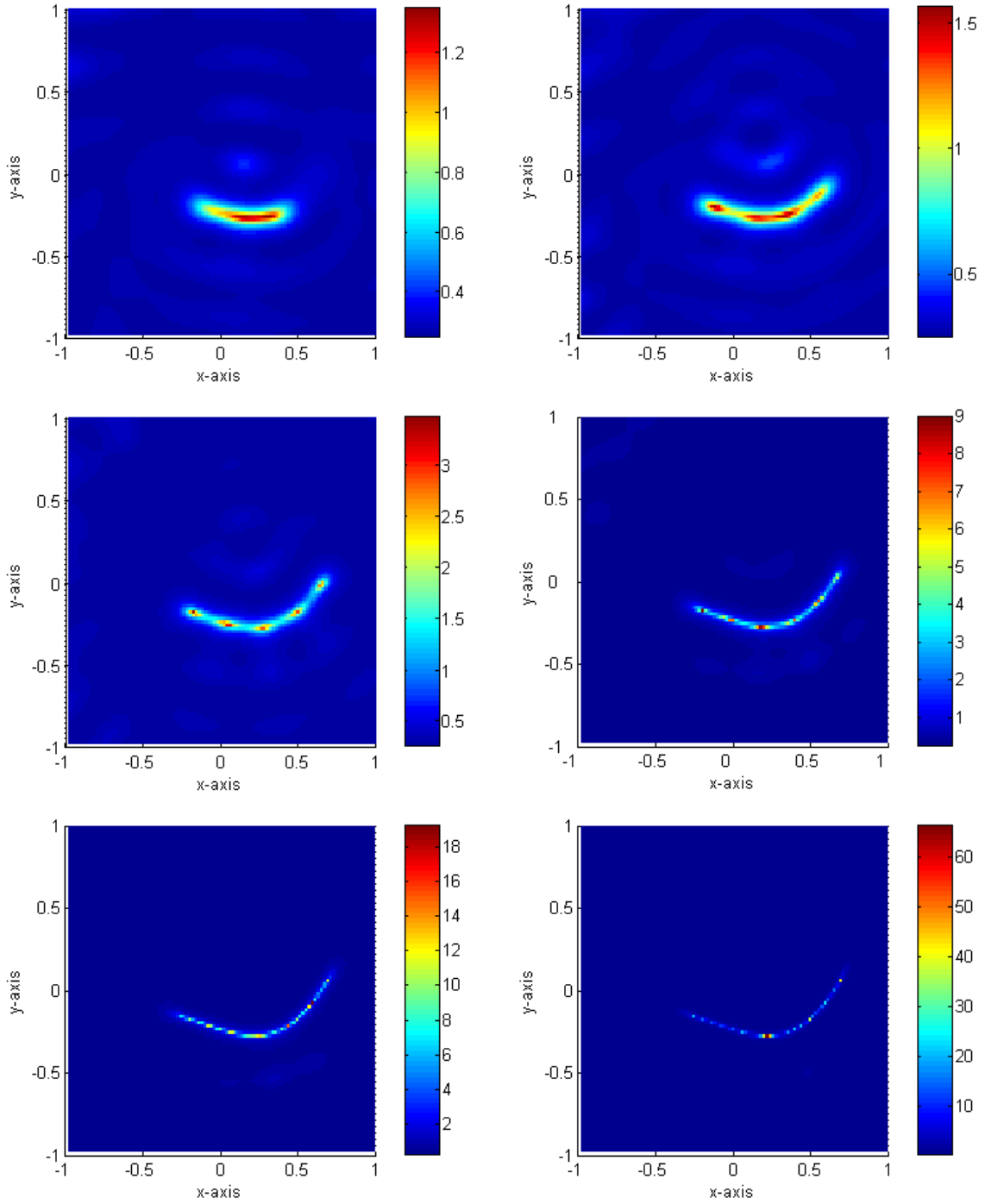


FIG. 2.4 – Maps of  $W_a(z)$ ,  $z \in \tilde{\Omega}$ ,  $a = 1$ , assuming 3 (top-left), 4 (top-right), 5 (middle-left), 6 (middle-right), 7 (bottom-left) and 8 (bottom-right) singular values in the signal subspace, for  $N = 16$  incidences and  $\lambda = 0.6$  wavelength, when the inclusion is  $\Gamma_3$ , with dielectric contrast of 5.

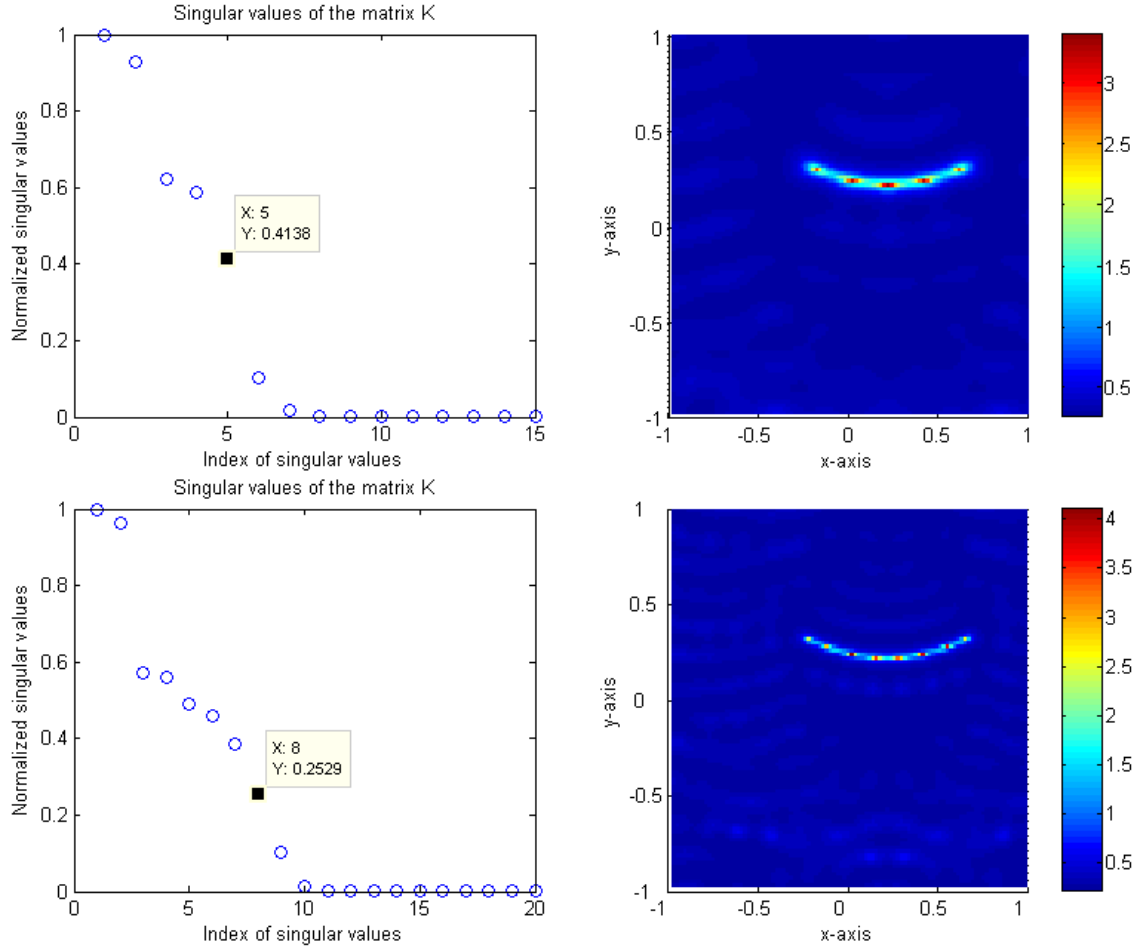


FIG. 2.5 – Distributions of normalized singular values of matrix  $K$  (left column) and maps of  $W_a(z)$ ,  $z \in \tilde{\Omega}$ ,  $a = 1$  (right column), for  $N = 15$  incidences and  $\lambda = 0.5$  wavelength (top line), for  $N = 20$  and  $\lambda = 0.3$  (bottom line), when the inclusion is  $\Gamma_2$ , with dielectric contrast of 5.

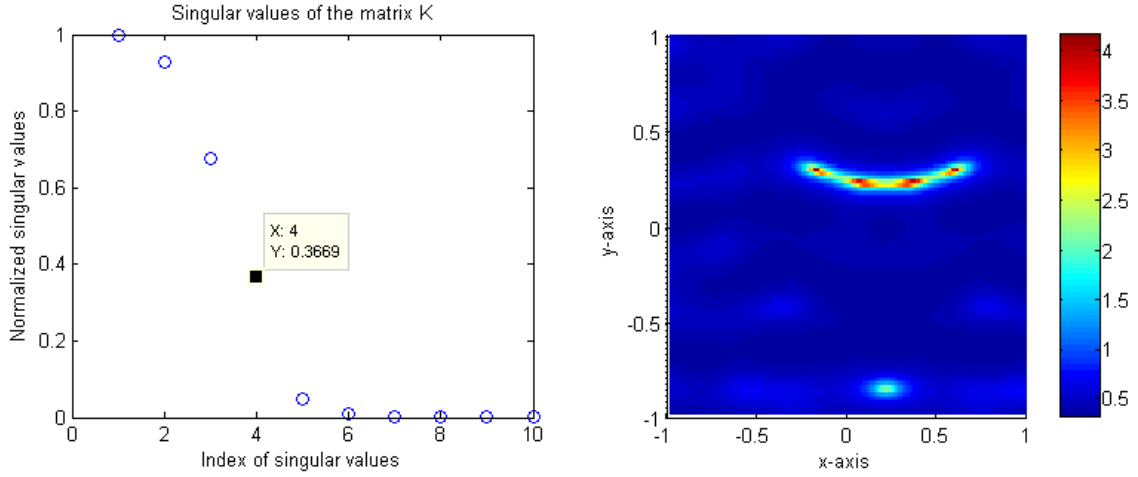


FIG. 2.6 – Distribution of normalized singular values of matrix  $K$  (left) and map of  $W_a(z)$ ,  $z \in \tilde{\Omega}$ ,  $a = 1$  (right), for  $N = 10$  incidences and 0.7 wavelength when the inclusion is  $\Gamma_2$ , with dielectric contrast of 5.

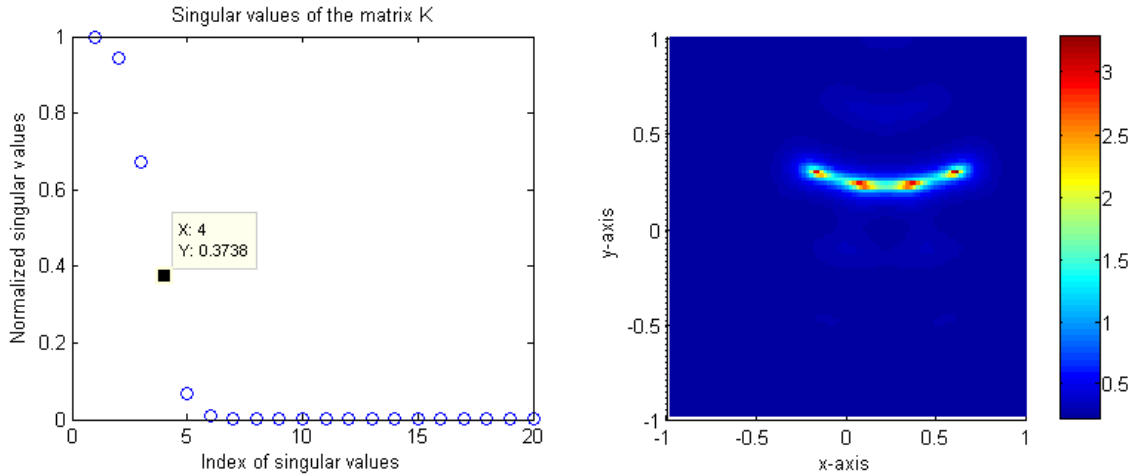


FIG. 2.7 – Same as in figure 2.6, save  $N = 20$ .

in both cases, 4 well-defined peaks being observed along the sought supporting curve.

Complementary sets of images of  $\Gamma_3$ , one at high frequency ( $\lambda = 0.2$ ), one at low frequency ( $\lambda = 0.8$ ), are displayed in Fig. 2.8. They exemplify how the spectrum enlarges, and how the number of peaks grows (from 4 to 13) and their sharpness as well, when the frequency is increased, a  $\lambda/2$  interval always separating the peaks (the image resolution improves in absolute terms, not in electromagnetics terms, the along-the-curve resolution remains of the half wavelength).

Now, we apply the algorithm to an oscillating inclusion. The configuration is the same as previously save the search domain  $\tilde{\Omega} = [-1.5, 1.5] \times [-1.5, 1.5]$ . Two  $\sigma_j$  are chosen for illustration (see Fig. 2.9) :

$$\begin{aligned}\sigma_4 &= \{(z, 0.5z^2 + 0.1 \sin(4\pi(z+1))) : z \in (-1, 1)\} \\ \sigma_5 &= \{(z, 0.5z^2 + 0.05 \sin(20\pi(z+1)) - 0.01 \cos(15\pi z)) : z \in (-1, 1)\}.\end{aligned}$$

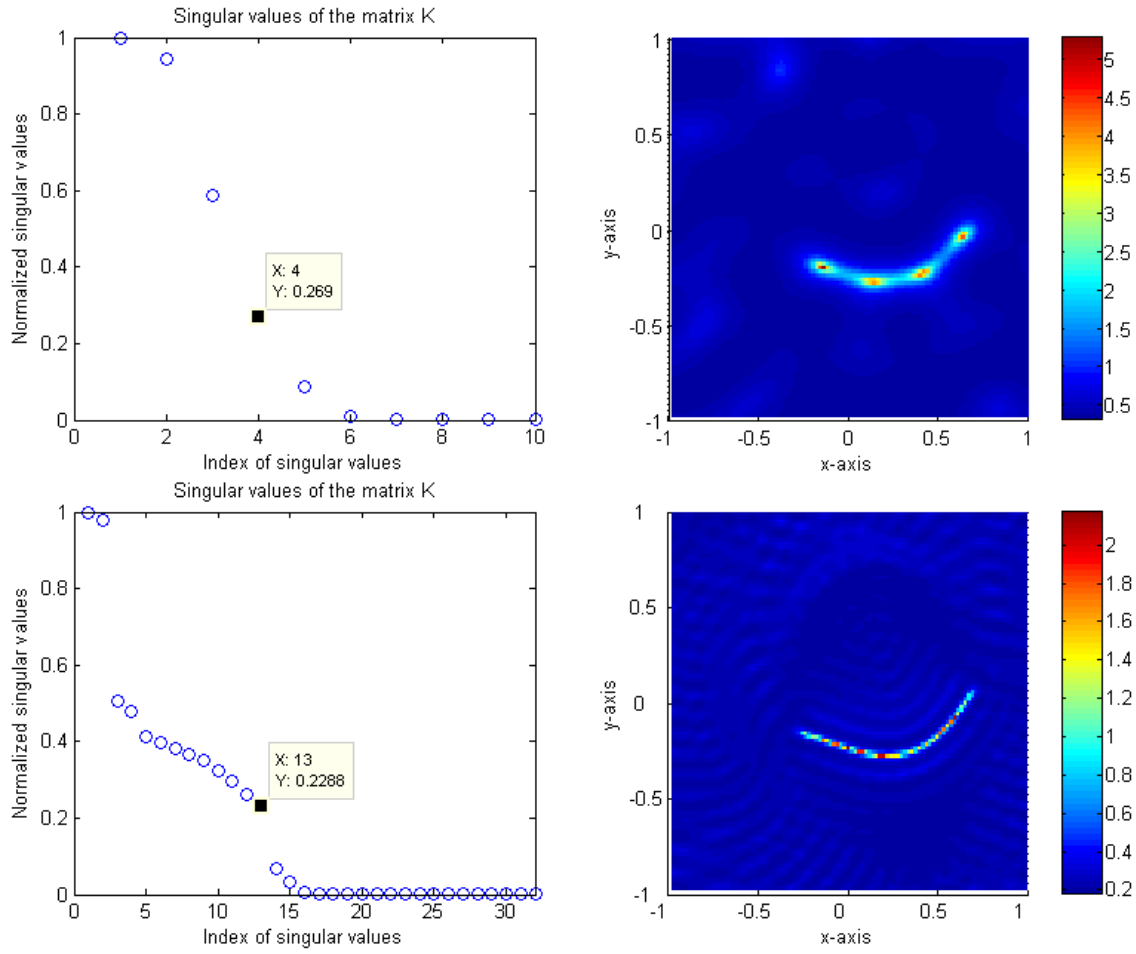


FIG. 2.8 – Distributions of normalized singular values of matrix  $K$  (left column) and maps of  $W_a(z)$ ,  $z \in \tilde{\Omega}$ ,  $a = 1$  (right column), for  $N = 10$  incidences and  $\lambda = 0.8$  wavelength (top line), for  $N = 32$  and  $\lambda = 0.2$  (bottom line), when the inclusion is  $\Gamma_3$ , with dielectric contrast of 5.

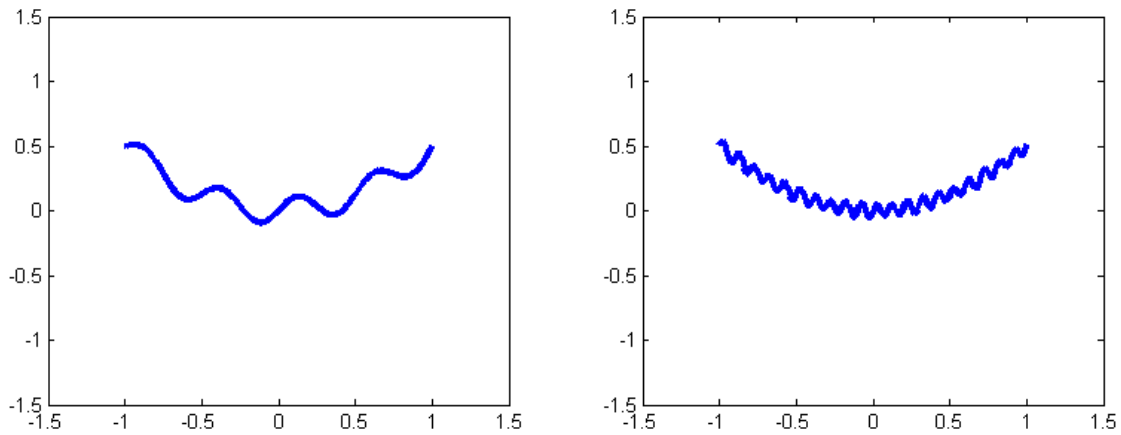


FIG. 2.9 – Shape of  $\Gamma_4$  (left),  $\Gamma_5$  (right).

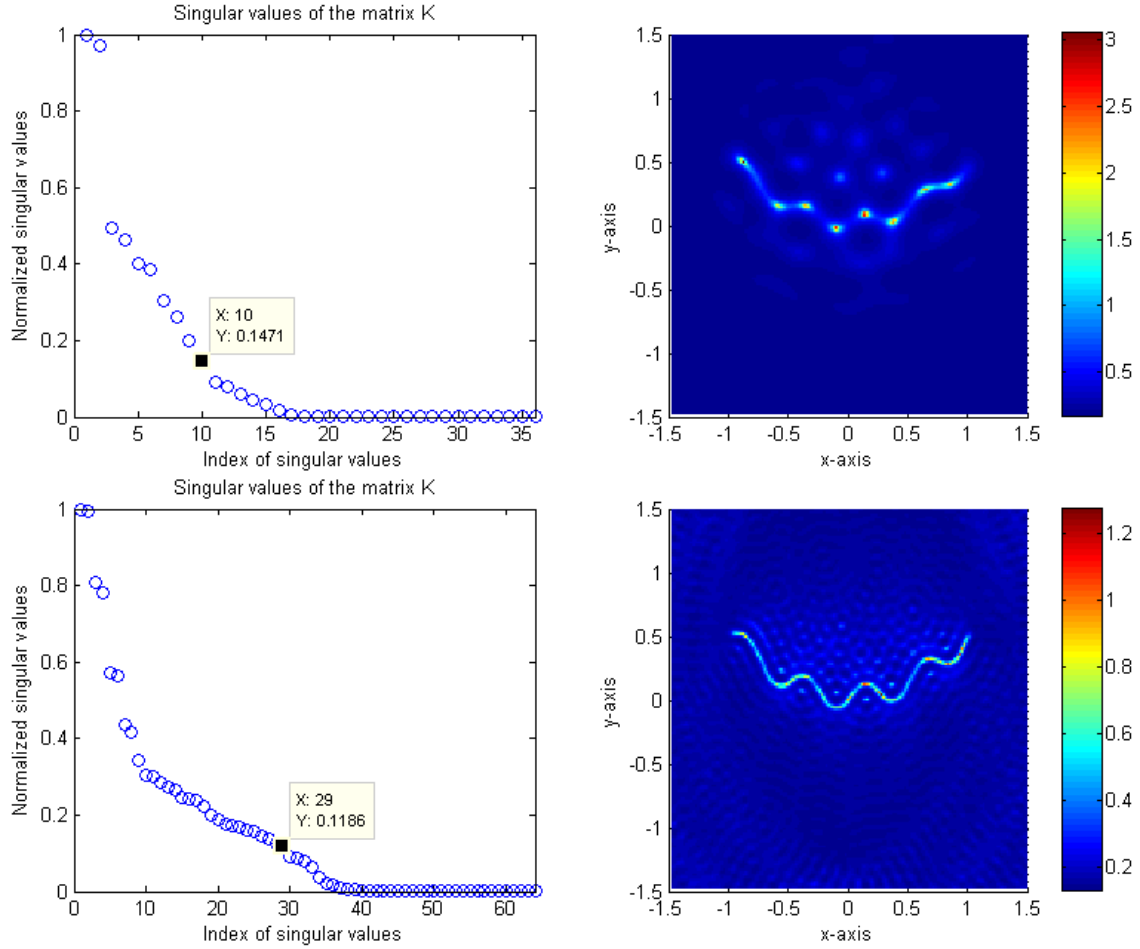


FIG. 2.10 – Distributions of normalized singular values of matrix  $K$  (left column) and maps of  $W_a(z)$ ,  $z \in \tilde{\Omega}$ ,  $a = 1$  (right column), for  $N = 36$  incidences and  $\lambda = 0.6$  wavelength (top line), for  $N = 64$  and  $\lambda = 0.2$  (bottom line), when the inclusion is  $\Gamma_4$ , with dielectric contrast of 5.

Let us consider  $\Gamma_4$ . Typical results are in figure 2.10 at  $\lambda = 0.6$  and  $\lambda = 0.2$ . Imaging is rather coarse at the low wavelength, better at the high one. The thresholding still looks convenient, whilst a high value of  $N$  is to be taken as expected.

For the case of a more oscillating inclusion  $\Gamma_5$ , the results are not so good, as is seen in Fig. 2.11. Nevertheless, we can still say that a good initial guess is obtained at low computational cost, to be improved upon by an appropriate iterative algorithm.

#### 2.5.4 On inverse crime and the use of other datasets

As it has been insisted upon already, instead of using (2.10) to obtain the scattered field datasets, one could employ an asymptotic formulation involving the solution of a second-kind Fredholm integral equation along the supporting curve, linked to the thinness of the inclusion [61]. Images of a thin penetrable inclusion from the first-order data or from the ones calculated according to this alternative formulation are almost indistinguishable, refer to center row of Fig. 2.12.



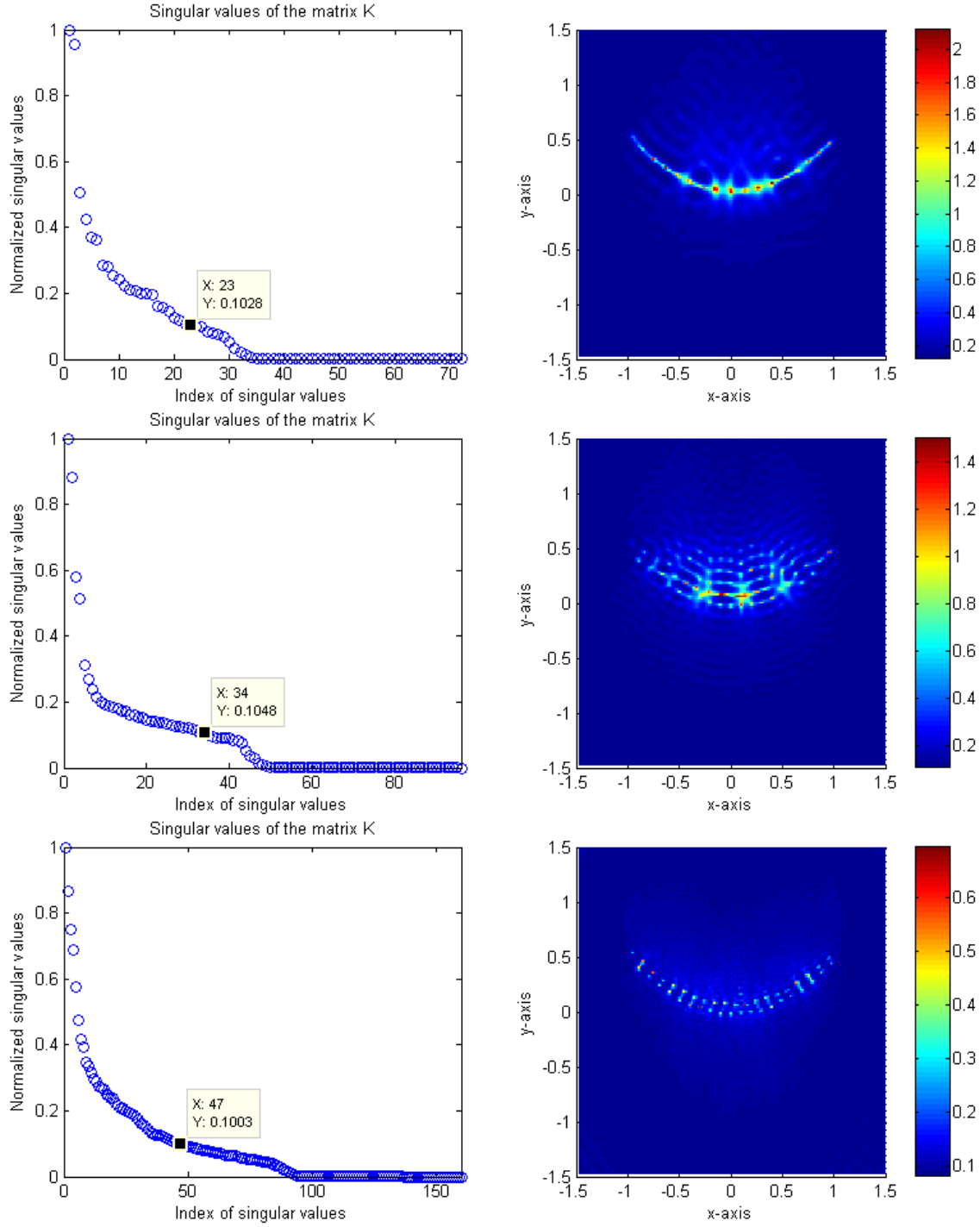


FIG. 2.11 – The distribution of normalized singular values of the matrix  $K$  (Left column) and maps of  $W_a(z)$  when  $a = 1$  (right column), for all points  $z \in \tilde{\Omega}$  for  $N = 72$  incidences and a 0.3 wave length (top row), for  $N = 96$  incidences and a 0.2 wave length (center row) and for  $N = 160$  incidences and a 0.1 wave length (bottom row) when the thin inclusion is  $\Gamma_5$ , with dielectric contrast of 5.

In line with the preceding illustration, images can be produced from scattered field data computed by a brute-force Method-of-Moments(MoM) solution algorithm [72] (solution algorithm is M. Lambert's courtesy, L2S) applied to a domain integral formulation in the case of a supporting straight segment, the main challenge being to cover the inclusion with pixels small enough with respect both to the wavelength and to the inclusion thickness, and not too numerous overall. Such images in effect appear to be very much like those built up from the first-order data, whatever be the assumed thickness  $h = 0.015$  in the solution algorithm, refer to bottom row of figure 2.12 and  $h = 0.0025$ , 0.005 and 0.01, refer to Fig. 2.13.

To generate the data one could also apply the discrete formula (2.15)

$$K_{jl} \approx (\varepsilon - \varepsilon_0) \frac{|\sigma|}{M} \sum_{m=1}^M e^{ik_0(\theta_j + \theta_l) \cdot x_m}.$$

This is a fictitious situation since  $M$  is unknown, and this would be pure inverse crime, yet the results are comforting as follows. The normalized singular values and images resulting from this formula are displayed in Fig. 2.14. The top line of figure 2.14 shows the distribution of normalized singular values and imaging result when  $M = 8$ . The map  $W_a(z)$  clearly shows that there are eight points regularly distributed along the supporting curve  $\sigma$ , and separated by the half-wavelength. The center and bottom line of Fig. 2.14 show the distribution of normalized singular values and imaging result when  $M = 64$  and  $M = 128$ , respectively. The distribution of normalized singular values and imaging results do not depend much upon the value of  $M$  chosen. In short, the MUSIC estimator built upon the singular value decomposition of the MSR matrix due to the thin inclusion peaks regularly on the inclusion curve, independently of the data model used to calculate the MSR matrix (as long as  $h$  is small enough, obviously), since results are alike whatever this model.

### 2.5.5 Robustness with respect to noise

Let us assume at this stage of the analysis that noise is added onto the (first-order) data, i.e., for every  $x \in \mathbb{R}^2$ ,

$$u_{\text{noise}}(x) = \{1 + \xi \times (\text{rnd}_1(-1, 1) + i \text{rnd}_2(-1, 1))\} u(x)$$

where  $\text{rnd}_1(-1, 1)$  and  $\text{rnd}_2(-1, 1)$  are distinct arbitrary real values between  $-1$  and  $1$ .

An image of  $\Gamma_1$  for the case  $\xi = 5 \times 10^{-2}$  is in Fig. 2.15 at  $\lambda = 0.8$ . Although the distribution of log-scaled singular values is significantly different, one can easily find proper singular values and obtain a rather accurate image via the normalizing method. For the case of the curved thin inclusion  $\Gamma_3$  with noise  $\xi = 3 \times 10^{-1}$ , the same phenomenon occurs, refer to Fig. 2.16. As expected, in both cases, adding noise tends to decrease the quality of the image with respect to the noiseless case (more variations in the dark zone, less sharp peaks along the inclusion curve).

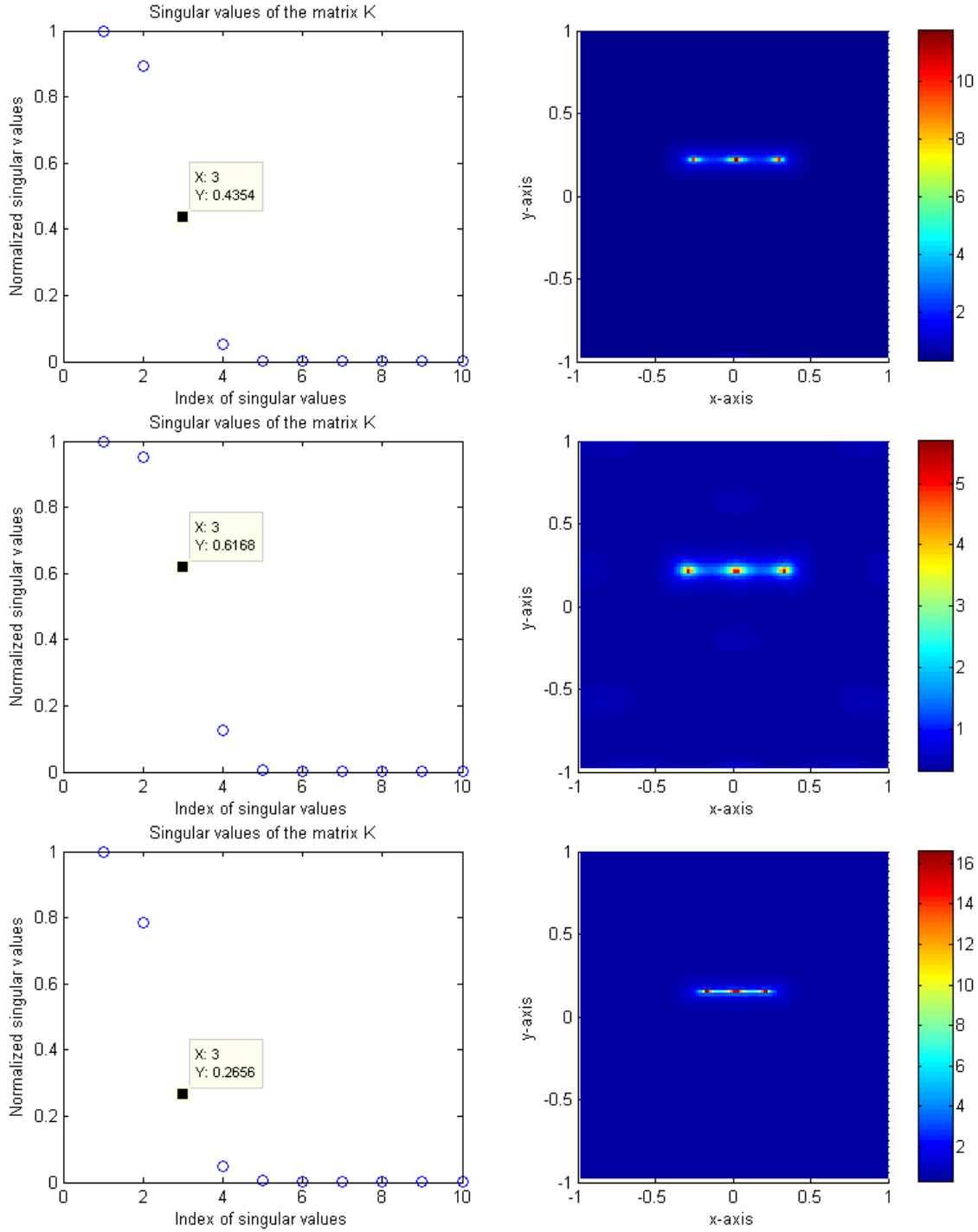


FIG. 2.12 – Distribution of normalized singular values of the MSR matrix  $K$  (left column) and maps of  $W(z)$ ,  $z \in \tilde{\Omega}$  (right column), for  $N = 10$  incidences and a  $\lambda = 0.8$  wavelength when the inclusion is  $\Gamma_1$ . The datasets are generated by solving formula (2.10) (top row), second-kind Fredholm integral equation of [61] (center row), and by using a MOM solution algorithm for  $h = 0.015$  (bottom row).

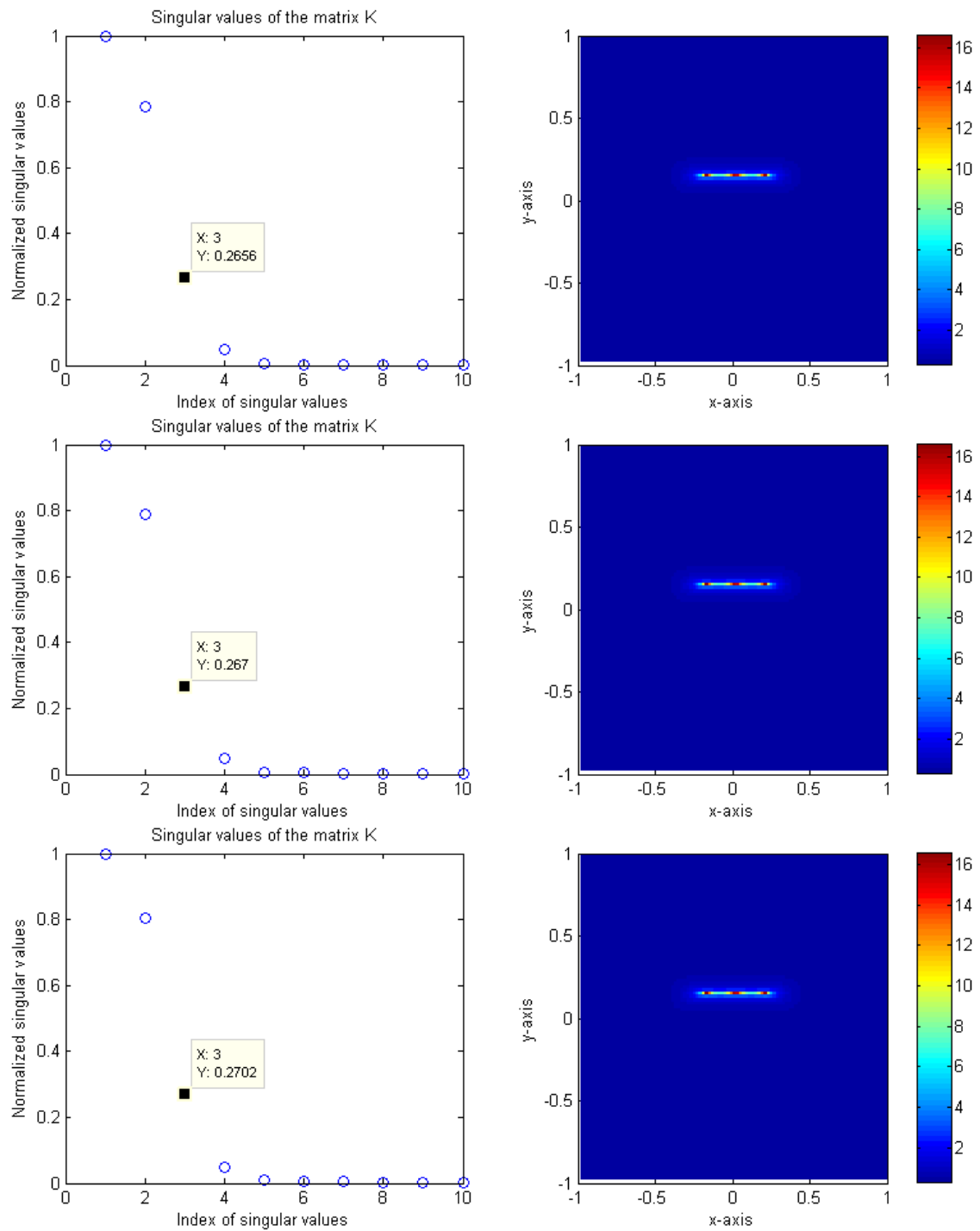


FIG. 2.13 – Same as in Fig. 2.12. The datasets are generated by using a MOM solution algorithm for  $h = 0.0025$  (top row),  $0.005$  (center row) and  $0.01$  (bottom row).

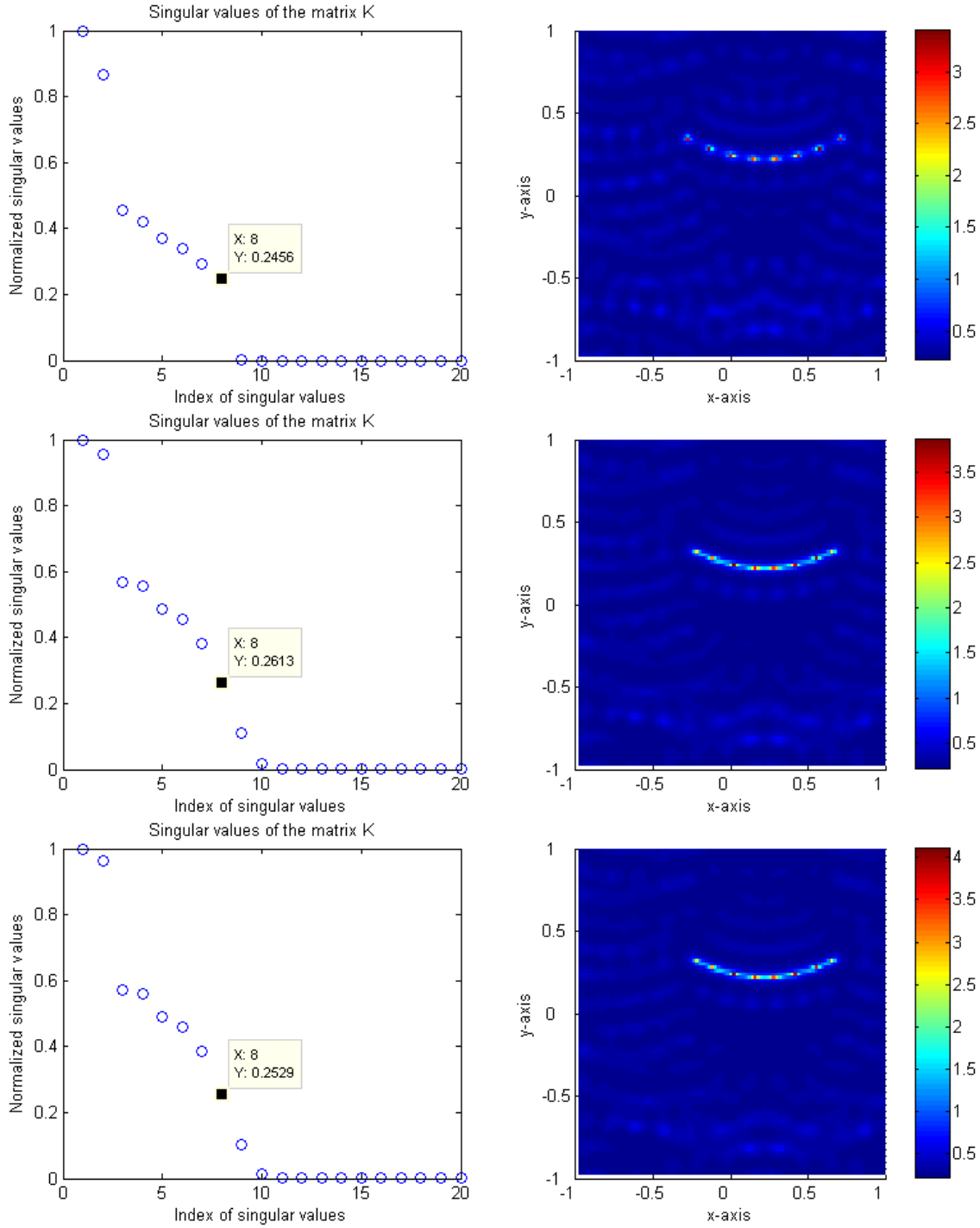


FIG. 2.14 – Applying the discrete formula (2.15). Distributions of normalized singular values of matrix  $K$  (left column) and maps of  $W_a(z)$ ,  $z \in \tilde{\Omega}$ ,  $a = 1$  (right column), with  $M = 8$  (top line),  $M = 64$  (center line) and  $M = 128$  (bottom line) for  $N = 20$  incidences and  $\lambda = 0.3$  wavelength, when the inclusion is  $\Gamma_2$ , with dielectric contrast of 5.

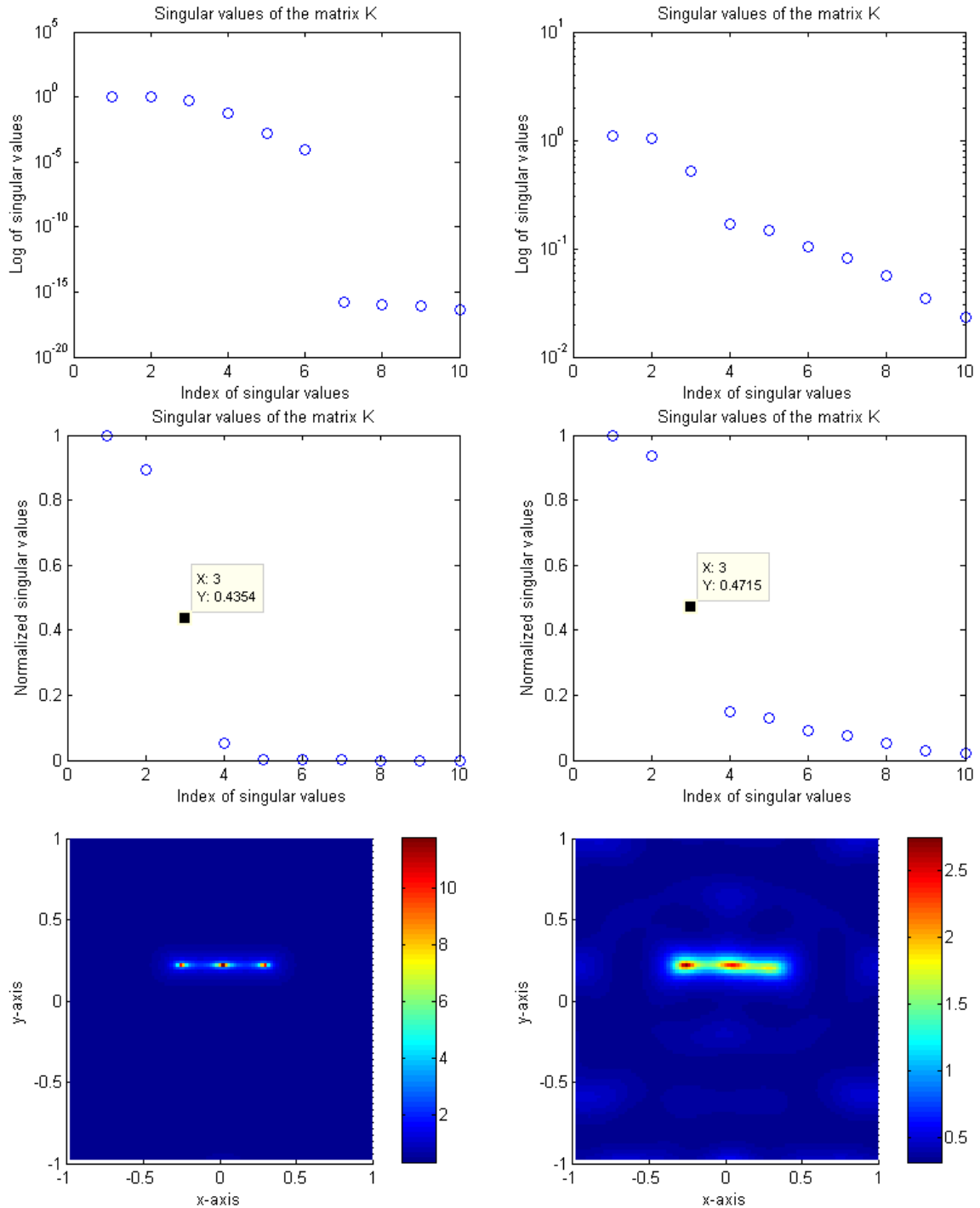


FIG. 2.15 – The distribution of log-scaled (top row) and normalized (center row) singular values of the matrix  $K$  and maps of  $W_a(z)$  when  $a = 1$  (bottom row) without noise (left column) and with noise added ( $\xi = 5 \times 10^{-2}$ ) for all points  $z \in \tilde{\Omega}$  for  $N = 10$  incidences and a 0.8 wave length when the thin inclusion is  $\Gamma_1$  with dielectric contrast of 5.

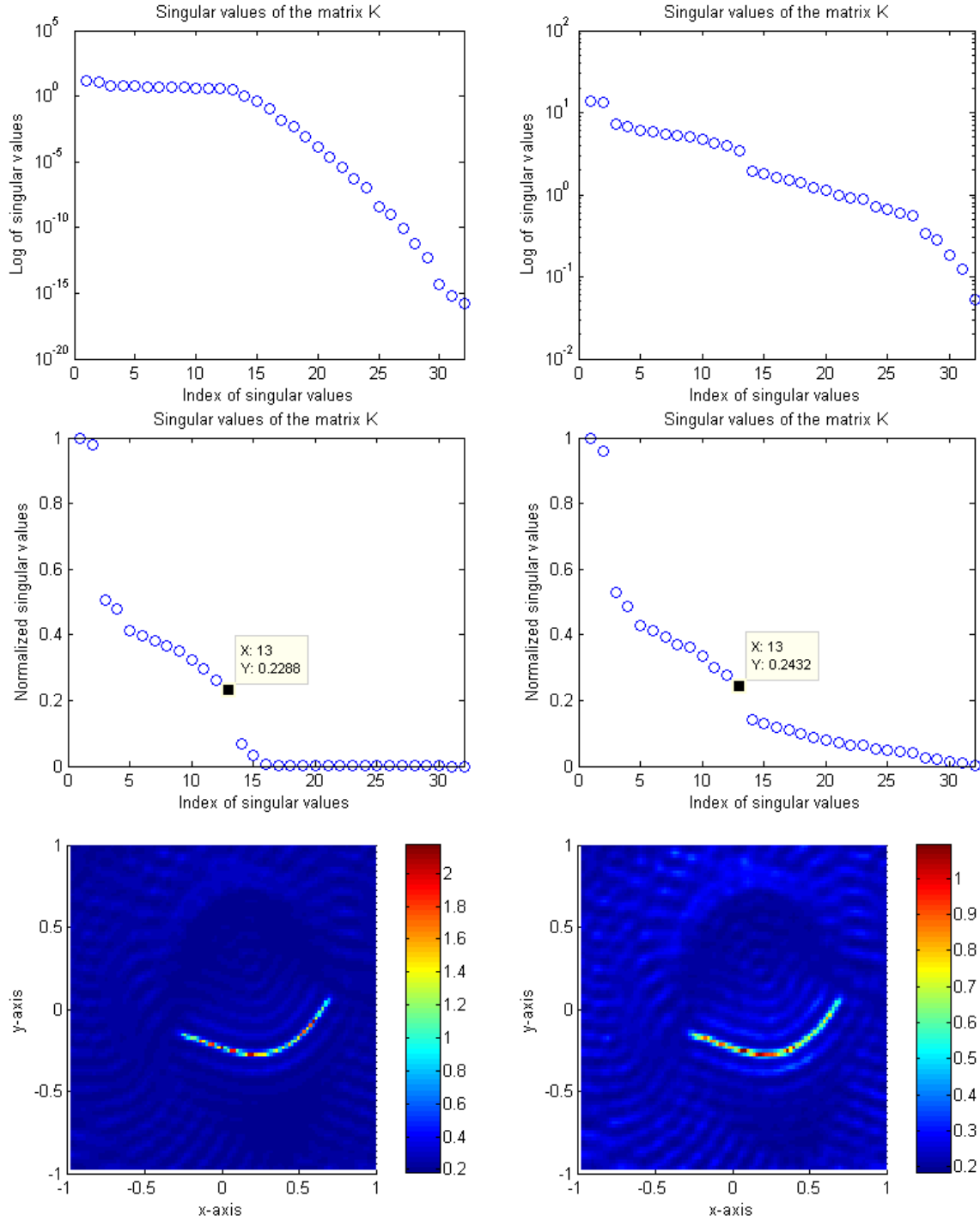


FIG. 2.16 – The distribution of log-scaled (top row) and normalized (center row) singular values of the matrix  $K$  and maps of  $W_a(z)$  when  $a = 1$  (bottom row) without noise (left column) and with noise added ( $\xi = 3 \times 10^{-1}$ ) for all points  $z \in \tilde{\Omega}$  for  $N = 32$  incidences and a 0.2 wave length when the thin inclusion is  $\Gamma_3$  with dielectric contrast of 5.

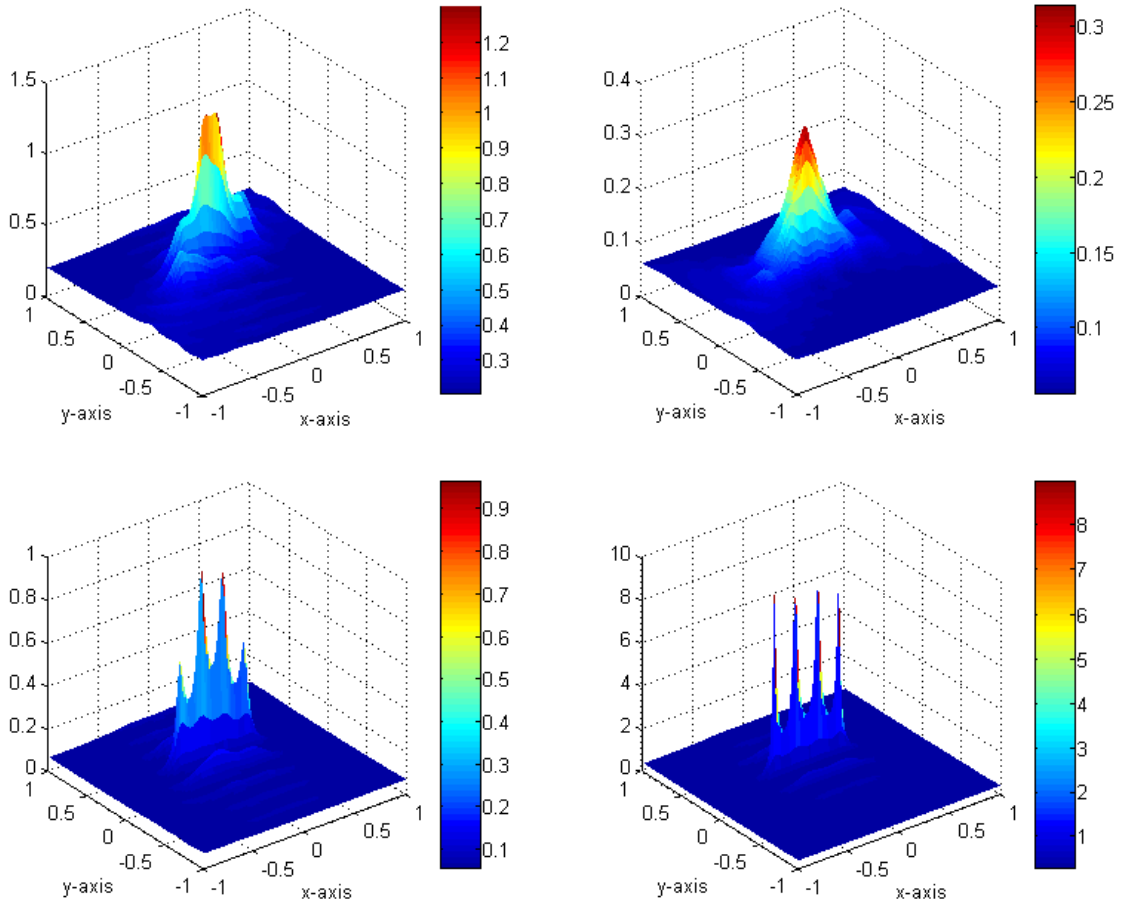


FIG. 2.17 – 3-D maps of  $W_b(z)$ ,  $z \in \tilde{\Omega}$ ,  $b = (1, 1)$  (top-left),  $b = (5, 1)$  (top-right),  $b = (1, 5)$  (bottom-left),  $b = (0, 1)$  (bottom-right), for  $N = 24$  incidences and a  $\lambda = 0.5$  wavelength, when the inclusion is  $\Gamma_1$  and has a magnetic contrast of 5.

### 2.5.6 Permeability contrast only ( $\mu \neq \mu_0$ , $\varepsilon = \varepsilon_0$ )

### 2.5.7 Estimation of the best $b$

In this configuration, to properly choose the vector  $b = (b_1, b_2)$  is a strong supplementary prerequisite to good imaging, in addition to the choice of the threshold (kept at 0.1) and of the number of illuminations (at least twice more than in the purely dielectric case, as a reminder). The following four cases have been studied :  $b_1 = b_2$  ( $b_1 = b_2 = 1$ ) ;  $b_1 > b_2$  ( $b_1 = 5$ ,  $b_2 = 1$ ) ;  $b_1 < b_2$  ( $b_1 = 1$ ,  $b_2 = 5$ ) ; and  $b_1 < b_2$  ( $b_1 = 0$ ,  $b_2 = 1$ ). Results are displayed in Fig. 2.17, limiting ourselves to  $\Gamma_1$  of permeability  $\mu = 5$ , and using  $N = 24$  incident directions and a 0.5 wavelength. They appear the best whenever  $b_2 > b_1$ , with excellent ones for  $b = (0, 1)$ . Let us emphasize that this value  $b$  is but the unit normal vector  $n$  to  $\sigma_1$ —before carrying the imaging one cannot know that normal vector, and one is faced with a nonlinear inversion problem if one would like to get the best  $b$  simultaneously with the distribution of points along the unknown curve.

When the permeability of the thin inclusion is less than the background one (i.e., if  $\mu < \mu_0$ ), the choice of  $b$  must be otherwise. Similar to the previous one, the following



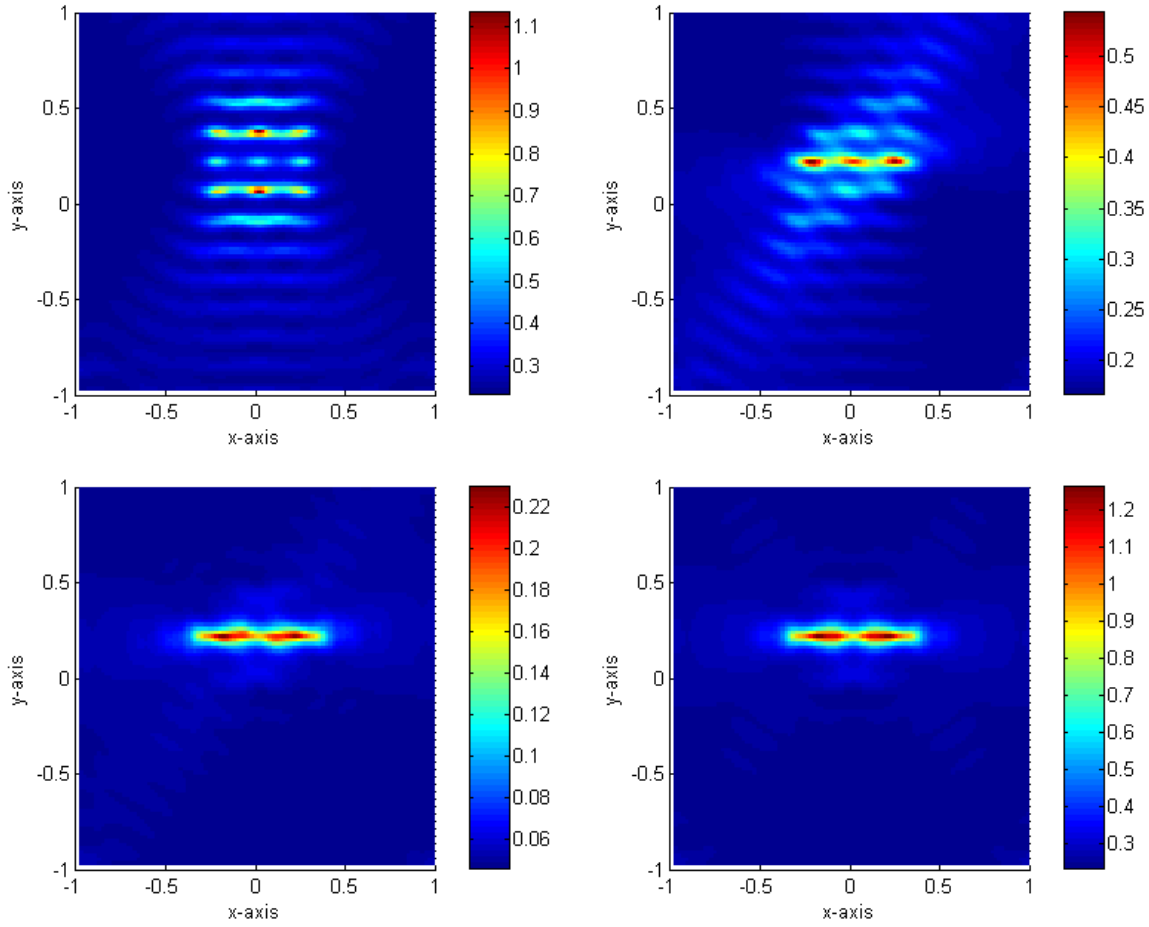


FIG. 2.18 – 3-D maps of  $W_b(z)$ ,  $z \in \tilde{\Omega}$ ,  $b = (0, 1)$  (top-left),  $b = (1, 1)$  (top-right),  $b = (5, 1)$  (bottom-left),  $b = (1, 0)$  (bottom-right), for  $N = 32$  incidences and a  $\lambda = 0.3$  wavelength, when the inclusion is  $\Gamma_1$  and has a magnetic contrast of 0.2.

four cases have been studied :  $b_1 < b_2$  ( $b_1 = 0$ ,  $b_2 = 1$ ) ;  $b_1 = b_2$  ( $b_1 = b_2 = 1$ ) ;  $b_1 > b_2$  ( $b_1 = 5$ ,  $b_2 = 1$ ) ; and  $b_1 > b_2$  ( $b_1 = 1$ ,  $b_2 = 0$ ). Results are displayed in Fig. 2.18, limiting ourselves to  $\Gamma_1$  of permeability  $\mu = 0.2$ , and using  $N = 32$  incident directions and a 0.3 wavelength. They appear the best whenever  $b_1 > b_2$ , with excellent ones for  $b = (1, 0)$ . Notice that this value  $b$  is now the unit tangential vector  $\tau$  to  $\sigma_1$ .

From these two examples, one can say that the best way for choosing  $b$  appears to be

$$b = \begin{cases} \tau(x) & \text{if } \mu < \mu_0 \\ n(x) & \text{if } \mu > \mu_0 \end{cases} .$$

Although, estimating the tangential (and also normal) vector of the supporting curve  $\sigma$  should not be an easy task, we can obtain a good image with the value of  $b = (1, 0)$  and  $b = (0, 1)$  for  $\mu < \mu_0$  and  $\mu > \mu_0$  respectively. In this permeability contrast case, as we already said, we focus on the imaging of thin inclusion of permeability  $\mu > \mu_0$ .

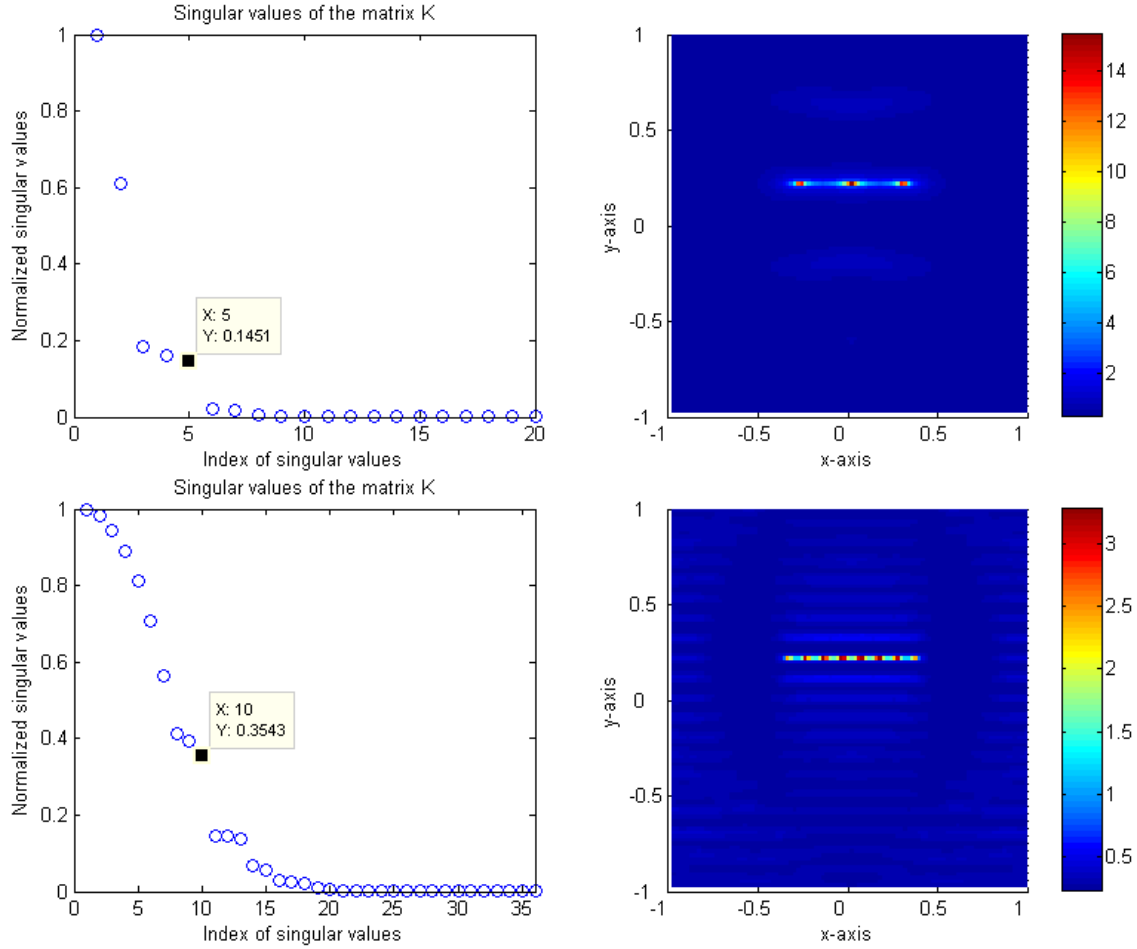


FIG. 2.19 – Distributions of normalized singular values of matrix  $K$  (left column) and maps of  $W_b(z)$ ,  $z \in \tilde{\Omega}$ ,  $b = (0, 1)$  (right column), for  $N = 20$  incidences and  $\lambda = 0.8$  wavelength (top line), for  $N = 36$  and  $\lambda = 0.2$  (bottom line), when the inclusion is  $\Gamma_1$ , with magnetic contrast of 5.

### 2.5.8 Further examples

Let us now consider the retrievals of the three  $\Gamma$  as in previous section and investigate whether length estimates follow also. The straight segment of  $\Gamma_1$  as is displayed in Fig. 2.19 is well amenable to thresholding and very good images are obtained. Results in the case of  $\Gamma_2$  are not as good, refer to Fig. 2.20, yet the imaging procedure still appears fairly reliable, the few ghost replicas which are exhibited in the maps (mostly at the shortest wavelengths) being of much lower amplitude than the ones of the sharp peaks that are regularly spanning  $\sigma$ . Those calculated in the case of  $\Gamma_3$  look alike, refer to Fig. 2.21, with possible weak replicas still, reliability overall remaining fair.

### 2.5.9 Permittivity and permeability contrasts ( $\mu \neq \mu_0$ , $\varepsilon \neq \varepsilon_0$ )

Even more than previously, the choice of the projection vector, here  $c = (c_1, c_2, c_3)$ , is a key matter. One will not detail hereinafter the many potential choices, those being tested apart in systematic fashion, and one will just indicate that  $c = (1, 0, 1)$  was one

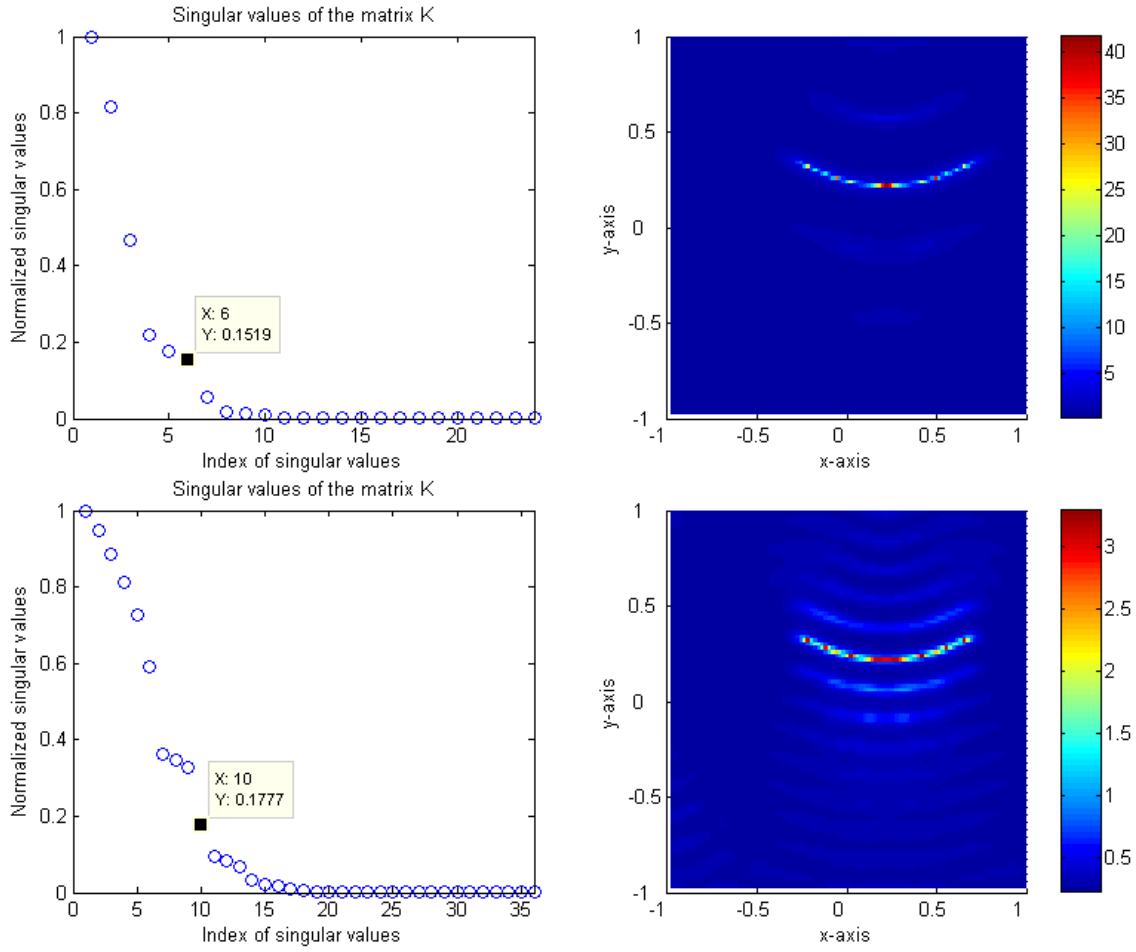


FIG. 2.20 – Distributions of normalized singular values of matrix  $K$  (left column) and maps of  $W_b(z)$ ,  $z \in \tilde{\Omega}$ ,  $b = (0, 1)$  (right column), for  $N = 24$  incidences and  $\lambda = 0.7$  wavelength (top line), for  $N = 36$  and  $\lambda = 0.3$  (bottom line), when the inclusion is  $\Gamma_2$ , with magnetic contrast of 5.

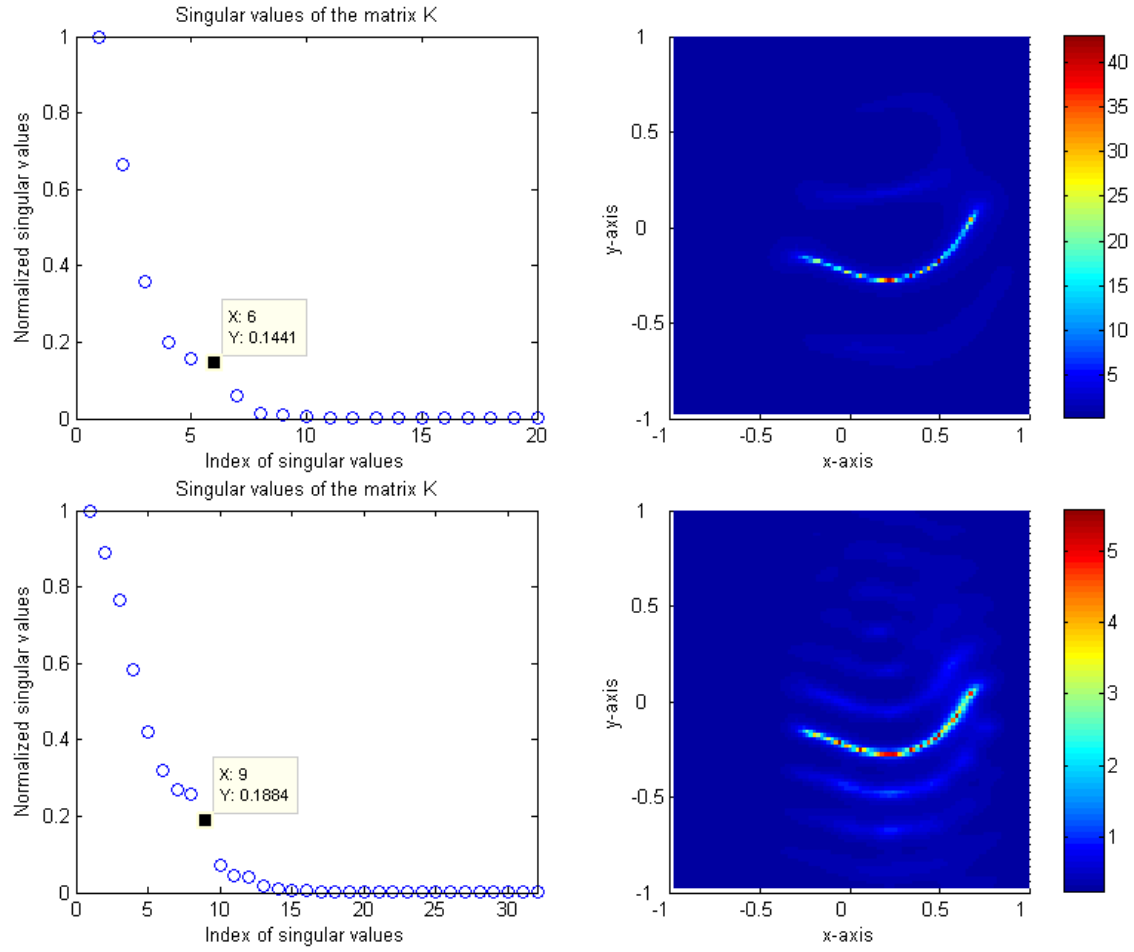


FIG. 2.21 – Distributions of normalized singular values of matrix  $K$  (left column) and maps of  $W_b(z)$ ,  $z \in \tilde{\Omega}$ ,  $b = (0, 1)$  (right column), for  $N = 20$  incidences and  $\lambda = 0.8$  wavelength (top line), for  $N = 32$  and  $\lambda = 0.4$  (bottom line), when the inclusion is  $\Gamma_3$ , with magnetic contrast of 5.

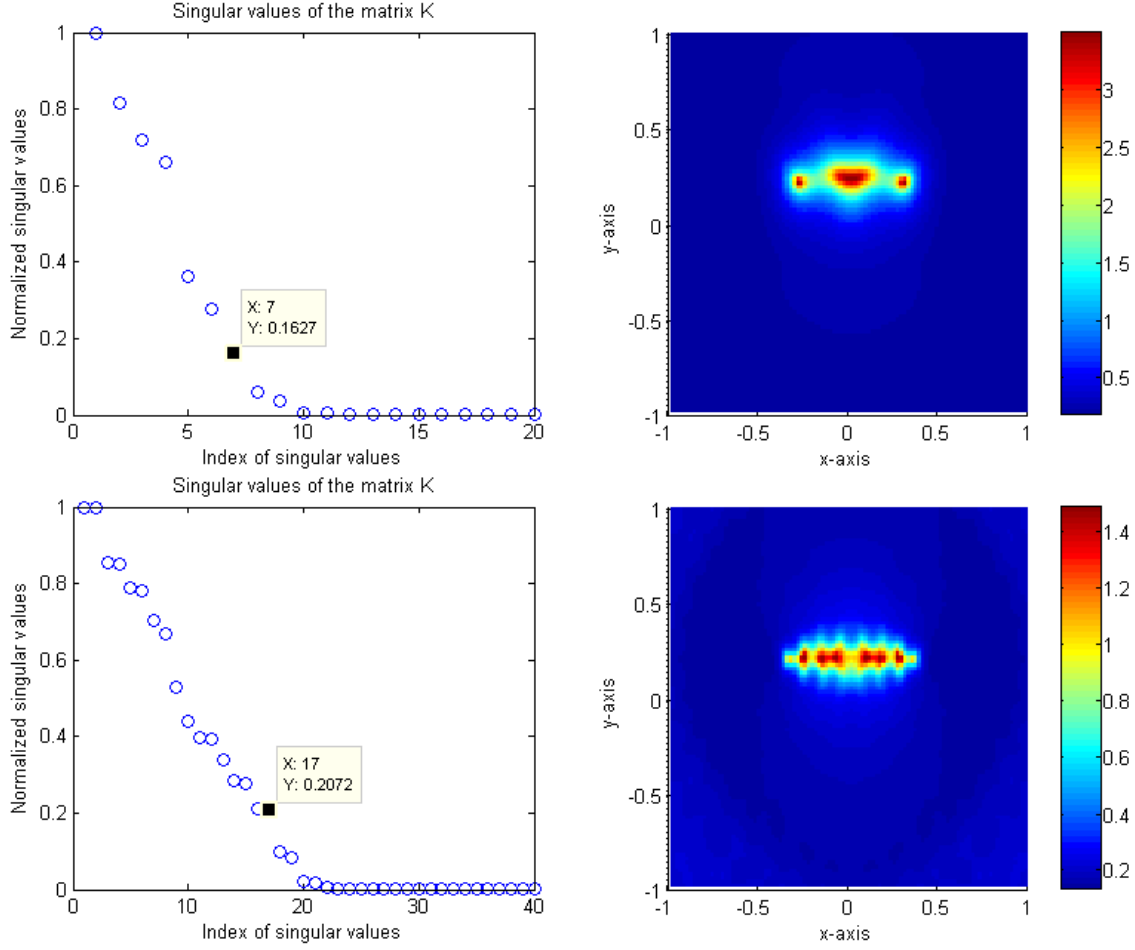


FIG. 2.22 – Distributions of normalized singular values of matrix  $K$  (left column) and maps of  $W_c(z)$ ,  $z \in \tilde{\Omega}$ ,  $c = (1, 0, 1)$  (right column), for  $N = 20$  incidences and  $\lambda = 0.6$  wavelength (top line), for  $N = 40$  and  $\lambda = 0.2$  (bottom line), when the inclusion is  $\Gamma_1$ , with dielectric and magnetic contrast.

choice, among others, which has been revealed satisfactory, and which is the one made from now on.

Let us first consider  $\Gamma_1$ . Typical results are exhibited in Fig. 2.22 at two wavelengths,  $\lambda = 0.6$  and  $\lambda = 0.2$ . A rather coarse imaging is achieved at the high wavelength, a better resolved one at the low wavelength, the retrieval being less effective than in the purely dielectric or purely magnetic case, however. Let us notice that the thresholding seems convenient, whilst a high value of  $N$  is to be taken as expected.

In contrast with the above results, the imaging scheme might yield rather poor results in a number of configurations as is exemplified in Fig. 2.23, with no obvious improvement provided by attempting to optimize the threshold further on. The same phenomenon is observed with  $\Gamma_2$ , the results remaining acceptable yet again not as good as in the single contrast cases, the influence of the threshold being not small, refer to figure 2.24.

As for  $\Gamma_3$ , even though some results with it are better than others (always strongly depending on threshold, number of incident waves, and wavelength of operation), it is often hard to distinguish the curve shape, as is for example obvious in Fig. 2.25;

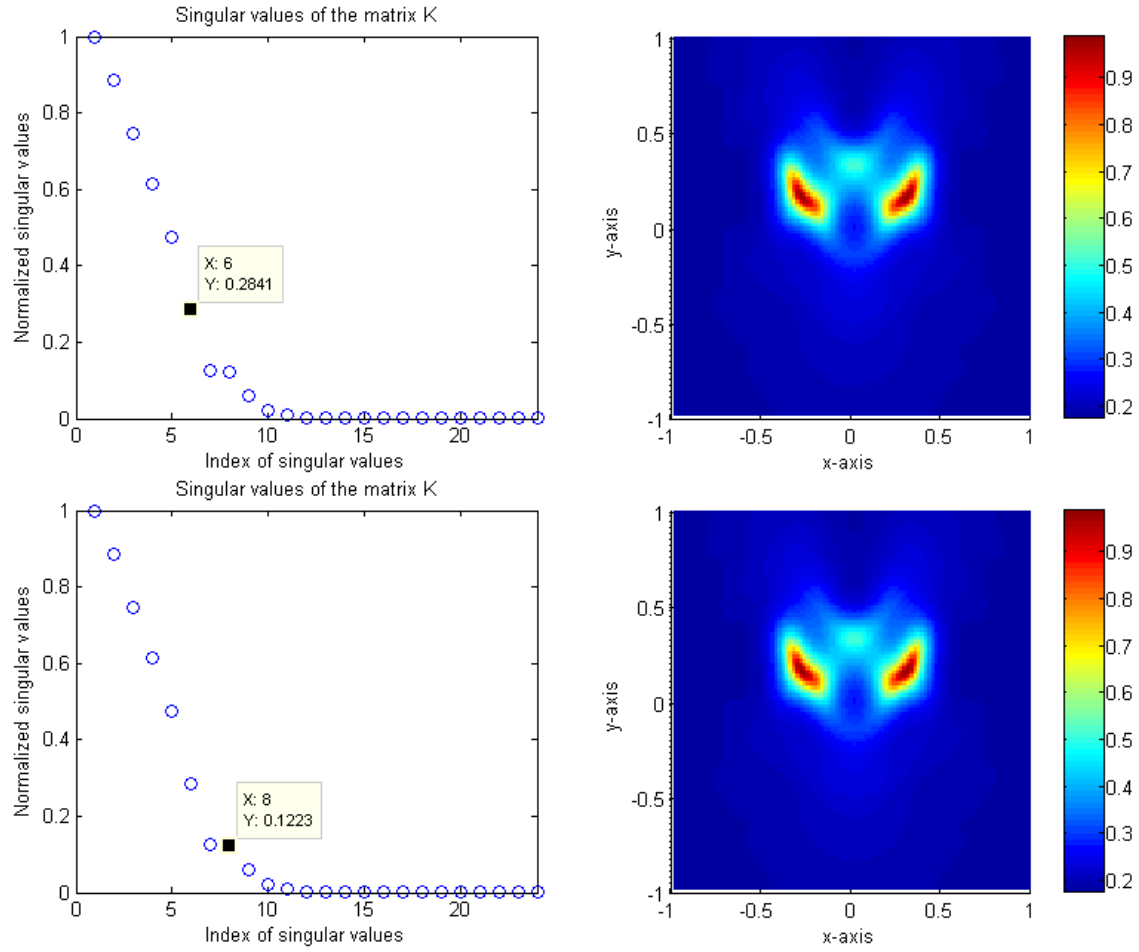


FIG. 2.23 – Distributions of normalized singular values of matrix  $K$  (left column) and maps of  $W_c(z)$ ,  $z \in \tilde{\Omega}$ ,  $c = (1, 0, 1)$  (right column), for  $N = 24$  incidences and  $\lambda = 0.5$  wavelength, using 6 (top row) and 8 (bottom row) singular values for imaging, when the inclusion is  $\Gamma_1$ , with dielectric and magnetic contrasts of 5 each.

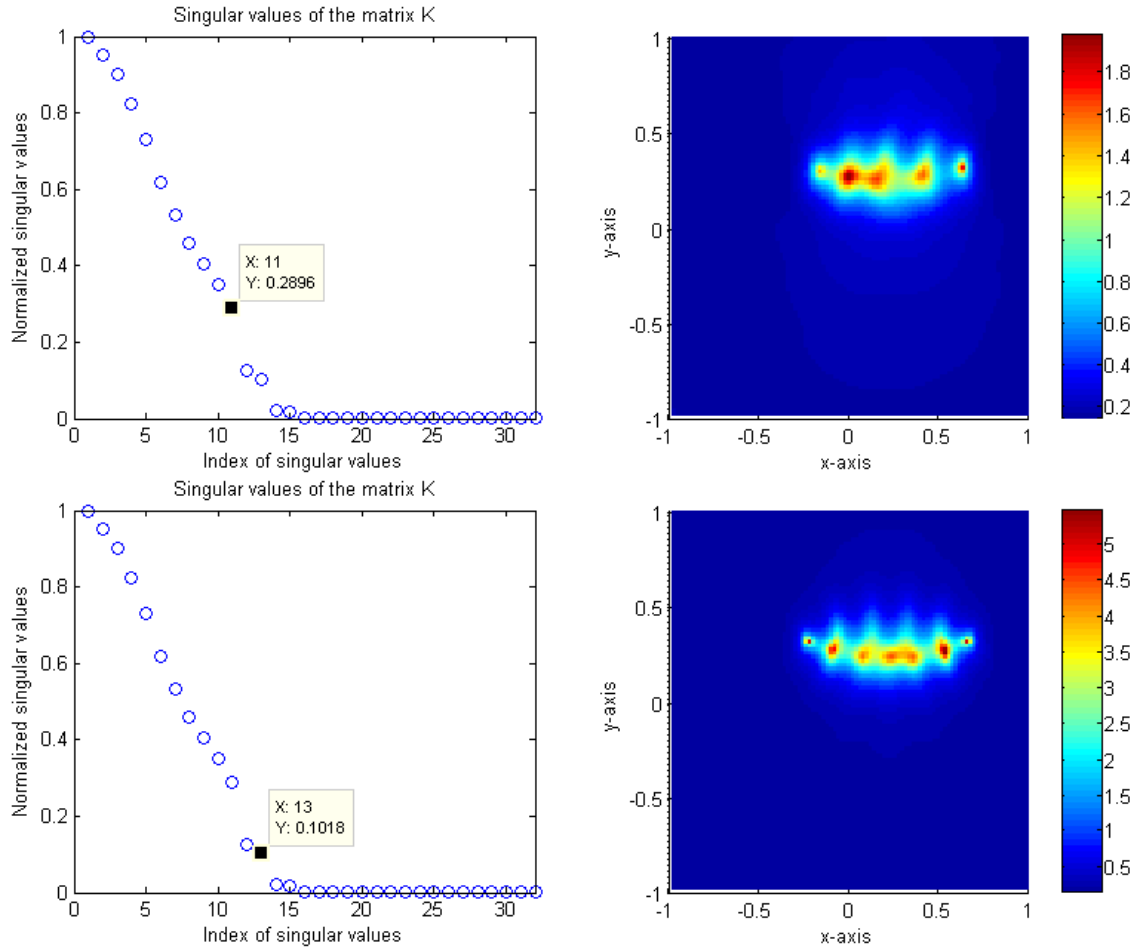


FIG. 2.24 – Distributions of normalized singular values of matrix  $K$  (left column) and maps of  $W_c(z)$ ,  $z \in \tilde{\Omega}$ ,  $c = (1, 0, 1)$  (right column), for  $N = 32$  incidences and a  $\lambda = 0.4$  wavelength, using 13 (top row) and 11 (bottom row) singular values for imaging, when the inclusion is  $\Gamma_2$ , with dielectric and magnetic contrast of 5 each.

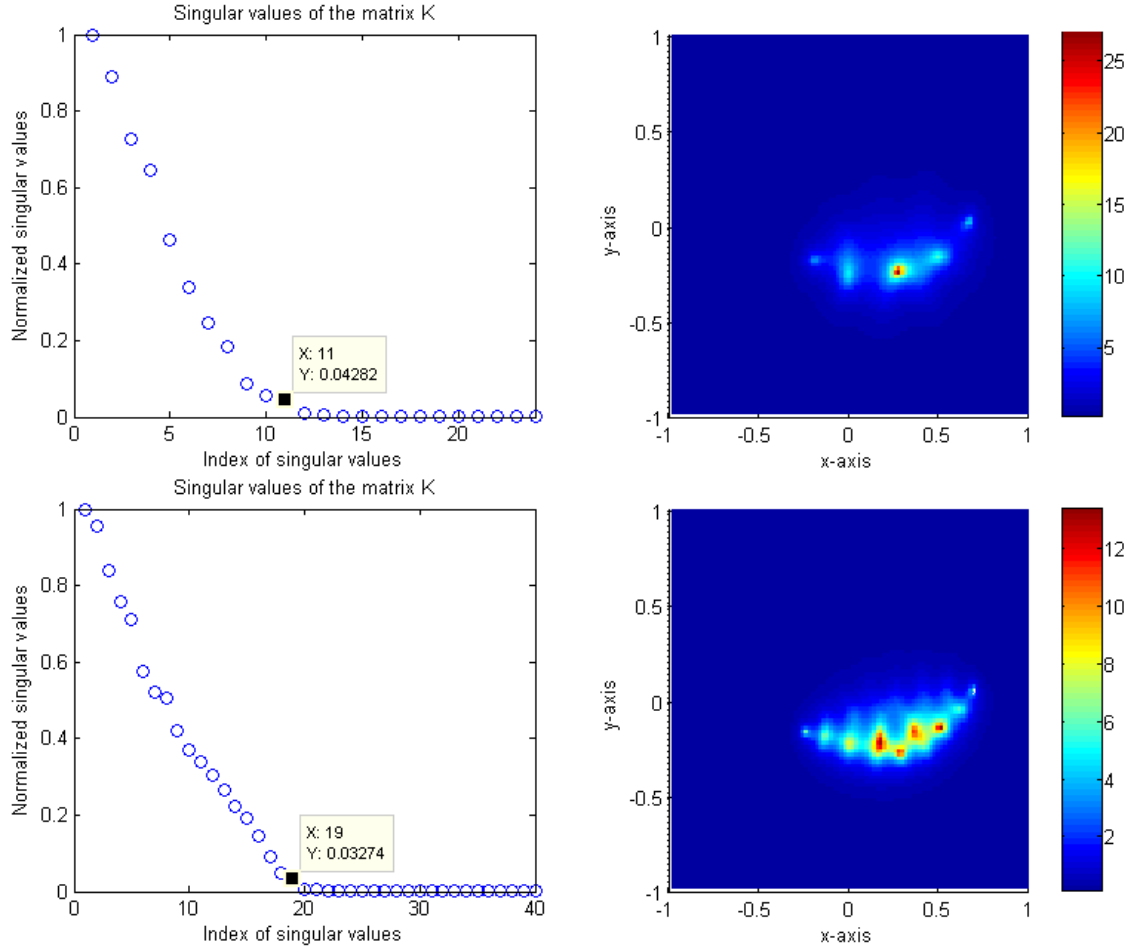


FIG. 2.25 – Distributions of normalized singular values of matrix  $K$  (left column) and maps of  $W_c(z)$ ,  $z \in \tilde{\Omega}$ ,  $c = (1, 0, 1)$  (right column), for  $N = 24$  incidences and a  $\lambda = 0.6$  wavelength, using 11 (top row) and 19 (bottom row) singular values for imaging, when the inclusion is  $\Gamma_3$ , with dielectric and magnetic contrast of 5 each.

nevertheless, it illustrates in particular that a high number of singular values, from the numerical point-of-view, enables us to better appraise the supporting line, with a blurred result still.

### 2.5.10 Extension to multiple inclusions

Both the mathematical setting and the numerical analysis could be extended in rather straightforward fashion to the case of multiple inclusions. The derivation will not be provided herein, only examples of images via the MUSIC-type algorithm are shown in several figures, Fig. 2.26 for identical contrasts of permittivity, 2.27 for different contrasts of permittivity, and 2.29 now for different contrasts of permeability, all at the same wavelength of 0.5 (except 0.7 for Fig. 2.27). The imaged inclusions are made of  $\Gamma_3$ , as previously introduced, and a (moved, mirrored) copy of  $\Gamma_2^1$ , letting  $\Gamma_{\text{Multi}} = \Gamma_2 \cup \Gamma_3$ .

It appears that the results, once chosen proper singular values as exemplified in Fig.

<sup>1</sup>Its supporting curve is  $\sigma_2 = \{(z, -0.5(z - 0.2)^2 + 0.4) : z \in (-0.3, 0.7)\}$ .



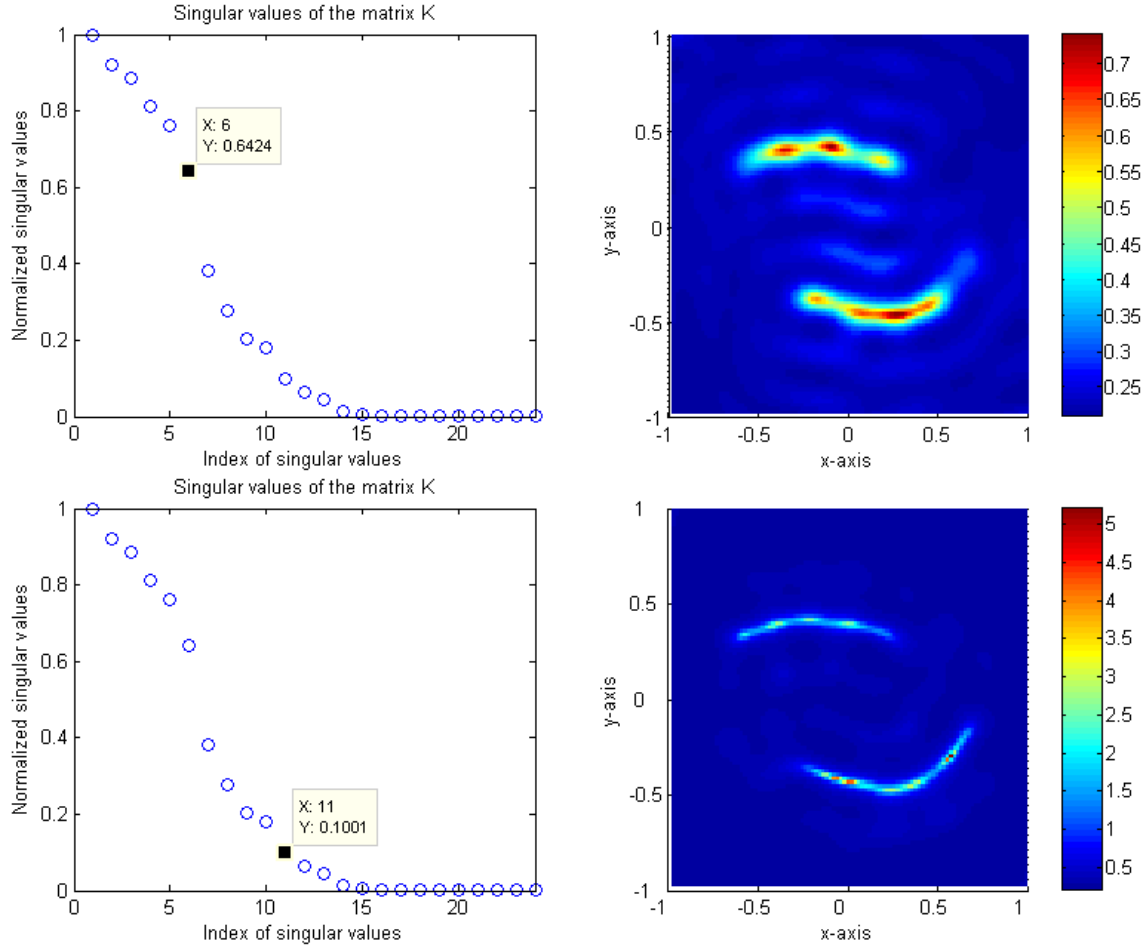


FIG. 2.26 – Distributions of normalized singular values of matrix  $K$  (left column) and maps of  $W_a(z)$ ,  $z \in \tilde{\Omega}$ ,  $a = 1$  (right column), assuming 6 (top row) or 11 (bottom row) singular values in the signal subspace, for  $N = 24$  incidences and  $\lambda = 0.5$  wavelength, when the inclusion is  $\Gamma_{\text{Multi}}$ , with same dielectric contrast of 5.

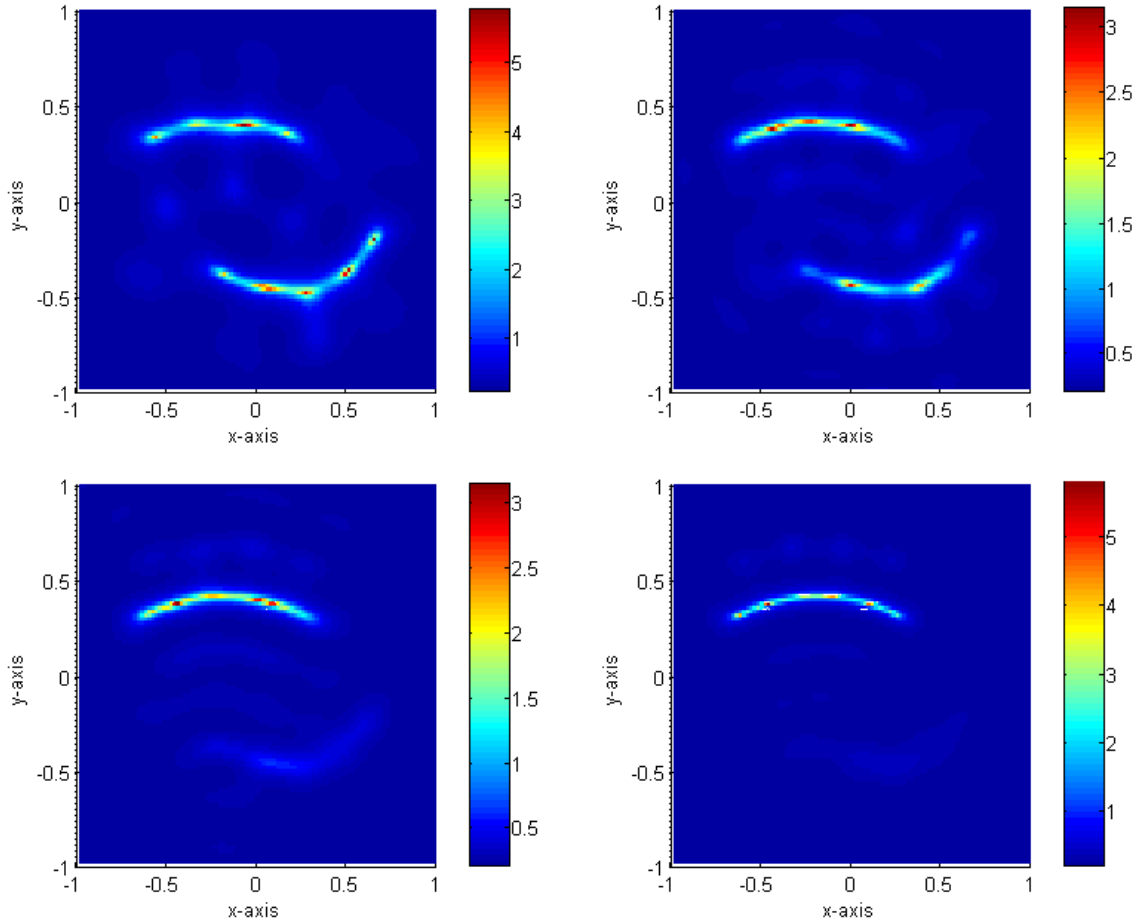


FIG. 2.27 – Maps of  $W_a(z)$ ,  $z \in \tilde{\Omega}$ ,  $a = 1$  for  $N = 20$  incidences and 0.7 wave length, when the inclusion is  $\Gamma_{\text{Multi}}$ , with same dielectric contrasts of 5 (top left), distinct contrasts of 5 and 3 (top right), of 10 and 3 (bottom left) and of 5 and 0.5 (bottom right), the inclusion of higher contrast being the upper one displayed in the maps.

2.26 ( $M = 6$  is visibly too small a value, yet one still distinguishes the two inclusions even though the resolution is poor,  $M = 11$  as provided by application of the usual criterion of magnitude is associated to much better results), are strongly function of the respective contrasts of the two inclusions.

That is, if an inclusion has a much smaller value of permittivity or permeability than the other one, this inclusion does not significantly affect the scattering matrix and as a consequence it cannot be retrieved via the algorithm, refer to Fig. 2.28. Let us stress that electromagnetic coupling between inclusions, since this coupling would be impacting the higher-order terms in the asymptotic formulation, is neglected in the calculation of the MSR matrix, but the fact the MSR matrix results from a sum of independent terms does not mean that the singular values can be effectively attributed to one specific inclusion, unless (as said before) one inclusion does not really sign in the dataset.

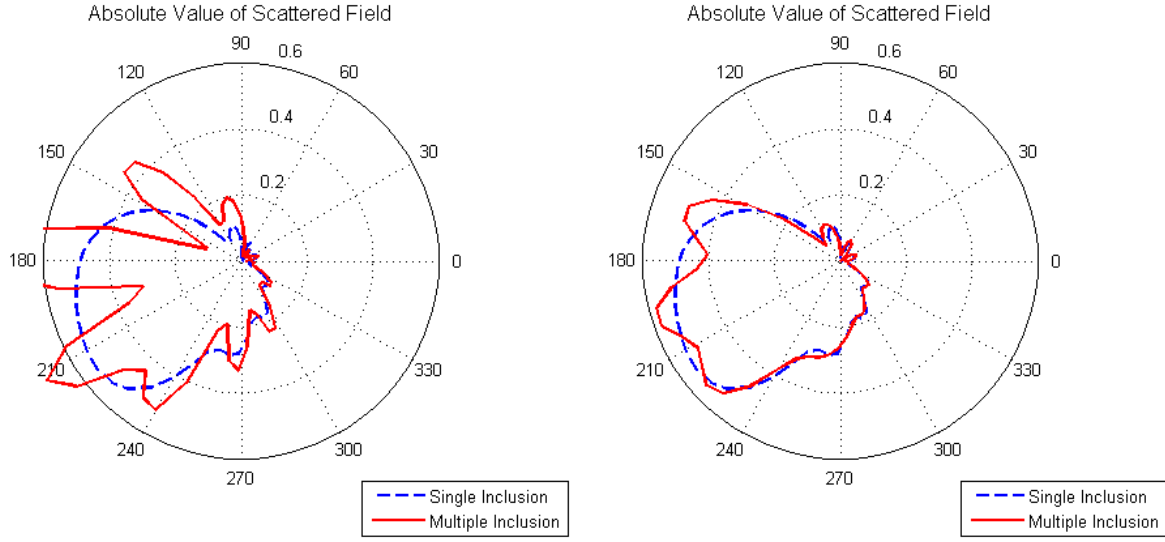


FIG. 2.28 – Absolute value of scattered field for single inclusion  $\Gamma_2$  (blue dashed line) and multiple inclusions  $\Gamma_{\text{Multi}}$  (red solid line) with distinct contrasts of 5 and 3 (left), of 5 and 0.5 (right).

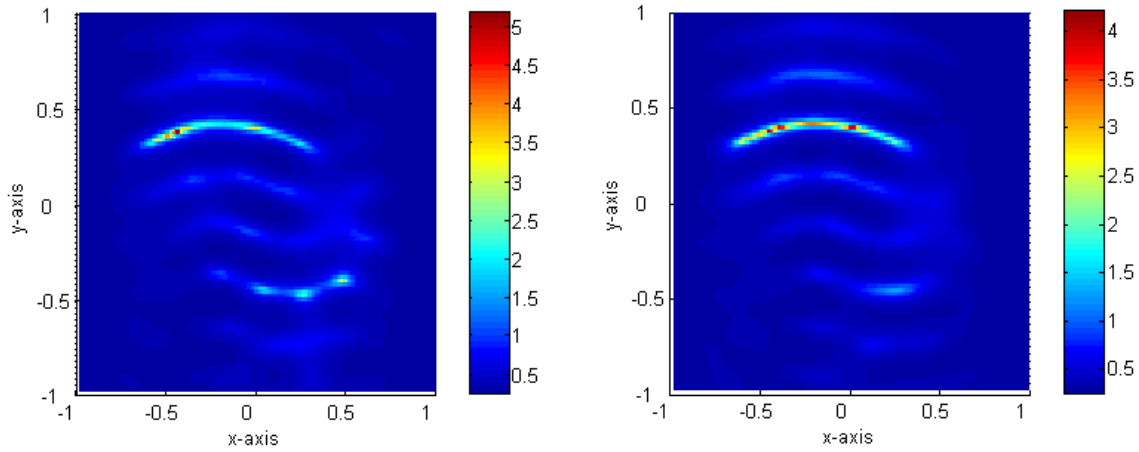


FIG. 2.29 – Maps of  $W_b(z)$ ,  $z \in \tilde{\Omega}$ ,  $b = (0, 1)$  for  $N = 32$  incidences and 0.5 wave length, when the inclusion is  $\Gamma_{\text{Multi}}$ , with distinct magnetic contrasts of 5 and 3 (left) and of 10 and 3 (right), the inclusion of higher contrast being the upper one displayed in the maps.

## 2.6 Conclusion

The above investigation shows that it is feasible, from the Multi-Static Response matrix of a thin penetrable inclusion analyzed in the framework of an appropriate small-thickness asymptotic formulation, to put together a MUSIC-type imaging algorithm which yields the supporting curve of the sought inclusion, using several models of the MSR matrix in the numerical practice.

The present work is illustrated by a number of numerical simulations which show that the method is robust at least when the inclusion differs from its surrounding by its dielectric permittivity or by its magnetic permeability, on the condition that one has a large enough set of illuminations and observations (with respect to the expected length of the supporting curve measured in terms of the half wavelength, and function of the type of electromagnetic contrast, e.g., twice higher for a permeability contrast than for a permittivity contrast), the case of both contrasts being far less straightforward to deal with. Also, similar imaging performances from MSR matrices calculated by an alternative boundary-integral asymptotic formulation and by an exact domain integral formulation, in addition to the handling of noisy data, alleviate worries on inverse crime.

As is not surprising, the resolution along the supporting curve of the inclusion is of the order of the half wavelength in the embedding medium (by identifying the retrieved curve to the line of crest of the peaks emerging in the above map) and in best cases is a very small fraction of the wavelength orthogonally to it. The investigation, just exemplified herein, of multiple inclusions has also shown that they could be imaged independently if not of too different contrasts, again provided that the number of pertinent singular values is well chosen, and considering that higher-order terms in the resulting MSR matrix are not accounted for, like with the single-inclusion case.

Recently acquired, preliminary images in the Dirichlet and Neumann case (perfect thin screen) from exact data tend to suggest that the efficiency of the method holds true in situations of interest not reduced to the case of penetrable inclusions, refer to chapter 4. Yet it remains to provide an asymptotic field formulation that accounts for the two extremities of the inclusion from which the MSR matrix could be analyzed in sound theoretical fashion. Results on this issue, as well as on level-set evolution of inclusions in chapter 3, will be the subject of subsequent contributions.

### 3 Reconstruction of Thin Electromagnetic Inclusions by a Level Set Method

In this chapter, we consider a technique of electromagnetic imaging (at a single, non-zero frequency) which uses the level set evolution method for reconstructing a thin screen with dielectric or magnetic contrast with respect to the embedding homogeneous medium. Emphasis is on proof of concept, the scattering problem being so far based on a two-dimensional model. To do so, two level set functions are employed; the first one describes location and shape, and the other one connectivity and length. Speeds of evolution of level set functions are calculated via Fréchet derivatives. Several numerical experiments on noiseless and noisy data as well illustrate how the proposed method behaves.

#### 3.1 Introduction

In order to properly start the analysis, let us first introduce the mathematical model that one is focusing onto from now on, before a brief recapitulation of known results and the presentation of the structure of the chapter.

Let  $\Omega \subset \mathbb{R}^2$  be a two-dimensional homogeneous domain with smooth enough boundary  $\partial\Omega$ . This domain contains a thin inclusion which has a fixed thickness  $2h$  denoted as  $\Gamma$  and which is localized in the neighborhood of a curve  $\sigma$ . That is,

$$\Gamma = \{\mathbf{x} + \eta \mathbf{n}(\mathbf{x}) : \mathbf{x} \in \sigma, \eta \in (-h, h)\}, \quad (3.1)$$

where the supporting  $\sigma$  is a simple, smooth curve in  $\Omega$  (with strictly positive distance from its boundary  $\partial\Omega$ , if there were any at finite distance),  $\mathbf{n}(\mathbf{x})$  is the unit normal to  $\sigma$  at  $\mathbf{x}$ , and  $h$  is a positive constant which specifies the thickness of the inclusion (small with respect to the wavelength in  $\Omega$ , see next), refer to Fig. 3.1. The electric permittivity and magnetic permeability at a given (single) non-zero frequency of operation are assumed to be known; they are finite-valued and differ (either one or both of them) from the ones of the homogeneous embedding medium. The unknown information on the inclusion is its location, shape, and connectivity (that is, there may be more than one thin inclusion, the support curve  $\sigma$  being cut in two parts, for example, to model two such inclusions, with the restriction that these parts be of the same electromagnetic properties).

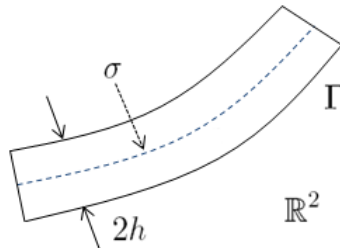


FIG. 3.1 – Sketch of the two-dimensional thin inclusion  $\Gamma$

Constitutive materials are characterized by their dielectric permittivity and magnetic permeability at a given frequency  $\omega$ . Let  $0 < \varepsilon_0 < +\infty$  and  $0 < \mu_0 < +\infty$  denote the

permittivity and permeability of the embedding domain  $\Omega$ , and  $0 < \varepsilon < +\infty$  and  $0 < \mu < +\infty$  the ones of the inclusion  $\Gamma$ . Then, one has the piecewise constant dielectric permittivity

$$\varepsilon(\mathbf{x}) = \begin{cases} \varepsilon_0 & \text{for } \mathbf{x} \in \Omega \setminus \bar{\Gamma}, \\ \varepsilon & \text{for } \mathbf{x} \in \Gamma, \end{cases} \quad (3.2)$$

and magnetic permeability

$$\mu(\mathbf{x}) = \begin{cases} \mu_0 & \text{for } \mathbf{x} \in \Omega \setminus \bar{\Gamma}, \\ \mu & \text{for } \mathbf{x} \in \Gamma. \end{cases} \quad (3.3)$$

If there is no inclusion, i.e., in the homogeneous domain,  $\mu(\mathbf{x})$  and  $\varepsilon(\mathbf{x})$  are equal to  $\mu_0$  and  $\varepsilon_0$  respectively. For convenience, one also defines  $\gamma(\mathbf{x}) = 1/\mu(\mathbf{x})$  and  $\rho(\mathbf{x}) = \omega^2 \varepsilon(\mathbf{x})$  at strictly positive operation frequency  $\omega$ . Similarly,  $\gamma_0 = 1/\mu_0$  and  $\rho_0 = \omega^2 \varepsilon_0$ . Notice that in this chapter, for the sake of simplicity, we set  $\mu_0$  and  $\varepsilon_0$  are equal to 1.

At strictly positive operation frequency  $\omega$  (wavenumber  $k_0 = \omega\sqrt{\varepsilon_0\mu_0}$ ), let  $u(\mathbf{x})$  be the time-harmonic total field which satisfies the Helmholtz equation

$$\nabla \cdot \left( \frac{1}{\mu(\mathbf{x})} \nabla u(\mathbf{x}) \right) + \omega^2 \varepsilon(\mathbf{x}) u(\mathbf{x}) = 0 \quad \text{in } \Omega \quad (3.4)$$

with boundary condition

$$\frac{1}{\mu_0} \frac{\partial u(\mathbf{x})}{\partial \nu(\mathbf{x})} = \frac{1}{\mu_0} \frac{\partial e^{ik_0 \theta \cdot \mathbf{x}}}{\partial \nu(\mathbf{x})} = g(\mathbf{x}) \quad \text{on } \partial\Omega \quad (3.5)$$

where  $\nu(\mathbf{x})$  represents the unit outward normal to  $\mathbf{x} \in \partial\Omega$ , and  $\theta = (\theta_x, \theta_y)$  is a two-dimensional vector on the unit circle  $S^1$  in  $\mathbb{R}^2$ , i.e.,  $\theta$  satisfies  $\theta \cdot \theta = 1$ . Similarly, the incident field  $u_0(\mathbf{x})$  satisfies the homogeneous Helmholtz equation

$$\nabla \cdot \left( \frac{1}{\mu_0} \nabla u_0(\mathbf{x}) \right) + \omega^2 \varepsilon_0 u_0(\mathbf{x}) = 0 \quad \text{in } \Omega$$

with boundary condition

$$\frac{1}{\mu_0} \frac{\partial u_0(\mathbf{x})}{\partial \nu(\mathbf{x})} = \frac{1}{\mu_0} \frac{\partial e^{ik_0 \theta \cdot \mathbf{x}}}{\partial \nu(\mathbf{x})} = g(\mathbf{x}) \quad \text{on } \partial\Omega.$$

To summarize, the inclusion could be seen as a thin (not infinitely) piece of penetrable material (as an ideal model of a crack in an otherwise homogenous region of space, for example) which is possibly made of two or more disjoint parts. This inclusion is scattering off some prescribed incident electromagnetic waves with which one is intending to probe it, the model being so far limited to a two-dimensional (scalar) scattering case.

So, the main purpose of this chapter is to show how we could be reconstructing this thin inclusion by means of a properly constructed level set method of evolution —refer to [38] for an in-depth review of the topic of level set evolutions for imaging purposes, and to a set of classical references like [64, 65]. In the present case, however, and in contrast with pioneering investigations of the level set methodology as applied to thin inclusions as it was illustrated in [2], the full-wave scattering case is investigated whereas in the cited reference the authors were investigating the somewhat more restrictive conductivity

case. Yet, the investigation herein is admittedly strongly inspired from [2], in particular on handling the fact that an open curve in a two-dimensional space, is appropriately represented by two level set functions, the first one being associated with the location and shape of the support curve, and the other one enabling to cut this curve at the inclusion tips (maybe into several parts as well).

At this point, let us underline that we do not intend here to go into a detailed discussion on how to retrieve a thin screen by alternative methods in the electromagnetic realm. A thorough analysis is already available in [2], which has already been mentioned as a key paper for the present-day challenge. Complementary material is also found in [4, 5, 54] for what concerns the conductivity problem particularly. So, we refer the reader to those references for further reading and also to contribution [68] submitted at the time of writing which focuses onto MUSIC-type imaging of screens and introduces further references of interest.

The present chapter goes as follows. In section 3.2, the modeling of the thin inclusion via two level set functions is presented. In section 3.3, we introduce the basic concepts of shape deformation and its representation by a level set function, and we derive the needed Fréchet derivatives by means of an adjoint technique. In section 3.4, we explain how to evolve such two level set functions. The reconstruction algorithm is sketched in section 3.5. In section 3.6 we present several numerical experiments for demonstrating the performance of the proposed algorithm. A short conclusion follows.

## 3.2 Representing thin inclusion with two level set functions

In this section, we represent the thin inclusion by two different level set functions. For a more detailed description, we suggest [2, 38]. Throughout the section, we assume that the level set function  $\varphi$  is a continuously differentiable function. With this feature in mind, we define a thin inclusion represented by  $\varphi$  in the following way. Let

$$\begin{aligned}\Omega_0 &= \{\mathbf{x} \in \mathbb{R}^2 : \varphi(\mathbf{x}) \leq 0\} \\ \partial\Omega_0 &= \{\mathbf{x} \in \mathbb{R}^2 : \varphi(\mathbf{x}) = 0\}.\end{aligned}$$

Notice that  $\partial\Omega_0$  is called the zero level set. With this representation, we define the thin region  $\Omega_T$  of thickness  $2h$  as follows (see Fig. 3.2) :

$$\Omega_T = \Omega_0 \cap \{\mathbf{y} \in \mathbb{R}^2 : \mathbf{y} = \mathbf{x} - \eta \mathbf{n}(\mathbf{x}) \text{ for } \mathbf{x} \in \partial\Omega_0, 0 \leq \eta \leq 2h\}. \quad (3.6)$$

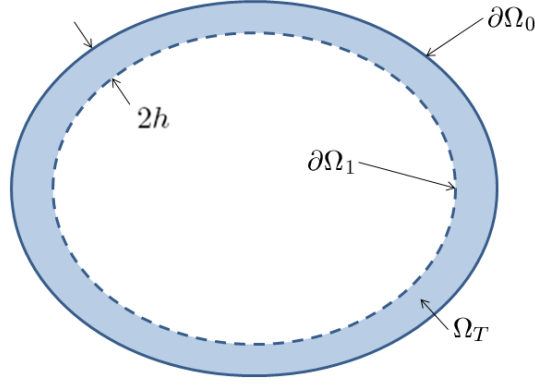
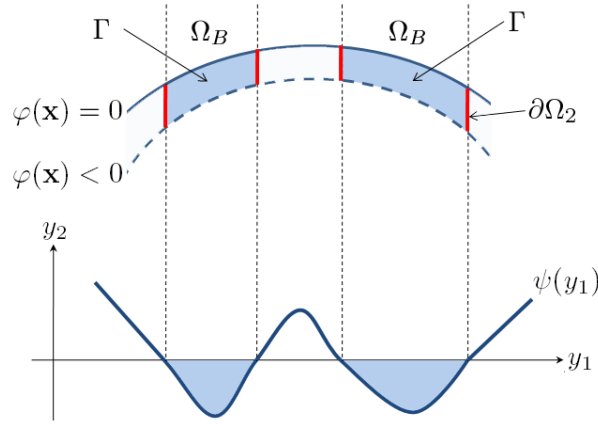
The inner boundary is  $\partial\Omega_1 = \partial\Omega_T \setminus \partial\Omega_0$ .

In order to describe the thin region of finite length (which is connected or disconnected) in  $\Omega$ , we assume that another level set function  $\psi$  is also a continuously differentiable function. Let us define a band structure  $\Omega_B \subset \mathbb{R}^2$  by (see Fig. 3.3)

$$\Omega_B = \{\mathbf{x} = (x_1, x_2) \in \mathbb{R}^2 : \psi(x_1) < 0\}. \quad (3.7)$$

With the representation (3.6) and (3.7), we finally describe the thin inclusion  $\Gamma$  as

$$\Gamma = (\Omega_T \cap \Omega_B) \cap \Omega.$$

FIG. 3.2 – Representation of the thin region by a level set function  $\varphi$ .FIG. 3.3 – Representation of the thin region by two level set functions  $\varphi$  and  $\psi$ .

and boundaries  $\partial\Gamma_0 = \partial\Gamma \cap \partial\Omega_0$ ,  $\partial\Gamma_1 = \partial\Gamma \cap \partial\Omega_1$  and  $\partial\Omega_2$  of  $\Gamma$  for evolving at crack tips

$$\partial\Omega_2 = \{\mathbf{y} = (y_1, y_2) \in \partial\Gamma : \psi(y_1) = 0\}.$$

### 3.3 Shape deformation by calculus of variations

In this section, we introduce a basic concept of shape deformation and of its representation via a level set function. The method is about the deformation of an already existing thin inclusion, say  $\Gamma^{(n)}$  at a  $n$ -th time step of evolution, into the normal direction with an optimal velocity (see Fig. 3.4).

#### 3.3.1 Gradient directions

In order to obtain the optimal velocity of level set functions, we have to introduce proper residual operators. For convenience, let us introduce the parameter distribution  $b(\mathbf{x})$  as

$$b(\mathbf{x}) = \begin{cases} b_0 & \text{for } \mathbf{x} \in \Omega \setminus \bar{\Gamma}, \\ b & \text{for } \mathbf{x} \in \Gamma. \end{cases} \quad (3.8)$$



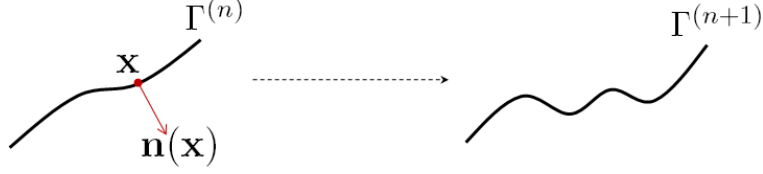


FIG. 3.4 – Shape deformation of an already existing thin inclusion  $\Gamma^{(n)}$  at a  $n$ -th time step of evolution to the normal direction with optimal velocity.

Notice that, below, the parameter distribution  $b(\mathbf{x})$  specifies the parameters  $\gamma(\mathbf{x}) = 1/\mu(\mathbf{x})$  or  $\rho(\mathbf{x}) = \omega^2 \varepsilon(\mathbf{x})$  of the inclusion at a given frequency.

For a given thin inclusion  $\Gamma$ , we denote the measured data (or ‘true’ data) which satisfy (3.4) as  $u_{\text{true}}$  and similarly, for a given existing thin inclusion (or appropriate initial guess)  $\Gamma^{(n)}$ , we denote the measured data as  $u_{\text{meas}}$ . Due to the discrepancy of shapes between  $\Gamma$  and  $\Gamma^{(n)}$ , the parameter distributions are also different and this is causing the discrepancy between  $u_{\text{true}}$  and  $u_{\text{meas}}$ . Hence, for a given parameter distribution  $b$ , we can define the residual operator  $\mathcal{R}$  :

$$\mathcal{R}(b) = u_{\text{true}} - u_{\text{meas}} \quad \text{on} \quad \partial\Omega.$$

With this residual operator, we get the least-square cost functional

$$\mathcal{T}(b) = \frac{1}{2} \|\mathcal{R}(b)\|_{\partial\Omega}^2 = \frac{1}{2} \langle \mathcal{R}(b), \mathcal{R}(b) \rangle_{\partial\Omega} = \frac{1}{2} \int_{\partial\Omega} \mathcal{R}(b) \mathcal{R}(b)^* dS \quad (3.9)$$

where  $*$  is the mark of complex conjugate. We henceforth assume that  $\mathcal{R}(b)$  admits the expansion

$$\mathcal{R}(b + \delta b) = \mathcal{R}(b) + \mathcal{R}'(b)\delta b + O(\|\delta b\|_{\Omega}^2)$$

for a sufficiently small perturbation  $\delta b$ . If the linear operator  $\mathcal{R}'(b)$  exists, it is denoted as the *Fréchet derivative* of  $\mathcal{R}(b)$ . Then, the least-square cost functional also satisfies

$$\mathcal{T}(b + \delta b) = \mathcal{T}(b) + \text{Re} \langle \mathcal{R}'(b)^* \mathcal{R}(b), \delta b \rangle_{\Omega} + O(\|\delta b\|_{\Omega}^2), \quad (3.10)$$

where  $\text{Re}$  is the real part of corresponding quantity, the operator  $\mathcal{R}'(b)^*$  is the adjoint of  $\mathcal{R}'(b)$  with respect to spaces  $\partial\Omega$  and  $\Omega$  :

$$\langle \mathcal{R}'(b)^* \mathcal{R}(b), \delta b \rangle_{\Omega} = \langle \mathcal{R}(b), \mathcal{R}'(b)\delta b \rangle_{\partial\Omega}$$

and

$$\mathcal{R}'(b)^* \mathcal{R}(b)$$

the *gradient direction* of  $\mathcal{T}$  in  $b$ .

Thus, in order to find the variation of  $\mathcal{T}(b)$  for obtaining the optimal velocity of level set functions, we have to compute  $\delta b$  and the gradient direction  $\mathcal{R}'(b)^* \mathcal{R}(b)$ .

### 3.3.2 Calculation of $\delta b$ due to shape deformation

First, let us consider the parameter change  $\delta b$  due to the evolution of the first level set function  $\varphi$ . When every point  $\mathbf{x} \in \partial\Gamma_0$  moves by a small distance  $\mathbf{d}(\mathbf{x})$ ,  $\partial\Gamma_0$  is

deformed, refer to Fig. 3.5. Let us specify that the distance can be represented as

$$\mathbf{d}(\mathbf{x}) = F_1(\mathbf{x})\mathbf{n}(\mathbf{x})\tau \quad (3.11)$$

for some scalar function  $F(\mathbf{x})$  and time step  $\tau$ . In order to move  $\partial\Gamma_1$ , let us assume that every point  $\mathbf{y} \in \Gamma$  can be written in the form

$$\mathbf{y} = \mathbf{x} - 2\eta\mathbf{n}(\mathbf{x})$$

for  $\mathbf{x} \in \partial\Gamma_0$  and  $0 \leq \eta \leq 2h$ . Since the boundaries  $\partial\Gamma_0$  and  $\partial\Gamma_1$  are smooth, both  $\mathbf{x}$  and  $\eta$  are uniquely determined by  $\mathbf{y}$ . So, we can straightforwardly assume that when the point  $\mathbf{x} \in \Gamma_0$  moves,  $\mathbf{y}$  moves into the same direction and with the same distance of  $\mathbf{x}$ .

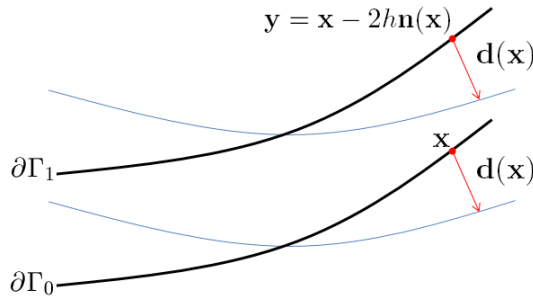


FIG. 3.5 – Deformation of a thin inclusion.

By adopting the interpretation of  $\delta b$  in [38], the change of  $\partial\Gamma_0$  induces

$$\delta b|_{\partial\Gamma_0} = (b - b_0)\mathbf{n}(\mathbf{x}) \cdot \mathbf{d}(\mathbf{x})\delta_{\partial\Gamma_0}(\mathbf{x})\chi_{\Omega_B}(\mathbf{x}) \quad (3.12)$$

where  $\delta_{\partial\Gamma_0}$  is the Dirac delta function concentrated on  $\partial\Gamma_0$  and  $\chi_{\Omega_B}$  is the characteristic function of  $\Omega_B$ .

Since  $\mathbf{y} \in \partial\Gamma_1$  moves into the same direction and with the distance of  $\mathbf{x}$ , we can say that  $\mathbf{n}(\mathbf{y}) = -\mathbf{n}(\mathbf{x})$ ,  $\mathbf{d}(\mathbf{x}) = \mathbf{d}(\mathbf{y})$ ,  $\delta_{\partial\Gamma_1}(\mathbf{y}) = \delta_{\partial\Gamma_0}(\mathbf{x} + 2h\mathbf{n}(\mathbf{x}))$  and  $\mathbf{x}, \mathbf{y} \in \Omega_B$ . That is, a change of  $\partial\Gamma_1$  induces

$$\begin{aligned} \delta b|_{\partial\Gamma_1} &= (b - b_0)\mathbf{n}(\mathbf{y}) \cdot \mathbf{d}(\mathbf{y})\delta_{\partial\Gamma_1}(\mathbf{y})\chi_{\Omega_B}(\mathbf{y}) \\ &= -(b - b_0)\mathbf{n}(\mathbf{x}) \cdot \mathbf{d}(\mathbf{x})\delta_{\partial\Gamma_0}(\mathbf{x} + 2h\mathbf{n}(\mathbf{x}))\chi_{\Omega_B}(\mathbf{x}). \end{aligned} \quad (3.13)$$

By using (3.12) and (3.13), we immediately obtain the total change of  $\delta b$  as

$$\delta b = (b - b_0)\mathbf{n}(\mathbf{x}) \cdot \mathbf{d}(\mathbf{x})[\delta_{\partial\Gamma_0}(\mathbf{x}) - \delta_{\partial\Gamma_0}(\mathbf{x} + 2h\mathbf{n}(\mathbf{x}))]\chi_{\Omega_B}(\mathbf{x}). \quad (3.14)$$

Using the relationship between (3.11), (3.14) and (3.10), we get

$$\begin{aligned} \mathcal{T}(b + \delta b) &= \mathcal{T}(b) \\ &+ \text{Re}\langle \mathcal{R}'(b)^* \mathcal{R}(b), (b - b_0)F_1(\mathbf{x})\tau[\delta_{\partial\Gamma_0}(\mathbf{x}) - \delta_{\partial\Gamma_0}(\mathbf{x} + 2h\mathbf{n}(\mathbf{x}))]\chi_{\Omega_B}(\mathbf{x}) \rangle_{\Omega} \\ &+ O(\|\delta b\|_{\Omega}^2), \end{aligned}$$

which yields the descent direction as follows :

$$F_1(\mathbf{x}) = -\text{Re}[\mathcal{R}'(b)^*\mathcal{R}(b)](b - b_0) \{ \delta_{\partial\Gamma_0}(\mathbf{x}) - \delta_{\partial\Gamma_0}(\mathbf{x} + 2h\mathbf{n}(\mathbf{x})) \}, \quad (3.15)$$

for  $\mathbf{x} \in \partial\Gamma_0$ .

Next, let us consider the parameter change  $\delta b$  due to the evolution of the second level set function  $\psi$ . Let us assume that every point  $\mathbf{y} = (y_1, y_2) \in \partial\Omega_2$  moves a small distance  $d(y_1)$  into the outward direction  $\mathbf{n}_{\partial\Omega_2}(\mathbf{y}) = \pm(1, 0)$ . Then, similarly with the previous analysis, when the point  $\mathbf{y} \in \partial\Omega_2$  moves to  $\mathbf{y} + d(y_1)\mathbf{n}_{\partial\Omega_2}(\mathbf{y})$ , it induces a parameter change as

$$\delta b|_{\partial\Gamma_2} = (b - b_0)d(y_1)\delta_{\partial\Gamma_2}(\mathbf{y})\chi_{\Omega_T}(\mathbf{y}). \quad (3.16)$$

Plugging (3.16) into (3.10), we can get

$$\begin{aligned} \mathcal{T}(b + \delta b) &= \mathcal{T}(b) \\ &+ \text{Re}\langle \mathcal{R}'(b)^*\mathcal{R}(b), (b - b_0)d(y_1)\delta_{\partial\Gamma_2}(\mathbf{y})\chi_{\Omega_T}(\mathbf{y}) \rangle_{\Omega} + O(\|\delta b\|_{\Omega}^2). \end{aligned}$$

Since the distance function  $d$  only depends upon the variation  $y_1$  of  $\mathbf{y} = (y_1, y_2)$ , we obtain the following descent direction

$$F_2(y_1) = -\text{Re} \int_{\partial\Omega_2} \mathcal{R}'(b)^*\mathcal{R}(b)(b - b_0)\delta_{\partial\Omega_2}(\mathbf{y})\chi_D(\mathbf{y})dy_2, \quad (3.17)$$

for  $\mathbf{y} = (y_1, y_2) \in \partial\Omega_2$ .

### 3.3.3 Calculation of the gradient direction

Proper calculation of the gradient direction  $\mathcal{R}'(b)^*\mathcal{R}(b)$  is an essential task if we wish to build up a satisfactory evolution of a level set function. In order to do it in practice, we have to investigate the linear change  $\delta u$  due to a small perturbation  $\delta b$ . Before starting, let us introduce the Fréchet derivative  $\mathcal{R}'(b)$  which is satisfying (see [14, Chapter 10] or [26, Theorem 5])

$$\mathcal{R}'(b)\delta b = \delta u \quad \text{on} \quad \partial\Omega. \quad (3.18)$$

Calculation of the gradient direction is carried out in succession for the following two cases of interest :

1. The first case :  $\gamma = \gamma_0, \rho \neq \rho_0$
  2. The second case :  $\gamma \neq \gamma_0, \rho = \rho_0$ .
1. *The first case* :  $\gamma = \gamma_0, \rho \neq \rho_0$ . In order to obtain the descent direction of the level sets, we consider the following problem :

$$\gamma\Delta u + \rho u = 0 \quad \text{in} \quad \Omega \quad (3.19)$$

with boundary condition

$$\gamma \frac{\partial u}{\partial \nu} = g \quad \text{on} \quad \partial\Omega. \quad (3.20)$$

the residual being as already said

$$\mathcal{R}(\rho) = u_{\text{true}} - u_{\text{meas}}. \quad (3.21)$$

In order to observe the relationship between  $\delta u$  and  $\delta \rho$ , we apply  $u + \delta u$  and  $\rho + \delta \rho$  to formula (3.19) and (3.20) instead of  $u$  and  $\rho$ , respectively. Then (3.19) becomes

$$\begin{aligned} 0 &= \gamma \Delta(u + \delta u) + (\rho + \delta \rho)(u + \delta u) \\ &= (\gamma \Delta u + \rho u) + (\gamma \Delta \delta u + \delta \rho u + \rho \delta u + \delta \rho \delta u) \end{aligned} \quad (3.22)$$

Let us assume that the term  $\delta \rho \delta u$  is negligible. Then,  $u$  satisfies (3.19), the identity (3.22) becomes

$$(\gamma \Delta + \rho) \delta u = -\delta \rho u \quad \text{in } \Omega \quad (3.23)$$

and (3.20) becomes

$$\gamma \frac{\partial(u + \delta u)}{\partial \nu} = \gamma \frac{\partial u}{\partial \nu} + \gamma \frac{\partial \delta u}{\partial \nu} = g + \gamma \frac{\partial \delta u}{\partial \nu} = g$$

, which implies

$$\gamma \frac{\partial \delta u}{\partial \nu} = 0 \quad \text{on } \partial \Omega. \quad (3.24)$$

From (3.23), (3.24) and (3.18), we obtain the following relationship.

**Theorem 3.1** *Let  $\mathcal{R}(\rho)$  be defined as (3.21). Then,  $\mathcal{R}'(\rho)^* \mathcal{R}(\rho)$  is given by*

$$\mathcal{R}'(\rho)^* \mathcal{R}(\rho) = u^* z.$$

Here,  $u$  satisfies (3.19) and (3.20), and  $z$  solves the following adjoint equation :

$$(\gamma \Delta + \rho) z = 0 \quad \text{in } \Omega \quad (3.25)$$

with boundary condition

$$\gamma \frac{\partial z}{\partial \nu} = \mathcal{R}(\rho) \quad \text{on } \partial \Omega. \quad (3.26)$$

*Proof.* From identity (3.23), we can get

$$\begin{aligned} \int_{\Omega} u^* z (\delta \rho)^* d\mathbf{x} &= \int_{\Omega} z (\delta \rho u)^* d\mathbf{x} = - \int_{\Omega} z \{(\gamma \Delta + \rho) \delta u\}^* d\mathbf{x} \\ &= - \int_{\partial \Omega} z \left( \gamma \frac{\partial \delta u}{\partial \nu} \right)^* dS + \int_{\partial \Omega} \gamma \frac{\partial z}{\partial \nu} \delta u^* dS - \int_{\Omega} (\gamma \Delta + \rho) z \delta u^* d\mathbf{x} \\ &= \int_{\partial \Omega} \gamma \frac{\partial z}{\partial \nu} \delta u^* dS = \langle \mathcal{R}(\rho), \delta u \rangle_{\partial \Omega} = \langle \mathcal{R}(\rho), \mathcal{R}'(\rho) \delta \rho \rangle_{\partial \Omega} \end{aligned}$$

Therefore, we immediately obtain  $\mathcal{R}'(\rho)^* \mathcal{R}(\rho) = u^* z$  as follows

$$\langle u^* z, \delta \rho \rangle_{\Omega} = \int_{\Omega} u^* z (\delta \rho)^* d\mathbf{x} = \langle \mathcal{R}(\rho), \mathcal{R}'(\rho) \delta \rho \rangle_{\partial \Omega} = \langle \mathcal{R}'(\rho)^* \mathcal{R}(\rho), \delta \rho \rangle_{\Omega}.$$

2. *The second case :  $\gamma \neq \gamma_0$ ,  $\rho = \rho_0$ .* Similarly with the first case, in order to obtain the descent directions of the level sets, we consider the following problem :

$$\nabla \cdot (\gamma \nabla u) + \rho u = 0 \quad \text{in } \Omega \quad (3.27)$$

with boundary condition

$$\gamma \frac{\partial u}{\partial \nu} = g \quad \text{on } \partial \Omega, \quad (3.28)$$

the residual being defined as previously as

$$\mathcal{R}(\gamma) = u_{\text{true}} - u_{\text{meas}}. \quad (3.29)$$

In order to observe the relationship between  $\delta u$  and  $\delta\gamma$ , we apply  $u + \delta u$  and  $\gamma + \delta\gamma$  to the formula (3.27) and (3.28) instead of  $u$  and  $\gamma$ , respectively. Then, (3.27) becomes

$$\begin{aligned} 0 &= \nabla \cdot ((\gamma + \delta\gamma)\nabla(u + \delta u)) + \rho(u + \delta u) \\ &= \nabla \cdot (\gamma\nabla u) + \nabla \cdot (\delta\gamma\nabla u) + \nabla \cdot (\gamma\nabla\delta u) + \nabla \cdot (\delta\gamma\nabla\delta u) + \rho u + \rho\delta u \end{aligned} \quad (3.30)$$

Let us assume that the term  $\nabla \cdot (\delta\gamma\nabla\delta u)$  is negligible; since  $u$  satisfies (3.27), the identity (3.30) becomes

$$\nabla \cdot (\gamma\nabla\delta u) + \rho\delta u = -\nabla \cdot (\delta\gamma\nabla u) \quad \text{in } \Omega \quad (3.31)$$

and (3.28) becomes

$$(\gamma + \delta\gamma)\frac{\partial(u + \delta u)}{\partial\nu} = \gamma\frac{\partial u}{\partial\nu} + \gamma\frac{\partial\delta u}{\partial\nu} = g + \gamma\frac{\partial\delta u}{\partial\nu} = g$$

implying that

$$\gamma\frac{\partial\delta u}{\partial\nu} = 0 \quad \text{on } \partial\Omega \quad (3.32)$$

From (3.31), (3.32) and (3.18) we can obtain the following relationship.

**Theorem 3.2** *Let  $\mathcal{R}(\gamma)$  be defined as (3.29). Then,  $\mathcal{R}'(\gamma)^*\mathcal{R}(\gamma)$  is given by*

$$\mathcal{R}'(\gamma)^*\mathcal{R}(\gamma) = \nabla u^* \cdot \nabla z.$$

Here,  $u$  satisfies (3.27) and (3.28), and  $z$  solves the following adjoint equation

$$\nabla \cdot (\gamma\nabla z) + \rho z = 0 \quad \text{in } \Omega \quad (3.33)$$

with boundary condition

$$\gamma\frac{\partial z}{\partial\nu} = -\mathcal{R}(\gamma) \quad \text{on } \partial\Omega. \quad (3.34)$$

*Proof.* From the identity (3.31), we get

$$\begin{aligned} \int_{\Omega} (\nabla u^* \cdot \nabla z)(\delta\gamma)^* d\mathbf{x} &= \int_{\Omega} \nabla z \cdot (\delta\gamma\nabla u)^* d\mathbf{x} \\ &= \int_{\partial\Omega} z \left( \delta\gamma \frac{\partial u}{\partial\nu} \right)^* dS - \int_{\Omega} z \nabla \cdot (\delta\gamma\nabla u)^* d\mathbf{x} \\ &= \int_{\Omega} z \{ \nabla \cdot (\gamma\nabla\delta u) + \rho\delta u \}^* d\mathbf{x} \\ &= \int_{\partial\Omega} z \left( \gamma \frac{\partial\delta u}{\partial\nu} \right)^* dS - \int_{\Omega} \nabla z \cdot (\gamma\nabla\delta u)^* d\mathbf{x} + \int_{\Omega} z(\rho\delta u)^* d\mathbf{x} \\ &= - \int_{\Omega} \gamma \nabla z \cdot \nabla\delta u^* d\mathbf{x} + \int_{\Omega} \rho z \delta u^* d\mathbf{x} \\ &= - \int_{\partial\Omega} \gamma \frac{\partial z}{\partial\nu} (\delta u)^* dS + \int_{\Omega} \{ \nabla \cdot (\gamma\nabla z) + \rho z \} \delta u^* d\mathbf{x} \\ &= - \int_{\partial\Omega} \gamma \frac{\partial z}{\partial\nu} (\delta u)^* dS = \langle \mathcal{R}(\gamma), \delta u \rangle_{\partial\Omega} = \langle \mathcal{R}(\gamma), \mathcal{R}'(\gamma)\delta\gamma \rangle_{\partial\Omega} \end{aligned}$$

Therefore, we immediately obtain  $\mathcal{R}'(\gamma)^*\mathcal{R}(\gamma) = \nabla u^* \cdot \nabla z$  as follows

$$\langle \nabla u^* \cdot \nabla z, \delta\gamma \rangle_{\Omega} = \int_{\Omega} \nabla u^* \cdot \nabla z (\delta\gamma)^* d\mathbf{x} = \langle \mathcal{R}(\gamma), \mathcal{R}'(\gamma)\delta\gamma \rangle_{\partial\Omega} = \langle \mathcal{R}'(\gamma)^*\mathcal{R}(\gamma), \delta\gamma \rangle_{\Omega}.$$

### 3.4 Evolution of level set functions $\varphi$ and $\psi$

Let us use formula (3.11) and set  $\tau \rightarrow 0$ . Then, the evolution of the level set function  $\phi$  (herein, this can be  $\varphi$  or  $\psi$ ) satisfies the Hamilton-Jacobi type equation

$$\frac{\partial \varphi(\mathbf{x})}{\partial t} + F |\nabla \varphi(\mathbf{x})| = 0.$$

From formulas (3.15), (3.17) and theorems 3.1, 3.2, we can choose the descent directions of the first and second level sets as follows.

1. The descent direction  $F_1(\mathbf{x})$  for the first level set can go as

$$F_1(\mathbf{x}) = -\text{Re}[\mathcal{R}'(b)^* \mathcal{R}(b)](b - b_0) \{ \delta_{\partial \Gamma_1}(\mathbf{x}) - \delta_{\partial \Gamma_1}(\mathbf{x} + 2h\mathbf{n}(\mathbf{x})) \}, \quad \mathbf{x} \in \partial \Omega_0 \quad (3.35)$$

and the iterative procedure for the first level set function  $\varphi$  can be

$$\varphi^{(n+1)} = \varphi^{(n)} + \tau_T^{(n)} F_1^{(n)} |\nabla \varphi^{(n)}|. \quad (3.36)$$

2. The descent direction  $F_2(\mathbf{x})$  for the second level set reads as

$$F_2(x_1) = -\text{Re} \int_{\partial \Omega_2} \mathcal{R}'(b)^* \mathcal{R}(b)(b - b_0) \delta_{\partial \Omega_2}(\mathbf{x}) \chi_D(\mathbf{x}) dx_2, \quad \mathbf{x} = (x_1, x_2) \in \partial \Omega_2 \quad (3.37)$$

and the iterative procedure for the second level set function  $\psi$  can be

$$\psi^{(n+1)} = \psi^{(n)} + \tau_B^{(n)} F_2^{(n)} |\nabla \psi^{(n)}|. \quad (3.38)$$

Let us emphasize again that the parameter  $b(\mathbf{x})$  indicates  $\gamma(\mathbf{x}) = 1\mu(\mathbf{x})$  or  $\rho(\mathbf{x}) = \omega^2 \varepsilon(\mathbf{x})$  of the inclusion at a given frequency<sup>2</sup>.

**Remark 3.3** *In the above sentence, the descent direction  $F_2(x_1)$  of (3.37) is defined on  $\partial \Omega_2$ . However, in the numerical simulations,  $F_2(\mathbf{x})$  must be applied not only onto  $\partial \Omega_2$  but also for all  $x_1$  contained in some interval which is depending upon the domain  $\Omega^3$ . A more detailed discussion can be found in [2, 38].*

### 3.5 Reconstruction algorithm

In the previous section, essential factors for evolving level sets  $\varphi$  and  $\psi$  have been derived. In this section, we introduce the reconstruction algorithm itself.

Let us denote the initial guesses (functions) as  $\varphi^{(0)}(\mathbf{x})$  and  $\psi^{(0)}(\mathbf{x})$ . Also, let us assume that the  $n$ -th level set functions  $\varphi^{(n)}$  and  $\psi^{(n)}$  have been obtained in the previous step. The iteration procedure can be summarized as follows :

**Step 1** For a thin inclusion  $\Gamma$  and  $\Gamma^{(n)}$ , calculate the residual

$$\mathcal{R}(b) = u_{\text{true}} - u_{\text{meas}} \quad \text{on} \quad \partial \Omega$$

by solving the forward problem (3.19), (3.20) or (3.27), (3.28).

<sup>2</sup>In the numerical simulations, we will use the parameter difference  $b - b_0$  as  $\varepsilon - \varepsilon_0$  or  $(1/\mu) - (1/\mu_0)$  instead of  $\rho - \rho_0$  or  $\gamma - \gamma_0$ .

<sup>3</sup>In the numerical simulations, refer to section 3.6, we will choose  $\Omega$  as a unit disk centered at  $(0, 0)$  in  $\mathbb{R}^2$ . In this case,  $F_2(\mathbf{x})$  must be applied for all  $x_1 \in (-1, 1)$ .

**Step 2** With  $\mathcal{R}(b)$ , solve the adjoint problem (3.25), (3.26) or (3.33), (3.34) and obtain the gradient direction

$$\mathcal{R}'(b)^* \mathcal{R}(b).$$

**Step 3** Calculate the descent direction  $F_1$  and  $F_2$  by (3.35) and (3.37), respectively.

**Step 4** Evolve the level set functions  $\varphi^{(n)}$  and  $\psi^{(n)}$ . In this step, applying suitable regularization (for smoothing the descent directions  $F_1$  and  $F_2$ , see [2, 38]) as needed.

**Step 5** Update the parameter distribution  $b^{(n+1)}(\mathbf{x})$  following formula (3.8).

When the residual converges or oscillates around some stable value, stop the process. If not, go back to Step 1.

### 3.6 Numerical Examples

In order to perform the numerical simulations, we choose the homogeneous domain  $\Omega$ , which is containing a thin inclusion, as a unit disk centered at  $(0, 0)$  in  $\mathbb{R}^2$ . Throughout this section, the thickness  $h$  of all thin inclusions  $\Gamma$  is set to 0.015 and parameters  $\mu, \mu_0, \varepsilon$  and  $\varepsilon_0$  are chosen as 5, 1, 5 and 1, respectively. Since  $\gamma_0$  and  $\varepsilon_0$  are set to unity, the applied frequency reads as  $\omega = 2\pi/\lambda$ , at wavelength  $\lambda$ , i.e., the boundary condition (3.20) and (3.28) can be read as

$$g(\mathbf{x}) = \frac{1}{\mu_0} \frac{\partial u(\mathbf{x})}{\partial \nu(\mathbf{x})} = \frac{\partial e^{i\omega\theta \cdot \mathbf{x}}}{\partial \nu(\mathbf{x})} = i\omega\theta \cdot \nu(\mathbf{x}) e^{i\omega\theta \cdot \mathbf{x}}$$

for every  $\mathbf{x} \in \partial\Omega$ . Within this setting, we solve the (exact) forward problems (3.19), (3.20), (3.27), (3.28) and the adjoint problems (3.25), (3.26), (3.33), (3.34) via a standard Finite Element Method (FEM) method.

For a successful evolution of level sets  $\varphi$  and  $\psi$ , the choice of the time step  $\Delta t$  is very important. In this chapter, we have chosen the time step as

$$\Delta t \equiv \Delta t(s) = 3 \times 10^{-s}$$

for some positive integer  $s$ . More detailed discussions can be found in references [38, 64] and we recommend also [72, Section 3.2.3].

As for the least-square functional  $\mathcal{T}$  at given frequency, which is already introduced in (3.9), we introduce its discrete normalized version as

$$\mathcal{T}_{\mathcal{N}} = \frac{\sum_{j=1}^{N_{\text{meas}}} |u_{\text{true}}(\mathbf{x}_j) - u_{\text{meas}}(\mathbf{x}_j)|^2}{\sum_{j=1}^N |u_{\text{meas}}(\mathbf{x}_j)|^2},$$

for  $\mathbf{x}_j \in \partial\Omega$ . In this section, since  $\Omega$  is an unit circle, the  $\mathbf{x}_j$  are selected as

$$\mathbf{x}_j = \left( \cos \frac{2\pi(j-1)}{N_{\text{meas}}}, \sin \frac{2\pi(j-1)}{N_{\text{meas}}} \right) \quad \text{for } j = 1, 2, \dots, N_{\text{meas}}.$$

Finally, two  $\Gamma_j$  are chosen for the sake of illustration :

$$\Gamma_j = \{\mathbf{x} + \eta \mathbf{n}(\mathbf{x}) : \mathbf{x} \in \sigma_j, \eta \in (-h, h)\}, \quad j = 1, 2, \quad (3.39)$$

item	value
applied wavelength	0.7
incident direction	$(\cos(\pi/2), \sin(\pi/2))$
time step	$\Delta t(4)$
$N_{\text{meas}}$	96

TAB. 3.1 – Test configuration for  $\Gamma_1$  in the permittivity contrast case.

with the support curves

$$\begin{aligned}\sigma_1 &= \{(z, 0.5z^2 + 0.1) : z \in (-0.5, 0.5)\} \\ \sigma_2 &= \{(z, 2z^3 - 0.1z^2 + 0.1z) : z \in (-0.5, 0.5)\}.\end{aligned}$$

**Remark 3.4** *For a successful evolution, we need a good initial guess, close enough (closeness being in practice concluded upon from numerical experimentation) to the unknown scatterer. Without, and since the cost functional of interest is reduced in gradient-like fashion, we might suffer from large computational costs, refer to Fig. 3.7. True, we could obtain an imaging result at far lower low computational cost (and choose it as an initial guess), refer to [4, 5, 54] whenever we are able to work at zero or close to zero frequency, here only aiming at finding the tips of the inclusion and its orientation at the tips; whereas in the propagative regime as of now, a MUSIC-type non-iterative algorithm could work quite well, refer to [66, 67, 68], and now provide the full support curve (or at least an approximation thereof). In the present work, we assume that the location of the end points of  $\Gamma$  has been identified unless otherwise specified. By connecting them via a straight line, we can choose it as an initial support curve  $\sigma$ .*

### 3.6.1 Permittivity contrast only ( $\mu = \mu_0, \varepsilon \neq \varepsilon_0$ )

For the first example, let us consider the reconstruction of  $\Gamma_1$ . The test configuration is found in Tab. 3.1.

Based on this configuration, the initial guess, the true shape, the state of the evolved curve after up to 200 iterations and the overall evolution of the normalized residual  $\mathcal{T}_{\mathcal{N}}$  are displayed in Fig. 3.6. This shows that  $\Gamma_1$  is successfully reconstructed and that the residual decreases quite well accordingly.

Fig. 3.7 shows the evolution of the support curve in the same  $\Gamma_1$  case (see Tab. 3.1), now letting the end points different from the true ones as made so far (the initial guess is the straight line  $\{(z, 0.425) : z \in (-0.5, 0.5)\}$  with end-points  $(-0.5, 0.425)$  and  $(0.5, 0.425)$ .) Although we have performed 500 iterations, further iterations (at higher computational costs) would be required for a successful evolution.

Another configuration for the reconstruction of  $\Gamma_2$  is given in Table 3.2.

With this configuration, the initial guess, the true shape, the state of the evolved curve up to 200 iterations, and the evolution of the normalized residual  $\mathcal{T}_{\mathcal{N}}$  are illustrated, refer to Fig. 3.8. In harmony with the previous example,  $\Gamma_2$  is successfully reconstructed overall and that the residual decreases quite well.



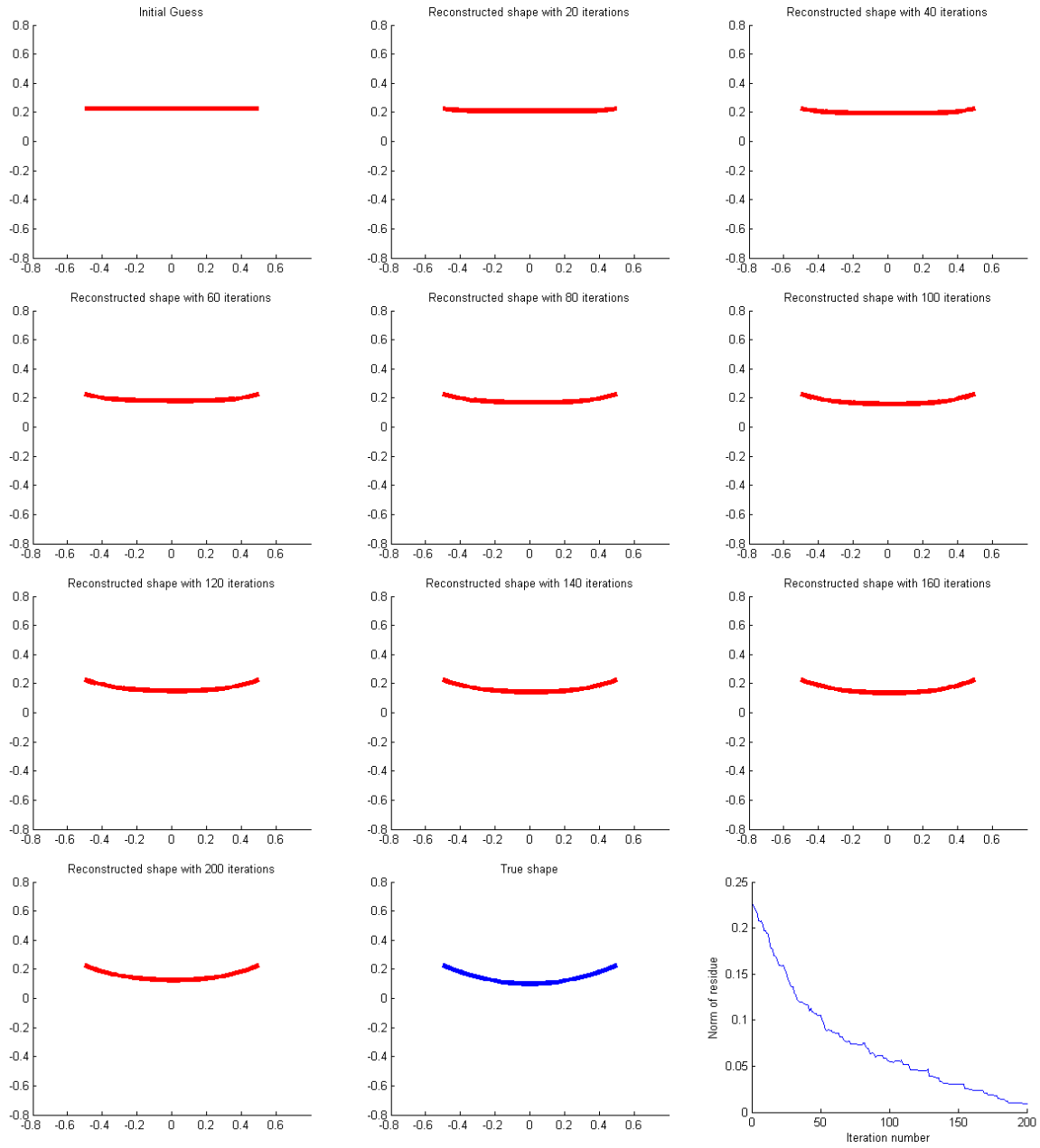


FIG. 3.6 – Reconstruction of  $\Gamma_1$  for the permittivity contrast case. From top to bottom, left to right initial guess, after 20, 40, 60, 80, 100, 120, 140, 160, 200 iterations, true shape and normalized norm of data residuals for each iteration.

item	value
applied wavelength	0.6
incident direction	$(\cos(\pi/6), \sin(\pi/6))$
time step	$\Delta t(5)$
$N_{\text{meas}}$	100

TAB. 3.2 – Test configuration for  $\Gamma_2$  in the permittivity contrast case.

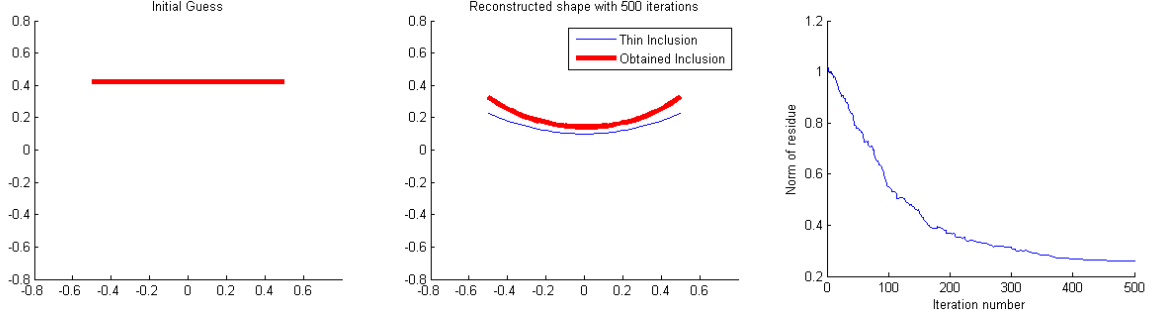


FIG. 3.7 – Same as Fig. 3.6. Left to right initial guess, after 500 iterations, true shape and normalized norm of data residuals for each iteration.

item	value
applied wavelength	0.6
incident direction	$(\cos(\pi/2), \sin(\pi/2))$
time step	$\Delta t(4)$
$N_{\text{meas}}$	128

TAB. 3.3 – Test configuration for  $\Gamma_3$  in the permittivity contrast case.

At this stage of the analysis, let us assume that noise is added to the data, i.e., for every  $\mathbf{x} \in \partial\Omega$ ,

$$u_{\text{noise}}(\mathbf{x}) = \{1 + \xi \times (\text{rnd}_1(-1, 1) + i\text{rnd}_2(-1, 1))\} u(\mathbf{x})$$

where  $\text{rnd}_1(-1, 1)$  and  $\text{rnd}_2(-1, 1)$  are distinct, arbitrary real values between  $-1$  and  $1$ .

Let us consider the reconstruction of  $\Gamma_1$  in the same test configuration as in Table 3.1 for the case  $\xi = 3 \times 10^{-2}$  and  $\xi = 3 \times 10^{-1}$ , refer to Figs. 3.9 and 3.10, respectively. By comparing the results to those displayed in Fig. 3.6,  $\Gamma_1$  appears quite successfully reconstructed and the residual decreases well in accord.

Now, let us consider the reconstruction of multiple (we limit ourselves to two parts, in effect) thin inclusions :

$$\Gamma_3 = \{\mathbf{x} + \eta \mathbf{n}(\mathbf{x}) : \mathbf{x} \in \sigma_3, \eta \in (-h, h)\} \quad (3.40)$$

with the two support curves

$$\sigma_3 = \{(z, 0.5z^2 + 0.1) : z \in (-0.5, -0.2) \cup (0.2, 0.5)\}.$$

A test configuration for the reconstruction of  $\Gamma_3$  is given in Table 3.3.

In Fig. 3.11, the initial guess, the true shape, the evolution of the support curve  $\sigma_3$  up to 250 iterations and the one of normalized residual  $\mathcal{T}_{\mathcal{N}}$  are displayed. Here, the thin inclusion appears to be dividing itself into the two parts after 60 iterations, both evolving somewhat independently thereafter. This shows that the method can be applied not only to a single thin inclusion but also to divided ones, without specific assumption on the parts (again, with same electromagnetic parameters).

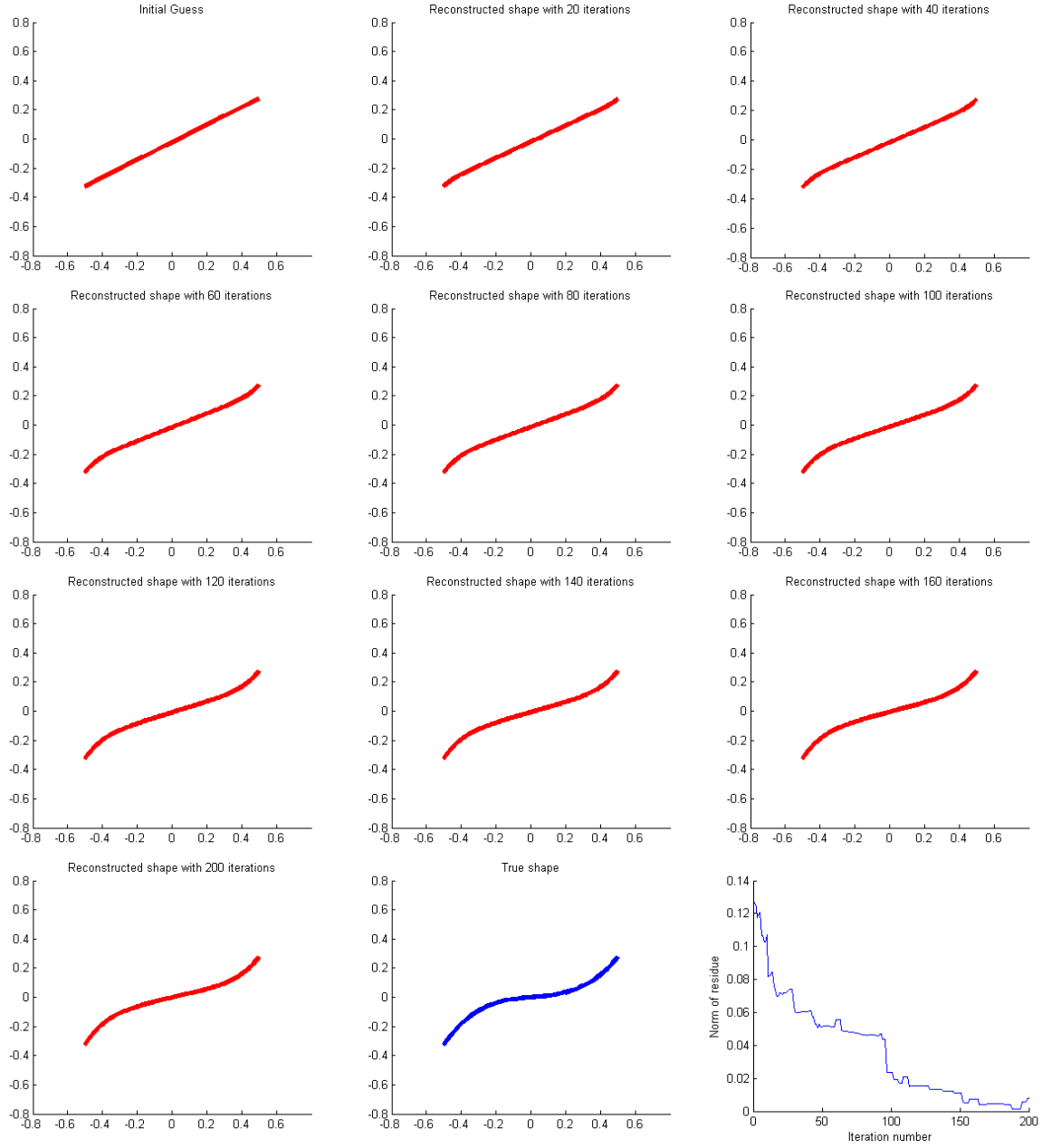
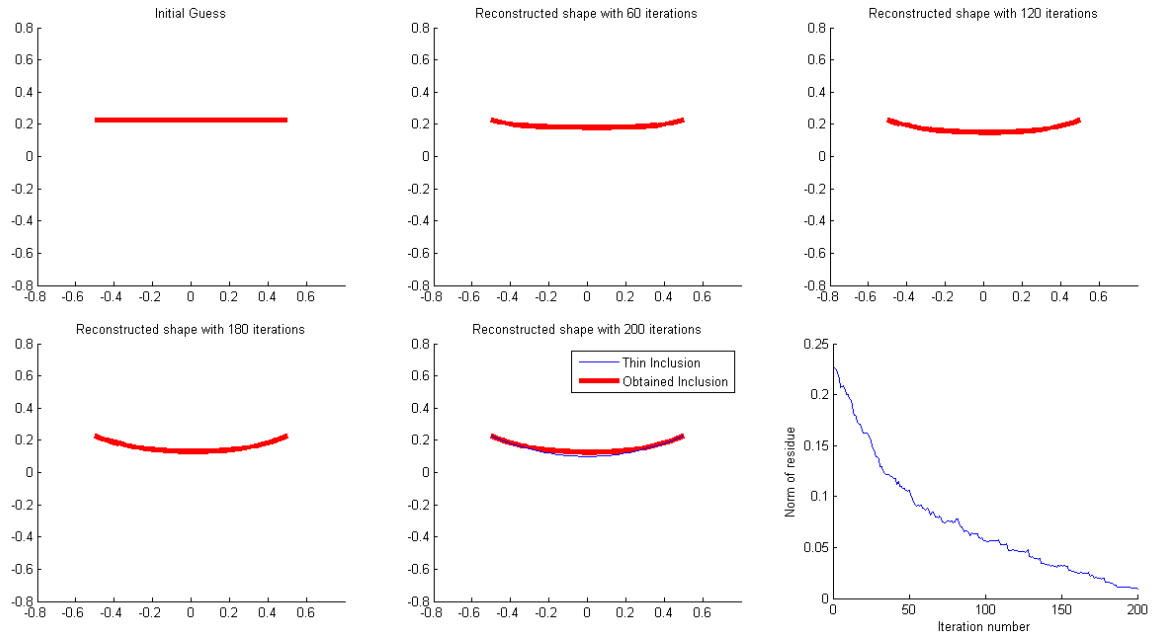
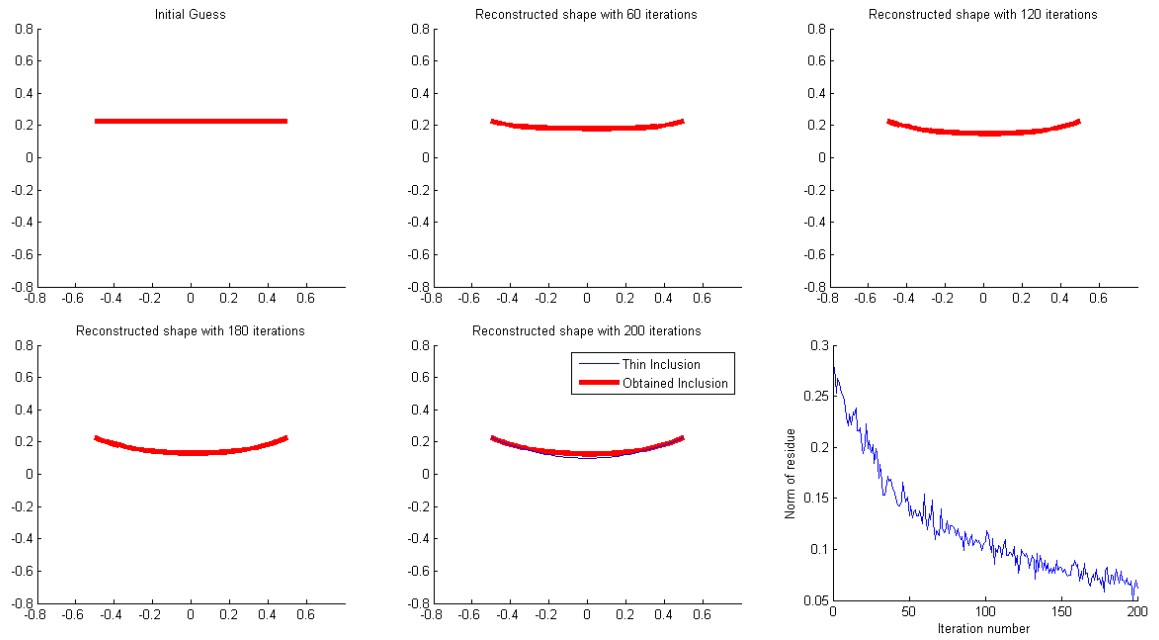


FIG. 3.8 – Reconstruction of  $\Gamma_2$  for the permittivity contrast case. From top to bottom, left to right initial guess, after 20, 40, 60, 80, 100, 120, 140, 160, 200 iterations, true shape and normalized norm of data residuals for each iteration.

FIG. 3.9 – Same as in Fig. 3.6 with some noise  $\xi = 3 \times 10^{-2}$ .FIG. 3.10 – Same as in Fig. 3.6 with some noise  $\xi = 3 \times 10^{-1}$ .

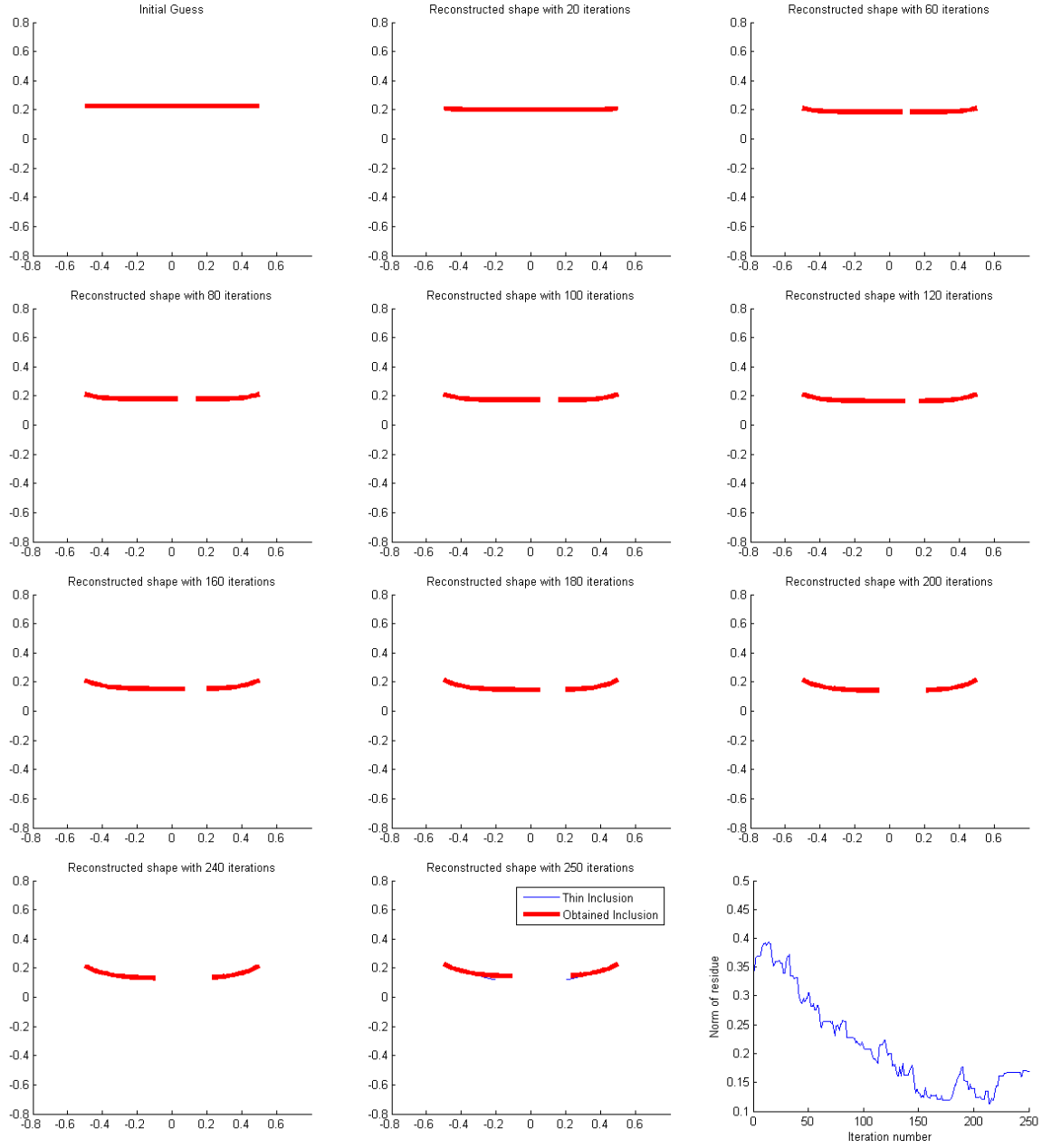


FIG. 3.11 – Reconstruction of  $\Gamma_3$  for the permittivity contrast case. From top to bottom, left to right initial guess, after 20, 60, 80, 100, 120, 160, 180, 200, 240, 250 iterations with supporting curve  $\sigma_3$  and normalized norm of data residuals for each iteration.

item	value
applied wavelength	0.7
incident direction	$(\cos(\pi/2), \sin(\pi/2))$
time step	$\Delta t(5)$
$N_{\text{meas}}$	112

TAB. 3.4 – Test configuration for  $\Gamma_1$  in the permeability contrast case.

item	value
applied wavelength	0.6
incident direction	$(\cos(3\pi/4), \sin(3\pi/4))$
time step	$\Delta t(5)$
$N_{\text{meas}}$	128

TAB. 3.5 – Test configuration for  $\Gamma_2$  in the permeability contrast case.

### 3.6.2 Permeability contrast only ( $\mu \neq \mu_0$ , $\varepsilon = \varepsilon_0$ )

Let us first consider the reconstruction of  $\Gamma_1$  in the case of a permeability contrast. The test configuration is described in Tab. 3.4.

In Fig. 3.12, the initial guess, the true shape, the evolution of the curve up to 200 iterations, and the one of the normalized residual  $\mathcal{T}_{\mathcal{N}}$  are displayed. We can say that  $\Gamma_1$  is successfully reconstructed and the residual decreases quite well accordingly.

Another configuration for the reconstruction of  $\Gamma_2$  is shown in Table 3.5. Results are displayed in Fig. 3.13. In this figure the initial guess, the true shape, the evolution of the curve up to 250 iterations and the one of the normalized residual  $\mathcal{T}_{\mathcal{N}}$  are illustrated.

Let us further consider the reconstruction of  $\Gamma_2$  in the same test configuration as depicted in Tab. 3.5 for the noisy cases  $\xi = 3 \times 10^{-2}$  and  $\xi = 3 \times 10^{-1}$ , refer to Figs. 3.14 and 3.15, respectively. By comparing to the results illustrated in Fig. 3.13, although the normalized least-square cost for noisy data is more oscillating than for noiseless data, we conclude that  $\Gamma_2$  is successfully retrieved.

Let us now consider the retrieval of multiple (two parts again) thin inclusions. Let us start with  $\Gamma_3$  as in the permittivity contrast case. First, we assume that all four end points of  $\Gamma_3$  have been found beforehand<sup>4</sup>. Here, due to the very close initial guess, under the same test configuration as mentioned in Table 3.4, only 18 iterations are necessary to yield a good result, refer to Fig. 3.16.

Now, let us consider a division of  $\Gamma_2$  in two, which is represented as

$$\Gamma_4 = \{\mathbf{x} + \eta \mathbf{n}(\mathbf{x}) : \mathbf{x} \in \sigma_4, \eta \in (-h, h)\} \quad (3.41)$$

with the two support curves

$$\sigma_4 = \{(z, 2z^3 - 0.1z^2 + 0.1z) : z \in (-0.5, -0.15) \cup (0.15, 0.5)\}.$$

<sup>4</sup>In the permittivity case, we have been assuming that only two end points have been identified in the two-part case.

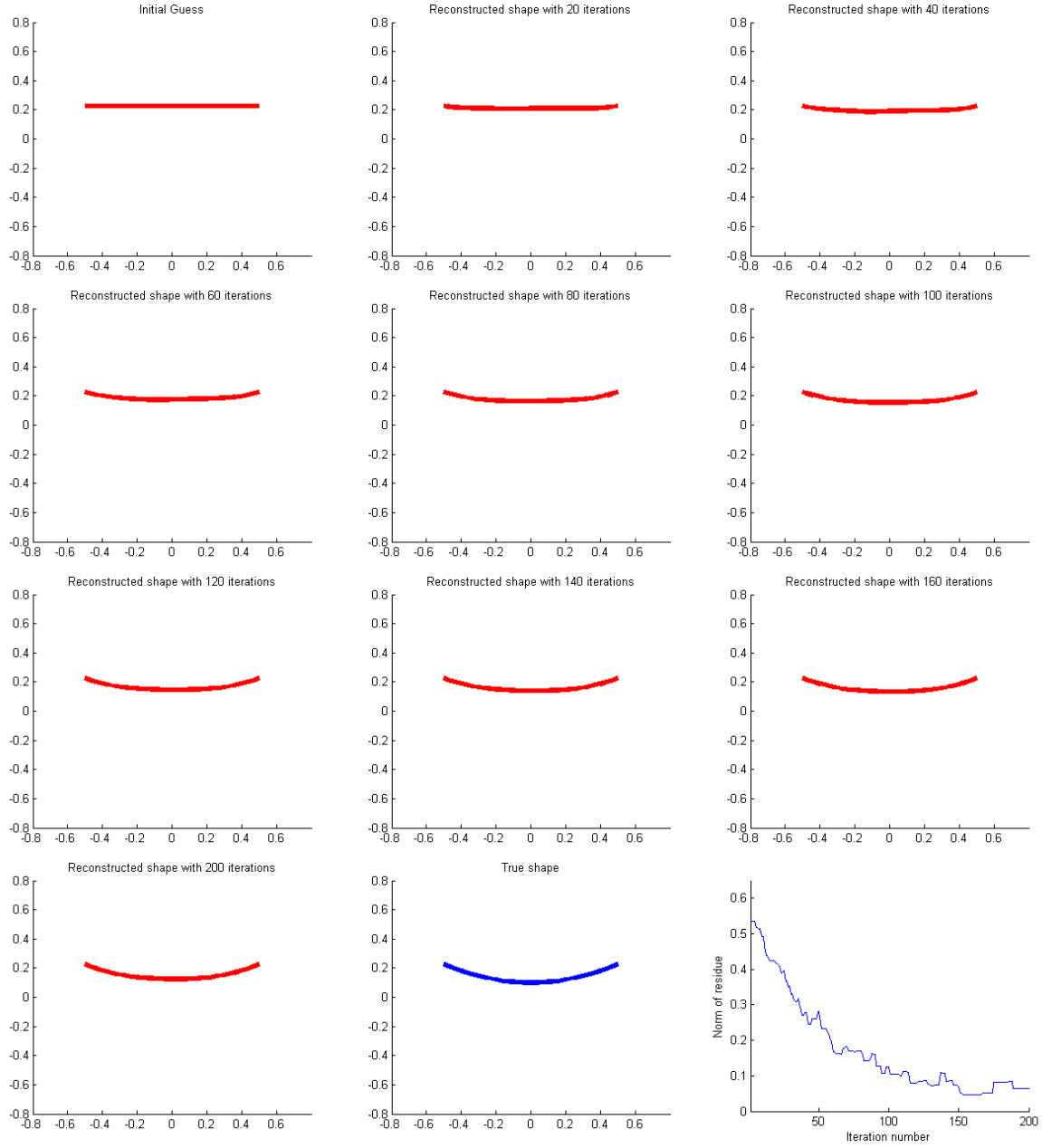


FIG. 3.12 – Reconstruction of  $\Gamma_1$  for the permeability contrast case. From top to bottom, left to right initial guess, after 20, 40, 60, 80, 100, 120, 140, 160, 200 iterations, true shape and normalized norm of data residuals for each iteration.

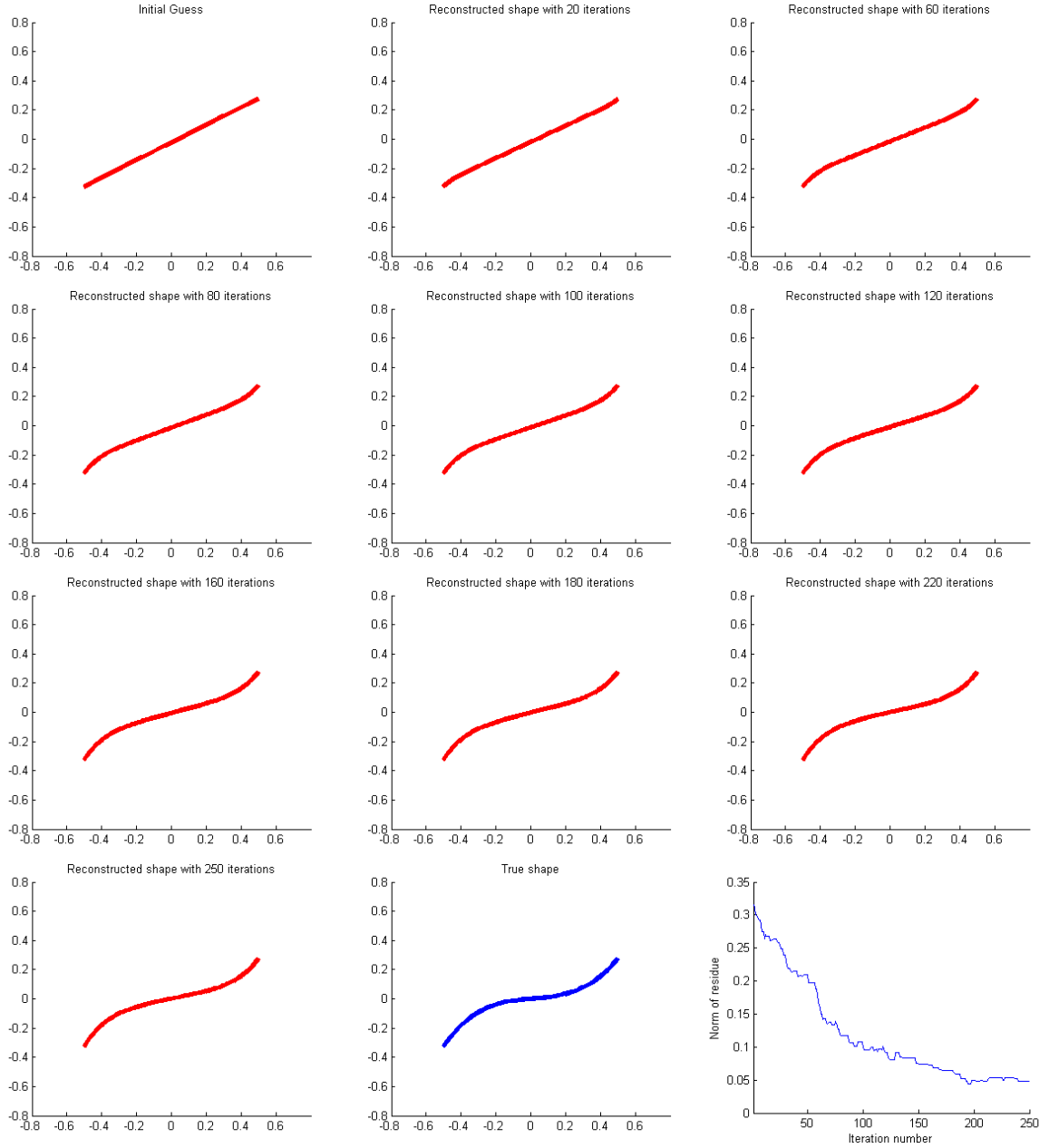


FIG. 3.13 – Reconstruction of  $\Gamma_2$  for the permeability contrast case. From top to bottom, left to right initial guess, after 20, 60, 80, 100, 120, 160, 180, 220, 250 iterations, true shape and normalized norm of data residuals for each iteration.



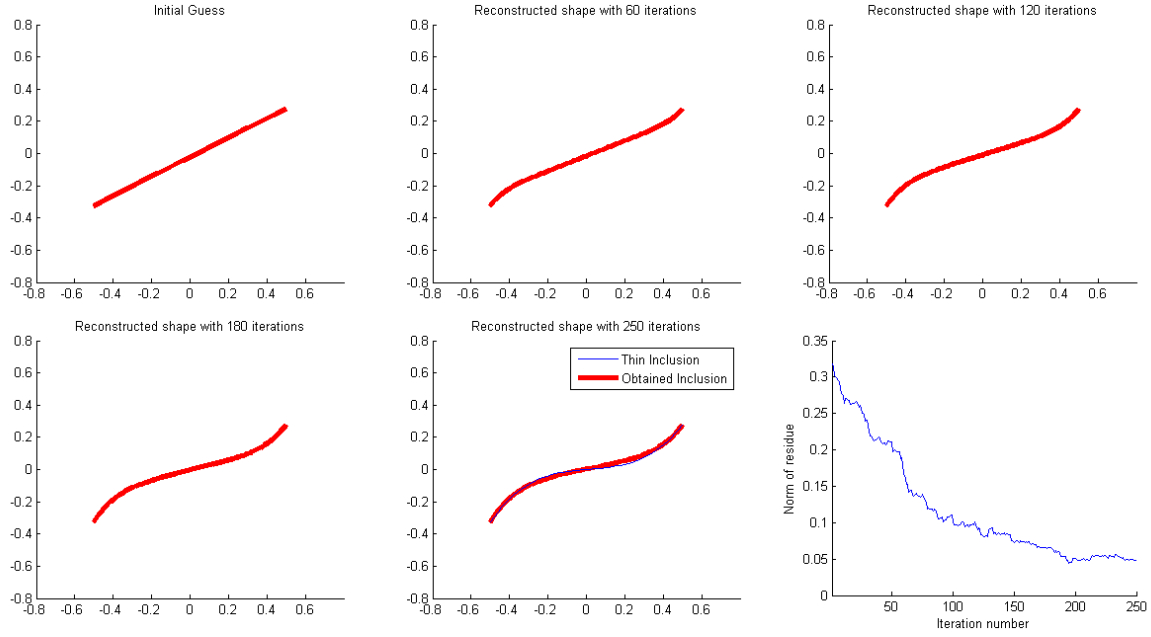


FIG. 3.14 – Same as in Fig. 3.13 with some noise  $\xi = 3 \times 10^{-2}$ .

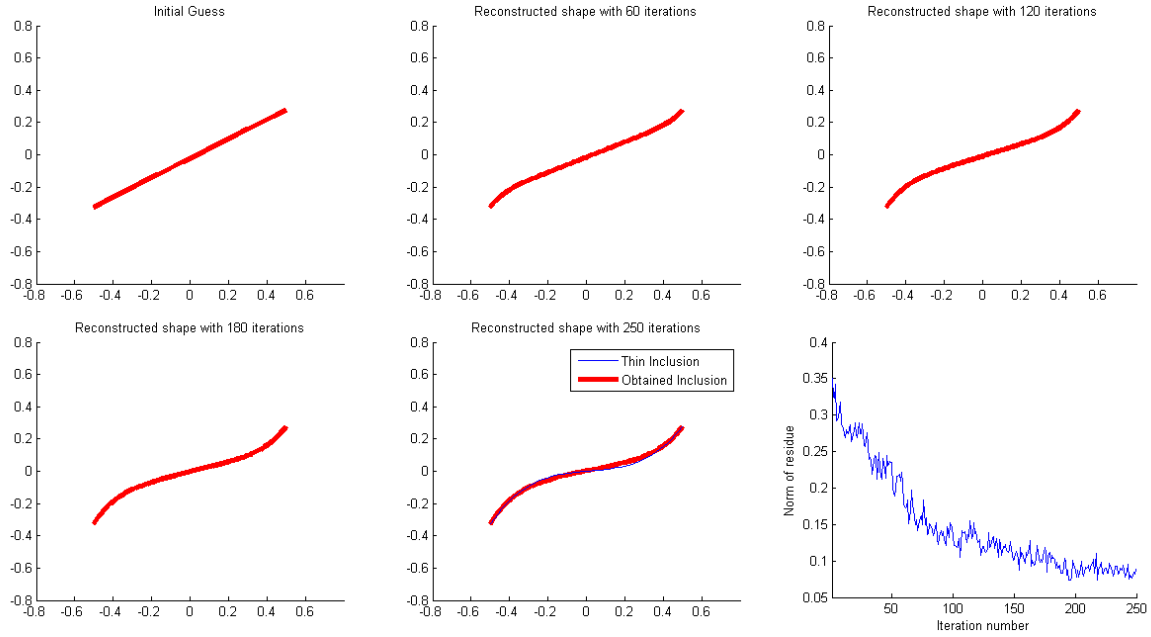


FIG. 3.15 – Same as in Fig. 3.13 with some noise  $\xi = 3 \times 10^{-1}$ .

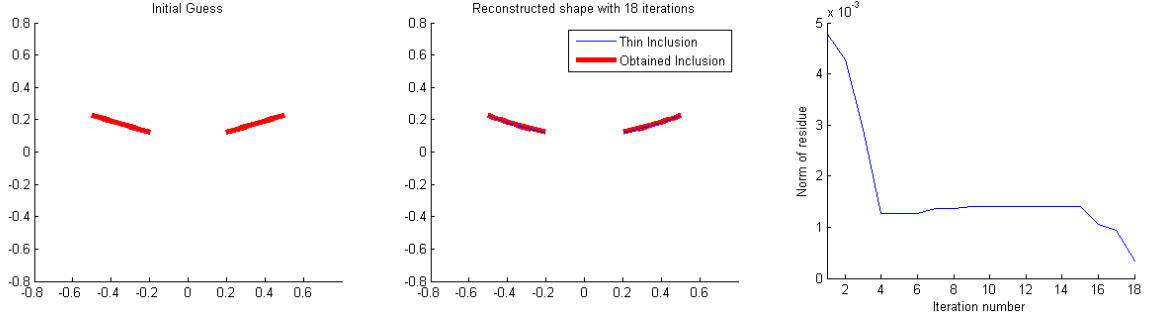


FIG. 3.16 – Reconstruction of  $\Gamma_3$  for the permeability contrast case. From left to right initial guess, 18 iterations, true shape and normalized norm of data residuals for each iteration.

In the same test configuration as mentioned in Tab. 3.5, the initial guess, the true shape, a typical evolution of the retrieved support curve, and the one of normalized residual  $\mathcal{T}_N$  are displayed in Fig. 3.17.

In Figs. 3.18 and 3.19, we further illustrate the reconstruction in presence of noise, here of the multiple thin inclusion  $\Gamma_4$ , for the cases  $\xi = 3 \times 10^{-2}$  and  $\xi = 3 \times 10^{-1}$ , respectively.

In brief, from the various numerical experiments illustrated in Figs. 3.9, 3.10, 3.14, 3.15, 3.18 and 3.19, it appears that the proposed solution method does not significantly suffer from the noise input here.

### 3.7 Conclusion

A level set method of evolution aimed at the electromagnetic retrieval of a thin inclusion, with purely dielectric or magnetic contrast with respect to the embedding homogeneous medium, has been proposed herein. Employing two level set functions, the first one to describe its location and shape and the second one to describe its connectivity and length, enables us to retrieve single and multiple thin inclusions, using a rigorous derivation of gradient directions via Fréchet derivatives (by solving an adjoint problem each time) in order to access to suitable velocities of evolution. Numerical simulations show that the proposed technique is stable and efficient, even in the presence of noise, with somewhat better results in the permittivity case than in the permeability one.

However, this work is still preliminary in the sense that even in a 2-D scalar scattering case as ours, there remain open issues, especially regarding the evolution of the inclusion tips, and the fact that breaking the inclusion into parts as allowed still means that the electromagnetic parameters of the said parts remain the same (and are always assumed to be known). As for real-world issues, this work should be extended to three-dimensional, vector scattering cases, which is an issue requiring both the availability of a proper computational tool of the electromagnetic fields that will be due to a non-necessarily planar screen and the ability of handling level sets of higher dimension. Again, how to best describe edges and corner tips might be demanding as well.

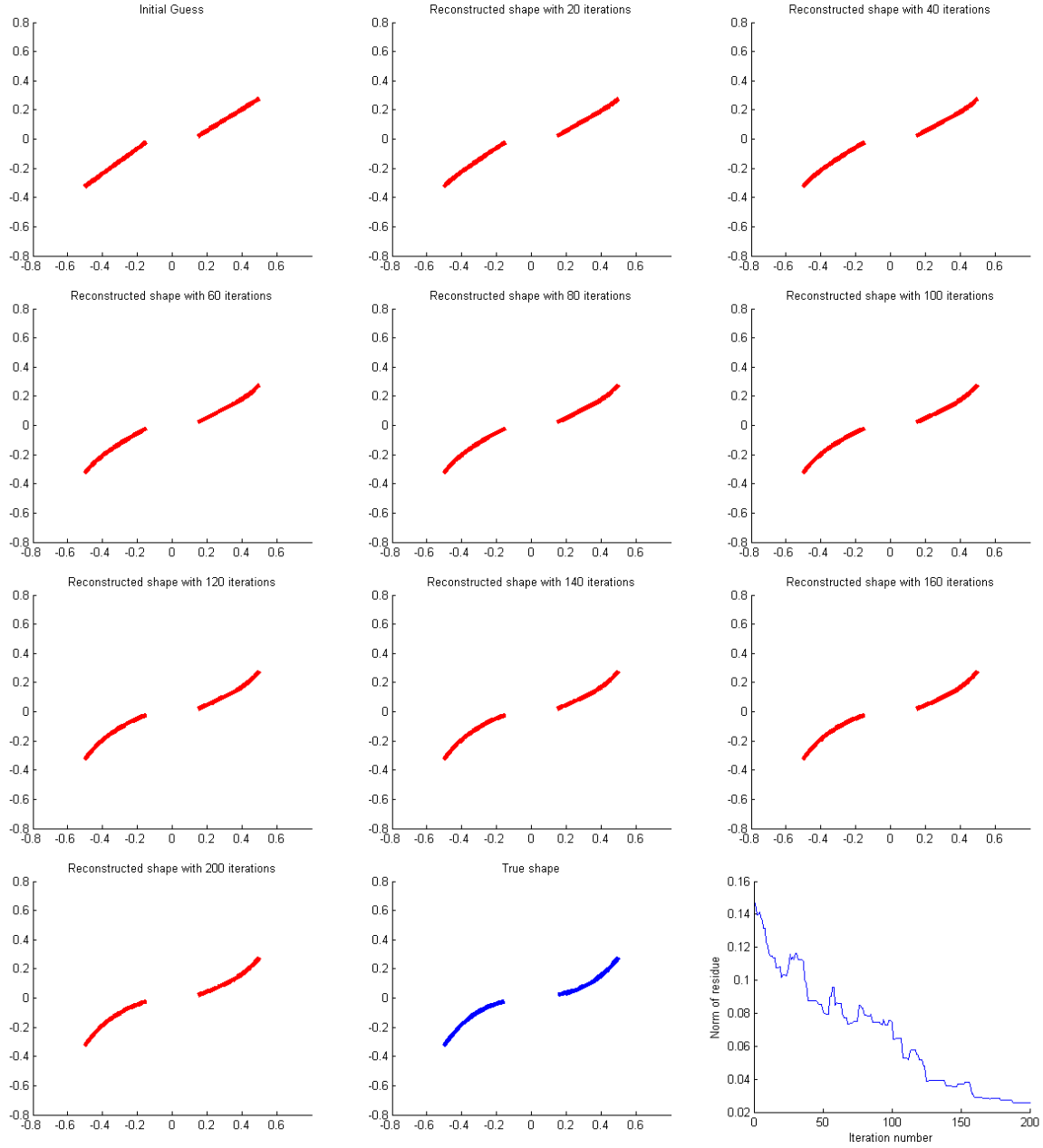


FIG. 3.17 – Reconstruction of  $\Gamma_4$  for the permeability contrast case. From top to bottom, left to right initial guess, 20, 40, 60, 80, 100, 120, 140, 160, 200 iterations, true shape and normalized norm of data residuals for each iteration.

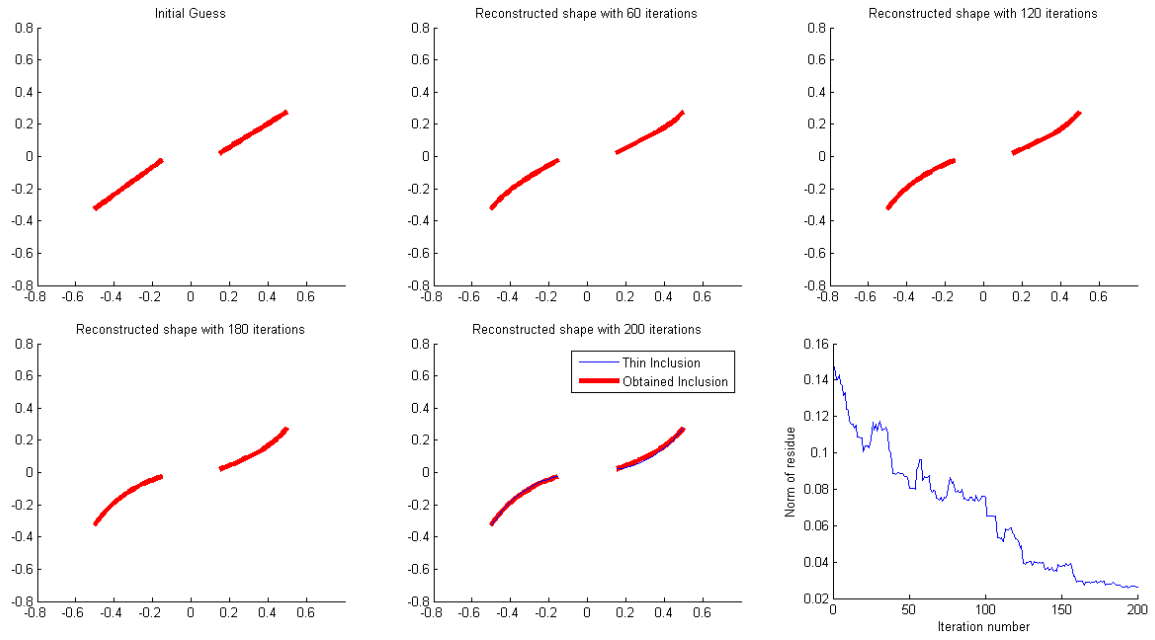


FIG. 3.18 – Same as in Fig. 3.17 with some noise  $\xi = 3 \times 10^{-2}$ .

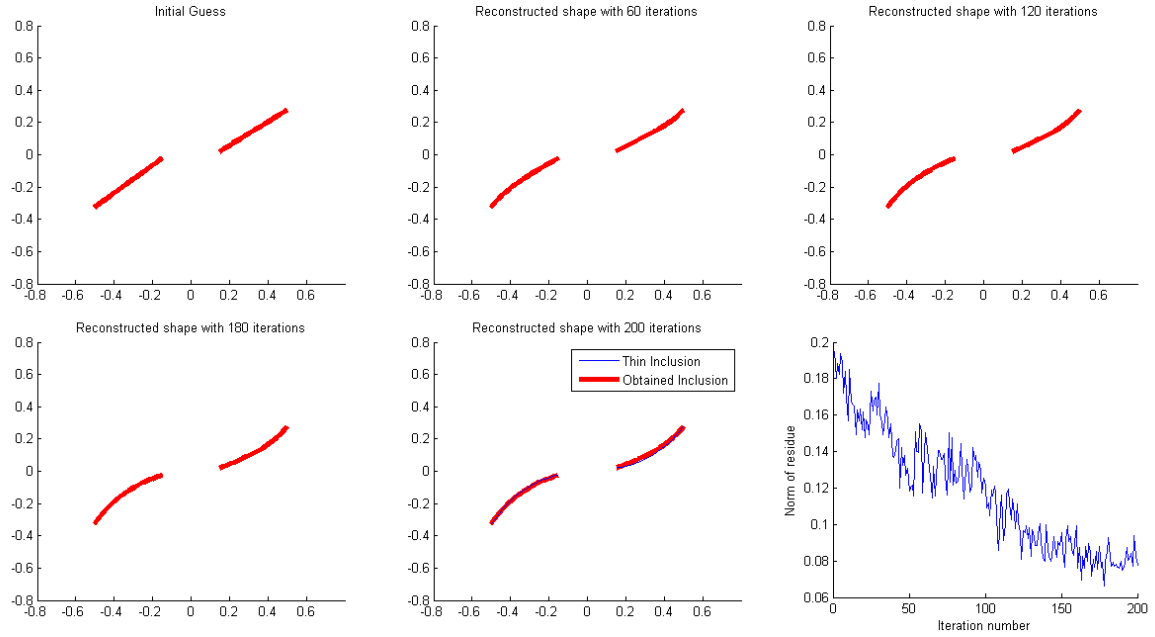


FIG. 3.19 – Same as in Fig. 3.17 with some noise  $\xi = 3 \times 10^{-1}$ .

## Deuxième partie

# Reconstruction of Impenetrable Cracks

## Sommaire

---

<b>4</b>	<b>Reconstruction of Perfectly Conducting Cracks</b>	<b>101</b>
4.1	Introduction . . . . .	101
4.2	Helmholtz equation and direct scattering problem . . . . .	101
4.2.1	Existence and uniqueness of solution . . . . .	103
4.2.2	The far-field pattern . . . . .	104
4.3	MUSIC type algorithm for imaging of screens . . . . .	105
4.4	Numerical examples : Dirichlet boundary condition case . . . . .	106
4.4.1	Reconstruction of a single crack . . . . .	107
4.4.2	Extension to multiple cracks . . . . .	115
4.5	Numerical examples : Neumann boundary condition case . . . . .	119
4.6	Conclusion . . . . .	131
<b>5</b>	<b>Asymptotic Imaging of Perfectly Conducting Cracks</b>	<b>132</b>
5.1	Introduction and problem formulations . . . . .	132
5.2	Preliminary results . . . . .	133
5.3	Asymptotic expansion . . . . .	135
5.4	MUSIC-type imaging . . . . .	137
5.5	Numerical simulations for imaging of small cracks . . . . .	139
5.5.1	Imaging of a single small crack . . . . .	140
5.5.2	Size estimation . . . . .	141
5.5.3	Direction estimation . . . . .	142
5.5.4	Imaging of multiple small cracks . . . . .	143
5.5.5	Imaging of two closely located cracks . . . . .	143
5.6	Deformation of an extended crack . . . . .	146
5.7	Initial guess for an extended crack . . . . .	150
5.7.1	Use of the concept of topological derivative . . . . .	150
5.7.2	A MUSIC-type approach . . . . .	152
5.8	Numerical simulations for imaging extended cracks . . . . .	152
5.8.1	Initial guess through the topological derivative . . . . .	153
5.8.2	Simulation of the MUSIC-type algorithm . . . . .	154
5.9	An optimization approach for extended cracks . . . . .	157
5.10	Conclusion . . . . .	158

---

## 4 Reconstruction of Perfectly Conducting Cracks

We propose an algorithm for the imaging of one or more perfectly conducting cracks (screens) in a homogeneous space  $\mathbb{R}^2$ . It is based on a factorization of the measured Multi-Static Response (MSR) matrix. Operating at a fixed nonzero frequency, it yields the shape of the cracks from scattered far-fields. Due to the fact that there is no iteration needed, it is fast, stable and efficient. Various numerical experiments exhibit how the proposed technique behaves.

### 4.1 Introduction

The inverse scattering problem for time-harmonic acoustic, electromagnetic waves from a crack in two-dimensions with Dirichlet boundary conditions has been considered in [52]. In this paper, the integral equation over a crack is used to prove the existence and uniqueness of the solution and compute it with a Nyström solution method. Based on this, the author in [59] extends it to a Neumann problem. Opposite to the fact that the above is for ‘smooth’ cracks only, the author in [60] has considered the direct scattering problem both for the Dirichlet and Neumann conditions with various cracks, for example, piecewise smooth, semi-infinite screens, etc.

Throughout the literature, Newton-type iteration schemes have been suggested for the inverse scattering problem. Yet, for successful application of these schemes, one needs a good initial guess, close enough to the unknown object. Without, one might suffer from large computational costs. Moreover, iterative schemes often require calculation of the Fréchet derivative of the far-field operator and regularization terms that depend on the specific problem at hand.

In this chapter, we consider the inverse scattering problem for non-iterative imaging of single and multiple, perfectly conducting cracks from a measured far-field pattern for the scattering of time-harmonic plane waves. The chapter is organized as follows. In section 4.2, the direct scattering problem for the perfectly conducting crack is introduced and the far-field pattern of the scattered field is described. In section 4.3, the factorization method of the Multi-Static Response (MSR) matrix is carried out and the MUSIC-type algorithm is discussed. In section 4.4 and 4.5, a set of numerical results is proposed, spectra of MSR matrices, images of single and multiple screens.

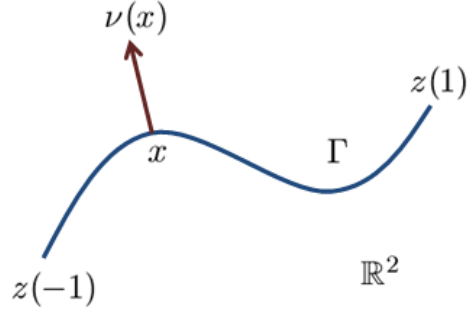
We might refer to references [29, 30, 35, 51, 52] that investigate the linear sampling method, as another reconstruction algorithm for imaging in inverse scattering linked to the MUSIC algorithm.

### 4.2 Helmholtz equation and direct scattering problem

Let  $\Gamma \subset \mathbb{R}^2$  be an oriented piecewise smooth nonintersecting arc without cusp which describes the crack, i.e.,

$$\Gamma = \{z(s) : s \in [-1, 1]\}$$

where  $z : [-1, 1] \longrightarrow \mathbb{R}^2$  is an injective piecewise  $C^3$  function (see Fig. 4.1).

FIG. 4.1 – Illustration of two-dimensional crack  $\Gamma$ .

Let us take  $u$  as  $E_3$  from (2.4) of chapter 2, then  $u$  satisfies the two-dimensional Helmholtz equation

$$\Delta u(x) + k^2 u(x) = 0 \quad \text{in } \mathbb{R}^2 \setminus \Gamma \quad (4.1)$$

with positive wave number  $k = \omega \sqrt{\mu \varepsilon}$ . Let us assume from now on that the crack is perfectly conducting. The electromagnetic field thus cannot penetrate into  $\Gamma$ , i.e,  $u$  satisfies the Dirichlet boundary condition on  $\Gamma$ , say

$$u(x) = 0 \quad \text{on } \Gamma. \quad (4.2)$$

If one takes  $u$  as  $H_3$  from (2.5) of chapter 2, then  $u$  satisfies the same Helmholtz equation (4.1) yet with the following Neumann boundary condition on  $\Gamma$  :

$$\frac{\partial u(x)}{\partial \nu(x)} = 0 \quad \text{on } \Gamma \setminus \{z(-1), z(1)\}. \quad (4.3)$$

where  $\nu(x)$  is a normal vector to  $\Gamma$  at  $x$ .

Let us notice that the total field can be decomposed as  $u(x) = u_0(x) + u_s(x)$ , into the given incident field  $u_0(x) = e^{ik\theta \cdot x}$  for an incident direction  $\theta \in S^1$  and the unknown scattered field  $u_s(x)$ , which is required to satisfy the Sommerfeld radiation condition

$$\lim_{|x| \rightarrow \infty} \sqrt{|x|} \left( \frac{\partial u_s(x)}{\partial |x|} - ik u_s(x) \right) = 0$$

uniformly in all directions  $\hat{x} = \frac{x}{|x|}$ . The determination of  $u_s$  is a special case of the following problem

$$\Delta u_s(x) + k^2 u_s(x) = 0 \quad \text{in } \mathbb{R}^2 \setminus \Gamma \quad (4.4)$$

which satisfies the Dirichlet boundary condition

$$u_s(x) = f(x) \quad \text{on } \Gamma \quad (4.5)$$

or the Neumann boundary condition

$$\frac{\partial u_s(x)}{\partial \nu(x)} = f(x) \quad \text{on } \Gamma \quad (4.6)$$

and the Sommerfeld radiation condition. Remind that from the boundary condition (4.2) and (4.3), we can set  $f(x) = -u_0(x)$  and  $f(x) = -\frac{\partial u_0(x)}{\partial \nu(x)}$  for the boundary conditions (4.5) and (4.6), respectively.

### 4.2.1 Existence and uniqueness of solution

Let us consider the case of the Dirichlet boundary problem. The author in [52] establishes the existence of a solution by searching it in the form of a single-layer potential

$$u_s(x) = \int_{\Gamma} \Phi(x, y) \varphi(y; \theta) dy \quad \text{for } x \in \mathbb{R}^2 \setminus \Gamma \quad (4.7)$$

with the two-dimensional fundamental solution to the Helmholtz equation

$$\Phi(x, y) = \frac{i}{4} H_0^1(k|x - y|) \quad \text{for } x \neq y,$$

in terms of the Hankel function  $H_0^1$  of order zero and of the first kind. The unknown density  $\varphi$  is assumed to be of the form

$$\varphi(x; \theta) = \frac{\tilde{\varphi}(x; \theta)}{\sqrt{|x - z(-1)| |x - z(1)|}} \quad \text{for } x \in \Gamma \setminus \{z(-1), z(1)\}.$$

Here  $\tilde{\varphi}$  is a continuous function on  $\Gamma$  and  $z(-1)$  and  $z(1)$  are end-points of  $\Gamma$ . Then for  $1 < p < 2$ ,  $\varphi \in L^p(\Gamma)$  and therefore, the single-layer potential (4.7) is continuous throughout  $\mathbb{R}^2$ . Hence, if the density  $\varphi$  is a solution to the integral equation

$$\int_{\Gamma} \Phi(x, y) \varphi(y; \theta) dy = f(x) \quad \text{for } x \in \Gamma \quad (4.8)$$

then the potential  $u_s$  of (4.7) solves the exterior Dirichlet problem. From [52, Theorem 2.5], the author shows if  $0 < \alpha < 1$ , for each boundary condition  $f \in C^{1,\alpha}(\Gamma)$  in (4.5), the Dirichlet problem for the exterior of an arc has a unique solution and this solution depends continuously on the boundary data.

For the Neumann boundary problem, the author in [59] establishes the existence of a solution by searching it in the following form of a double-layer potential

$$u_s(x) = \int_{\Gamma} \frac{\Phi(x, y)}{\partial \nu(y)} \psi(y; \theta) dy \quad \text{for } x \in \mathbb{R}^2 \setminus \Gamma. \quad (4.9)$$

For  $0 < \alpha < 1$ , the unknown density  $\psi$  is contained in a space of locally Hölder continuously differentiable functions on  $\Gamma$  which is

$$C_{\text{loc}}^{1,\alpha}(\Gamma \setminus \{z(-1), z(1)\}) = \{\psi \in C(\Gamma) : \psi(z(-1); \theta) = \psi(z(1); \theta) = 0, \psi' \in L^1(\Gamma)\}$$

where the prime indicates differentiation with respect to the arc length. By using the jump relations for the double layer potentials, if the density  $\psi$  is a solution to the hypersingular integral equation of the first kind

$$\frac{\partial}{\partial \nu(x)} \int_{\Gamma} \frac{\partial \Phi(x, y)}{\partial \nu(y)} \psi(y; \theta) dy = f(x) \quad \text{for } x \in \Gamma \setminus \{z(-1), z(1)\}, \quad (4.10)$$

then the potential  $u_s$  of (4.9) solves the exterior Neumann problem. Let us denote  $\tau(x)$  be a tangent vector to  $\Gamma \setminus \{z(-1), z(1)\}$  at  $x$ , then (4.10) becomes the following Maue's identity

$$\begin{aligned} f(x) &= \frac{\partial}{\partial \nu(x)} \int_{\Gamma} \frac{\partial \Phi(x, y)}{\partial \nu(y)} \psi(y; \theta) dy \\ &= \int_{\Gamma} \frac{\partial \Phi(x, y)}{\partial \tau(x)} \frac{\partial \psi(y; \theta)}{\partial \tau(x)} dy + k^2 \int_{\Gamma} \Phi(x, y) \psi(y; \theta) \nu(x) \cdot \nu(y) dy \end{aligned}$$



for  $x \in \Gamma \setminus \{z(-1), z(1)\}$ . Note that from the above identity, we can observe that the degree of singularity in the hypersingular integral equation (4.10) has been reduced. In [59, Theorem 2.3], the author shows that the Neumann problem for the exterior of an arc has a unique solution.

#### 4.2.2 The far-field pattern

Now, we derive an integral representation of the far-field pattern of the scattered field  $u_s$ . In order to derive it, we start from the fact that for densities  $\varphi$ , the first derivatives of the total field  $u$  can be extended as a continuous function from  $\mathbb{R}^2 \setminus \Gamma$  to  $\mathbb{R}^2 \setminus \{z(-1), z(1)\}$  with different limiting values on both sides of  $\Gamma$  by using the jump relations for the single-layer potentials. In particular, if we denote  $\nu(x)$  be a normal vector to  $\Gamma$  at  $x$ , then the limits of the following possible quantities exist

$$\begin{aligned} u(x) &= \lim_{h \rightarrow +0} u(x \pm h\nu(x)) \\ \frac{\partial u_{\pm}(x)}{\partial \nu(x)} &= \lim_{h \rightarrow +0} \nu(x) \cdot \nabla u(x \pm h\nu(x)) \\ -\varphi(x; \theta) &= \frac{\partial u_+(x)}{\partial \nu(x)} - \frac{\partial u_-(x)}{\partial \nu(x)} \\ -\psi(x; \theta) &= u_+(x) - u_-(x) \end{aligned}$$

for all  $x \in \Gamma \setminus \{z(-1), z(1)\}$ .

With this, for every incident field  $u_0$ , the total field  $u$  that satisfies a Dirichlet boundary condition can be derived by the following integral representation

$$\begin{aligned} u(x) &= u_0(x) + u_s(x) = u_0(x) + \int_{\Gamma} \Phi(x, y) \varphi(y; \theta) dy \\ &= u_0(x) - \int_{\Gamma} \left\{ \frac{\partial u_+(y)}{\partial \nu(y)} - \frac{\partial u_-(y)}{\partial \nu(y)} \right\} \Phi(x, y) dy \end{aligned}$$

for  $x \in \mathbb{R}^2 \setminus \Gamma$ .

The far-field pattern  $u_{\infty}$  of the scattered field  $u_s$  is defined on the two-dimensional unit circle  $S^1$ . It can be represented as

$$u_s(x) = \frac{e^{ik|x|}}{\sqrt{|x|}} \left\{ u_{\infty}(\hat{x}; \theta) + O\left(\frac{1}{|x|}\right) \right\}$$

uniformly in all directions  $\hat{x} = \frac{x}{|x|}$  and  $|x| \rightarrow \infty$ . Finally, from the above representation and the asymptotic formula for the Hankel function  $H_0^1$  (see section 4 in chapter 1) we can easily see that the far field pattern for the scattering of an incident field  $u_0$  from a perfectly conducting crack  $\Gamma$  is given by

$$u_{\infty}(\hat{x}; \theta) = -\frac{e^{i\frac{\pi}{4}}}{\sqrt{8\pi k}} \int_{\Gamma} \left\{ \frac{\partial u_+(y)}{\partial \nu(y)} - \frac{\partial u_-(y)}{\partial \nu(y)} \right\} e^{-ik\hat{x} \cdot y} dy, \quad \hat{x} \in S^1. \quad (4.11)$$

Similarly, the far-field pattern for the Neumann boundary problem can be derived

as

$$\begin{aligned} u_\infty(\hat{x}; \theta) &= \sqrt{\frac{k}{8\pi}} e^{-i\frac{\pi}{4}} \int_{\Gamma} \hat{x} \cdot \nu(y) e^{-ik\hat{x} \cdot y} \psi(y; \theta) dy \\ &= \sqrt{\frac{k}{8\pi}} e^{-i\frac{\pi}{4}} \int_{\Gamma} \hat{x} \cdot \nu(y) e^{-ik\hat{x} \cdot y} \{u_+(y) - u_-(y)\} dy \end{aligned} \quad (4.12)$$

for  $\hat{x} \in S^1$ .

### 4.3 MUSIC type algorithm for imaging of screens

In this section, we apply the far-field pattern formulas (4.11) and (4.12) in order to build up a MUSIC-type algorithm for non-iterative imaging of screens.

First, let us consider the Dirichlet boundary condition case. If we exclude the constant  $\frac{e^{i\frac{\pi}{4}}}{\sqrt{8\pi k}}$  from formula (4.11) then the MSR matrix  $K$  can be written as

$$K = \int_{\Gamma} \mathbf{U}_D(y) \mathbf{V}_D(y)^T dy \quad (4.13)$$

where  $\mathbf{U}_D(y)$  is the illumination vector

$$\begin{aligned} \mathbf{U}_D(y) &= (e^{-ik\hat{x}_1 \cdot y}, e^{-ik\hat{x}_2 \cdot y}, \dots, e^{-ik\hat{x}_N \cdot y})^T \Big|_{\hat{x}_j = -\theta_j} \\ &= (e^{ik\theta_1 \cdot y}, e^{ik\theta_2 \cdot y}, \dots, e^{ik\theta_N \cdot y})^T \end{aligned} \quad (4.14)$$

and where  $\mathbf{V}_D(y)$  is the resulting density vector

$$\mathbf{V}_D(y) = (\varphi(y; \theta_1), \varphi(y; \theta_2), \dots, \varphi(y; \theta_N))^T. \quad (4.15)$$

Here,  $\{\hat{x}_j\}_{j=1}^N \subset S^1$  is a discrete finite set of observation directions and  $\{\theta_l\}_{l=1}^N \subset S^1$  is the same number of incident directions.

Formula (4.13) is a factorization of the MSR matrix that separates the known incoming plane wave information from the unknown information. The range of  $K$  is determined by the span of the  $\mathbf{U}_D$  corresponding to the  $\Gamma$ , i.e., we can define a signal subspace by using a set of left singular vectors of  $K$  (see [46, Section 3]).

The imaging algorithm is similar to the one proposed in [46]. Let the singular value decomposition of the matrix  $K$  be  $K = V S \bar{W}^T$ , where  $V, W \in \mathbb{C}^{N \times N}$  are unitary matrices and where  $S$  is a real nonnegative diagonal matrix with components  $\lambda_1, \lambda_2, \dots, \lambda_N$  which satisfies

$$\lambda_1 \geq \lambda_2 \geq \dots \geq \lambda_M > 0 \quad \text{and} \quad \lambda_j = 0 \text{ for } j = M+1, M+2, \dots, N.$$

Alternatively,  $\lambda_j$ , for  $j = M+1, M+2, \dots, N$ , could merely be very small, below the noise level of the system represented by  $K$ . Then the first  $M$  columns of the matrix  $V$ ,  $\{v_1, v_2, \dots, v_M\}$ , provide an orthonormal basis for  $K$  and the rest of the matrix  $V$ ,  $\{v_{M+1}, v_{M+2}, \dots, v_N\}$ , provides a basis for the null (or noise) space of  $K$ . So, one can

form the projection onto the null (or noise) subspace : this projection is given explicitly by

$$P_{\text{noise}}(f) = \sum_{j>M} v_j \bar{v}_j^T f. \quad (4.16)$$

For any point  $z \in \mathbb{R}^2$ , define a vector  $g \in \mathbb{C}^N$  as

$$g = (e^{ik\theta_1 \cdot z}, e^{ik\theta_2 \cdot z}, \dots, e^{ik\theta_N \cdot z})^T \quad (4.17)$$

then an image of  $y_j$ ,  $j = 1, 2, \dots, M$ , follows from computing

$$W(z) = \frac{1}{\|P_{\text{noise}}(g)\|}. \quad (4.18)$$

The resulting plot of this estimator is expected to exhibit large peaks at the sought  $y_j$ .

Second, let us consider the Neumann boundary condition case. Eliminating the constant  $\sqrt{\frac{k}{8\pi}}e^{-i\frac{\pi}{4}}$  from formula (4.12) then the MSR matrix  $K$  can be written as

$$K = \int_{\Gamma} \mathbf{U}_N(y) \mathbf{V}_N(y)^T dy \quad (4.19)$$

where  $\mathbf{U}_N(y)$  is the illumination vector

$$\begin{aligned} \mathbf{U}_N(y) &= -(\hat{x}_1 \cdot \nu(y)e^{-ik\hat{x}_1 \cdot y}, \hat{x}_2 \cdot \nu(y)e^{-ik\hat{x}_2 \cdot y}, \dots, \hat{x}_N \cdot \nu(y)e^{-ik\hat{x}_N \cdot y})^T \Big|_{\hat{x}_j = -\theta_j} \\ &= (\theta_1 \cdot \nu(y)e^{ik\theta_1 \cdot y}, \theta_2 \cdot \nu(y)e^{ik\theta_2 \cdot y}, \dots, \theta_N \cdot \nu(y)e^{ik\theta_N \cdot y})^T \end{aligned} \quad (4.20)$$

and where  $\mathbf{V}_N(y)$  is the corresponding density vector

$$\mathbf{V}_N(y) = (\psi(y; \theta_1), \psi(y; \theta_2), \dots, \psi(y; \theta_N))^T. \quad (4.21)$$

Although (4.19) is a different factorization from (4.13), the imaging algorithm is very similar to the previous one (see [46, Section 4] also). For any point  $z \in \mathbb{R}^2$ , we define a vector  $g \in \mathbb{C}^N$  that reads, instead of (4.17), as

$$g = (\theta_1 \cdot \nu(z)e^{ik\theta_1 \cdot z}, \theta_2 \cdot \nu(z)e^{ik\theta_2 \cdot z}, \dots, \theta_N \cdot \nu(z)e^{ik\theta_N \cdot z})^T. \quad (4.22)$$

Since the unit normal  $\nu(z)$  is still unknown, for each point  $z_j$  of the search domain, we use a set of directions  $\nu_l$  for  $l = 1, 2, \dots, L$  and choose  $\nu_l(z_j)$  which is to maximize

$$W(z_j) = \frac{1}{\|P_{\text{noise}}(g)\|}. \quad (4.23)$$

The resulting plot of this estimator is expected to exhibit large peaks at the sought  $y_j$ .

#### 4.4 Numerical examples : Dirichlet boundary condition case (Figs. 4.2 to 4.16)

In this section, we present some numerical examples obtained with the MUSIC-type algorithms for imaging of screens. Throughout this section, similarly with the previous

chapter, we adopt the applied wave number of the form  $k = \frac{2\pi}{\lambda}$ ; here  $\lambda$  is the given wavelength, which will be varied between the low-frequency one of  $\lambda = 1$  and the high-frequency one of  $\lambda = 0.1$ .

Three  $\Gamma_j$  are chosen for illustration :

$$\begin{aligned}\Gamma_1 &= \left\{ \left( \frac{s}{2}, 0.3 \right) : s \in [-1, 1] \right\} \\ \Gamma_2 &= \left\{ \left( s, \frac{1}{2} \cos \frac{s\pi}{2} + \frac{1}{5} \sin \frac{s\pi}{2} - \frac{1}{10} \cos \frac{3s\pi}{2} \right) : s \in [-1, 1] \right\} \\ \Gamma_3 &= \left\{ \left( 2 \sin \frac{s}{2}, \sin s \right) : s \in \left[ \frac{\pi}{4}, \frac{7\pi}{4} \right] \right\}\end{aligned}$$

and the search domain  $\tilde{\Omega}$  is taken as  $\tilde{\Omega} = [-1, 1] \times [-1, 1]$  for the imaging of  $\Gamma_1$  and  $\Gamma_2$  and  $[-1, 3] \times [-2, 2]$  for  $\Gamma_3$ . For each  $z \in \tilde{\Omega}$ , the step size of  $z$  is taken of the order of 0.02. As for the observation directions  $\theta_l$ , they are taken as

$$\theta_l = \left( \cos \frac{2\pi(l-1)}{N}, \sin \frac{2\pi(l-1)}{N} \right) \quad \text{for } l = 1, 2, \dots, N.$$

It is worth mentioning that, due to the fact that the reliable and efficient solution of the direct problem indicated previously is very important, all the numerical data in this section, the elements  $u_\infty(\theta_j, \theta_l)$  for  $j, l = 1, 2, \dots, N$  of the dataset  $K$  are generated by the Nyström method for both the Dirichlet and Neumann boundary conditions as presented in [52, formula (4.11)] and [59, p. 354], respectively. After obtaining the dataset, the singular value decomposition of  $K = V S \bar{W}^T$  is performed. Once the singular values are computed, they are normalized with respect to the one of maximum amplitude. A detailed discussion of this normalization has been made in section 2.5 of chapter 2 and [68, Section 4].

#### 4.4.1 Reconstruction of a single crack

Before starting this section, we make the following remarks.

**Remark 4.1** *Let us consider an image of  $\Gamma_1$ . In figure 4.2, we observe that when the number  $N$  is not large enough, we can choose the nonzero singular values without normalizing them, but the imaging is poor. For example, when we choose  $N = 12$  and as wavelength of operation,  $\lambda = 0.5$ , we can observe that the first seven singular values are well distinguished from the five, much weaker remaining ones (top-left) without normalizing the singular values. However, when we use seven singular values to discriminate the noise subspace from the signal subspace, poor results appear (top-right). When we increase the number  $N$  to  $N = 20$  while keeping the same 0.5 wavelength, this phenomenon is but vanishing (bottom-left). Hence, if one wishes to get an acceptable imaging of a crack, normalizing the singular values is something needed.*

**Remark 4.2** *Instead of the scattered field dataset generated from the Nyström method, some authors in [60] introduce a similar formulation involving the solution of a second-kind Fredholm integral equation along the crack, refer to [60, Chapter 3]. Numerical*

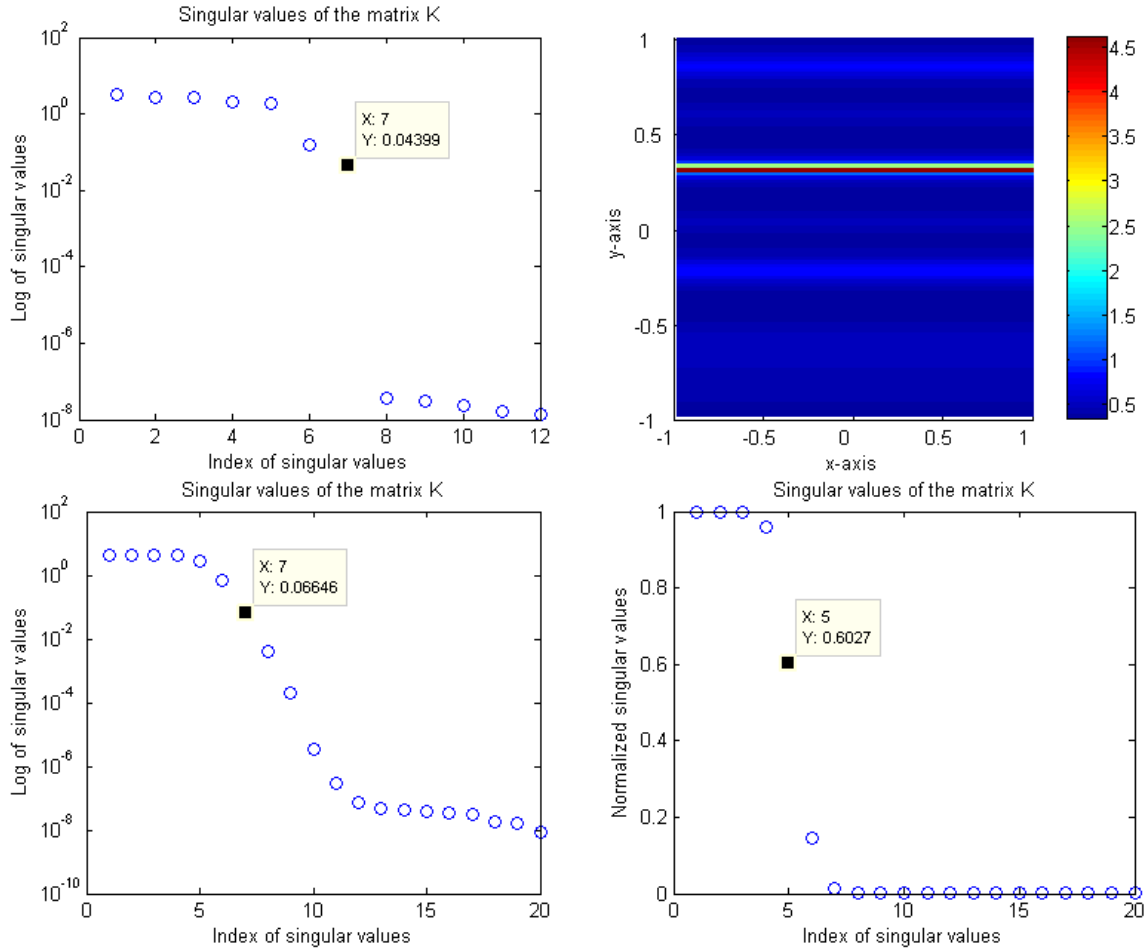


FIG. 4.2 – (Dirichlet boundary condition case) Top : Distribution of log-scaled singular values of the matrix  $K$  (left) and map of  $W(z)$  (right), for  $N = 12$  incidences and a 0.5 wavelength. Bottom : Distribution of log-scaled (left) and normalized (right) singular values of the matrix  $K$  respectively for  $N = 20$  incidences and a 0.5 wave length when the crack is  $\Gamma_1$ .

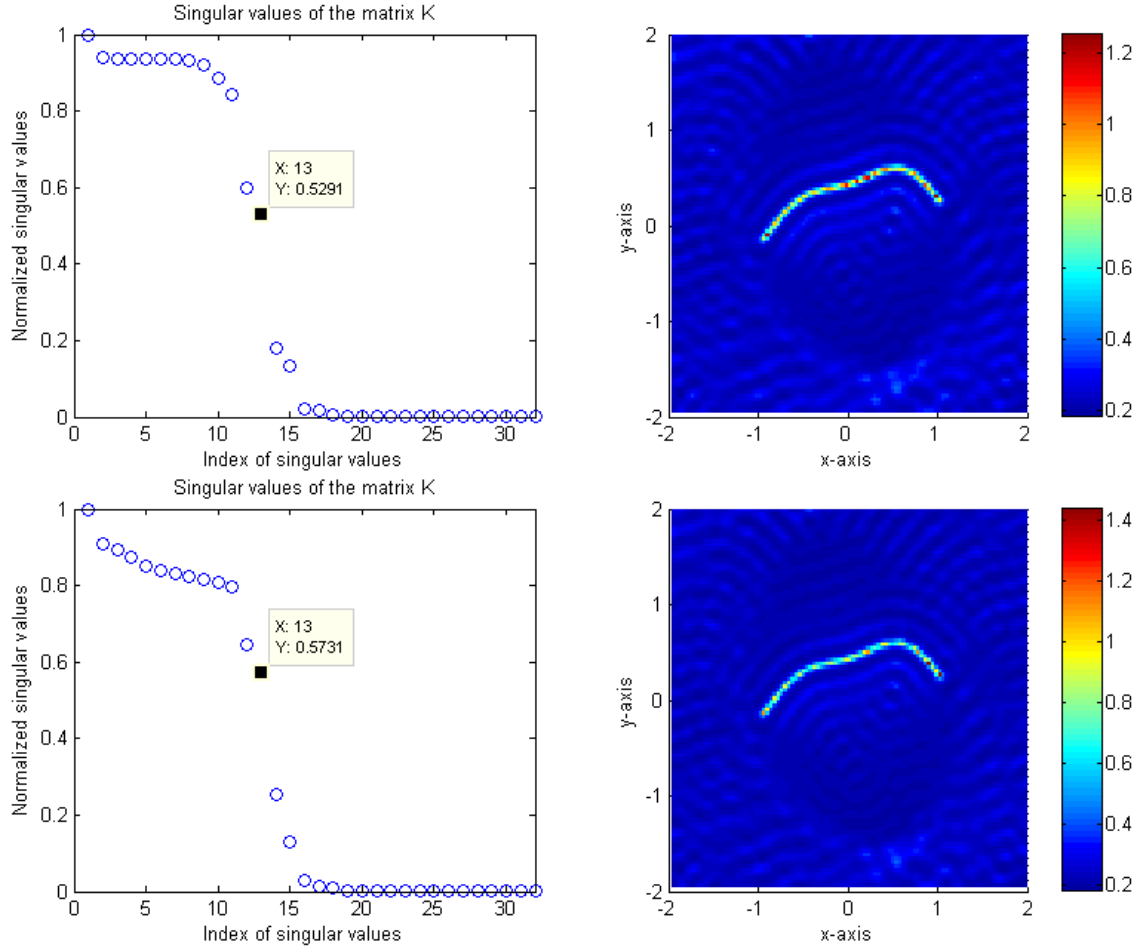


FIG. 4.3 – (Dirichlet boundary condition case) Distribution of normalized singular values of the MSR matrix  $K$  (left column) and maps of  $W(z)$ ,  $z \in \tilde{\Omega}$  (right column), for  $N = 32$  incidences and a  $\lambda = 0.4$  wavelength when the crack is  $\Gamma_2$ . Dataset generated by the Nyström method introduced in [52] (top row) and another one in [60].

*experimentation shows that images of a crack from the Nyström method or from the ones calculated via this alternative formulation are almost indistinguishable (see figure 4.3).*

Let us first work with  $\Gamma_1$ ,  $K$  being collected for  $N = 20$  and  $N = 32$ , and the wavelengths of operation  $\lambda = 0.4$  and  $\lambda = 0.2$ , respectively. Distributions of the normalized singular values of  $K$  and maps of  $W(z)$  are displayed in Fig. 4.4.

Each time, a small finite number of singular values (6 at  $\lambda = 0.4$ , 11 at  $\lambda = 0.2$ ) emerge from the remaining, much smaller ones, whilst images thereupon produced by projection onto singular vectors beyond the first 6 or 11 ones appear excellent, a small number of peaks being obtained, each peak being observed to be  $\lambda/2$  away from the next one. No problem of discrimination is faced, and this in effect remains true whenever a curve of zero curvature is to be imaged, whatever be its type of contrast and the conditions of illumination (if the ratio  $N/M$  is kept properly large).

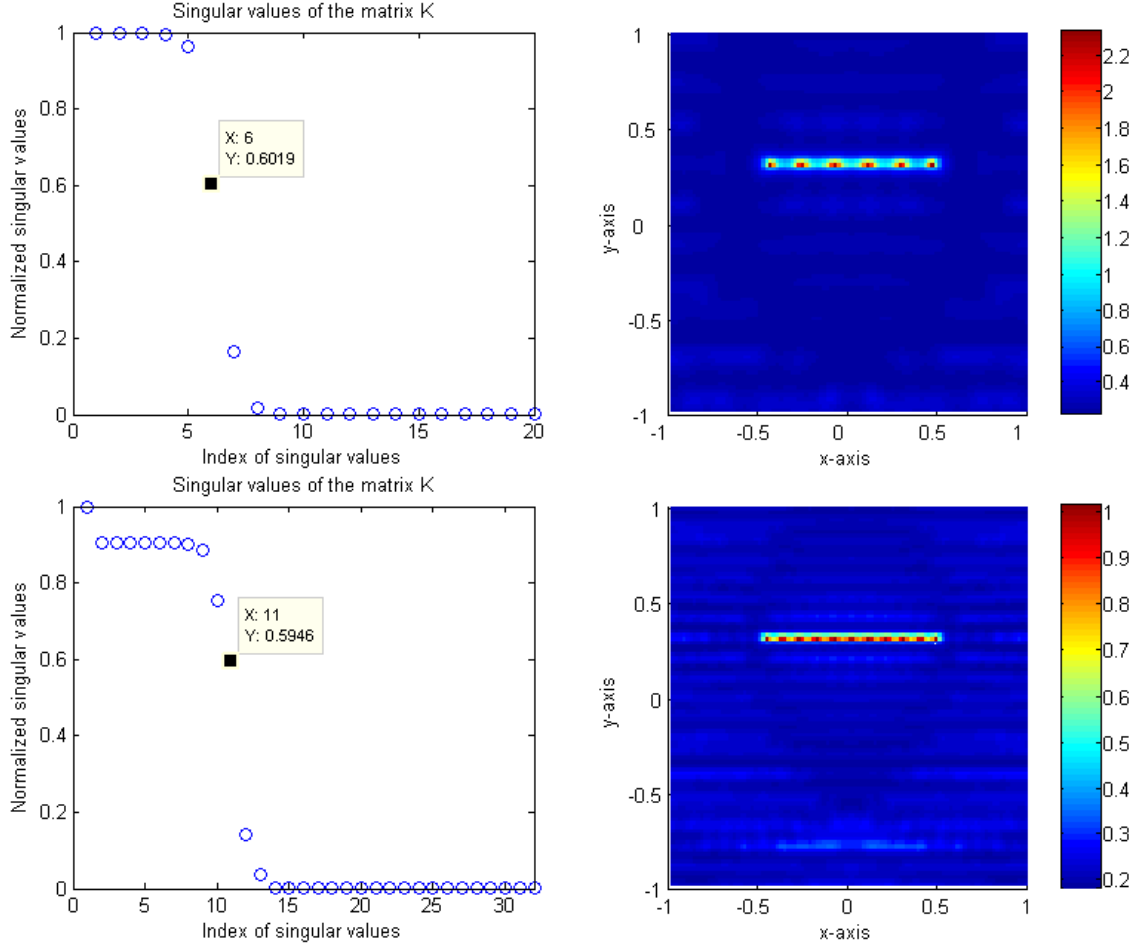


FIG. 4.4 – (Dirichlet boundary condition case) Distributions of normalized singular values of the matrix  $K$  (left column) and maps of  $W(z)$  (right column), for  $N = 20$  incidences and a 0.4 wavelength (top line), for  $N = 32$  incidences and a 0.2 wavelength (bottom line) when the crack is  $\Gamma_1$ .

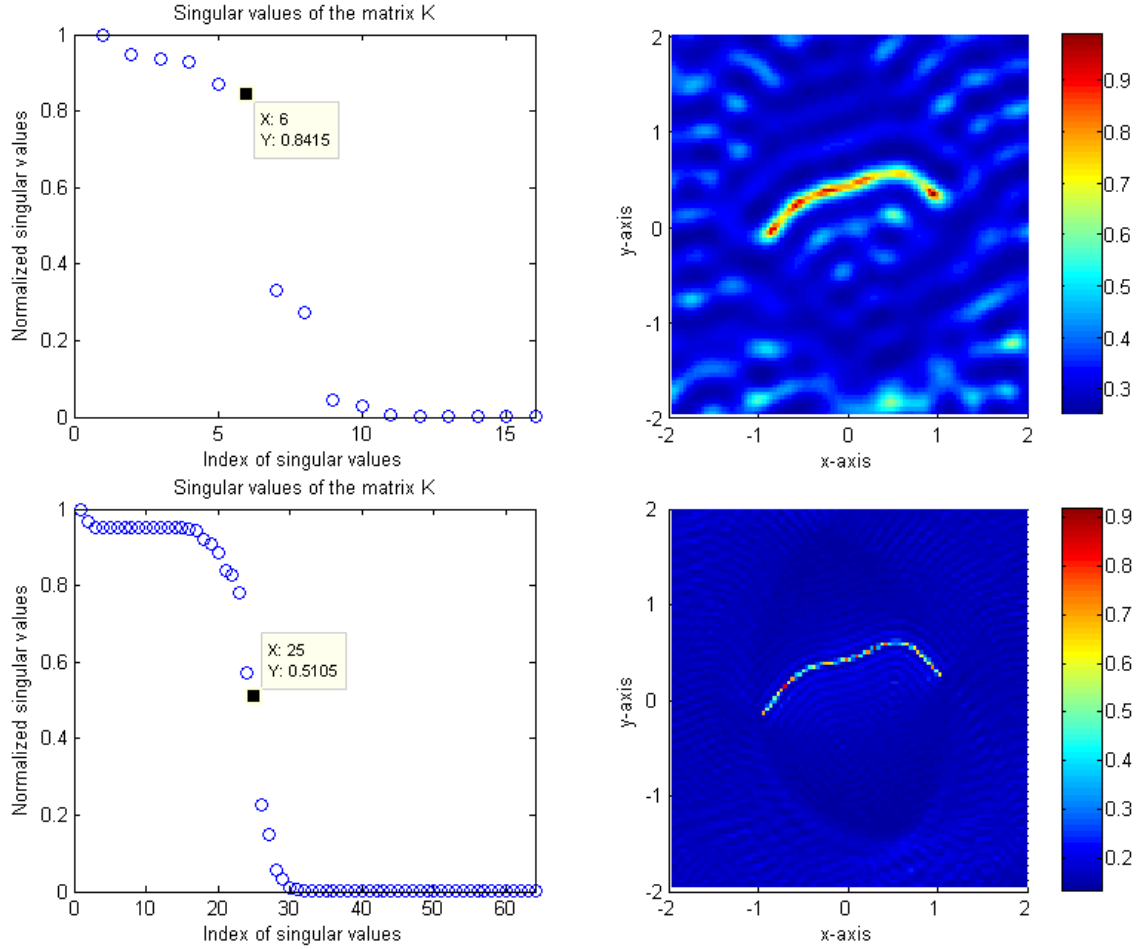


FIG. 4.5 – (Dirichlet boundary condition case) Distributions of normalized singular values of the matrix  $K$  (left column) and maps of  $W(z)$  (right column), for  $N = 16$  incidences and a 0.8 wavelength (top line), for  $N = 64$  incidences and a 0.2 wavelength (bottom line) when the crack is  $\Gamma_2$ .

Opposite to the penetrable inclusion case as dealt with in chapter 2, although the crack is not anymore a straight line, the discrimination for a curved crack is still obvious. As an example, let us consider the image of  $\Gamma_2$ , here using  $N = 16$  and  $N = 64$  incident directions and a wavelength of 0.8 and 0.2 respectively, refer to Fig. 4.5.

In addition, the discrimination for a complicated crack, though remaining obvious, is affected by unexpected isolated peaks of large magnitude. An image of  $\Gamma_3$ , here using  $N = 32$  incident directions and a wavelength  $\lambda = 0.7$ , shows that phenomenon in Fig. 4.6.

We have already examined and discussed a similar case from Fig. 2.7 in chapter 2. However, when we increase to  $N = 48$  illuminations for the imaging, these peaks do not disappear from the image. Hence, in order to eliminate them from the imaging results, we adopt a much smaller threshold of 0.1 or 0.01, refer to Fig. 4.7. Comparing with the imaging result in Fig. 4.6, we observe that this eliminates all or almost all isolated points from the images and offers a higher resolution.



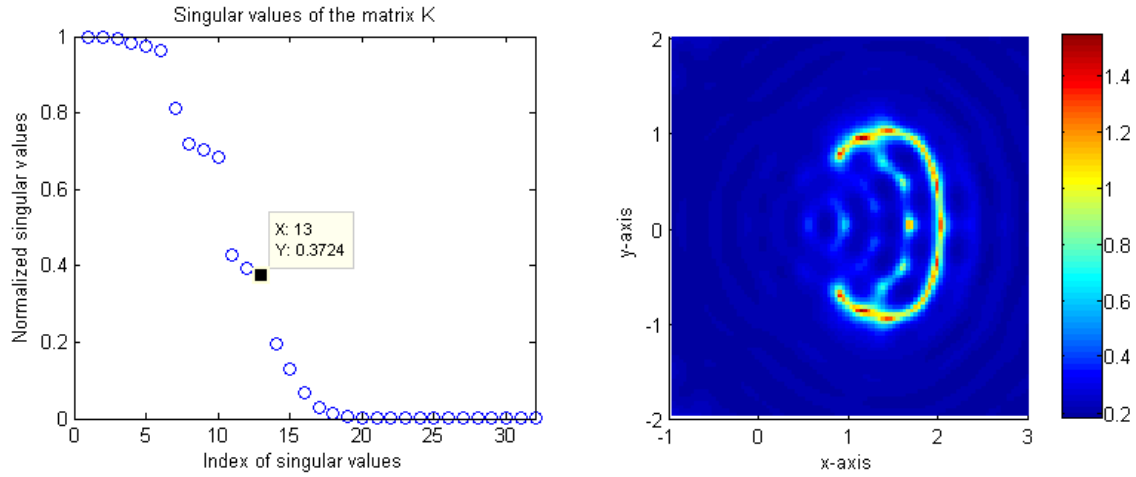


FIG. 4.6 – (Dirichlet boundary condition case) Distribution of normalized singular values of the matrix  $K$  (left) and map of  $W(z)$  (right), for  $N = 32$  incidences and a 0.7 wavelength when the crack is  $\Gamma_3$ .

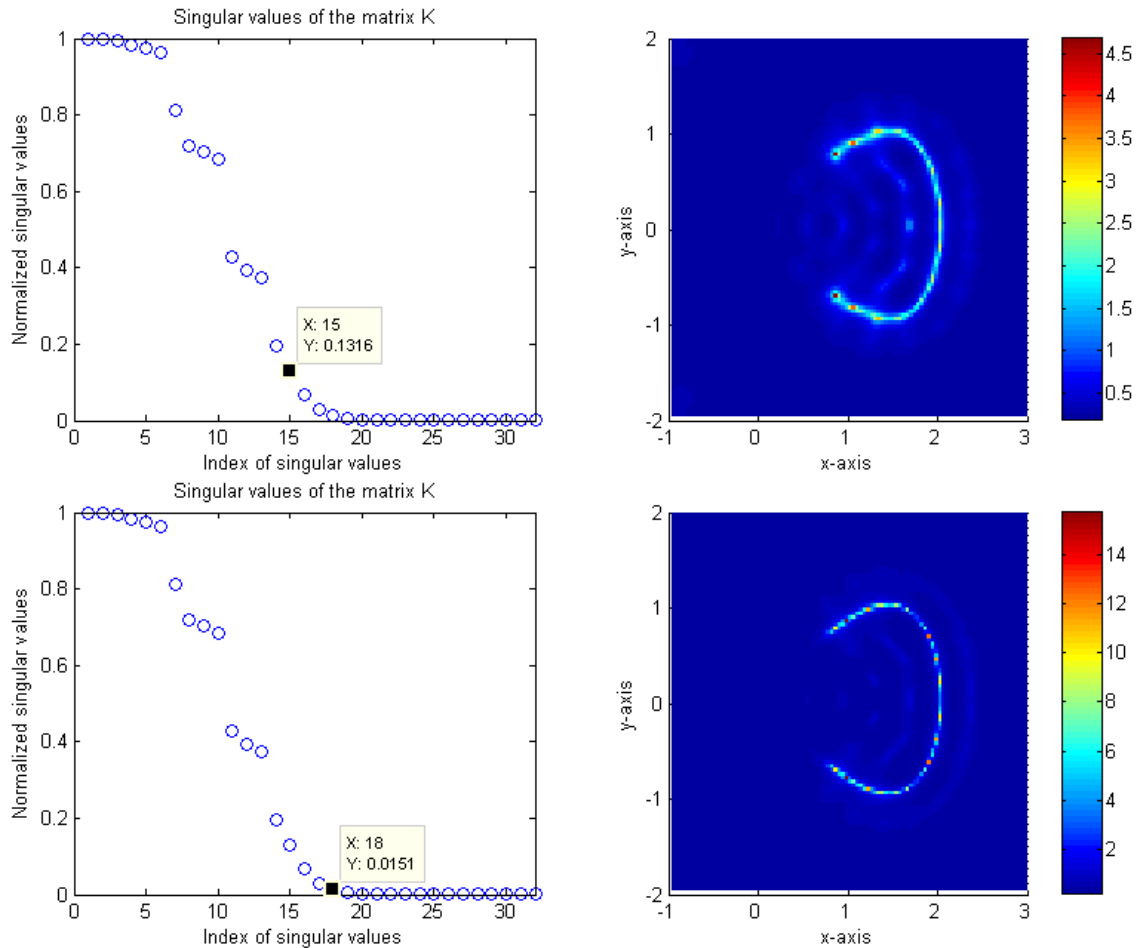


FIG. 4.7 – (Dirichlet boundary condition case) Distributions of normalized singular values of the matrix  $K$  (left) and maps of  $W(z)$  (right), for  $N = 32$  incidences and a 0.7 wavelength when the crack is  $\Gamma_3$ . For imaging, one has adopted a 0.1 threshold (top) and a 0.01 threshold (bottom).

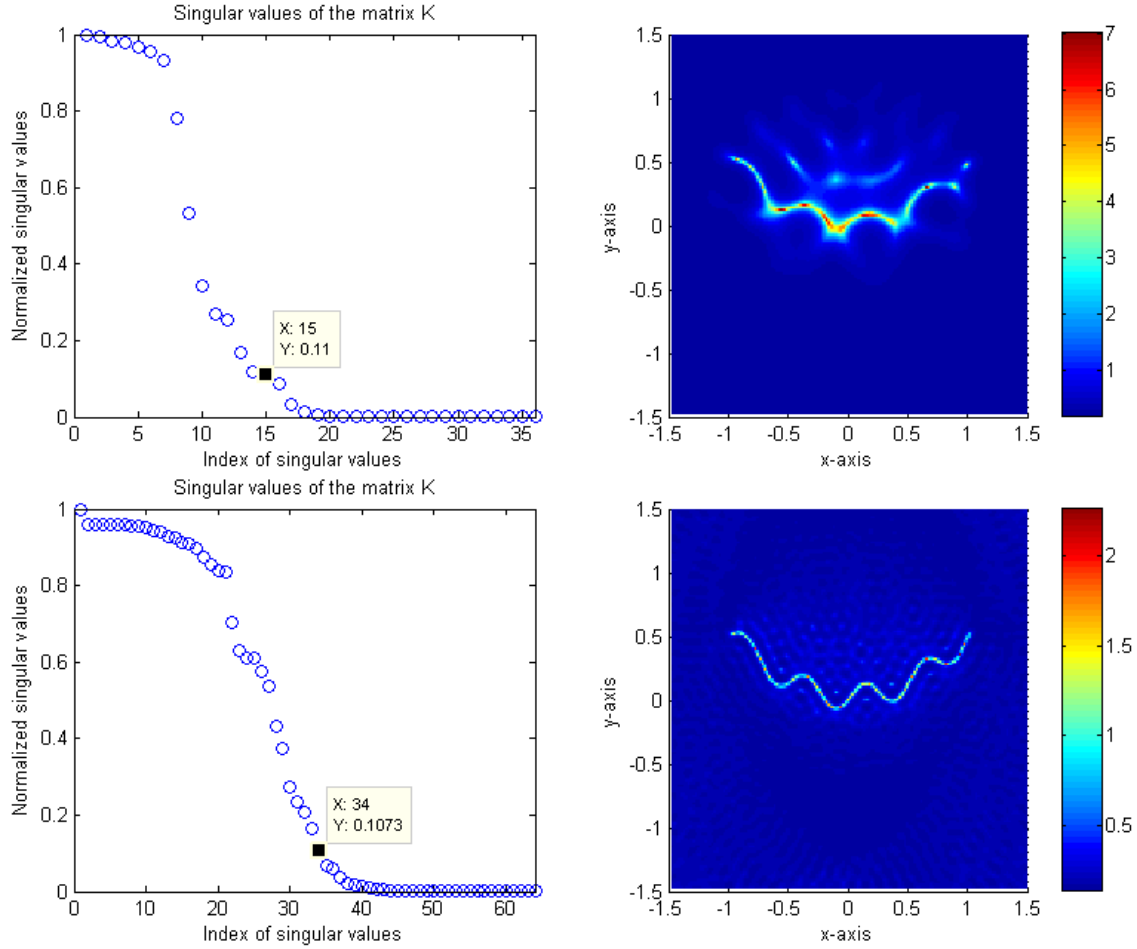


FIG. 4.8 – (Dirichlet boundary condition case) Distributions of normalized singular values of matrix  $K$  (left column) and maps of  $W(z)$ ,  $z \in \tilde{\Omega}$ , (right column), for  $N = 36$  incidences and  $\lambda = 0.6$  wavelength (top line), for  $N = 64$  and  $\lambda = 0.2$  (bottom line), when the crack is  $\Gamma_4$ .

Now, we apply the algorithm to an oscillating crack. The configuration is the same as previously save the search domain  $\tilde{\Omega} = [-1.5, 1.5] \times [-1.5, 1.5]$ . Two  $\Gamma_j$  are chosen for illustration (see Fig. 2.9 in subsection 2.5.2 of chapter 2) :

$$\begin{aligned}\Gamma_4 &= \{(z, 0.5z^2 + 0.1 \sin(4\pi(z+1))) : z \in (-1, 1)\} \\ \Gamma_5 &= \{(z, 0.5z^2 + 0.05 \sin(20\pi(z+1)) - 0.01 \cos(15\pi z)) : z \in (-1, 1)\}.\end{aligned}$$

Let us consider  $\Gamma_4$ . Typical results are in Fig. 4.8 at  $\lambda = 0.6$  and  $\lambda = 0.2$ . Similarly with the images in Fig. 2.10, the imaging is rather coarse at the low wavelength, better at the high one. The threshold looks convenient, whilst a high value of  $N$  is to be taken as expected.

For the case of a more oscillating crack  $\Gamma_5$ , the results are coarse, as is seen in Fig. 4.9, but they can be considered as an initial guess close to the true one of a Newton-type iteration method in line with [52].

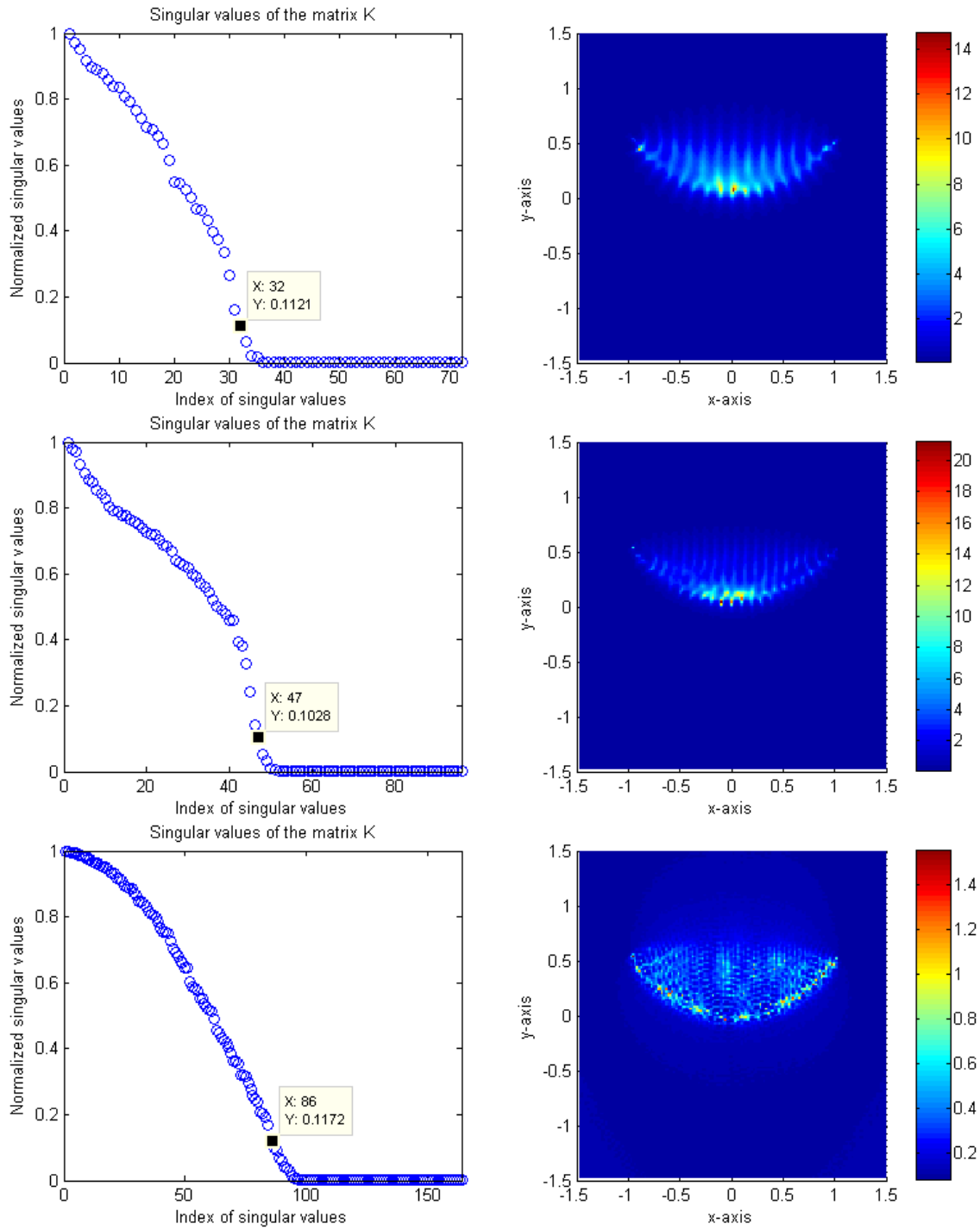


FIG. 4.9 – (Dirichlet boundary condition case) The distribution of normalized singular values of the matrix  $K$  (Left column) and maps of  $W(z)$  when  $a = 1$  (right column), for all points  $z \in \tilde{\Omega}$  for  $N = 72$  incidences and a  $0.3$  wavelength (top row), for  $N = 96$  incidences and a  $0.2$  wavelength (center row) and for  $N = 160$  incidences and a  $0.1$  wavelength (bottom row) when the crack is  $\Gamma_5$ .

Now, let us assume that some noise is added to the measured data, i.e., for every  $x \in \mathbb{R}^2$ ,

$$u_{\text{noise}}(x) = \{1 + \xi \times (\text{rnd}_1(-1, 1) + i\text{rnd}_2(-1, 1))\} u(x)$$

where  $\text{rnd}_1(-1, 1)$  and  $\text{rnd}_2(-1, 1)$  are an arbitrary real values between  $-1$  and  $1$ .

Let us consider an image of  $\Gamma_2$  with noise  $\xi = 3 \times 10^{-1}$ . Typical results are in Fig. 4.10 at  $\lambda = 0.4$ . Similarly with the Figs. 2.15 and 2.16 in subsection 2.5.2 of chapter 2, although the distribution of log-scaled singular values is significantly different and some blurring appears in the image, one can easily find proper singular values and obtain accurate image via normalizing method. For the case of  $\Gamma_3$  with noise  $\xi = 10^{-1}$ , one can verify a similar phenomenon, refer to Fig. 4.11.

#### 4.4.2 Extension to multiple cracks

Both the mathematical configuration and the numerical analysis could be extended in rather straightforward fashion to the case of multiple inclusions. One will not present the derivation herein and simply provide examples of imaging via the MUSIC-type algorithm in several figures.

Notice that the elements  $u_\infty(\theta_j, \theta_l)$  for  $j, l = 1, 2, \dots, N$  of dataset  $K$  are generated from the Nyström method applied to the multiple cracks. For reader's convenience, we stated this method in appendix since we have been unable to find such a derivation.

Let us consider the following cracks

$$\begin{aligned}\Gamma_a &= \sigma_1 \cup \sigma_2 \\ \Gamma_b &= \sigma_3 \cup \sigma_4\end{aligned}$$

where

$$\begin{aligned}\sigma_1 &= \{(s, -0.5(s - 0.2)^2 + 0.5) : s \in (-0.7, 0.3)\} \\ \sigma_2 &= \{(s, (s - 0.2)^3 + (s - 0.2)^2) - 0.4 : s \in (-0.3, 0.7)\} \\ \sigma_3 &= \left\{ \left( s - 0.5, \frac{1}{2} \cos \frac{s\pi}{2} + \frac{1}{5} \sin \frac{s\pi}{2} - \frac{1}{10} \cos \frac{3s\pi}{2} \right) : s \in [-1, 1] \right\} \\ \sigma_4 &= \left\{ \left( 2 \sin \frac{s}{2} + 0.5, \sin s \right) : s \in \left[ \frac{\pi}{4}, \frac{7\pi}{4} \right] \right\}.\end{aligned}$$

Notice that  $\sigma_1$  and  $\sigma_2$  are introduced in chapter 2 (see formula (2.33) and (2.34)) and  $\Gamma_3$  and  $\Gamma_4$  are moved copies of  $\Gamma_2$  and  $\Gamma_3$ , respectively.

Let us consider the imaging of  $\Gamma_a$ ,  $K$  being collected for  $N = 28$  and  $N = 48$ , and the wavelengths of operation  $\lambda = 0.5$  and  $\lambda = 0.3$ , respectively. Distributions of the normalized singular values of  $K$  and maps of  $W(z)$  are displayed in figure 4.12. Opposite to the penetrable inclusion case, refer to Fig. 2.26 in chapter 2, the discrimination is still obvious and desired images appear.

**Remark 4.3** When we choose as the number of incident directions,  $N = 24$ , and as the wavelength of operation  $\lambda = 0.8$ , some isolated points with peaks of large magnitude appears between two cracks. Notice that in the several examples in the single-crack case,

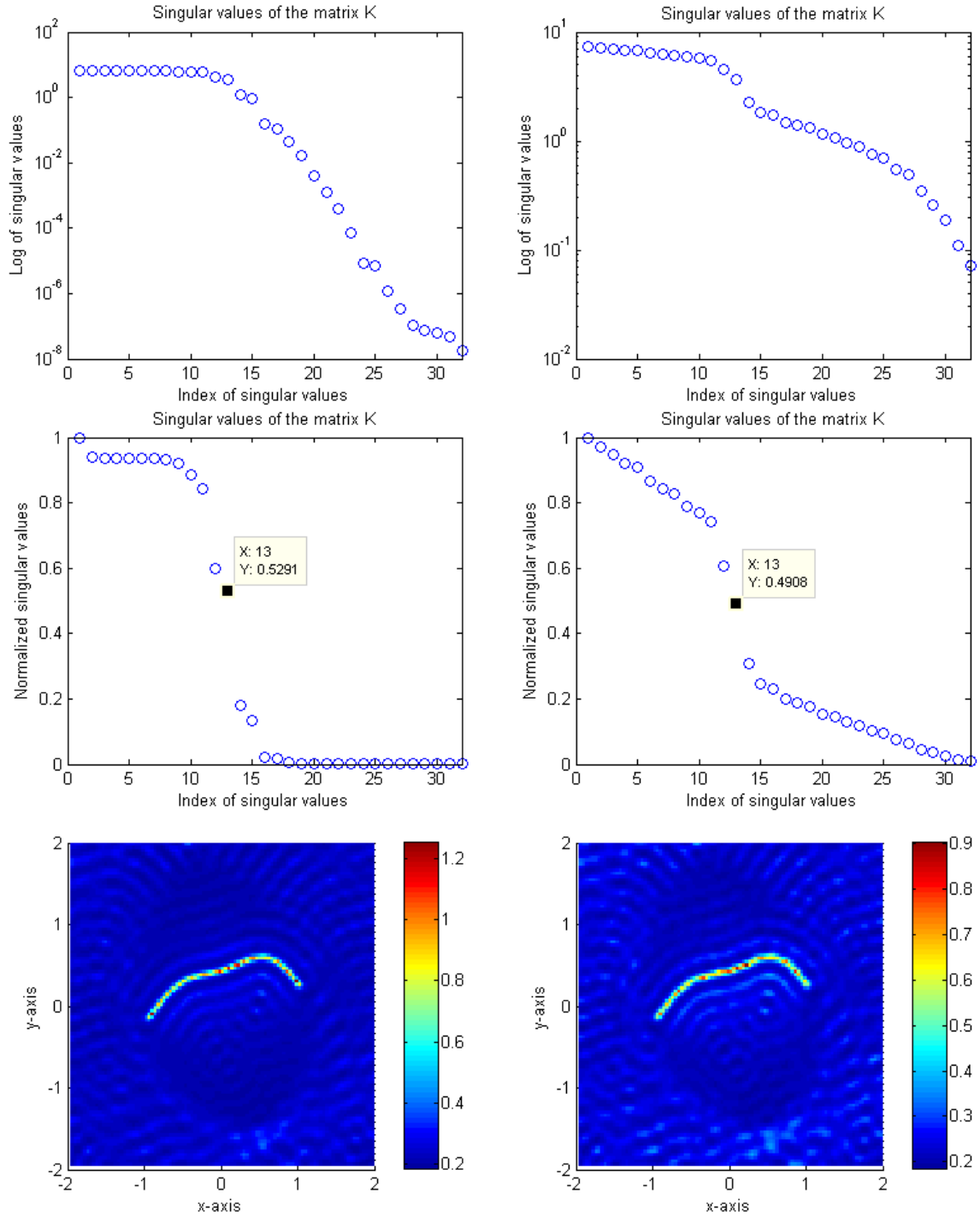


FIG. 4.10 – The distribution of log-scaled (top row) and normalized (center row) singular values of the matrix  $K$  and maps of  $W(z)$  (bottom row) without noise (left column) and some noise  $\xi = 3 \times 10^{-1}$  for all points  $z \in \tilde{\Omega}$  for  $N = 32$  incidences and a 0.4 wave length when the thin inclusion is  $\Gamma_2$ .

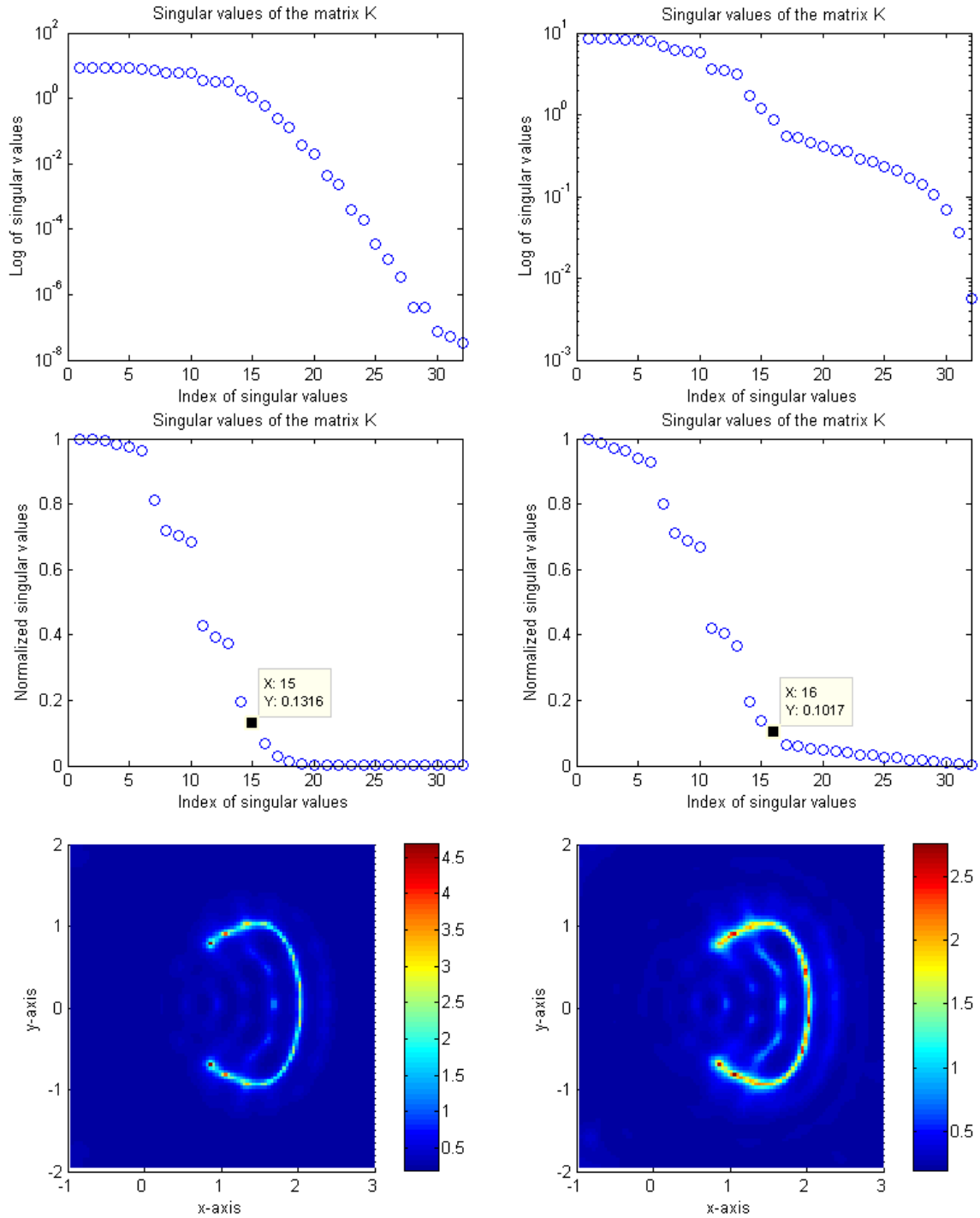


FIG. 4.11 – The distribution of log-scaled (top row) and normalized (center row) singular values of the matrix  $K$  and maps of  $W(z)$  (bottom row) without noise (left column) and some noise  $\xi = 10^{-1}$  for all points  $z \in \tilde{\Omega}$  for  $N = 32$  incidences and a 0.7 wave length when the thin inclusion is  $\Gamma_3$ .

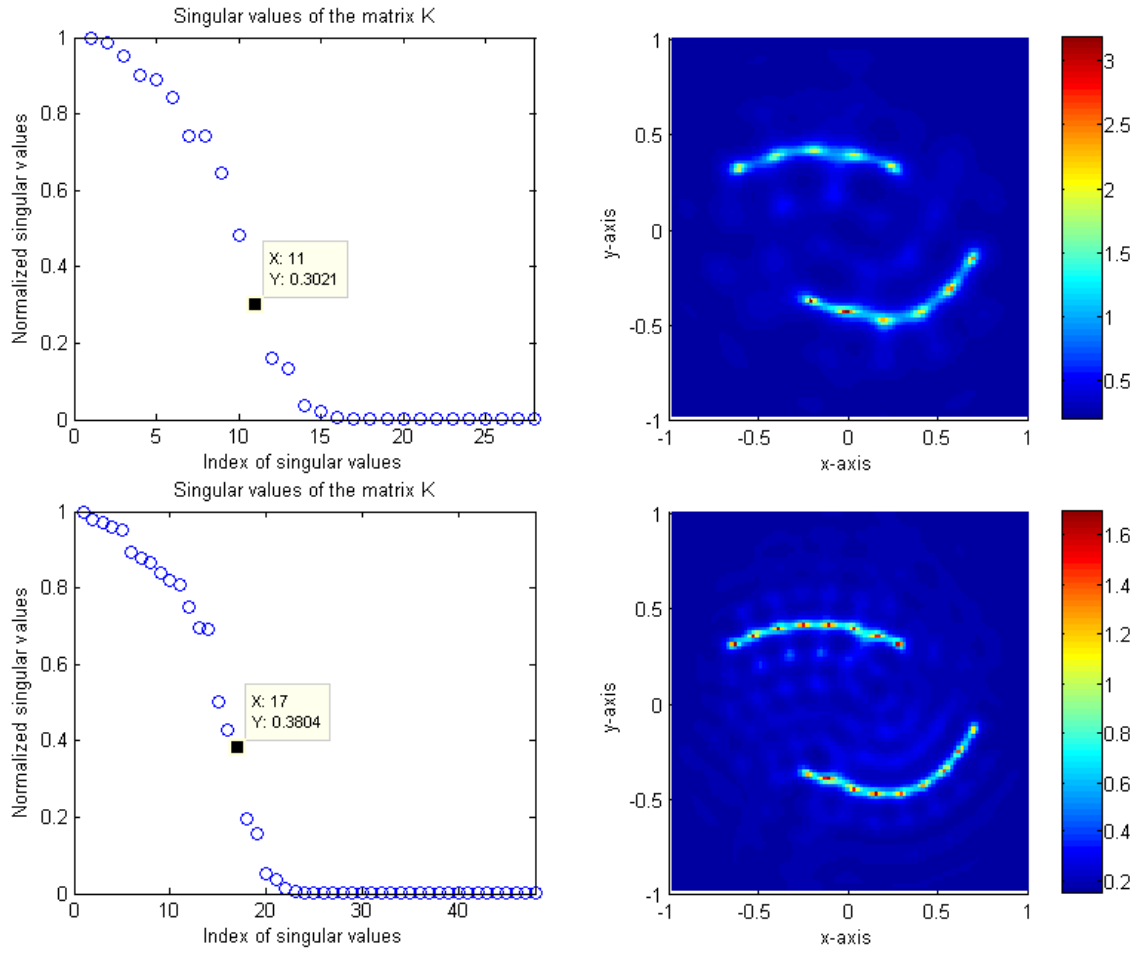


FIG. 4.12 – (Dirichlet boundary condition case) Distributions of normalized singular values of the matrix  $K$  (left column) and maps of  $W(z)$  (right column), for  $N = 28$  incidences and a 0.5 wavelength (top line), for  $N = 48$  incidences and a 0.3 wavelength (bottom line) when the crack is  $\Gamma_a$ .

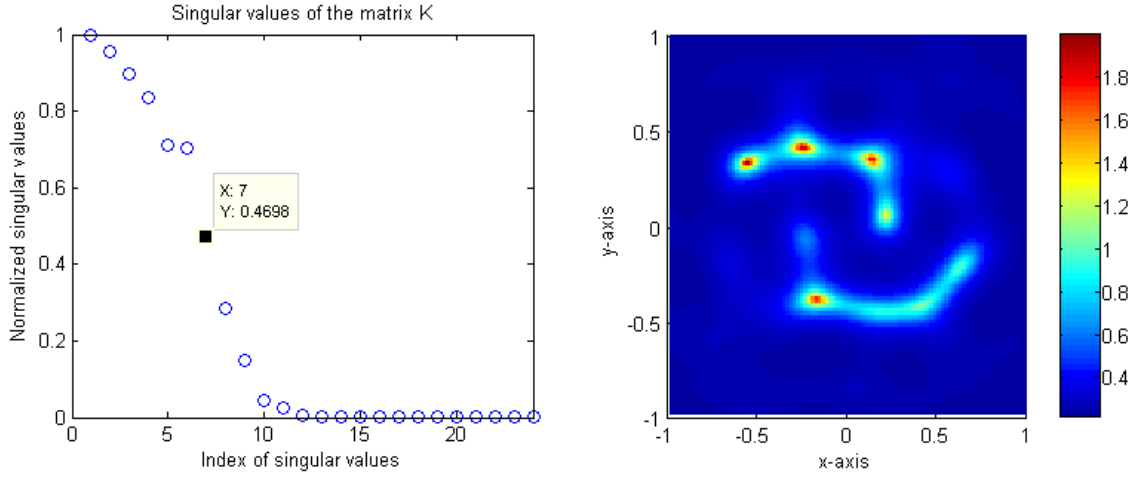


FIG. 4.13 – (Dirichlet boundary condition case) Distribution of normalized singular values of the MSR matrix  $K$  (left column) and map of  $W(z)$ , for  $N = 28$  incidences and a  $\lambda = 0.8$  wavelength when the crack is  $\Gamma_a$ .

some isolated points disappear when we adopt a large number of illuminations or a 0.1 (or 0.01) threshold but via the previous methods, the isolated point in Fig. 4.13 does not disappear. In order to eliminate this isolated point, one must apply more larger wavelength. In this example, this point still appeared when the wavelength of operation is smaller than 0.6 and disappeared when the wavelength of operation is larger than 0.5, i.e., we obtained proper imaging results.

When the shape of cracks is getting complex, the discrimination is still obvious but unexpected isolated points appear. As an example, let us image  $\Gamma_b$  (refer to Fig. 4.14) at  $\lambda = 0.5$  and  $\lambda = 0.3$ .

Similarly with the imaging of  $\Gamma_3$  (see Fig. 4.7), we can eliminate these isolated points, i.e., proper images can be achieved, by adopting a 0.1 or 0.01 threshold (see Fig. 4.15).

Now, we end up this section with the following remark.

**Remark 4.4** Similarly with the single-crack case, one can produce images from far-field data computed by the solution algorithm presented in [60, Chapter 4], refer to Fig. 4.16. By comparing bottom line of Fig. 4.12 and top line of Fig. 4.16, and bottom line of Fig. 4.14 and same line of Fig. 4.16, such images look very much alike those built up from the Nyström method applied to the multiple cracks.

## 4.5 Numerical examples : Neumann boundary condition case (Figs. 4.17 to 4.25)

In this section, we present some imaging results for the Neumann boundary condition. The configuration is the same as previously and we use a set of fixed directions  $\nu_l$  as

$$\nu_l = \left( \cos \frac{2\pi(l-1)}{L}, \sin \frac{2\pi(l-1)}{L} \right) \quad \text{for } l = 1, 2, \dots, L.$$



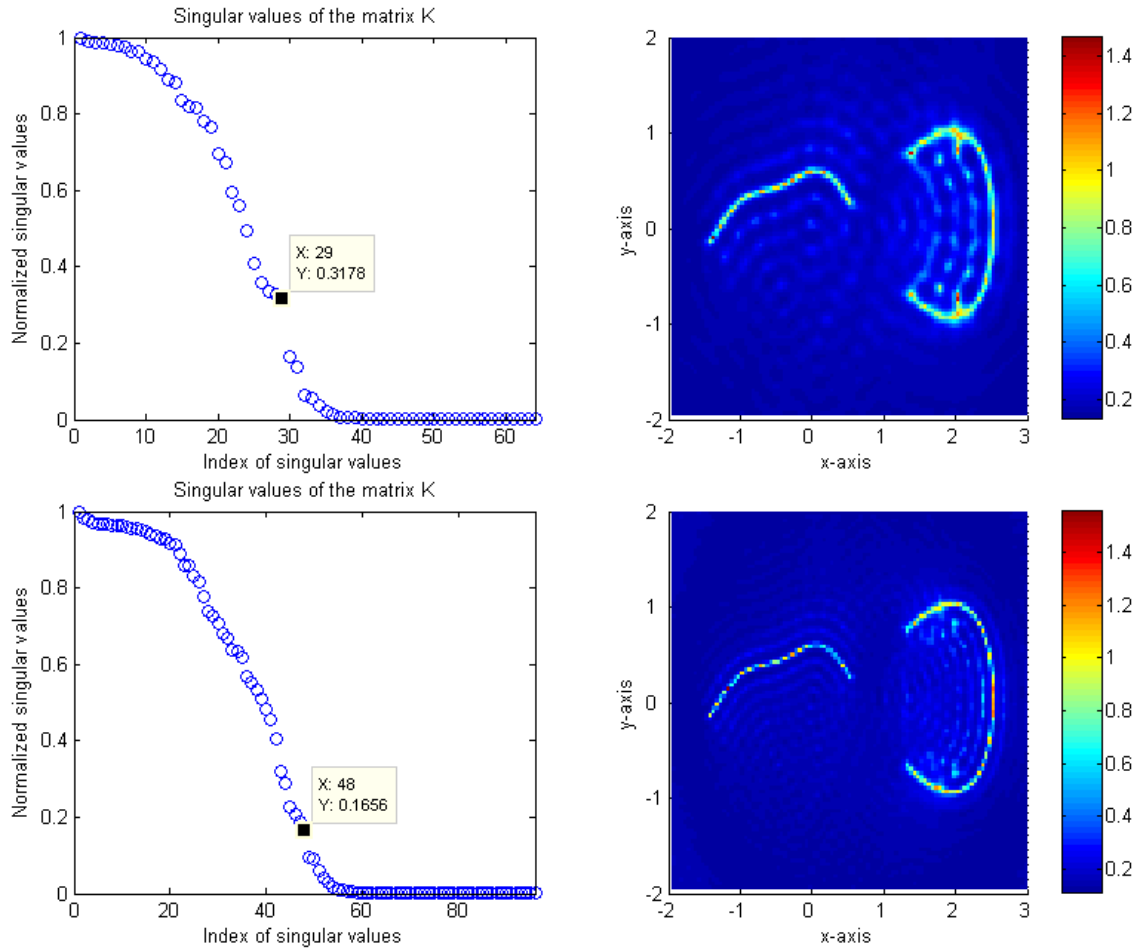


FIG. 4.14 – (Dirichlet boundary condition case) Distributions of normalized singular values of the matrix  $K$  (left column) and maps of  $W(z)$  (right column), for  $N = 64$  incidences and a 0.5 wavelength (top line), for  $N = 96$  incidences and a 0.3 wavelength (bottom line) when the crack is  $\Gamma_b$ .

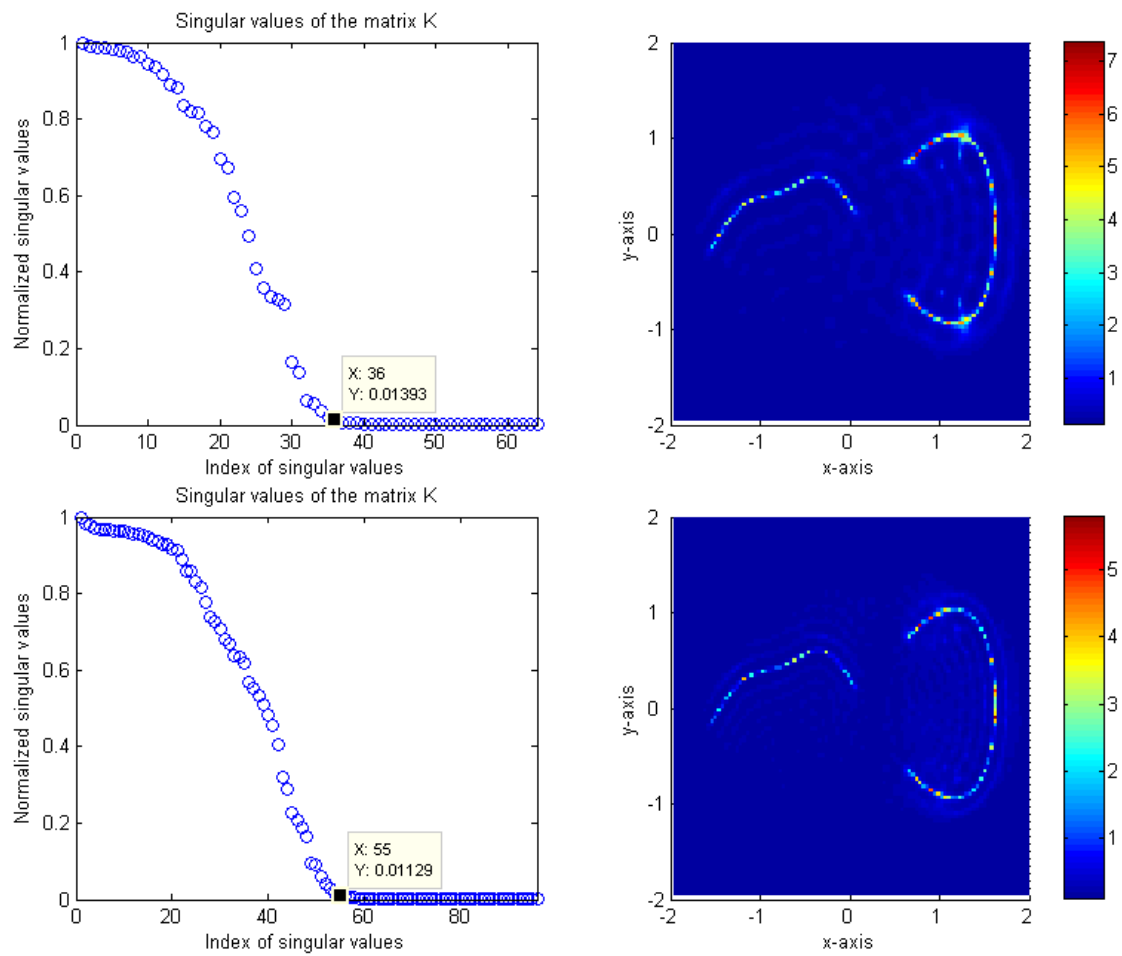


FIG. 4.15 – (Dirichlet boundary condition case) Same as Fig. 4.14 with 0.01 threshold.

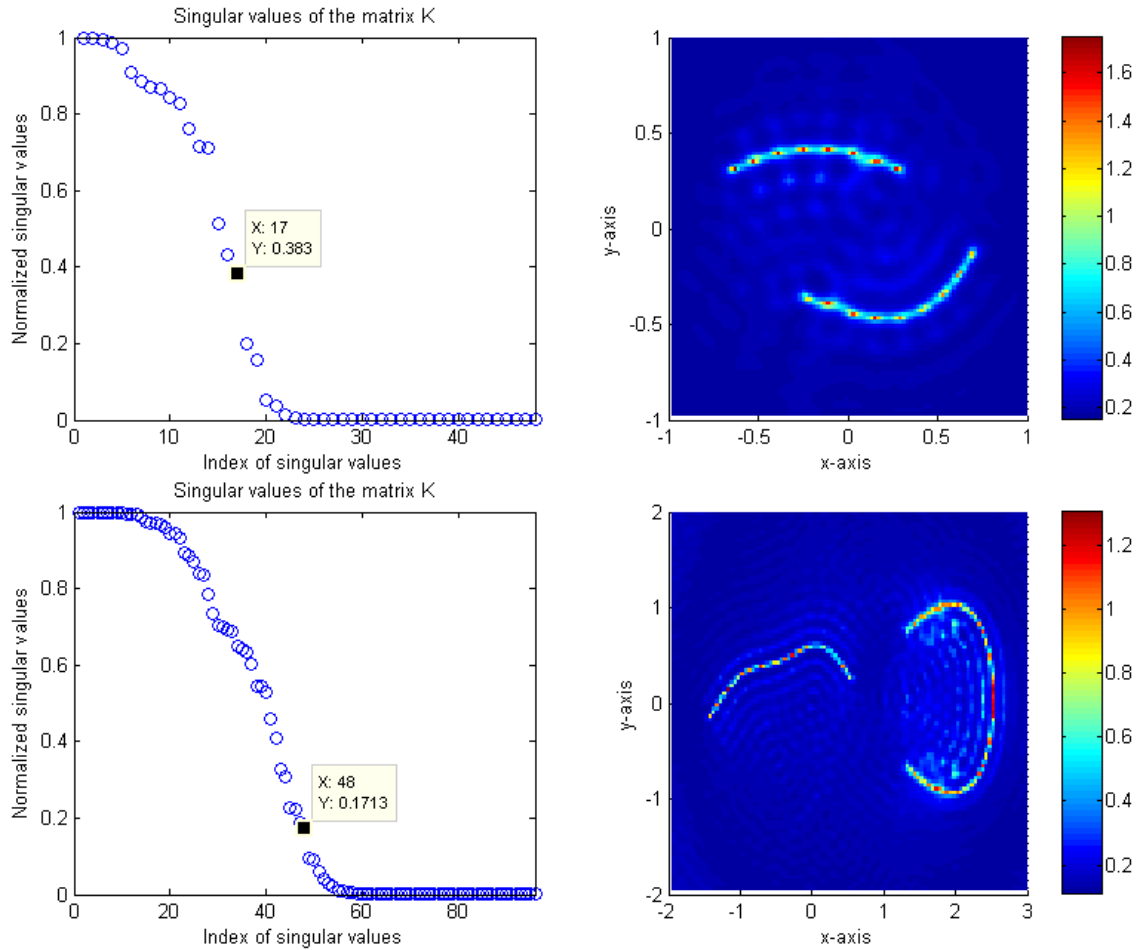


FIG. 4.16 – (Dirichlet boundary condition case) Distributions of normalized singular values of the matrix  $K$  (left column) and maps of  $W(z)$  (right column), for  $N = 48$  incidences and a 0.3 wavelength (top line) when the crack is  $\Gamma_a$ , for  $N = 96$  incidences and a 0.3 wavelength (bottom line) when the crack is  $\Gamma_b$ . Dataset generated by the method introduced in [60] (Compare to Fig. 4.12 and 4.14).

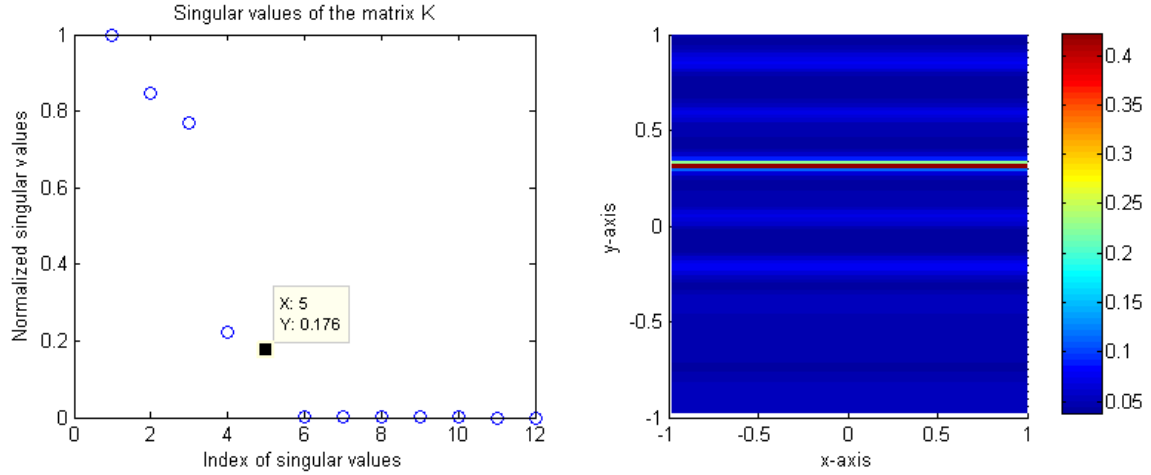


FIG. 4.17 – (Neumann boundary condition case) Distribution of normalized singular values of the matrix  $K$  (left column) and map of  $W(z)$  (right column), for  $N = 12$  incidences and a 0.5 wavelength when the crack is  $\Gamma_1$ .

Throughout this section, we use  $L = 16$  and  $32$  for the imaging of  $\Gamma_1$  and  $\Gamma_2$  and of  $\Gamma_3$ , respectively. Notice that this blindness of normal direction on  $\Gamma$  causes the slowness of imaging performance, i.e., large computational costs will be needed (approximately, 3 minutes required to obtain top line result of Fig. 4.18 and 30 minutes to obtain result of Fig. 4.25. All of images were obtained on a personal computer with a 1.73 GHz dual-core pentium processor).

Now, we start up this section with the following remarks.

**Remark 4.5** *Similarly with the Dirichlet boundary condition case, refer to remark 4.1, we observe that when the number  $N$  is not large enough, the image is coarse. For example, when we choose  $N = 12$  and as wavelength of operation,  $\lambda = 0.5$ , we can observe that the first five singular values are well distinguished from the seven. However, when we use five singular values to discriminate the noise subspace from the signal subspace, poor results appear. When we increase the number  $N$  to  $N = 16$  while keeping the same 0.5 wavelength, this phenomenon is but vanishing, refer to Fig. 4.18.*

For the imaging of  $\Gamma_1$ ,  $K$  is collected for  $N = 16$  and  $N = 32$ , and the wavelengths of operation  $\lambda = 0.5$  and  $\lambda = 0.2$ , respectively. Distributions of the normalized singular values of  $K$  and maps of  $W(z)$  are displayed in Fig. 4.18.

In contrast with the Dirichlet boundary condition case, see Fig. 4.5, when the crack is not anymore a straight line, a blurred image appears, refer to figure 4.19. In order to improve it, one can use a larger wavelength and a 0.01 threshold. This can be verified in Fig. 4.20.

Let us consider the imaging of  $\Gamma_3$ . Typical results are in Fig. 4.21 and 4.22 at  $\lambda = 0.7$  and  $\lambda = 0.3$ . Similarly with the previous result, imaging is rather coarse for the 0.1 threshold, better for the 0.01 threshold.

**Remark 4.6** *Similarly with the Dirichlet boundary condition case, one can generate images from far-field data computed by the solution algorithm presented in [60, Chapter*

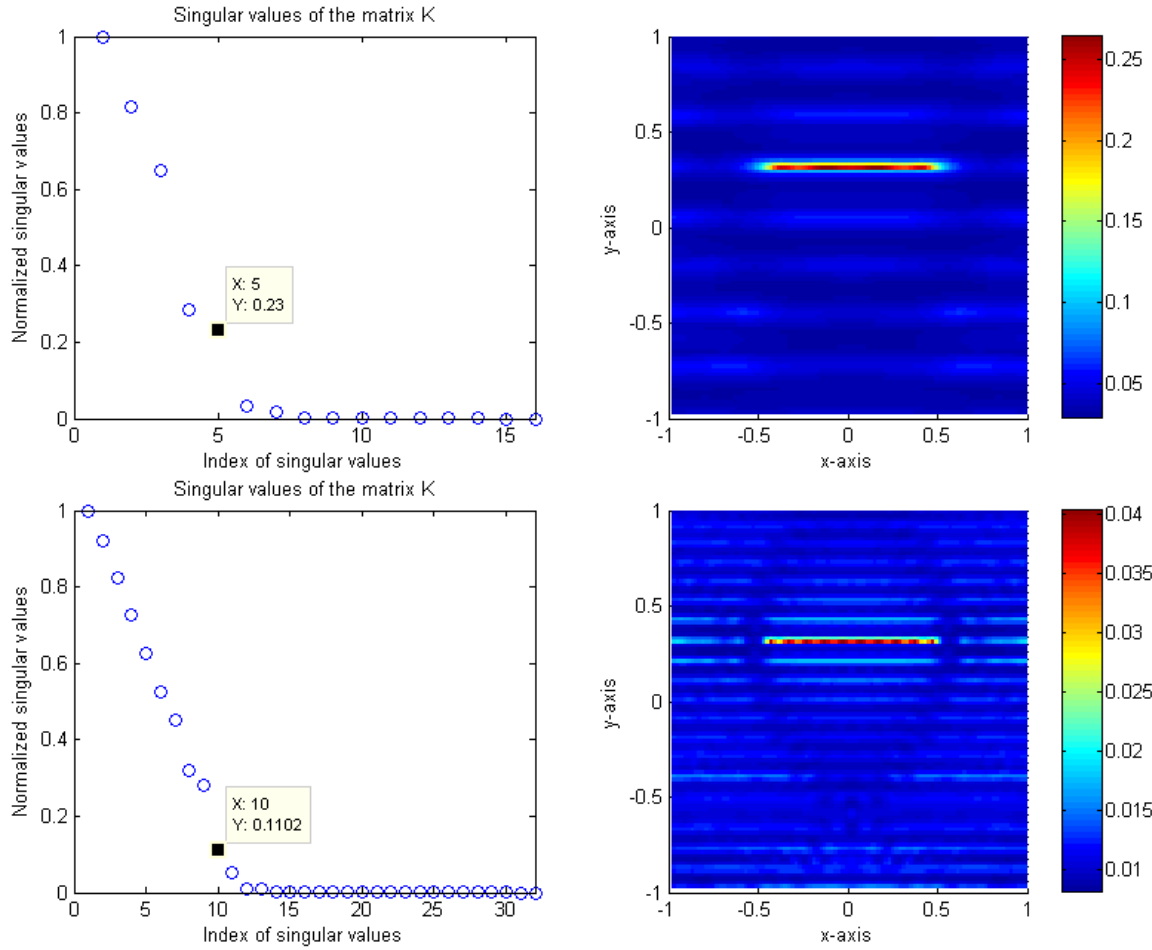


FIG. 4.18 – (Neumann boundary condition case) Distributions of normalized singular values of the matrix  $K$  (left column) and maps of  $W(z)$  (right column), for  $N = 16$  incidences and a 0.5 wavelength (top line), for  $N = 32$  incidences and a 0.2 wavelength (bottom line) when the crack is  $\Gamma_1$ .

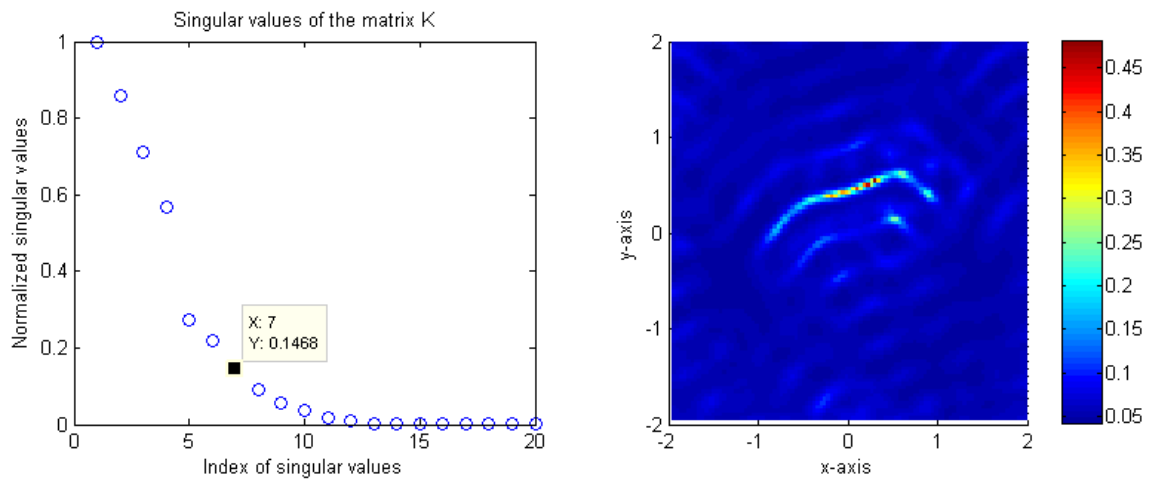


FIG. 4.19 – (Neumann boundary condition case) Distribution of normalized singular values of the matrix  $K$  (left column) and map of  $W(z)$  (right column), for  $N = 20$  incidences and a 0.8 wavelength when the crack is  $\Gamma_2$ .

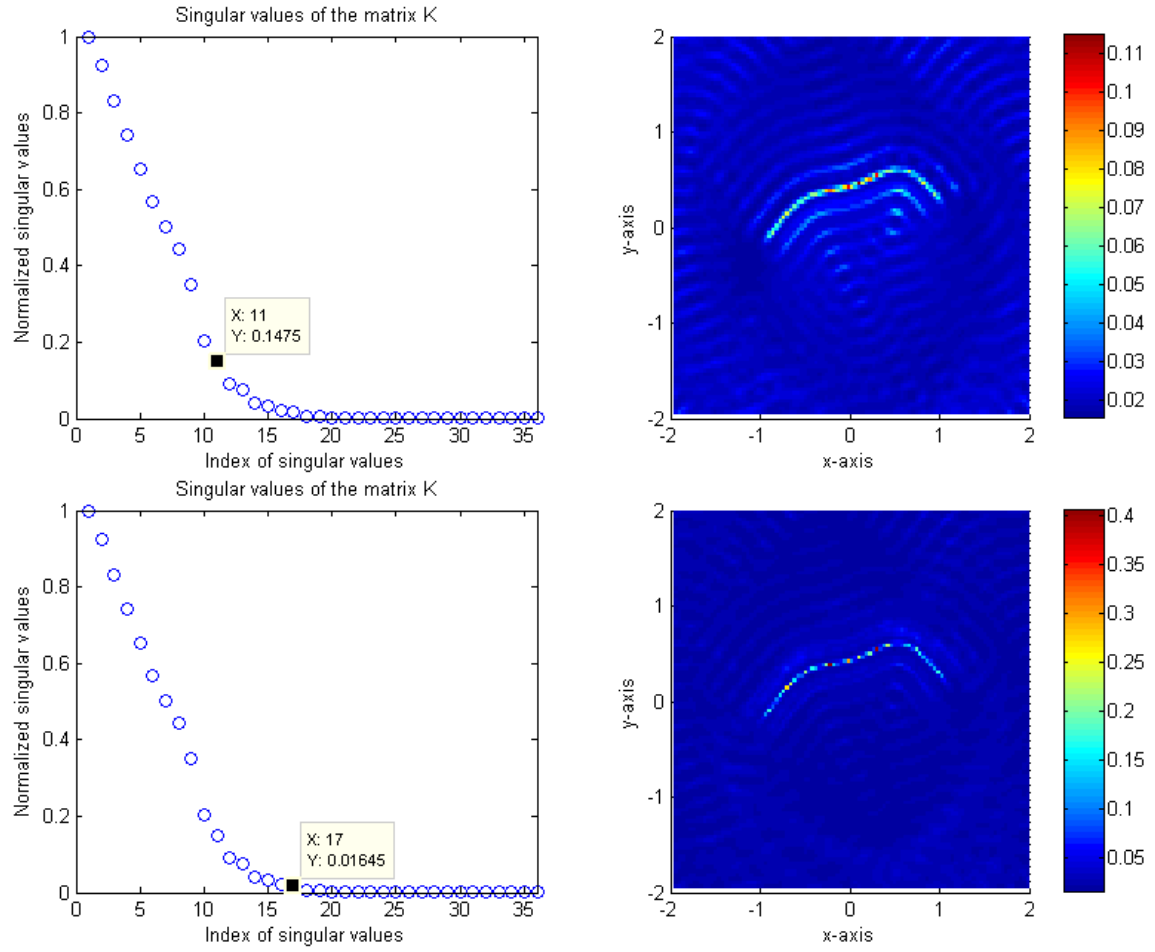


FIG. 4.20 – (Neumann boundary condition case) Distributions of normalized singular values of the matrix  $K$  (left column) and maps of  $W(z)$  (right column), for  $N = 36$  incidences and a  $0.4$  wavelength when the crack is  $\Gamma_2$ .  $0.1$  (top) and  $0.01$  (bottom) threshold used for imaging.

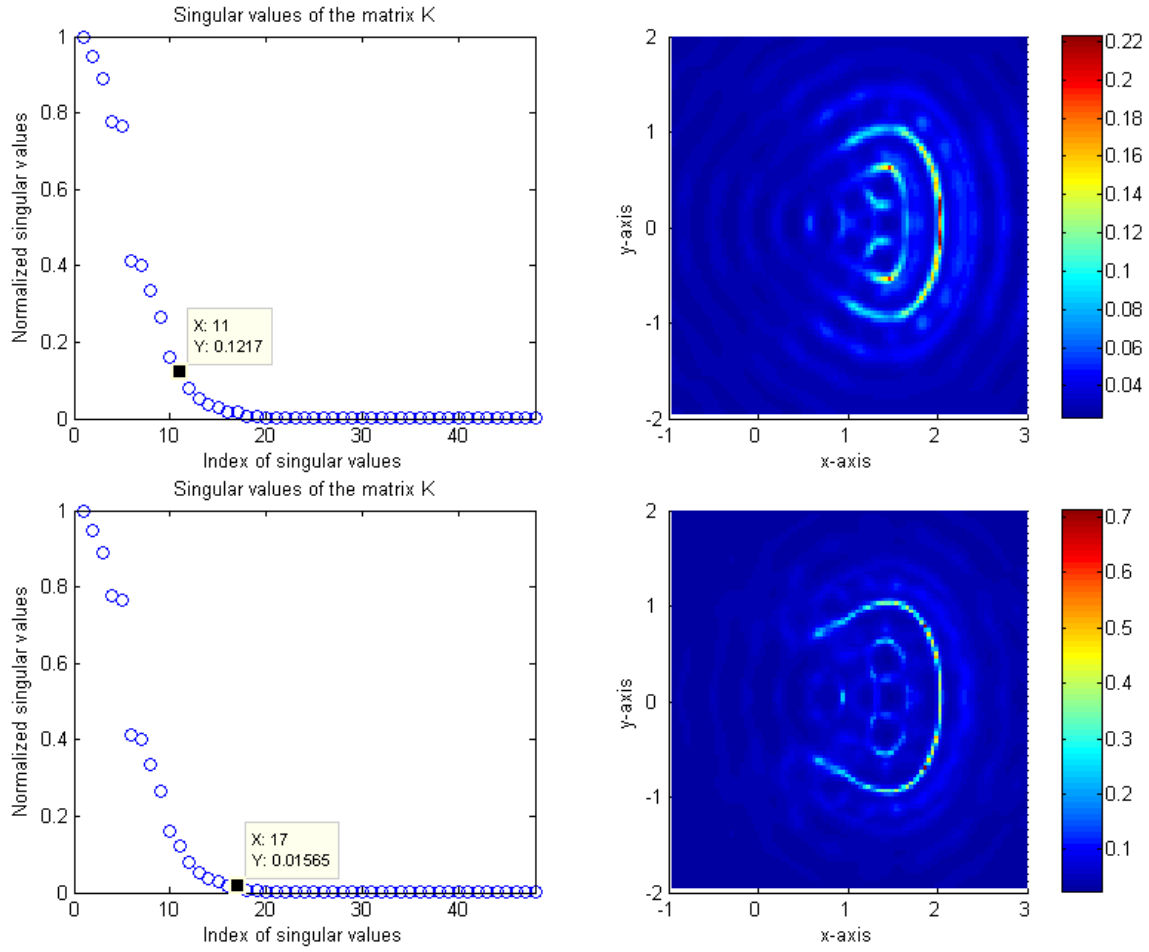


FIG. 4.21 – (Neumann boundary condition case) Distributions of normalized singular values of the matrix  $K$  (left column) and maps of  $W(z)$  (right column), for  $N = 48$  incidences and a 0.7 wavelength when the crack is  $\Gamma_3$ . 0.1 (top) and 0.01 (bottom) threshold used for imaging.

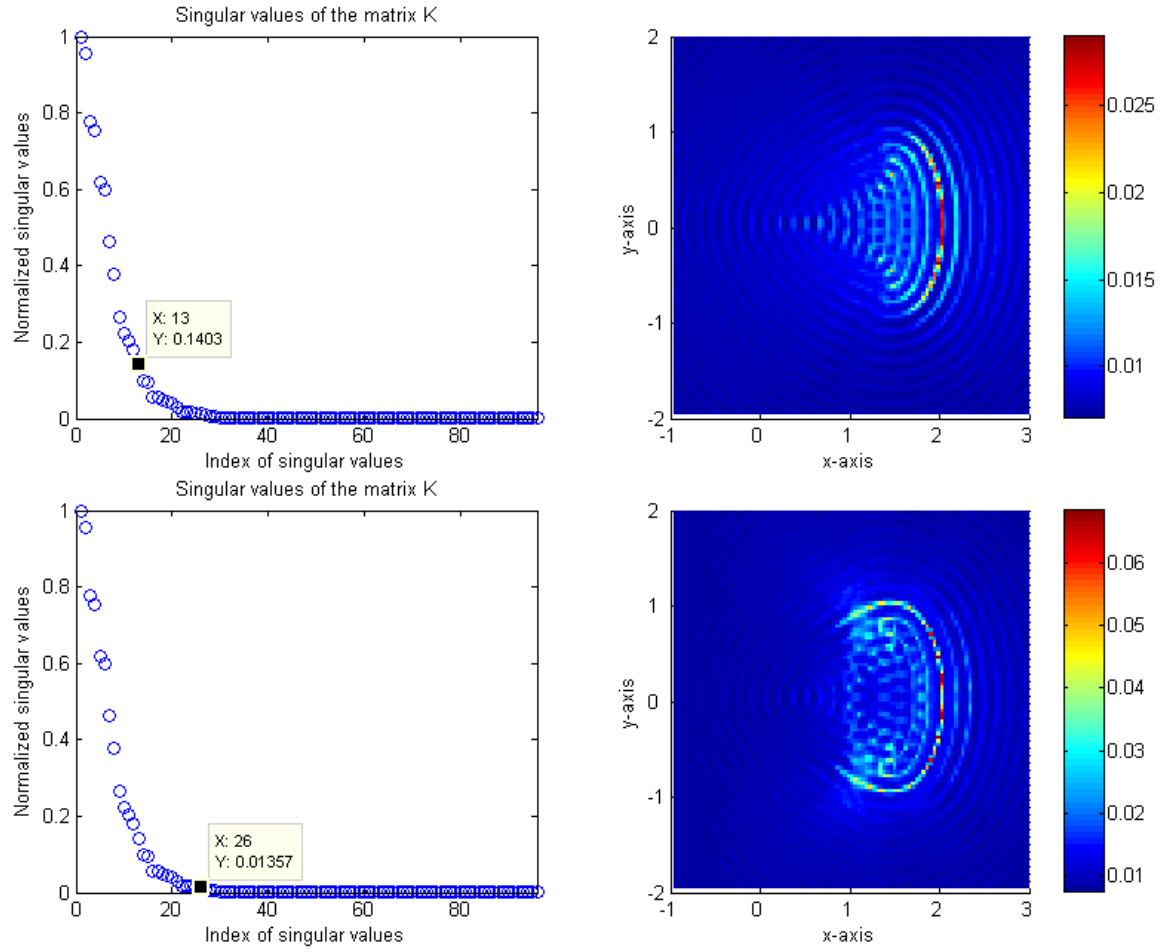


FIG. 4.22 – (Neumann boundary condition case) Distributions of normalized singular values of the matrix  $K$  (left column) and maps of  $W(z)$  (right column), for  $N = 96$  incidences and a  $0.3$  wavelength when the crack is  $\Gamma_3$ .  $0.1$  (top) and  $0.01$  (bottom) threshold used for imaging.



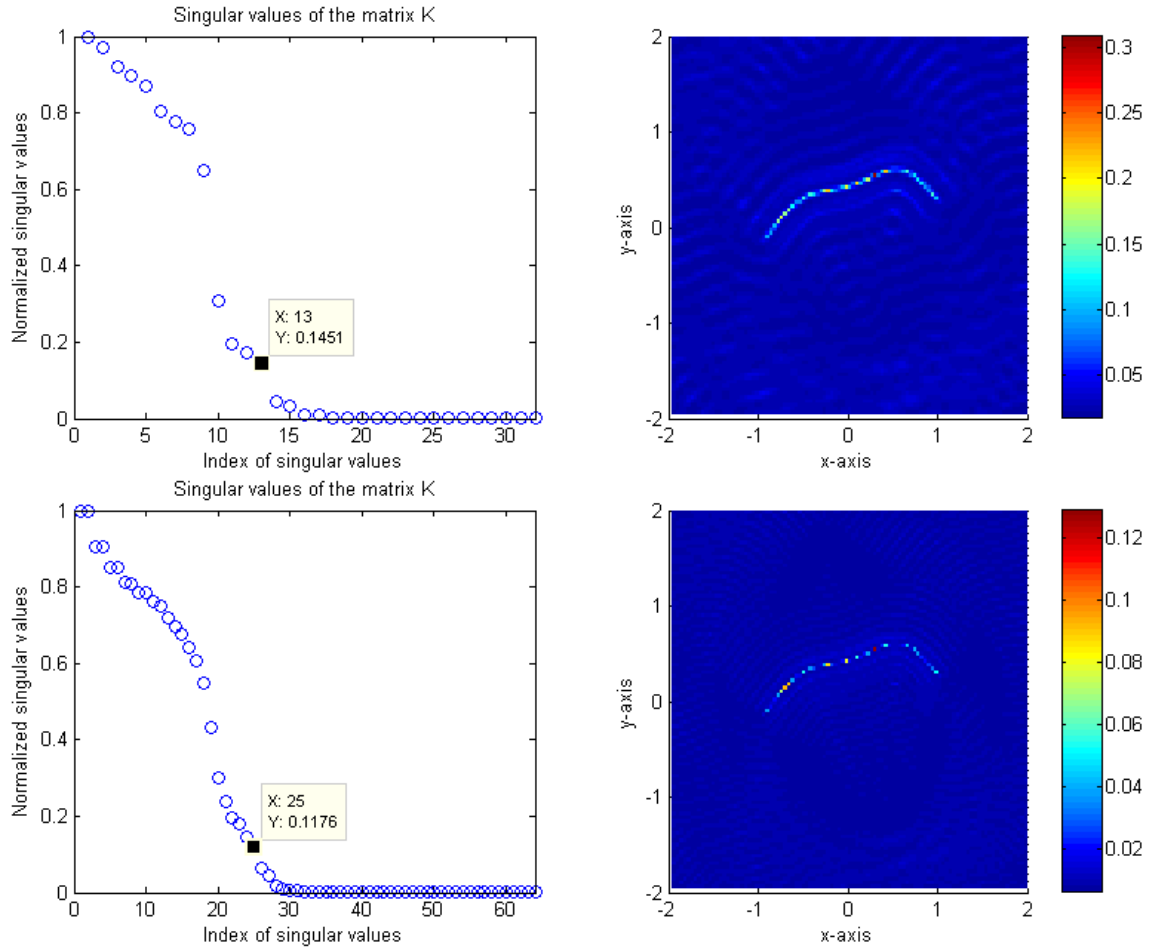


FIG. 4.23 – (Neumann boundary condition case) Distribution of normalized singular values of the MSR matrix  $K$  (left column) and maps of  $W(z)$ ,  $z \in \tilde{\Omega}$  (right column), for  $N = 32$  incidences and a  $\lambda = 0.4$  wavelength (top line), for  $N = 64$  incidences and a  $\lambda = 0.2$  wavelength (bottom line) when the crack is  $\Gamma_2$ . Dataset generated by the solution algorithm introduced in [60]. (Compare to Fig. 4.20)

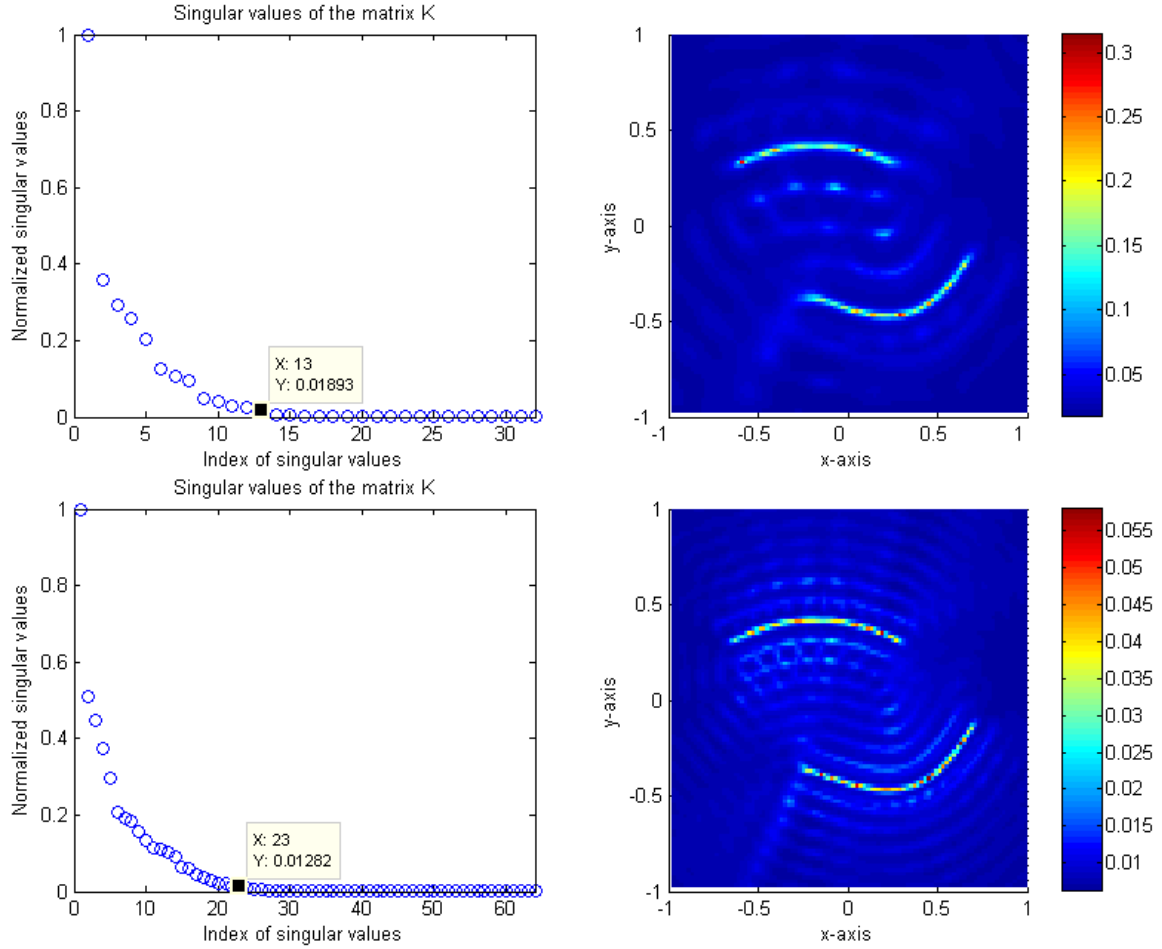


FIG. 4.24 – (Neumann boundary condition case) Distributions of normalized singular values of the matrix  $K$  (left column) and maps of  $W(z)$  (right column), for  $N = 32$  incidences and a 0.4 wavelength (top line), for  $N = 64$  incidences and a 0.2 wavelength (bottom line) when the crack is  $\Gamma_a$ .

3], refer to Fig. 4.23. By comparing Fig. 4.20, such images look very much alike those built up from the Nyström method.

Let us apply the algorithm to the imaging of two (or more) inclusions (skipping all mathematical details). Before stating the results, let us mention that the dataset  $K$  is generated by solving the linear systems introduced in [60, Chapter4] and a 0.01 threshold is adopted for higher resolution. Moreover, we use  $L = 32$  directions for imaging of  $\Gamma_a$  and  $L = 64, 128$  directions for  $\Gamma_b$  respectively.

Results for  $\Gamma_a$  are shown in Fig. 4.24,  $K$  being collected for  $N = 32$  and  $N = 64$ , and for the wavelengths of operation  $\lambda = 0.4$  and  $\lambda = 0.2$ , respectively. As in the permeability contrast case in previous chapter 2, the few copies of the crack which appear in the maps are of much lower amplitude than the true one (see figures 2.19, 2.20 and 2.21 in chapter 2). From the images of  $\Gamma_b$  refer to Fig. 4.25, we can verify this phenomenon.

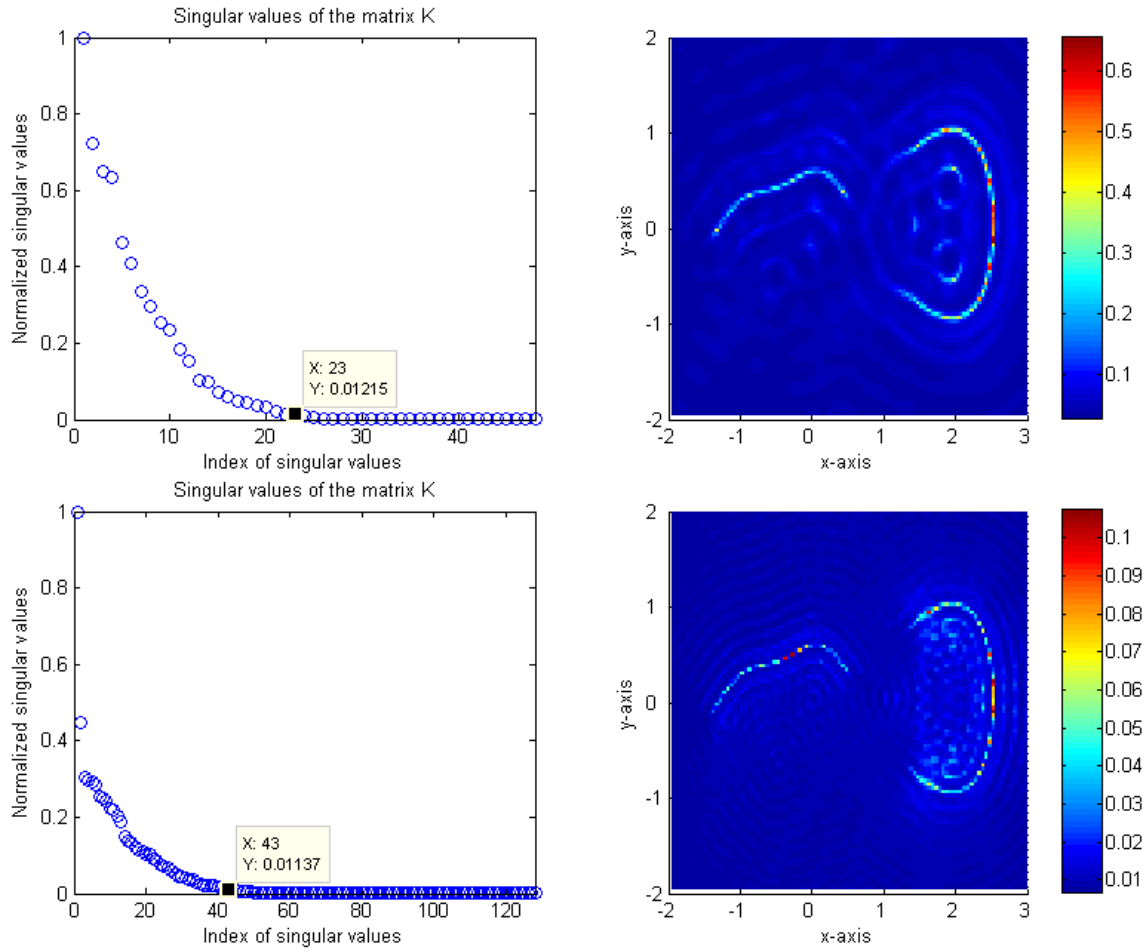


FIG. 4.25 – (Neumann boundary condition case) Distributions of normalized singular values of the matrix  $K$  (left) and maps of  $W(z)$  (right), for  $N = 48$  incidences and a  $0.7$  wavelength (top line) with  $L = 64$  normal directions, for  $N = 128$  incidences and a  $0.3$  wavelength (bottom line) with  $L = 128$  normal directions when the crack is  $\Gamma_b$ .

## 4.6 Conclusion

In this chapter, we have proposed a non-iterative imaging algorithm for impenetrable screens modeled via a Dirichlet or Neumann boundary condition based on a factorization of the MSR matrix. Several numerical results show that this algorithm is fast, stable and efficient. Such non-iterative imaging results could provide initial guesses of a level-set evolution [2] or of a Newton-type algorithm [52].

For effective performance of the imaging of a crack with Neumann boundary condition, the mathematical formulation for the choice of the normal direction on the crack still requires further investigation however.

## 5 Asymptotic Imaging of Perfectly Conducting Cracks

In this chapter, we consider cracks with Dirichlet boundary conditions. We first derive an asymptotic expansion of the boundary perturbations that are due to the presence of a small crack. Based on this formula, we design a non-iterative approach for locating a collection of small cracks. In order to do so, we construct a response matrix from the boundary measurements. The location and the length of the crack are estimated, respectively, from the projection onto the noise space and the first significant singular value of the response matrix. Indeed, the direction of the crack is estimated from the second singular vector. We then consider an extended crack with Dirichlet boundary conditions. We rigorously derive an asymptotic expansion for the boundary perturbations that are due to a shape deformation of the crack. To reconstruct an extended crack from many boundary measurements, we develop two methods for obtaining a good guess. Several numerical experiments show how the proposed techniques for imaging small cracks as well as those for obtaining good initial guesses toward reconstructing an extended crack behave.

### 5.1 Introduction and problem formulations

The purpose of this chapter is to design new efficient methods to detect cracks, linear or nonlinear, inside a conductor from the boundary measurements. We also perform some numerical experiments using the proposed algorithms to test their performance and efficiency.

Let  $\Sigma$  be a crack inside a bounded conductor  $\Omega \subset \mathbb{R}^2$ , which is a  $\mathcal{C}^2$  curve. We assume that the crack is at some distance from  $\partial\Omega$ , i.e., there is a positive constant  $c$  such that

$$\text{dist}(\Sigma, \partial\Omega) \geq c. \quad (5.1)$$

With the crack inside, the relevant boundary value problem is

$$\begin{cases} \Delta u + \omega^2 u = 0 & \text{in } \Omega \setminus \overline{\Sigma}, \\ u = 0 & \text{on } \Sigma, \\ \frac{\partial u}{\partial \nu} = g \in L^2(\partial\Omega) & \text{on } \partial\Omega. \end{cases} \quad (5.2)$$

We will assume that  $\omega^2$  is not an eigenvalue of (5.2) so that the problem is well-posed. The problem we will consider in this chapter is to detect  $\Sigma$  from the boundary measurement  $u|_{\partial\Omega}$  for several Neumann data  $g$ .

We first deal with a linear crack of small size. Suppose that  $\Sigma$  is a line segment (or a collection of them) of length  $2\epsilon$ . We emphasize that in this case, if  $\omega^2$  is not a Neumann eigenvalue of  $-\Delta$  in  $\Omega$ , it follows from [14, Chapter 5] that problem (5.2) has a unique solution for  $\epsilon$  small enough. We derive an asymptotic expansion formula of  $u$  on  $\partial\Omega$  as  $\epsilon$  goes to zero. Based on this formula, we design a non-iterative approach for locating a collection of cracks. Our approach is of MUSIC-type (MUSIC stands for Multiple Signal Classification). We start with constructing a response matrix from the boundary measurements. The singular value decomposition of such response matrix yields an estimate of the location and the size of the cracks. We perform numerical tests

to show the validity of our algorithm. A size estimate of the crack obtained from the first significant singular eigenvalue of the response matrix is in a good match with the actual value. It is shown that the significant singular values can not yield an estimation of the direction of the crack. However, using the second singular vector we can estimate the direction of the crack. For related works on MUSIC-type imaging we refer the reader, for instance, to [70, 32, 56, 9, 13].

In the second part of the chapter, we consider an extended crack with Dirichlet boundary conditions. We first develop and test numerically two different ways of constructing a good initial guess from many boundary measurements. The first method is based on the concept of topological derivative. The second algorithm is to use a standard MUSIC-type projection approach. To do so, we construct a response matrix as in the case of cracks of small size. We then discuss optimization procedures for the purpose of refining the reconstruction and obtaining better image of the crack. To compute the shape derivative of the associated cost functionals, we rigorously derive an asymptotic expansion for the boundary perturbations that are due to a shape deformation of the crack.

For related works on crack identification, we refer the reader to [28, 62, 23, 58, 39, 19, 49, 75, 22, 51, 27] and the references therein.

## 5.2 Preliminary results

Let  $\Sigma = \Sigma_\epsilon$  be a narrow crack inside a bounded conductor  $\Omega \subset \mathbb{R}^2$ . Assume for the sake of simplicity that

$$\Sigma_\epsilon = \left\{ (x, 0) : -\epsilon \leq x \leq \epsilon \right\}.$$

Set  $\varphi^\epsilon$  to be the jump of the normal derivative of  $u$ , the solution to (5.2) on the crack  $\Sigma_\epsilon$ :

$$\varphi^\epsilon := \left. \frac{\partial u}{\partial \nu} \right|_+ - \left. \frac{\partial u}{\partial \nu} \right|_- \quad \text{on } \Sigma_\epsilon. \quad (5.3)$$

Here the subscripts  $+$  and  $-$  indicate the limits from above and below, respectively.

Suppose that  $\omega^2$  is not a Neumann eigenvalue on  $\Omega$  and let  $U$  be the background solution, that is, the solution to

$$\begin{cases} \Delta U + \omega^2 U = 0 & \text{in } \Omega, \\ \frac{\partial U}{\partial \nu} = g & \text{on } \partial\Omega. \end{cases} \quad (5.4)$$

Let  $N_\Omega^\omega(x, z)$ , for  $x, z \in \Omega$ , be the Neumann function for  $\Omega$ , namely, the solution to

$$\begin{cases} (\Delta_x + \omega^2) N_\Omega^\omega(x, z) = -\delta_z(x) & \text{in } \Omega, \\ \frac{\partial N_\Omega^\omega}{\partial \nu_x}(x, z) = 0 & \text{for } x \in \partial\Omega. \end{cases} \quad (5.5)$$

By Green's formula, one can easily see that

$$u(x) - U(x) = \int_{\Sigma_\epsilon} N_\Omega^\omega(x, y) \varphi^\epsilon(y) dy, \quad x \in \Omega, \quad (5.6)$$

where  $\varphi^\epsilon$  defined by (5.3). In particular, the following integral equation holds :

$$\mathcal{A}_\epsilon^\omega[\varphi^\epsilon](x) := \int_{\Sigma_\epsilon} N_\Omega^\omega(x, y) \varphi^\epsilon(y) dy = -U(x), \quad (x, 0) \in \Sigma_\epsilon. \quad (5.7)$$

Note that we write  $N_\Omega^\omega(x, y)$  for  $N_\Omega^\omega((x, 0), (y, 0))$  and  $\varphi^\epsilon(y)$  for  $\varphi^\epsilon(y, 0)$  for the sake of simplicity.

Endowed with the norm

$$\|\varphi\|_{\mathcal{X}^\epsilon} = \left( \int_{-\epsilon}^\epsilon \sqrt{\epsilon^2 - x^2} |\varphi(x)|^2 dx \right)^{1/2},$$

the set  $\mathcal{X}^\epsilon$ , defined by

$$\mathcal{X}^\epsilon = \left\{ \varphi : \int_{-\epsilon}^\epsilon \sqrt{\epsilon^2 - x^2} |\varphi(x)|^2 dx < +\infty \right\}, \quad (5.8)$$

is a Hilbert space. Define

$$\mathcal{Y}^\epsilon = \left\{ \psi \in \mathcal{C}^0([- \epsilon, \epsilon]) : \psi' \in \mathcal{X}^\epsilon \right\}, \quad (5.9)$$

where  $\psi'$  is the distributional derivative of  $\psi$ . The set  $\mathcal{Y}^\epsilon$  is a Hilbert space with the norm

$$\|\psi\|_{\mathcal{Y}^\epsilon} = \left( \|\psi\|_{\mathcal{X}^\epsilon}^2 + \|\psi'\|_{\mathcal{X}^\epsilon}^2 \right)^{1/2}.$$

Writing

$$N_\Omega^\omega(x, y) = -\frac{1}{2\pi} \ln|x - y| + R_N^\omega(x, y), \quad (5.10)$$

where  $(x, y) \mapsto R_N^\omega(x, y)$  is  $\mathcal{C}^{1,\alpha}$  in both  $x$  and  $y$  for some  $\alpha$  with  $0 < \alpha < 1$ , the operator  $\mathcal{A}_\epsilon^\omega$  can be decomposed as

$$\mathcal{A}_\epsilon^\omega = -\frac{1}{2\pi} \mathcal{L}_\epsilon + \mathcal{R}_\epsilon^\omega, \quad (5.11)$$

where

$$\mathcal{L}_\epsilon[\varphi](x) = \int_{-\epsilon}^\epsilon \ln|x - y| \varphi(y) dy,$$

and

$$\mathcal{R}_\epsilon^\omega[\varphi](x) = \int_{-\epsilon}^\epsilon R_N^\omega(x, y) \varphi(y) dy.$$

We recall from, for instance, [14, Chapter 5] the following lemmas.

**Lemma 5.1** *For all  $0 < \epsilon < 2$ , the integral operator  $\mathcal{L}_\epsilon : \mathcal{X}^\epsilon \mapsto \mathcal{Y}^\epsilon$  is invertible. For a given function  $\psi \in \mathcal{Y}^\epsilon$ ,  $\mathcal{L}_\epsilon^{-1}[\psi] \in \mathcal{X}^\epsilon$  is given by*

$$\mathcal{L}_\epsilon^{-1}[\psi](x) = -\frac{1}{\pi^2 \sqrt{\epsilon^2 - x^2}} \int_{-\epsilon}^\epsilon \frac{\sqrt{\epsilon^2 - y^2} \psi'(y)}{x - y} dy + \frac{a(\psi)}{\pi (\ln \frac{\epsilon}{2}) \sqrt{\epsilon^2 - x^2}} \quad (5.12)$$

for  $x \in ] - \epsilon, \epsilon [$ , where the constant  $a(\psi)$  is defined by

$$a(\psi) = \psi(x) + \mathcal{L}_\epsilon \left[ \frac{1}{\pi^2 \sqrt{\epsilon^2 - y^2}} \int_{-\epsilon}^\epsilon \frac{\sqrt{\epsilon^2 - z^2} \psi'(z)}{y - z} dz \right](x). \quad (5.13)$$

In view of (5.12) and (5.13), we have

$$\mathcal{L}_\epsilon^{-1}[1](x) = \frac{1}{\pi(\ln \frac{\epsilon}{2})\sqrt{\epsilon^2 - x^2}}, \quad (5.14)$$

and

$$\mathcal{L}_\epsilon^{-1}[y](x) = -\frac{x}{\pi\sqrt{\epsilon^2 - x^2}}. \quad (5.15)$$

**Lemma 5.2** *There exists a positive constant  $C$ , independent of  $\epsilon$ , such that*

$$\|\mathcal{L}_\epsilon^{-1} \mathcal{R}_\epsilon^\omega\|_{\mathcal{L}(\mathcal{X}^\epsilon, \mathcal{X}^\epsilon)} \leq \frac{C}{|\ln \epsilon|}, \quad (5.16)$$

where

$$\|\mathcal{L}_\epsilon^{-1} \mathcal{R}_\epsilon^\omega\|_{\mathcal{L}(\mathcal{X}^\epsilon, \mathcal{X}^\epsilon)} = \sup_{\varphi \in \mathcal{X}^\epsilon, \|\varphi\|_{\mathcal{X}^\epsilon}=1} \|\mathcal{L}_\epsilon^{-1} \mathcal{R}_\epsilon^\omega[\varphi]\|_{\mathcal{X}^\epsilon}.$$

### 5.3 Asymptotic expansion

Because of (5.7) and (5.11),  $\varphi^\epsilon$  is the solution in  $\mathcal{X}^\epsilon$  of the integral equation (5.7) or equivalently

$$-\frac{1}{2\pi} \mathcal{L}_\epsilon[\varphi^\epsilon] + \mathcal{R}_\epsilon^\omega[\varphi^\epsilon] = -U \quad \text{on } \Sigma_\epsilon. \quad (5.17)$$

Thus we have

$$\varphi^\epsilon - 2\pi \mathcal{L}_\epsilon^{-1} \mathcal{R}_\epsilon^\omega[\varphi^\epsilon] = 2\pi \mathcal{L}_\epsilon^{-1}[U],$$

and hence

$$\|\varphi^\epsilon\|_{\mathcal{X}^\epsilon} \leq C(\|\mathcal{L}_\epsilon^{-1} \mathcal{R}_\epsilon^\omega[\varphi^\epsilon]\|_{\mathcal{X}^\epsilon} + \|\mathcal{L}_\epsilon^{-1}[U]\|_{\mathcal{X}^\epsilon}).$$

Note that

$$\|\mathcal{L}_\epsilon^{-1}[U]\|_{\mathcal{X}^\epsilon} \leq C\|U\|_{\mathcal{Y}^\epsilon} \leq C\epsilon.$$

It then follows from (5.16) that if  $\epsilon$  is sufficiently small, then

$$\|\varphi^\epsilon\|_{\mathcal{X}^\epsilon} \leq C\epsilon \quad (5.18)$$

for some constant  $C$  independent of  $\epsilon$ .

Set

$$\tilde{\varphi}_\epsilon(x) := \epsilon\varphi^\epsilon(\epsilon x), \quad x \in ]-1, 1[.$$

One can easily see that

$$\|\tilde{\varphi}_\epsilon\|_{\mathcal{X}^1} = \|\varphi^\epsilon\|_{\mathcal{X}^\epsilon} \leq C\epsilon,$$

and that (5.17) reads now

$$-\frac{1}{2\pi} \int_{-1}^1 (\ln \epsilon + \ln |x - y|) \tilde{\varphi}_\epsilon(y) dy + \int_{-1}^1 R_N^\omega(\epsilon x, \epsilon y) \tilde{\varphi}_\epsilon(y) dy = -U(\epsilon x), \quad x \in ]-1, 1[.$$

Observe that

$$\int_{-1}^1 |\tilde{\varphi}_\epsilon(y)| dy \leq C\|\tilde{\varphi}_\epsilon\|_{\mathcal{X}^1} \leq C\epsilon.$$



By Taylor expansions, we obtain

$$-\frac{1}{2\pi} \mathcal{L}_1[\tilde{\varphi}_\epsilon] + C \left( -\frac{\ln \epsilon}{2\pi} + R_N^\omega(0, 0) \right) = -U(0) - \epsilon x \frac{\partial U}{\partial T}(0) + O(\epsilon^2),$$

where

$$C = \int_{-1}^1 \tilde{\varphi}_\epsilon(y) dy.$$

Here  $O(\epsilon^2)$  is in the  $\mathcal{X}^1$ -norm and  $\partial/\partial T$  denotes the tangential derivative on  $\Sigma_\epsilon$ . In view of (5.14) and (5.15), we now have

$$\tilde{\varphi}_\epsilon = \frac{2U(0)}{\ln(1/2)\sqrt{1-x^2}} + C \frac{-\ln \epsilon + 2\pi R_N^\omega(0, 0)}{\pi \ln(1/2)\sqrt{1-x^2}} - 2\epsilon \frac{\partial U}{\partial T}(0) \frac{x}{\sqrt{1-x^2}} + O(\epsilon^2),$$

where  $O(\epsilon^2)$  is in the  $\mathcal{Y}^1$ -norm.

By integrating both sides of the above identity, one can see that

$$C = \frac{2\pi U(0)}{\ln(1/2) + \ln \epsilon - 2\pi R_N^\omega(0, 0)} + O(\epsilon^2). \quad (5.19)$$

Therefore we get

$$\tilde{\varphi}_\epsilon(x) = \frac{2U(0)}{\sqrt{1-x^2}} \frac{1}{\ln(\epsilon/2) - 2\pi R_N^\omega(0, 0)} - 2\epsilon \frac{\partial U}{\partial T}(0) \frac{x}{\sqrt{1-x^2}} + O(\epsilon^2),$$

By scaling back, we obtain the following lemma.

**Lemma 5.3** *The following asymptotic expansion holds :*

$$\varphi^\epsilon(x) = \frac{2U(0)}{\ln(\epsilon/2)\sqrt{\epsilon^2-x^2}} \frac{1}{1 - \frac{2\pi R_N^\omega(0,0)}{\ln(\epsilon/2)}} - 2\epsilon \frac{\partial U}{\partial T}(0) \frac{x}{\sqrt{\epsilon^2-x^2}} + O(\epsilon^2). \quad (5.20)$$

Observe that the first and second terms in (5.20) are of order  $\frac{1}{|\ln \epsilon|}$  and  $\epsilon$  in  $\mathcal{X}_\epsilon$ -norms, respectively.

Substituting (5.20) into (5.6), we obtain

$$u(x) - U(x) = \frac{2\pi U(0)}{\ln(\epsilon/2)} \frac{1}{1 - \frac{2\pi R_N^\omega(0,0)}{\ln(\epsilon/2)}} N_\Omega^\omega(x, 0) - \pi \epsilon^2 \frac{\partial U}{\partial T}(0) \frac{\partial N_\Omega^\omega}{\partial T}(x, 0) + O(\epsilon^3), \quad (5.21)$$

uniformly on  $x \in \partial\Omega$ .

We finally obtain the following theorem :

**Theorem 5.4** *Let  $\Sigma_\epsilon$  be a linear crack of length  $2\epsilon$  whose center is at  $z$  satisfying (5.1). Then the following expansion holds*

$$u(x) - U(x) = \frac{2\pi U(z)}{\ln(\epsilon/2)} \frac{1}{1 - \frac{2\pi R_N^\omega(0,0)}{\ln(\epsilon/2)}} N_\Omega^\omega(x, z) - \pi \epsilon^2 \frac{\partial U}{\partial T}(z) \frac{\partial N_\Omega^\omega}{\partial T}(x, z) + O(\epsilon^3), \quad (5.22)$$

uniformly on  $x \in \partial\Omega$ .

We also have an asymptotic expansion for the Dirichlet problem :

$$\begin{cases} \Delta v + \omega^2 v = 0 & \text{in } \Omega \setminus \overline{\Sigma_\epsilon}, \\ v = 0 & \text{on } \Sigma_\epsilon, \\ v = f \in H^{1/2}(\partial\Omega) & \text{on } \partial\Omega. \end{cases} \quad (5.23)$$

Here,  $H^{1/2}(\partial\Omega)$  is the standard trace space.

Define  $V$  to be the background solution, that is, the solution to

$$\begin{cases} \Delta V + \omega^2 V = 0 & \text{in } \Omega, \\ V = f & \text{on } \partial\Omega, \end{cases} \quad (5.24)$$

and introduce  $G_\Omega^\omega(x, z)$ , for  $x, z \in \Omega$ , to be the Dirichlet function for  $\Omega$ , namely, the solution to

$$\begin{cases} (\Delta_x + \omega^2)G_\Omega^\omega(x, z) = -\delta_z(x) & \text{in } \Omega, \\ G_\Omega^\omega(x, z) = 0 & \text{for } x \in \partial\Omega. \end{cases} \quad (5.25)$$

Analogously to (5.10), we have

$$G_\Omega^\omega(x, y) = -\frac{1}{2\pi} \ln|x - y| + R_D^\omega(x, y),$$

where  $(x, y) \mapsto R_D^\omega(x, y)$  is  $\mathcal{C}^{1,\alpha}$  in both  $x$  and  $y$  for some  $\alpha$  with  $0 < \alpha < 1$ . The following asymptotic formula can be proved exactly as in Theorem 5.4.

**Theorem 5.5** *Let  $\Sigma_\epsilon$  be a linear crack of length  $2\epsilon$  whose center is at  $z$  satisfying (5.1). Then the following expansion holds*

$$\begin{aligned} \frac{\partial(v - V)}{\partial\nu}(x) &= \frac{2\pi V(z)}{\ln(\epsilon/2)} \frac{1}{1 - \frac{2\pi R_D^\omega(0,0)}{\ln(\epsilon/2)}} \frac{\partial G_\Omega^\omega}{\partial\nu(x)}(x, z) \\ &\quad - \pi\epsilon^2 \frac{\partial V}{\partial T}(z) \frac{\partial^2 G_\Omega^\omega}{\partial T(z) \partial\nu(x)}(x, z) + O(\epsilon^3), \end{aligned} \quad (5.26)$$

uniformly on  $x \in \partial\Omega$ .

## 5.4 MUSIC-type imaging

Suppose that  $\Omega$  contains  $m$  small cracks  $\Sigma_s$  located at  $z_s, s = 1, \dots, m$ . The cracks are well-separated from each other and from the boundary  $\partial\Omega$ . Let  $2\epsilon_s = |\Sigma_s|$ . Suppose that  $\epsilon_s = \alpha_s \epsilon$ , where  $\alpha_s = O(1)$  and  $2\epsilon$  is the order of magnitude of the lengths of the cracks.

Since  $\ln(\epsilon_s/2) = \ln(\epsilon/2) + O(|\ln \epsilon|^{-1})$ , one can see from Theorem 5.4 that

$$\int_{\partial\Omega} (u - U)(x) \frac{\partial V}{\partial\nu}(x) d\sigma(x) = \frac{2\pi}{\ln(\epsilon/2)} \sum_{s=1}^m U(z_s) V(z_s) + O\left(\frac{1}{|\ln \epsilon|^2}\right) \quad (5.27)$$

for any smooth  $V$  satisfying

$$(\Delta + \omega^2)V = 0 \quad \text{in } \Omega.$$

Let  $\{\theta_1, \dots, \theta_N\}$  be a set of  $N$  unit directions. Throughout this chapter, we suppose that they are equi-distributed on the unit circle. Choosing

$$U(x) = e^{i\omega\theta \cdot x} \quad \text{and} \quad V(x) = e^{-i\omega\theta' \cdot x}, \quad (5.28)$$

where  $\theta, \theta' \in \{\theta_1, \dots, \theta_N\}$ , leads to a standard MUSIC-type reconstruction of the locations  $\{z_s\}_{s=1}^m$  from the response matrix

$$A = (A_{ll'})_{l,l'=1}^N, \quad A_{ll'} = \frac{i}{N} \omega \int_{\partial\Omega} \theta_{l'} \cdot \nu(x) (u_l(x) - e^{i\omega\theta_l \cdot x}) e^{-i\omega\theta_{l'} \cdot x} d\sigma(x), \quad (5.29)$$

where  $u_l$  is the solution to (5.2) with  $g = i\omega(\nu \cdot \theta_l)e^{i\omega\theta_l \cdot x}$  and the division by  $N$  is for normalization. The approximation (5.27) shows

$$A_{ll'} \approx -\frac{2\pi}{N \ln(\epsilon/2)} \sum_{s=1}^m e^{i\omega(\theta_l - \theta_{l'}) \cdot z_s}. \quad (5.30)$$

If we define

$$g(z) = (e^{i\theta_1 \cdot z}, \dots, e^{i\theta_N \cdot z})^t, \quad z \in \Omega,$$

where  $t$  denotes the transpose, then the formula (5.30) clearly shows that the range of  $A$  is the space spanned by  $\{g(z_s) : s = 1, \dots, m\}$ . Therefore, in order to find the location  $z_s$  of cracks, we look for  $z$  such that

$$g(z) \in \text{Range}(A),$$

which is considered as the MUSIC characterization of the locations of cracks. The MUSIC algorithm is then to plot the imaging function

$$W(z) := \frac{1}{\|(I - P)g(z)\|} \quad \text{for } z \in \Omega, \quad (5.31)$$

where  $P$  is the orthogonal projection onto  $\text{Range}(A)$ . The function  $W(z)$  has large peaks at the locations of the cracks.

It is worth noticing that, in view of (5.30), the direction of the crack (the tangent vectors to  $\Sigma_s$ ) can not be obtained from the leading-order approximation in (5.21). Moreover, only the order of magnitude  $\epsilon$ , not  $\epsilon_s$ , can be estimated.

One may think that the higher-order terms in (5.21) may lead to an estimate of the directions of the cracks since they contain tangential derivatives of the solutions. In what follows, we show that it is the case.

Using such higher-order terms in (5.21), we obtain that

$$\begin{aligned} & \int_{\partial\Omega} (u - U)(x) \frac{\partial V}{\partial \nu}(x) d\sigma(x) \\ &= \sum_{s=1}^m \left[ \frac{2\pi}{\ln(\epsilon_s/2)} \frac{1}{1 - \frac{2\pi R_N^\omega(0,0)}{\ln(\epsilon/2)}} U(z_s) V(z_s) - \pi \epsilon_s^2 \frac{\partial U}{\partial T_s}(z_s) \frac{\partial V}{\partial T_s}(z_s) \right] + O(\epsilon^3). \end{aligned}$$

Therefore, if we choose  $U$  and  $V$  as in (5.28), it follows that

$$\begin{aligned} & \int_{\partial\Omega} (u - U)(x) \frac{\partial V}{\partial \nu}(x) d\sigma(x) \\ &= \sum_{s=1}^m \left[ \frac{2\pi}{\ln(\epsilon_s/2)} \frac{1}{1 - \frac{2\pi R_N^\omega(0,0)}{\ln(\epsilon/2)}} - \pi \epsilon_s^2 \omega^2 (\theta \cdot T_s)(\theta' \cdot T_s) \right] e^{i\omega(\theta - \theta') \cdot z_s} + O(\epsilon^3). \end{aligned} \quad (5.32)$$

Suppose for simplicity that  $m = 1$ , and let  $z$  be the center of the crack. From (5.32), one can see that  $A$  defined in (5.29) is given by

$$A \approx -\frac{2\pi}{\ln(\epsilon/2)N} \frac{1}{1 - \frac{2\pi R_N^\omega(0,0)}{\ln(\epsilon/2)}} v \otimes \bar{v} + \frac{\pi \epsilon_s^2 \omega^2}{N} w \otimes \bar{w}, \quad (5.33)$$

where

$$v = (e^{i\omega\theta_1 \cdot z}, \dots, e^{i\omega\theta_N \cdot z})^t \quad \text{and} \quad w = (\theta_1 \cdot T e^{i\omega\theta_1 \cdot z}, \dots, \theta_N \cdot T e^{i\omega\theta_1 \cdot z})^t. \quad (5.34)$$

Suppose that  $N$  is even. Then, since  $\theta_1, \dots, \theta_N$  are equi-distributed on the unit circle, we have

$$\bar{w} \cdot v = \bar{v} \cdot w = \sum_{l=1}^N \theta_l \cdot T = 0.$$

Therefore, (5.33) shows that  $A$  has only two significant singular values (eigenvalues in this case) given by

$$\tau^{(1)} = -\frac{2\pi}{\ln(\epsilon/2)} \frac{1}{1 - \frac{2\pi R_N^\omega(0,0)}{\ln(\epsilon/2)}}, \quad \tau^{(2)} = \pi \epsilon^2 \omega^2 \frac{1}{N} \sum_{l=1}^N (\theta_l \cdot T)^2, \quad (5.35)$$

whose normalized eigenvectors are given by  $v/\|v\|$  and  $w/\|w\|$ , respectively. Observe that  $\sum_{l=1}^N (\theta_l \cdot T)^2 \approx 1/2$  regardless of  $T$  if  $N$  is sufficiently large. In fact, one can easily see that

$$\lim_{N \rightarrow \infty} \frac{1}{N} \sum_{l=1}^N (\theta_l \cdot T)^2 = \frac{1}{2}, \quad \text{uniformly in } T.$$

We observe that since the eigenvector  $w$  contains information on  $\theta_j \cdot T$  for  $j = 1, \dots, N$ , it is easy to find  $T$  from  $w$ .

## 5.5 Numerical simulations for imaging of small cracks

In this section, results of numerical simulations for imaging of small cracks are presented. In order to perform the numerical simulation, we choose the homogeneous domain  $\Omega$ , which contains small cracks, as a unit disk centered at  $(0, 0)$  in  $\mathbb{R}^2$ . Throughout this section, the length of all cracks is set to 0.02, i.e.,  $\epsilon = 0.01$ .

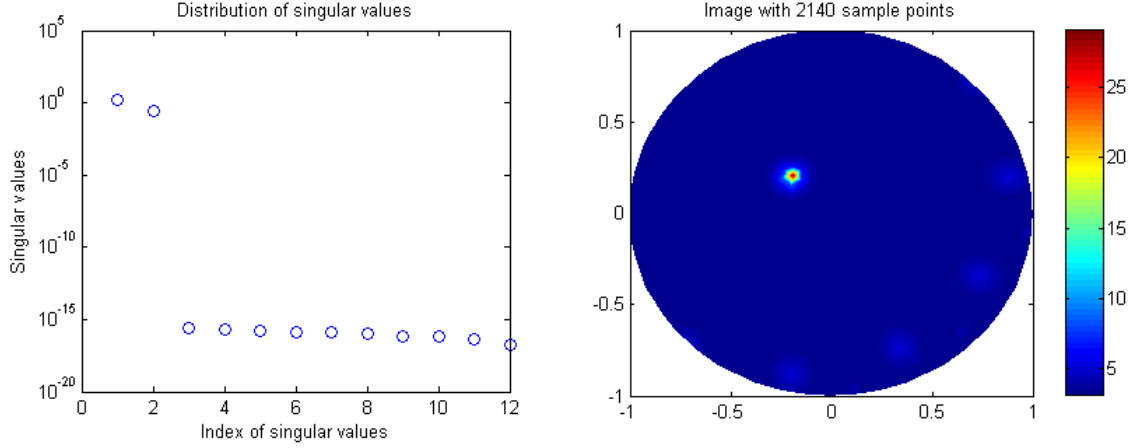


FIG. 5.1 – Distribution of singular values of the response  $A$  (left) and plots of  $W(z)$  for  $\Sigma_1$  using  $N = 12$  incident waves at the frequency  $\omega = \frac{2\pi}{0.5}$ . The data set was generated using (5.32).

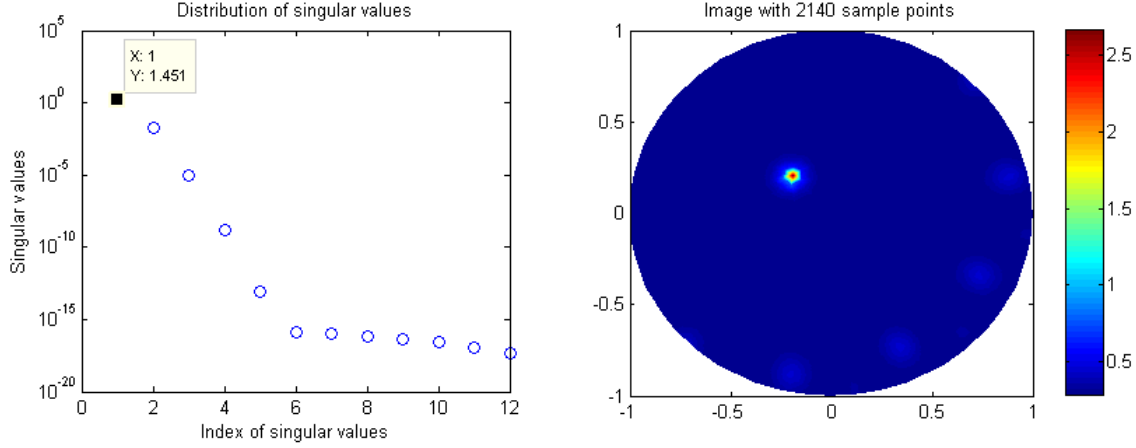


FIG. 5.2 – Results for  $\Sigma_1$  with the data set generated by solving forward problems, without noise.

### 5.5.1 Imaging of a single small crack

For illustration we choose the following two cracks :

$$\begin{aligned}\Sigma_1 &= \{(x - 0.2, 0.2) : -\epsilon \leq x \leq \epsilon\}, \\ \Sigma_2 &= \{R_{\pi/6}(x, 0) : -\epsilon \leq x \leq \epsilon\},\end{aligned}$$

where  $R_{\pi/6}$  is the rotation by  $\pi/6$ .

For simulation we take the number of directions  $N = 12$  and the wavelength  $\lambda = 0.5$ . The data set of the matrix  $A$  in (5.29) is collected in two different ways : by calculating (5.32) and by solving the forward problem (5.2). Figures 5.1 and 5.2 show the distributions of the singular values of the response matrix and plots of  $W(z)$  defined in (5.31). Both of them show that the location can be detected pretty accurately

Fig. 5.3 shows the results when we add a noise. A noise is added as follows : for a

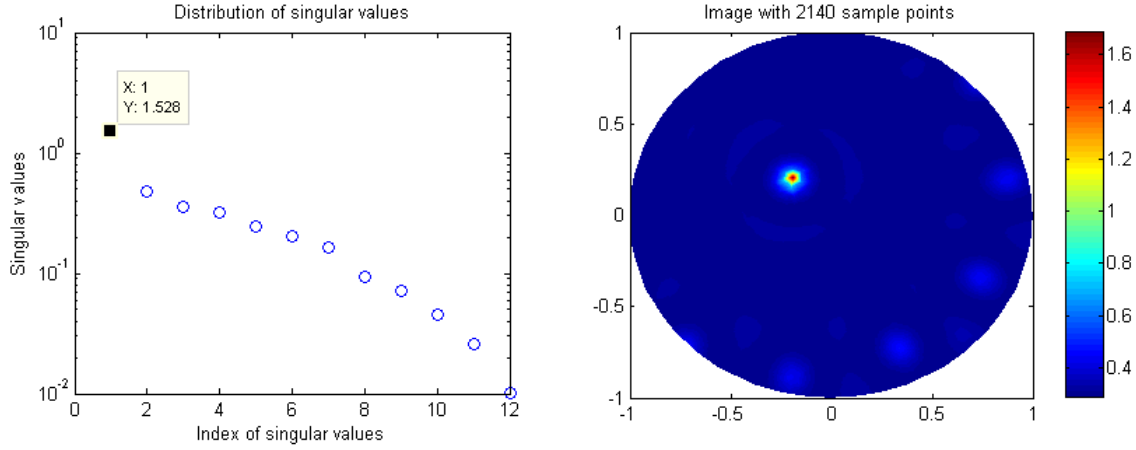


FIG. 5.3 – Results for  $\Sigma_1$  with the data set generated by solving forward problems, with 30% random noise ( $\xi = 0.3$ ).

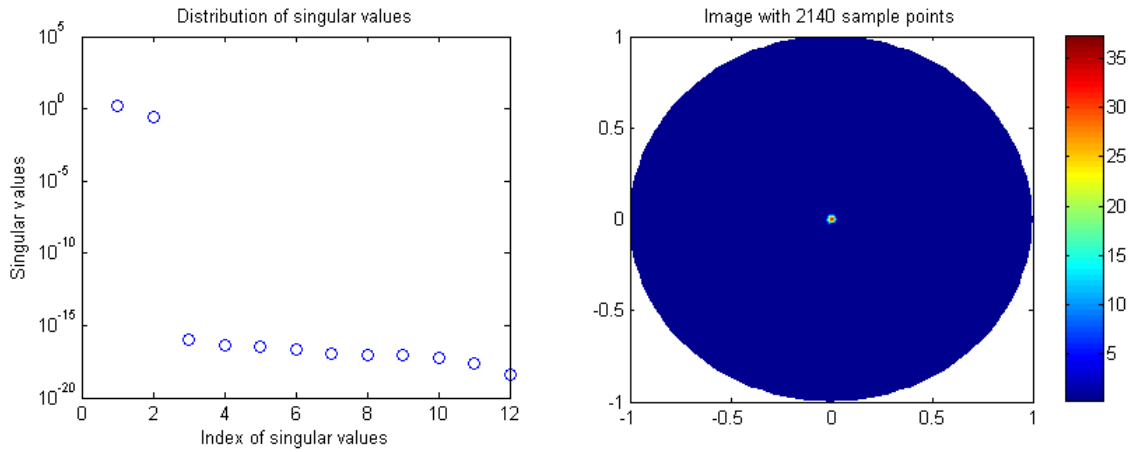


FIG. 5.4 – Results for  $\Sigma_2$  with the data set generated using (5.32).

numerical value  $\xi$

$$u_{\text{noise}}(x) = [1 + \xi \times (\text{rnd}_1(-1, 1) + i\text{rnd}_2(-1, 1))]u(x)$$

where  $\text{rnd}_1(-1, 1)$  and  $\text{rnd}_2(-1, 1)$  are arbitrary real values between  $-1$  and  $1$ . For this example we take  $\xi = 0.3$ . Although the distribution of singular values is quite different from the noiseless one and a few ghost replicas appear in the image, the location of  $\Sigma_1$  is successfully identified.

Figures 5.4 and 5.5 show results of reconstruction for  $\Sigma_2$ . Like  $\Sigma_1$ , the location is well identified.

Tab. 5.1 shows numerical values of reconstructed locations.

### 5.5.2 Size estimation

In the reconstruction of  $\Sigma_1$  in subsection 5.5.1, the first significant singular value of the response matrix is 1.451 when the data were collected by solving forward problems,

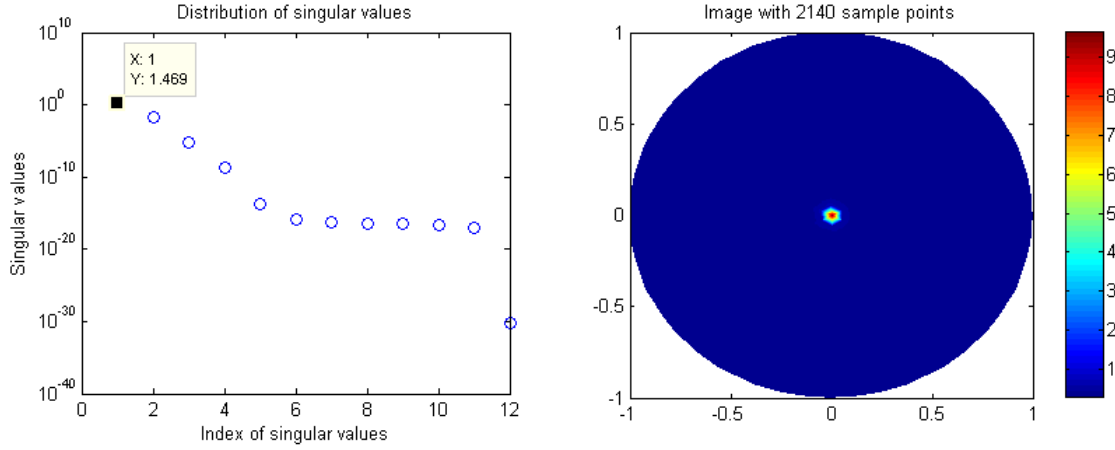
FIG. 5.5 – Results for  $\Sigma_2$  with the data set generated by solving forward problems.

Fig.	true location	reconstructed location
1	$(-0.2, 0.2)$	$(-0.1933, 0.2105)$
2	$(-0.2, 0.2)$	$(-0.1933, 0.2105)$
3	$(-0.2, 0.2)$	$(-0.1899, 0.2174)$
4	$(0, 0)$	$(0.00001506, 0.00008568)$
5	$(0, 0)$	$(0.001378, -0.003054)$

TAB. 5.1 – True and reconstructed locations.

and 1.528 when we add noise. In view of (5.30), the first significant singular value is given by

$$\tau^{(1)} \approx -\frac{2\pi}{\ln(\epsilon/2)}.$$

Therefore, the estimated  $\epsilon$  is 0.0132 in the noiseless case and 0.0164 in the noisy case. In both cases, the estimated value of  $\epsilon$  is close to the actual value, 0.01.

### 5.5.3 Direction estimation

Set, as before,  $N = 12$ . Thus the directions  $\theta_l$  are given by

$$\theta_l = \left( \cos \frac{2l}{12}\pi, \sin \frac{2l}{12}\pi \right).$$

Since

$$\theta_l \cdot T \approx \frac{w(l)}{e^{i\omega\theta_l \cdot z}},$$

where  $w(l)$  is the  $l$ -component of the second singular vector  $w$ , then the direction  $T$  can be recovered by looking at the maximum (or minimal) values of  $d_l := |w(l)|$ .

Consider first the small crack  $\Sigma_1$ . Then by using the dataset generated by solving forward problem, we find that  $d_l$  attains its maximal for  $l = 6$  and  $12$ , which shows that  $T$  is parallel to  $(1, 0)^t$ . If we consider  $\Sigma_2$ , then the maximum is attained for  $l = 1$  and  $l = 7$ . See Tab. 5.2.

$l$	value of $d_l$ for $\Sigma_1$	value of $d_l$ for $\Sigma_2$
1	0.8658	0.9994
2	0.5002	0.8660
3	0.0024	0.5004
4	0.5008	0.0001
5	0.8663	0.5006
6	0.9998	0.8661
7	0.8663	0.9996
8	0.5008	0.8661
9	0.0024	0.5006
10	0.5002	0.0001
11	0.8658	0.5004
12	0.9992	0.8660

TAB. 5.2 – Recovering the directions of the small cracks  $\Sigma_1$  and  $\Sigma_2$ .

#### 5.5.4 Imaging of multiple small cracks

We now consider imaging of multiple small cracks. Again two examples of multiple cracks,  $\Sigma^{(1)}$  and  $\Sigma^{(2)}$ , are chosen for illustration as follows :

$$\begin{aligned}\Sigma^{(1)} &= \Sigma_1^{(1)} \cup \Sigma_2^{(1)} := \{(x - 0.5, 0) : -\epsilon \leq x \leq \epsilon\} \cup \{(x + 0.5, 0) : -\epsilon \leq x \leq \epsilon\} \\ \Sigma^{(2)} &= \Sigma_1^{(2)} \cup \Sigma_2^{(2)} := \{(x - 0.5, -0.2) : -\epsilon \leq x \leq \epsilon\} \cup \{R_{\pi/4}(x + 0.5, 0.3) : -\epsilon \leq x \leq \epsilon\},\end{aligned}$$

where  $R_{\pi/4}$  is the rotation by  $\pi/4$ . It should be noted that cracks,  $\Sigma_1^{(j)}$  and  $\Sigma_2^{(j)}$ , in both examples are well-separated. We use  $N = 20$  for the number of directions of the incident waves and  $\lambda = 0.4$  for the wave length. The data set for the response matrix was generated in two different way as in subsection 5.5.1 : by using (5.32) and by solving forward problems.

Fig. 5.6 and 5.7 are for  $\Sigma^{(1)}$  and Figures 5.8 and 5.9 for  $\Sigma^{(2)}$ , without adding noise. One can see that the locations of multiple cracks are also successfully identified. It is interesting to observe that unlike the case of  $\Sigma^{(1)}$  where two peaks of  $W(z)$  have almost the same magnitudes,  $W(z)$  for  $\Sigma^{(2)}$  has a peak of much smaller magnitude at the rotated crack (the one on the right) than at the other one. Fig. 5.10 shows results when we add 30% ( $\xi = 0.3$ ) random noise. The location is well identified even under noise. Tab. 5.3 shows numerical values of reconstructed locations.

#### 5.5.5 Imaging of two closely located cracks

The purpose of numerical experiments in this section is to consider the resolution of the image. According to the Rayleigh resolution limit, any detail less than one-half of the wavelength can not be seen. See, for instance, [3].

In order to explore a resolution limit, we consider the following examples :

$$\begin{aligned}\Sigma^{(3)} &= \{(x - 0.1, 0) : -\epsilon \leq x \leq \epsilon\} \cup \{(x + 0.1, 0) : -\epsilon \leq x \leq \epsilon\}, \\ \Sigma^{(4)} &= \{(x - 0.05, 0) : -\epsilon \leq x \leq \epsilon\} \cup \{(x + 0.05, 0) : -\epsilon \leq x \leq \epsilon\}.\end{aligned}$$



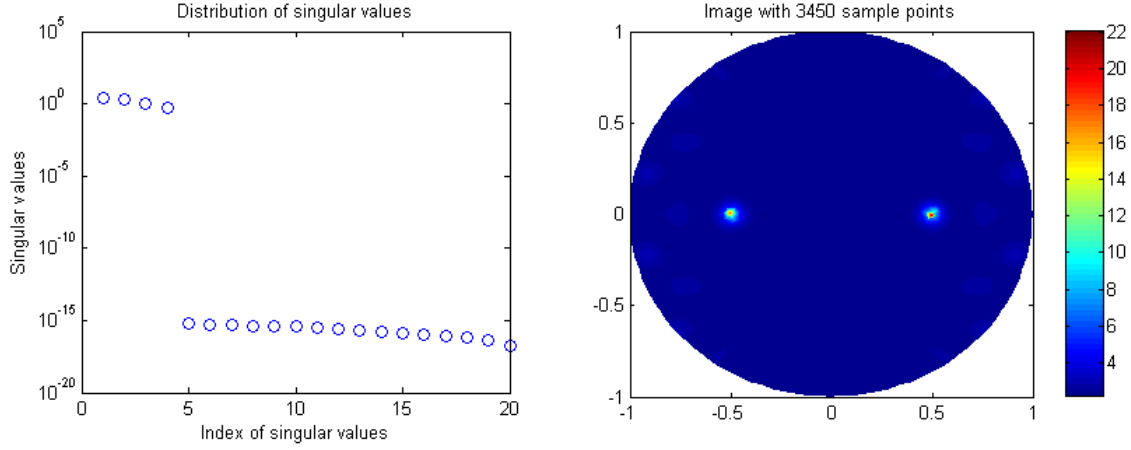


FIG. 5.6 – Distribution of singular values of the response matrix  $A$  (left) and plots of  $W(z)$  for  $\Sigma^{(1)}$  using  $N = 20$  incidences at the frequency  $\omega = \frac{2\pi}{0.4}$ , with the data set generated using (5.32).

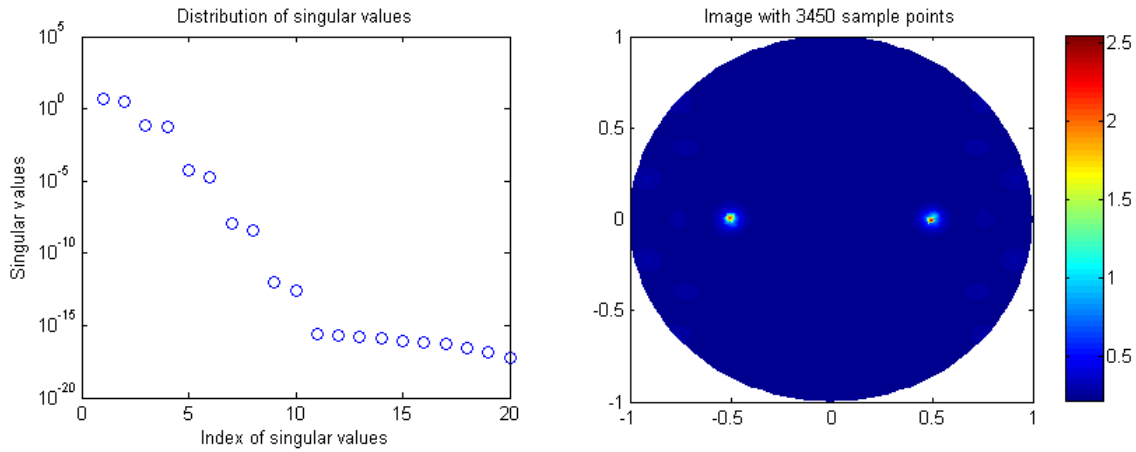


FIG. 5.7 – Results for  $\Sigma^{(1)}$  with the data set generated by solving the forward problems.

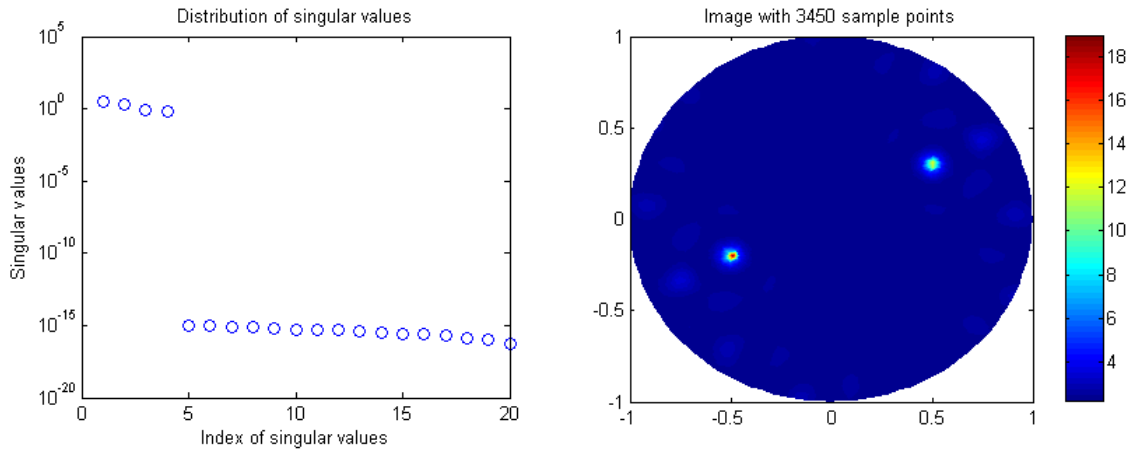


FIG. 5.8 – Results for  $\Sigma^{(2)}$  with data set generated using (5.32).

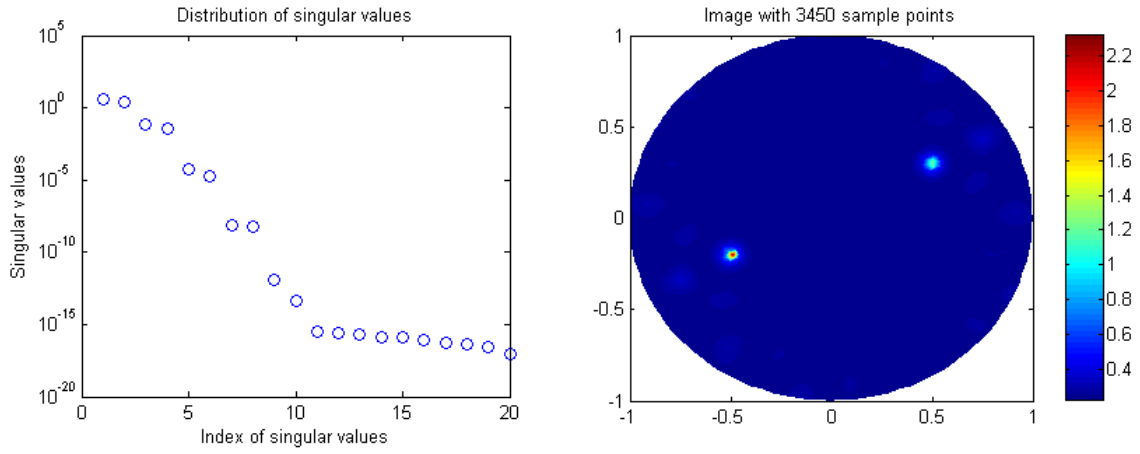


FIG. 5.9 – Results for  $\Sigma^{(2)}$  with data set generated by solving the forward problems, without noise.

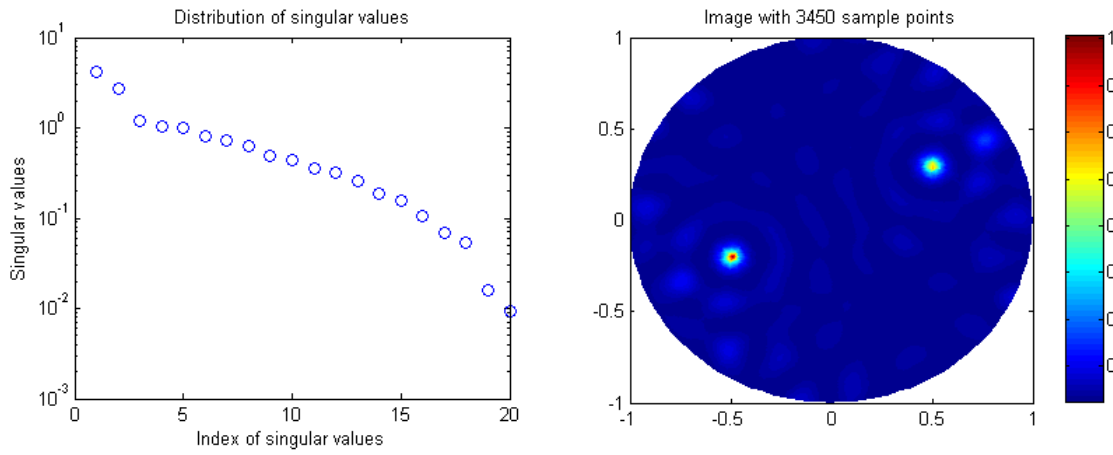


FIG. 5.10 – Results for  $\Sigma^{(2)}$  with data set generated by solving the forward problems, with noise  $\xi = 0.3$ .

Fig.	true locations	reconstructed locations
6	$(-0.5, 0), (0.5, 0)$	$(-0.5023, 0.00846), (0.4946, -0.005384)$
7	$(-0.5, 0), (0.5, 0)$	$(-0.5023, 0.00846), (0.4946, -0.005384)$
8	$(-0.5, -0.2), (0.5, 0.3)$	$(-0.4912, -0.1998), (0.5048, 0.3159)$
9	$(-0.5, -0.2), (0.5, 0.3)$	$(-0.4912, -0.1998), (0.5048, 0.3159)$
10	$(-0.5, -0.2), (0.5, 0.3)$	$(-0.4912, -0.1998), (0.5048, 0.3159)$
11 (on the left)	$(-0.1, 0), (0.1, 0)$	$(-0.03198, -0.0001345)$
11 (on the right)	$(-0.05, 0), (0.05, 0)$	$(-0.06345, -0.001372), (0.06473, 0.002353)$

TAB. 5.3 – True and reconstructed locations.

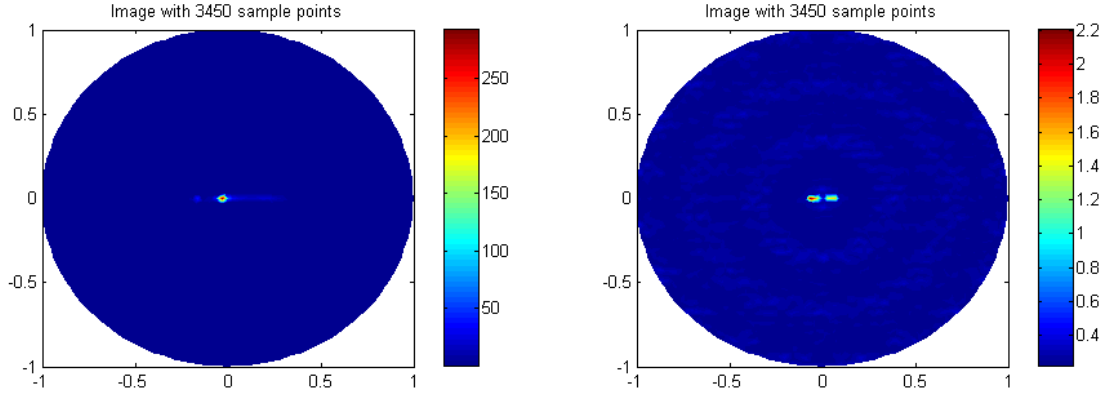


FIG. 5.11 – Left : image of  $\Sigma^{(3)}$  with the wavelength  $\lambda = 1$ . Right : image of  $\Sigma^{(4)}$  with  $\lambda = 0.05$ . The data set was generated by solving the forward problems.

Both  $\Sigma^{(3)}$  and  $\Sigma^{(4)}$  consist of two small cracks, whose distances are 0.2 and 0.1, respectively. We illuminate the medium containing  $\Sigma^{(3)}$  with plane waves of  $N = 20$  directions and of the wavelength  $\lambda = 1$ , while the medium containing  $\Sigma^{(4)}$  is illuminated with waves of the wavelength  $\lambda = 0.05$ .

Fig. 5.11 clearly shows that the waves of wavelength 1 can not distinguish two cracks of distance 0.2 in  $\Sigma^{(3)}$ , while the waves of wavelength 0.05 can distinguish two cracks in  $\Sigma^{(4)}$ , whose distance is even shorter than other ones.

## 5.6 Deformation of an extended crack

We now consider the problem of reconstructing an extended crack  $\Sigma$  which is not necessarily linear. For that purpose we first derive asymptotic expansion formula for the perturbation of the solution due to the perturbation of the crack.

Let  $a, b \in \mathbb{R}$ , with  $a < b$ , and let  $X(t) : [a, b] \rightarrow \mathbb{R}^2$  be the arc length parametrization of  $\Sigma$ , namely,  $X$  is a  $\mathcal{C}^2$ -function satisfying  $|X'(t)| = 1$  for all  $t \in [a, b]$  and

$$X := \left\{ x = X(t), \ t \in [a, b] \right\}.$$

Then  $X(a)$  and  $X(b)$  are the endpoints. The outward unit normal to  $\Sigma$ ,  $\nu(x)$ , is given by  $\nu(x) = R_{-\pi/2}X'(t)$ , where  $R_{-\pi/2}$  is the rotation by  $-\pi/2$ . Note that the unit tangential vector at  $x$  is given by  $T(x) = X'(t)$  and  $X'(t) \perp X''(t)$ . Set the curvature  $\tau(x)$  to be defined by

$$X''(t) = \tau(x)\nu(x).$$

Let

$$\tilde{X}(t) = X(t) + \epsilon h(t)\nu(x) = X(t) + \epsilon h(t)R_{-\pi/2}X'(t)$$

be a parametrization of  $\Sigma_\epsilon$  which is a perturbation of  $\Sigma$ . Suppose for the sake of simplicity that  $h(a) = h(b) = 0$ , i.e. the endpoints are fixed.

By  $\tilde{\nu}(\tilde{x})$ , we denote the outward unit normal to  $\Sigma_\epsilon$  at  $\tilde{x} = x + \epsilon h(t)\nu(x) \in \Sigma_\epsilon$ . Let us now invoke from [14, Section 3.3] the following expansions :  $\tilde{\nu}(\tilde{x})$  can be expanded as

$$\tilde{\nu}(\tilde{x}) = \nu(x) - \epsilon h'(t)T(x) + O(\epsilon^2), \quad x \in \Sigma. \quad (5.36)$$

Likewise, we get an expansion for the length element  $d\sigma_\epsilon(\tilde{x})$  :

$$d\sigma_\epsilon(\tilde{x}) = (1 - \epsilon\tau(x)h(t) + O(\epsilon^2)) d\sigma(x). \quad (5.37)$$

We also have

$$\begin{aligned} H_0^{(1)}(\omega|\tilde{x} - \tilde{y}|) &= H_0^{(1)}(\omega|x - y|) \\ &+ \epsilon\omega H_0^{(1)'}(\omega|x - y|) \frac{\langle x - y, h(t)\nu(x) - h(s)\nu(y) \rangle}{|x - y|} + O(\epsilon^2), \end{aligned} \quad (5.38)$$

where  $x = X(t)$  and  $y = X(s)$ . The term  $O(\epsilon^2)$  is uniform in both  $x$  and  $y$  on  $\Sigma$ .

Set

$$\mathcal{X}(\Sigma) = \left\{ \varphi : \int_{\Sigma} \sqrt{|X(b) - x||x - X(a)|} |\varphi(x)|^2 d\sigma(x) < +\infty \right\},$$

and

$$\|\varphi\|_{\mathcal{X}(\Sigma)} := \left( \int_{\Sigma} \sqrt{|X(b) - x||x - X(a)|} |\varphi(x)|^2 d\sigma(x) \right)^{\frac{1}{2}}.$$

We now introduce  $\mathcal{S}_\Sigma$  and  $\mathcal{S}_{\Sigma,h}^{(1)}$ , defined for any  $\phi \in \mathcal{X}(\Sigma)$  by

$$\mathcal{S}_\Sigma[\phi](x) = \frac{i}{4} \int_{\Sigma} H_0^{(1)}(\omega|x - y|) \phi(y) d\sigma(y),$$

and

$$\begin{aligned} \mathcal{S}_{\Sigma,h}^{(1)}[\phi](x) &= \frac{i}{4} \int_{\Sigma} \left[ \omega H_0^{(1)'}(\omega|x - y|) \frac{\langle x - y, h(t)\nu(x) - h(s)\nu(y) \rangle}{|x - y|} \right. \\ &\quad \left. - H_0^{(1)}(\omega|x - y|)\tau(y)h(s) \right] \phi(y) d\sigma(y). \end{aligned} \quad (5.39)$$

Let  $\Psi_\epsilon$  be the mapping from  $\Sigma$  onto  $\Sigma_\epsilon$  given by

$$\Psi_\epsilon(x) = x + \epsilon h(t)\nu(x), \quad x = X(t).$$

Then the following lemma is easily derived from (5.37) and (5.38) (see also [14, Section 3.3]).

**Lemma 5.6** *For any  $\tilde{\phi} \in \mathcal{X}(\Sigma_\epsilon)$ ,*

$$\left\| (\mathcal{S}_{\Sigma_\epsilon}[\tilde{\phi}]) \circ \Psi_\epsilon - \mathcal{S}_\Sigma[\phi] - \epsilon \mathcal{S}_{\Sigma,h}^{(1)}[\phi] \right\|_{\mathcal{X}(\Sigma)} \leq C\epsilon^2 \|\phi\|_{\mathcal{X}(\Sigma)}, \quad (5.40)$$

where  $\phi := \tilde{\phi} \circ \Psi_\epsilon$ .

Let us assume that the problem

$$\begin{cases} \Delta u + \omega^2 u = 0 & \text{in } \Omega \setminus \overline{\Sigma}, \\ u = 0 & \text{on } \Sigma, \\ \frac{\partial u}{\partial \nu} = g \in L^2(\partial\Omega) & \text{on } \partial\Omega, \end{cases} \quad (5.41)$$

is well-posed, namely,  $\omega^2$  is not an eigenvalue of the problem. Then, for  $\epsilon$  small enough, the following problem is also well-posed :

$$\begin{cases} \Delta u + \omega^2 u = 0 & \text{in } \Omega \setminus \overline{\Sigma_\epsilon}, \\ u = 0 & \text{on } \Sigma_\epsilon, \\ \frac{\partial u}{\partial \nu} = g & \text{on } \partial\Omega. \end{cases} \quad (5.42)$$

Let  $U_\Sigma$  and  $u$  be the respective solutions to (5.41) and (5.42). Let  $N_\Omega^\omega(x, y)$  be the Neumann function defined by (5.5) and  $U$  be the solution when there is no crack, i.e., the solution to (5.4). As before, we have by Green's formula,

$$(U_\Sigma - U)(x) = \int_{\Sigma} N_\Omega^\omega(x, y) \phi_\epsilon(y) d\sigma_\epsilon(\tilde{y}), \quad x \in \partial\Omega, \quad (5.43)$$

where  $\phi_\epsilon \in \mathcal{X}(\Sigma)$  is the solution to the integral equation

$$\mathcal{A}_\Sigma[\phi](x) := \int_{\Sigma} N_\Omega^\omega(x, y) \phi(y) d\sigma(y) = -U(x) \quad \text{on } \Sigma. \quad (5.44)$$

Likewise, we have

$$(u - U)(x) = \int_{\Sigma_\epsilon} N_\Omega^\omega(x, \tilde{y}) \tilde{\phi}_\epsilon(\tilde{y}) d\sigma_\epsilon(\tilde{y}) \quad \text{on } \partial\Omega, \quad (5.45)$$

where  $\tilde{\phi}_\epsilon \in \mathcal{X}(\Sigma_\epsilon)$  is the solution to

$$\int_{\Sigma_\epsilon} N_\Omega^\omega(\tilde{x}, \tilde{y}) \tilde{\phi}_\epsilon(\tilde{y}) d\sigma_\epsilon(\tilde{y}) = -U(\tilde{x}) \quad \text{on } \Sigma_\epsilon. \quad (5.46)$$

Let us prove that  $\mathcal{A}_\Sigma$  is invertible on  $\mathcal{X}(\Sigma)$ . Because of (5.11), one can see that  $\mathcal{A}_\Sigma$  is a compact operator on  $\mathcal{X}(\Sigma)$ . Suppose that  $\mathcal{A}_\Sigma[\phi] = 0$  on  $\Sigma$  for some  $\phi \in \mathcal{X}(\Sigma)$ . Define

$$v(x) = \int_{\Sigma} N_\Omega^\omega(x, y) \phi(y) d\sigma(y), \quad x \in \Omega.$$

Then  $v$  satisfies (5.41) with  $g = 0$  and therefore,  $v \equiv 0$  in  $\Omega$ . But,  $\phi$  is equal to the jump of the normal derivative of  $v$  on  $\Sigma$ , and hence  $\phi = 0$  on  $\Sigma$ . Thus  $\mathcal{A}_\Sigma$  is invertible on  $\mathcal{X}(\Sigma)$ .

Writing

$$N_\Omega^\omega(x, y) = \frac{i}{4} H_0^{(1)}(\omega|x - y|) + R_N^\omega(x, y),$$

where  $R_N^\omega(x, y)$  is of class  $\mathcal{C}^{1,\alpha}$ ,  $0 < \alpha < 1$ , one can see that (5.46) can be written as

$$\mathcal{S}_{\Sigma_\epsilon}[\tilde{\phi}_\epsilon](\tilde{x}) + \int_{\Sigma_\epsilon} R_N^\omega(\tilde{x}, \tilde{y}) \tilde{\phi}_\epsilon(\tilde{y}) d\sigma_\epsilon(\tilde{y}) = -U(\tilde{x}) \quad \text{on } \Sigma_\epsilon.$$

Since

$$U(\tilde{x}) = U(x) + \epsilon h(x) \nu(x) \cdot \nabla U(x) + O(\epsilon^2),$$

we use Lemma 5.6 to deduce that

$$\tilde{\phi}_\epsilon = \phi_\epsilon \circ \Psi_\epsilon + O(\epsilon^2),$$

where  $\phi_\epsilon$  satisfies

$$\left( \mathcal{S}_\Sigma + \mathcal{R}_\Sigma + \epsilon \mathcal{S}_{\Sigma,h}^{(1)} + \epsilon \mathcal{R}^{(1)} \right) [\phi_\epsilon](x) = -U(x) - \epsilon h(x) \nu(x) \cdot \nabla U(x) \quad \text{on } \Sigma.$$

Here the operators  $\mathcal{R}_\Sigma$  and  $\mathcal{R}^{(1)}$  are defined by

$$\mathcal{R}_\Sigma[\phi](x) = \int_{\Sigma} R_N^\omega(x, y) \phi(y) d\sigma(y),$$

and

$$\mathcal{R}^{(1)}[\phi](x) = \int_{\Sigma} \left[ -\tau(y) h(y) R_N^\omega(x, y) + \frac{\partial R_N^\omega}{\partial \nu(x)}(x, y) h(x) + \frac{\partial R_N^\omega}{\partial \nu(y)}(x, y) h(y) \right] \phi(y) d\sigma(y). \quad (5.47)$$

Put  $\mathcal{A}_\Sigma^{(1)} = \mathcal{S}_{\Sigma,h}^{(1)} + \mathcal{R}^{(1)}$ . Since  $\mathcal{S}_\Sigma + \mathcal{R}_\Sigma = \mathcal{A}_\Sigma$ , one can easily see that

$$\phi_\epsilon = \phi_0 + \epsilon \phi_1 + \dots, \quad (5.48)$$

where  $\phi_0$  and  $\phi_1$  are the unique solution to

$$\begin{cases} \mathcal{A}_\Sigma[\phi_0] &= -U \\ \mathcal{A}_\Sigma[\phi_1] + \mathcal{A}_\Sigma^{(1)}[\phi_0] &= -h \frac{\partial U}{\partial \nu}. \end{cases} \quad (5.49)$$

By inserting (5.37) and (5.48) into (5.45), we obtain the following theorem, which is our main result in this section.

**Theorem 5.7** *Let  $u$  and  $U_\Sigma$  denote the solutions to (5.42) and (5.41), respectively. For  $x \in \partial\Omega$ ,*

$$(u - U_\Sigma)(x) = \epsilon \int_{\Sigma} \left[ \left( \frac{\partial N_\Omega^\omega}{\partial \nu(y)}(x, y) h(y) - \tau(y) h(y) N_\Omega^\omega(x, y) \right) \phi_0(y) + N_\Omega^\omega(x, y) \phi_1(y) \right] d\sigma(y) + O(\epsilon^2),$$

where  $\phi_0, \phi_1 \in \mathcal{X}(\Sigma)$  are given by (5.49).

One can try to express  $u - U_\Sigma$  in terms of the Neumann function in the presence of the crack  $\Sigma$ , that is, the solution to

$$\begin{cases} (\Delta_x + \omega^2)\mathcal{N}_{\Sigma,\Omega}^\omega(x, z) = -\delta_z(x) & \text{in } \Omega \setminus \bar{\Sigma}, \\ \mathcal{N}_{\Sigma,\Omega}^\omega = 0 & \text{on } \Sigma, \\ \frac{\partial \mathcal{N}_{\Sigma,\Omega}^\omega}{\partial \nu_x}(x, z) = 0 & \text{for } x \in \partial\Omega. \end{cases}$$

Note that, even though such derivation is possible, it would be useless in practice (at least for optimization problems) since the computation of  $\mathcal{N}_{\Sigma,\Omega}^\omega$  is costly and involved.

Analogously to (5.27), for any  $f \in L^2(\partial\Omega)$ , one can see from Theorem 5.7 that

$$\begin{aligned} \int_{\partial\Omega} (u - U_\Sigma)(x) f(x) d\sigma(x) \\ = \epsilon \int_{\Sigma} \left[ \left( \frac{\partial V}{\partial \nu}(y) h(y) - \tau(y) h(y) V(y) \right) \phi_0(y) + V(y) \phi_1(y) \right] d\sigma(y), \end{aligned} \quad (5.50)$$

where  $V$  is the solution to

$$\begin{cases} (\Delta + \omega^2)V = 0 & \text{in } \Omega, \\ \frac{\partial V}{\partial \nu} = f & \text{on } \partial\Omega. \end{cases}$$

One shall now express  $\int_{\Sigma} V(y) \phi_1(y) d\sigma(y)$  in terms of  $h$ . Define  $W \in \mathcal{X}(\Sigma)$  as the solution to  $\mathcal{A}_\Sigma[W] = V$  on  $\Sigma$ . Using (5.49), one computes

$$\int_{\Sigma} V \phi_1 d\sigma = \int_{\Sigma} W \mathcal{A}_\Sigma[\phi_1] d\sigma = - \int_{\Sigma} h \frac{\partial U}{\partial \nu} W d\sigma - \int_{\Sigma} \mathcal{A}_\Sigma^{(1)}[\phi_0] W d\sigma.$$

Therefore,

$$\begin{aligned} \int_{\partial\Omega} (u - U_\Sigma)(x) f(x) d\sigma(x) = \epsilon \int_{\Sigma} \left[ \left( \frac{\partial V}{\partial \nu}(y) h(y) - \tau(y) h(y) V(y) \right) \phi_0(y) \right. \\ \left. - h(y) \frac{\partial U}{\partial \nu}(y) W(y) - \mathcal{A}_\Sigma^{(1)}[\phi_0](y) W(y) \right] d\sigma(y). \end{aligned} \quad (5.51)$$

## 5.7 Initial guess for an extended crack

### 5.7.1 Use of the concept of topological derivative

There are many possible ways to get a good initial guess. One of them is to use the concept of topological derivative [21]. The topological derivative measures the influence of creating a small crack at a certain point inside the domain  $\Omega$ .

We first construct  $\tilde{u}_D^{(l)}$  and  $\tilde{u}_N^{(l)}$  as the solutions to

$$\begin{cases} \Delta \tilde{u}_D^{(l)} + \omega^2 \tilde{u}_D^{(l)} = 0 & \text{in } \Omega, \\ \tilde{u}_D^{(l)} = u_{\text{meas}}^{(l)} & \text{on } \partial\Omega, \end{cases}$$

and

$$\begin{cases} \Delta \tilde{u}_N^{(l)} + \omega^2 \tilde{u}_N^{(l)} = 0 & \text{in } \Omega, \\ \frac{\partial \tilde{u}_N^{(l)}}{\partial \nu} = g^{(l)} & \text{on } \partial\Omega. \end{cases}$$

Then, using Theorems 5.4 and 5.5 we compute the topological derivative of the functional

$$J := \frac{1}{2} \sum_{l=1}^N \int_{\partial\Omega} \left| \frac{\partial \tilde{u}_D^{(l)}}{\partial \nu} - g^{(l)} \right|^2 + \int_{\partial\Omega} |\tilde{u}_N^{(l)} - u_{\text{meas}}^{(l)}|^2.$$

Suppose that  $\Omega$  contains a small crack  $\Sigma$  at the point  $z$  inside  $\Omega$  and of size  $2\epsilon$ . Denote by  $\tilde{u}_{D,\epsilon}^{(l)}$  and  $\tilde{u}_{N,\epsilon}^{(l)}$  the solutions of the following problems :

$$\begin{cases} \Delta \tilde{u}_{D,\epsilon}^{(l)} + \omega^2 \tilde{u}_{D,\epsilon}^{(l)} = 0 & \text{in } \Omega \setminus \bar{\Sigma}, \\ \tilde{u}_{D,\epsilon}^{(l)} = 0 & \text{on } \Sigma, \\ \tilde{u}_{D,\epsilon}^{(l)} = u_{\text{meas}}^{(l)} & \text{on } \partial\Omega, \end{cases}$$

and

$$\begin{cases} \Delta \tilde{u}_{N,\epsilon}^{(l)} + \omega^2 \tilde{u}_{N,\epsilon}^{(l)} = 0 & \text{in } \Omega \setminus \bar{\Sigma}, \\ \tilde{u}_{N,\epsilon}^{(l)} = 0 & \text{on } \Sigma, \\ \frac{\partial \tilde{u}_{N,\epsilon}^{(l)}}{\partial \nu} = g^{(l)} & \text{on } \partial\Omega. \end{cases}$$

It then follows from Theorems 5.4 and 5.5 that

$$\begin{aligned} & \frac{1}{2} \sum_{l=1}^N \int_{\partial\Omega} \left| \frac{\partial \tilde{u}_{D,\epsilon}^{(l)}}{\partial \nu} - g^{(l)} \right|^2 + \int_{\partial\Omega} |\tilde{u}_{N,\epsilon}^{(l)} - u_{\text{meas}}^{(l)}|^2 \\ &= \frac{1}{2} \sum_{l=1}^N \int_{\partial\Omega} \left| \frac{\partial \tilde{u}_D^{(l)}}{\partial \nu} - g^{(l)} \right|^2 + \int_{\partial\Omega} |\tilde{u}_N^{(l)} - u_{\text{meas}}^{(l)}|^2 + \frac{2\pi}{\ln(\epsilon/2)} d_T J(z) + o\left(\frac{1}{|\ln \epsilon|}\right). \end{aligned}$$

where

$$d_T J(z) = \text{Re} \sum_l \left( -p_D^{(l)}(z) \overline{\tilde{u}_D^{(l)}(z)} + p_N^{(l)}(z) \overline{\tilde{u}_N^{(l)}(z)} \right), \quad (5.52)$$

and the adjoint states  $p_D^{(l)}$  and  $p_N^{(l)}$  are defined as the solutions to

$$\begin{cases} \Delta p_D^{(l)} + \omega^2 p_D^{(l)} = 0 & \text{in } \Omega, \\ p_D^{(l)} = \frac{\partial \tilde{u}_D^{(l)}}{\partial \nu} - g^{(l)} & \text{on } \partial\Omega, \end{cases}$$

and

$$\begin{cases} \Delta p_N^{(l)} + \omega^2 p_N^{(l)} = 0 & \text{in } \Omega, \\ \frac{\partial p_N^{(l)}}{\partial \nu} = \tilde{u}_N^{(l)} - u_{\text{meas}}^{(l)} & \text{on } \partial\Omega. \end{cases}$$

The points where the topological derivative is the most negative are expected to be approximately on  $\Sigma_{\text{true}}$ . This would give an initial guess for  $\Sigma_{\text{true}}$ .



### 5.7.2 A MUSIC-type approach

An alternative way of getting a good initial guess is to use a standard MUSIC-type projection approach. See, for instance, [47, 54].

Let  $\{\theta_1, \dots, \theta_N\}$  be a set of  $N$  unit directions and let

$$g^{(l)}(x) = i\theta_l \cdot \nu(x) e^{i\omega\theta_l \cdot x} \quad \text{on } \partial\Omega \quad (5.53)$$

and

$$V^{(l)}(x) = e^{-i\omega\theta_l \cdot x} \quad \text{in } \Omega$$

for  $l = 1, 2, \dots, N$ . Construct the response matrix  $\tilde{A} = (\tilde{A}_{ll'})$  given by

$$(A_{\text{meas}})_{ll'} = \int_{\partial\Omega} u_{\text{meas}}^{(l)} \frac{\partial V^{(l')}}{\partial \nu} d\sigma - \int_{\partial\Omega} g^{(l)} V^{(l')} d\sigma.$$

Note that an integration by parts shows that

$$(A_{\text{meas}})_{ll'} = - \int_{\Sigma_{\text{true}}} \left[ \frac{\partial u_{\text{meas}}^{(l)}}{\partial \nu} \right] V^{(l')} d\sigma. \quad (5.54)$$

We want to reconstruct an initial guess for  $\Sigma_{\text{true}}$  from  $A_{\text{meas}} = ((A_{\text{meas}})_{ll'})$ .

We plot the imaging function

$$W(z) := \frac{1}{\|(I - P)g(z)\|} \quad \text{for } z \in \Omega,$$

where  $P$  is the orthogonal projection onto the range of the response matrix  $A_{\text{meas}}$ . As shown by the numerical examples, the function  $W(z)$  has large peaks at points on the crack. This can be explained using (5.54). The matrix  $A_{\text{meas}}$  describes in fact the far-field behavior ( $|y| \rightarrow +\infty$ ,  $y/|y| = \theta_{l'}$ ) of

$$- \int_{\Sigma_{\text{true}}} \left[ \frac{\partial u_{\text{meas}}^{(l)}}{\partial \nu} \right] (x) \bar{\Gamma}_{\omega}(x, y) d\sigma(x),$$

where  $\Gamma_{\omega}(x, y)$  is the outgoing Green function of the Helmholtz equation. Divide the crack into segments of size of order half the wavelength. Having in mind the resolution limit, only one point at each segment will contribute at the image space of the response matrix  $A_{\text{meas}}$ . Each of these points can in principle be imaged using the standard MUSIC imaging function. The resolution of the image provided by this technique is of order the half-wavelength. Since the measurements are done at the boundary of  $\Omega$ , higher-resolution in imaging the extended crack can be achieved using the optimization algorithm briefly described in the last section.

## 5.8 Numerical simulations for imaging extended cracks

In this section, we present results of numerical simulations using the two approaches we described in the previous subsections to image extended cracks. For simulation, we choose the homogeneous domain  $\Omega$  as a unit disk centered at  $(0, 0)$  in  $\mathbb{R}^2$ . Here the data sets are generated by solving forward problems.

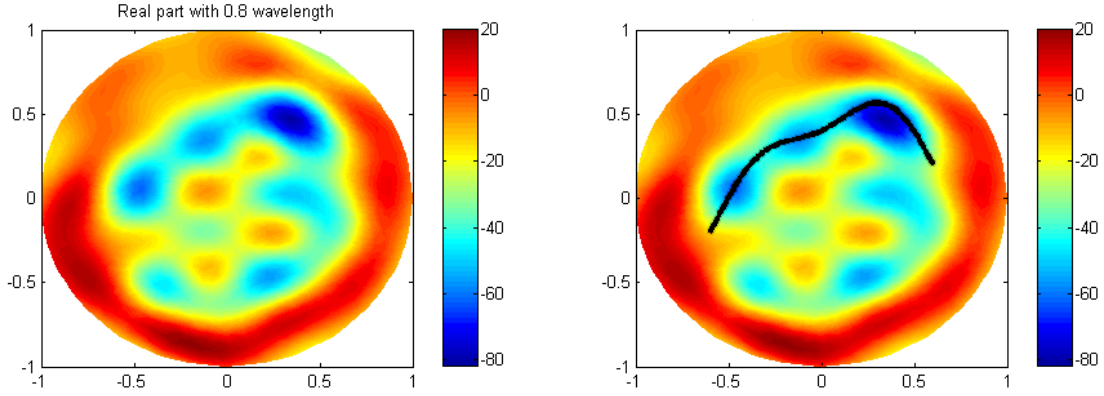


FIG. 5.12 – Image of  $d_T J(z)$  when applied frequency is  $\omega = \frac{2\pi}{0.8}$ . Black colored line is the true crack.

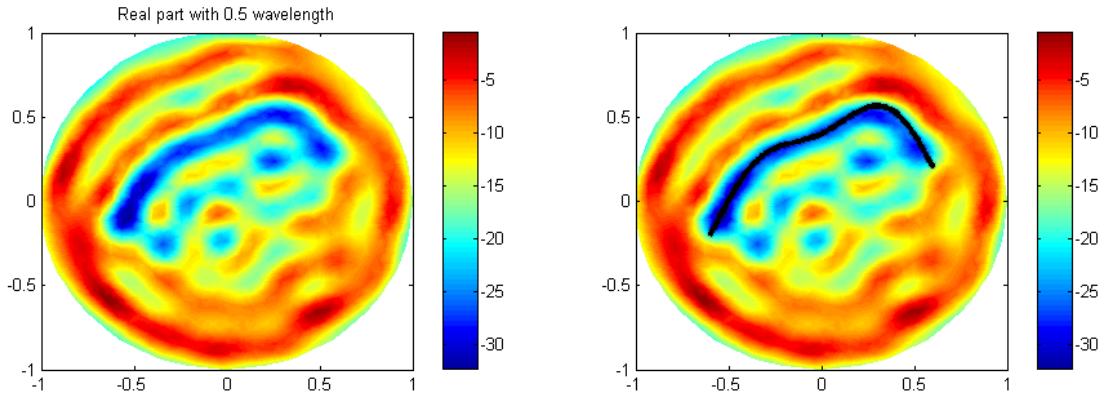


FIG. 5.13 – Image of  $d_T J(z)$  when  $\omega = \frac{2\pi}{0.5}$ , without noise

### 5.8.1 Initial guess through the topological derivative

We first implement the method of deriving a good initial guess described in the previous section. An extended crack chosen for illustration is

$$\Sigma^{(5)} = \left\{ \left( 0.6s, 0.5 \cos \frac{s\pi}{2} + 0.5 \sin \frac{s\pi}{2} - 0.1 \cos \frac{3s\pi}{2} \right) : s \in [-1, 1] \right\}. \quad (5.55)$$

The operating wavelengths are 0.8 in Fig. 5.12 and 0.5 in Figures 5.13 and 5.14.

Fig. 5.12 is the plot of values of  $d_T J(z)$  for all  $z \in \Omega$ . One can easily notice that the points where the topological derivative is the most negative value appears in the neighborhood of  $\Sigma_{\text{true}}$ . A smooth curve connecting most negative values can be taken as an initial guess. One can notice from Fig. 5.13 that if we increase the frequency of the waves, then the region of most negative values shrinks and becomes close to the actual crack, and hence provides a better initial guess. Fig. 5.14 shows the result when we add 30% ( $\xi = 0.3$ ) noise. The result is still reasonably good, which tells that this method is robust even under presence of noise.

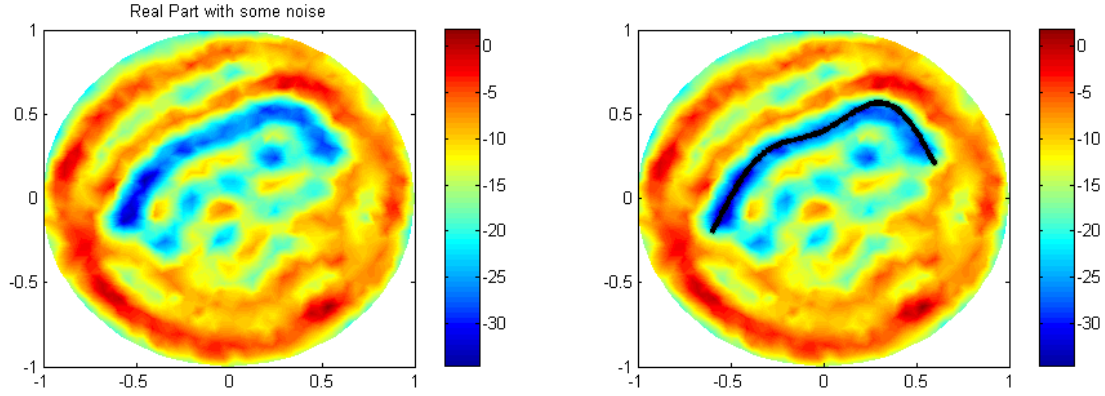


FIG. 5.14 – Image of  $d_T J(z)$  when  $\omega = \frac{2\pi}{0.5}$ , with noise  $\xi = 0.3$ .

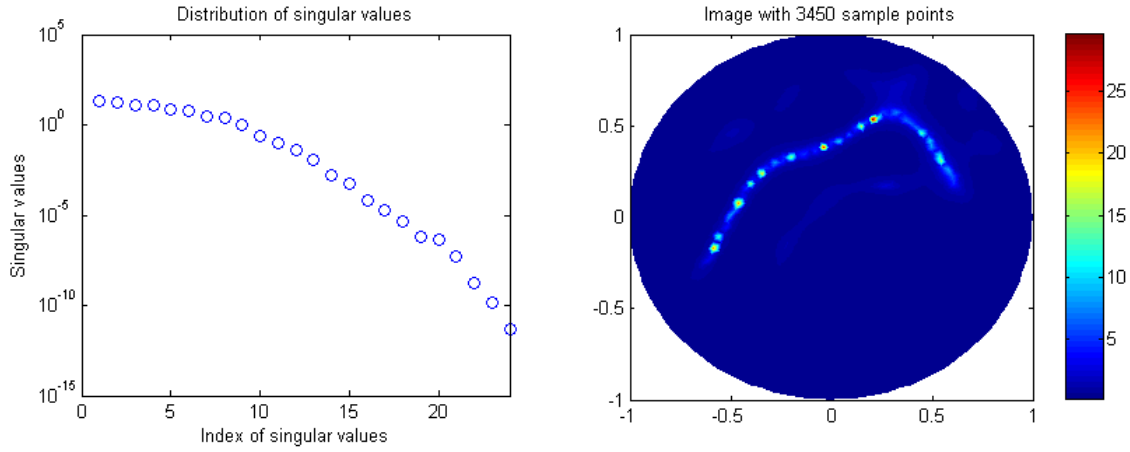


FIG. 5.15 – The distribution of singular values of the  $A_{\text{meas}}$  (left) and the plot of  $W(z)$  for  $\Sigma^{(5)}$ .  $N = 24$  and  $\lambda = 0.6$ . Without noise.

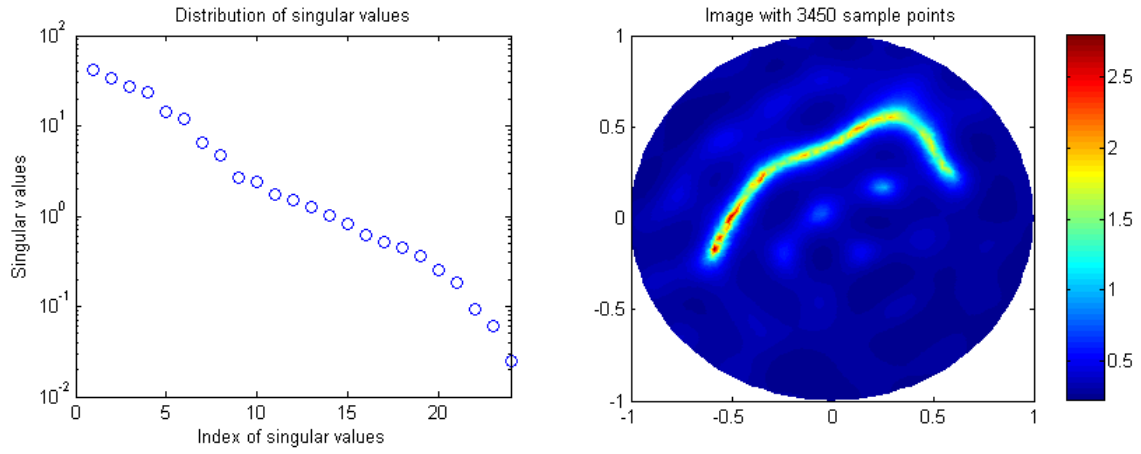
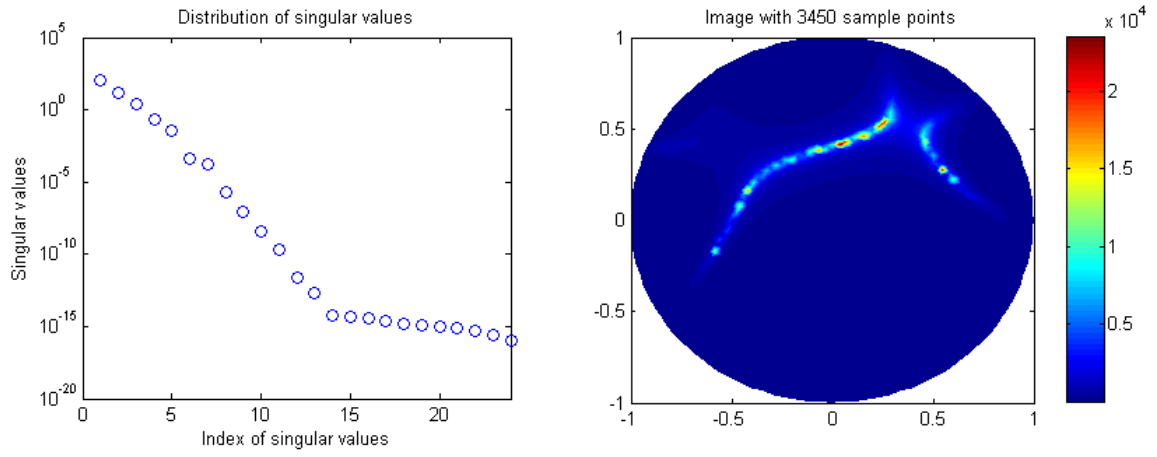
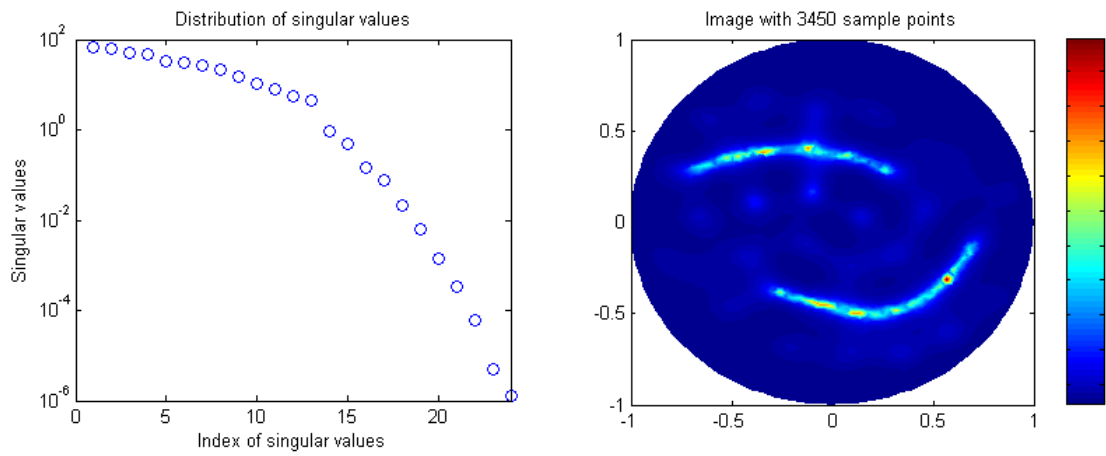
### 5.8.2 Simulation of the MUSIC-type algorithm

We now implement the MUSIC-type projection algorithm proposed in the previous section. We use  $\Sigma^{(5)}$  given in (5.55) as our crack.

In order to obtain a data set of the response matrix  $A_{\text{meas}}$  in (5.29), we solve forward problems for  $N = 24$  incident directions at the wavelength  $\lambda = 0.6$ . Figure 5.15 and Fig. 5.16 show the reconstructed images without noise and with noise,  $\xi = 0.03$ , respectively. With this noise level, the reconstruction is satisfactory. Figure 5.17 is to show what happens if we increase the wavelength. There the wavelength is  $2\pi$  and the image is clearly deteriorated.

We then apply the algorithm for imaging of multiple extended cracks,

$$\Sigma^{(6)} = \Sigma_1^{(6)} \cup \Sigma_2^{(6)},$$

FIG. 5.16 – Same as Fig. 5.15, with noise  $\xi = 0.03$ .FIG. 5.17 – Same as Fig. 5.15, but  $\lambda = 2\pi$ .FIG. 5.18 – The distribution of singular values of  $A_{\text{meas}}$  (left) and the plot of  $W(z)$  for  $\Sigma^{(6)}$ .  $N = 24$  and  $\lambda = 0.5$ . Without noise.

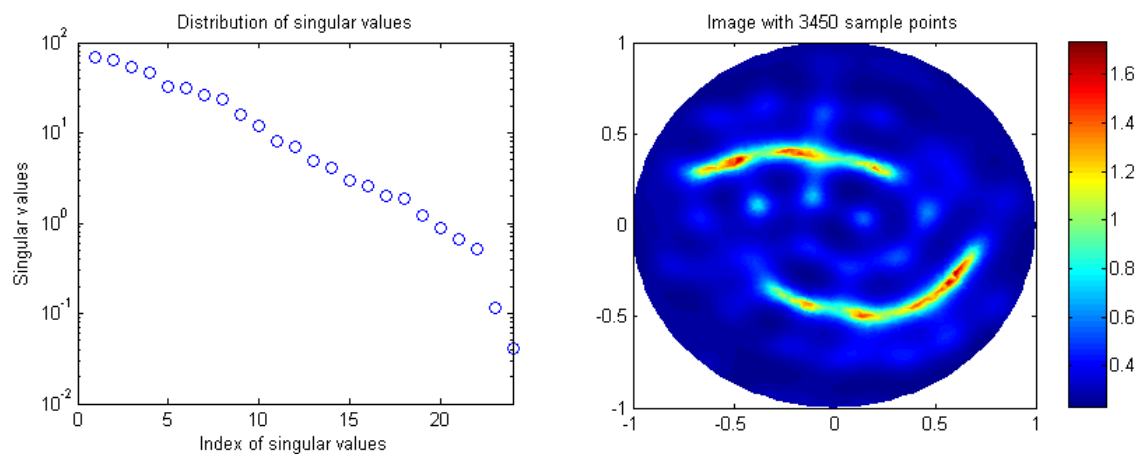


FIG. 5.19 – Same as Fig. 5.18, but with noise  $\xi = 0.05$ .

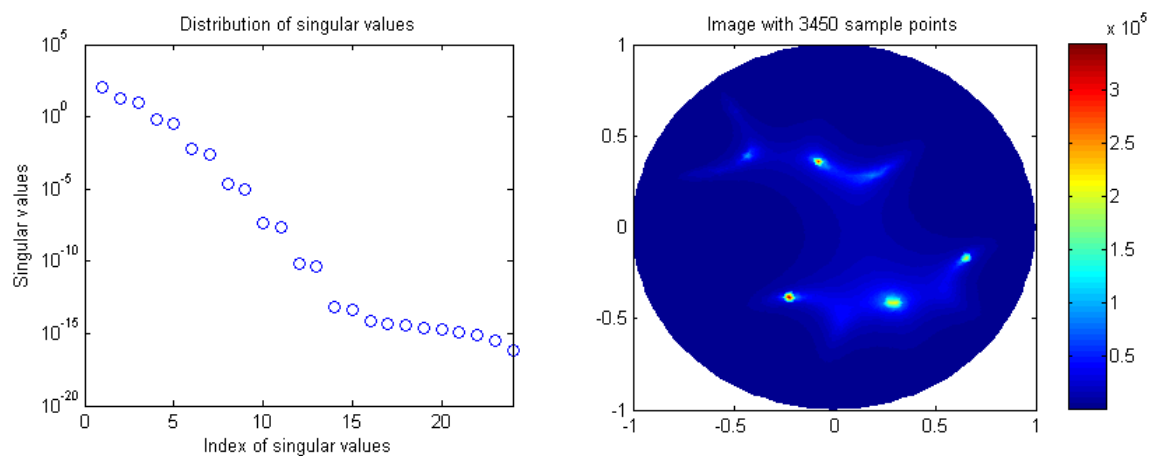


FIG. 5.20 – Same as Fig. 5.18, but with  $\lambda = 2\pi$ .

where

$$\begin{aligned}\Sigma_1^{(6)} &= \{(s, -0.5(s - 0.2)^2 + 0.5) : s \in (-0.7, 0.3)\}, \\ \Sigma_2^{(6)} &= \{(s, (s - 0.2)^3 + (s - 0.2)^2) - 0.4 : s \in (-0.3, 0.7)\}.\end{aligned}$$

The data set of matrix  $A_{\text{meas}}$  is collected with  $N = 24$  and  $\lambda = 0.5$ . Fig. 5.18 and Fig. 5.19 show the reconstructed images of  $\Sigma^{(6)}$  without noise and with noise,  $\xi = 0.05$ , respectively. Fig. 5.20 shows the image when the wavelength is increase to  $2\pi$ .

## 5.9 An optimization approach for extended cracks

Let, as before,  $\{\theta_1, \dots, \theta_N\}$  be a set of  $N$  unit directions and let  $g^{(l)}$  be given by (5.53). In this last section, we briefly mention about a new optimal control approach in order to achieve better reconstruction than the MUSIC-type algorithm.

Let  $u_{\text{meas}}^{(l)}$  be the solution to

$$\begin{cases} \Delta u_{\text{meas}}^{(l)} + \omega^2 u_{\text{meas}}^{(l)} = 0 & \text{in } \Omega \setminus \overline{\Sigma_{\text{true}}}, \\ u_{\text{meas}}^{(l)} = 0 & \text{on } \Sigma_{\text{true}}, \\ \frac{\partial u_{\text{meas}}^{(l)}}{\partial \nu} = g^{(l)} & \text{on } \partial\Omega. \end{cases}$$

Suppose now that  $\Omega$  contains a crack  $\tilde{\Sigma}$  away from the boundary. Denote  $\tilde{u}^{(l)}$  the solution to

$$\begin{cases} \Delta \tilde{u}^{(l)} + \omega^2 \tilde{u}^{(l)} = 0 & \text{in } \Omega \setminus \tilde{\Sigma}, \\ \tilde{u}^{(l)} = 0 & \text{on } \tilde{\Sigma}, \\ \frac{\partial \tilde{u}^{(l)}}{\partial \nu} = g^{(l)} & \text{on } \partial\Omega. \end{cases}$$

A standard approach would be to minimize over  $\Sigma$  the functional

$$\frac{1}{2} \sum_{l=1}^N \|\tilde{u}^{(l)} - u_{\text{meas}}^{(l)}\|_{L^2(\partial\Omega)}^2.$$

In [7], we have suggested a new approach toward inclusion reconstruction which applies here. In the context of extended crack reconstruction, our approach would be to minimize over  $\tilde{\Sigma}$  at the step  $(n + 1)$

$$J(\tilde{\Sigma}) := \frac{1}{2} \sum_{l=1}^N \sum_{j=1}^M \left| \int_{\partial\Omega} (\tilde{u}^{(l)} - u_{\text{meas}}^{(l)}) f_j \right|^2, \quad (5.56)$$

where  $\{f_j\}_{j=1}^M$  are chosen as the basis of the image space of a certain operator involving the crack reconstructed at the step  $n$ . The MUSIC-type algorithm we designed in the last section for obtaining an initial guess corresponds to the particular case of such

optimization algorithm where the functions  $f_j$  are freezed and simply chosen to be plane waves.

The shape derivative  $d_S J(\tilde{\Sigma})$ , which measures the sensitivity of shape perturbations, can be computed using (5.51). The implementation of this optimization algorithm would be the subject of a forthcoming work.

## 5.10 Conclusion

In this chapter, we have provided a MUSIC-type algorithm for locating and estimating the size of small perfectly conducting cracks. Our algorithm is based on a new asymptotic formula that describes the effect of a small crack on the boundary measurements and the construction of a response matrix from these boundary measurements. This algorithm has also been applied to get a very good initial guess in the case of extended cracks. Using the concept of topological derivative, a second algorithm has been tested. To achieve a better reconstruction with higher resolution, an original optimization approach has been proposed.

## Troisième partie

# Conclusion and Appendix

## Sommaire

---

<b>Conclusion and perspective</b>	<b>160</b>
<b>A Appendix</b>	<b>162</b>
A.1 Neumann function . . . . .	162
A.2 Identification of simple poles . . . . .	162
A.3 The Moore–Penrose generalized inverse . . . . .	164
A.4 The singular value decomposition . . . . .	164
A.5 Bessel functions . . . . .	165
A.6 Linear system for numerical simulation . . . . .	166
A.6.1 Linear system for single crack . . . . .	167
A.6.2 Linear system for multiple cracks . . . . .	169
A.7 Uniqueness result . . . . .	171
<b>Références</b>	<b>174</b>

---



## Conclusion and perspective

The main purpose of this thesis is to retrieve the shape of unknown two-dimensional cracks (inhomogeneity with small thickness) or screens (with Dirichlet/Neumann type boundary condition). This thesis is constructed into the following two parts.

In the first part, we have considered the reconstruction of penetrable thin inclusion (crack).

In chapter 1, we have developed a location search algorithm to find the end-points of conductivity cracks. This algorithm is very simple and efficient because no forward solver or iteration processing is needed. Moreover, obtained results show that despite their lack of theoretical precision this algorithm can be applied to the multiple non-rectangular cracks.

In chapter 2, we have designed a MUSIC-type algorithm for imaging of two-dimensional penetrable electromagnetic cracks of arbitrary shape. By examining the eigenvalue structure of Multi-Static Response matrix at a single time-harmonic frequency, we have successfully obtained an image of cracks via a careful thresholding of nonzero singular values. Through the several numerical results, we can conclude this algorithm is fast, effective and stable.

A level set technique is presented in chapter 3 in order to reconstruct the complete shape of penetrable electromagnetic cracks. In this technique two level set functions and calculation of the gradient direction is required to represent and evolve cracks, respectively. With the good initial guess which obtained in the previous chapters, several numerical results demonstrate that this technique give relatively accurate results and are sufficient for applying not only connected but also disconnected cracks.

Reconstruction of impenetrable cracks is considered in the second part.

A non-iterative MUSIC-type algorithm is proposed in chapter 4 to retrieve the screen with Dirichlet/Neumann boundary condition. This algorithm is based on the factorization of Multi-Static Response matrix at a single time-harmonic frequency. Through the experimental results via the same thresholding scheme, we can observe the efficiency of proposed algorithm.

In chapter 5, asymptotic imaging of narrow and extended cracks with Dirichlet boundary condition is considered. Based on the asymptotic expansion of the boundary perturbations due to the small crack, location of a set of small cracks have successfully retrieved via a MUSIC-type algorithm. Moreover, direction of single small crack is successfully recovered from the second singular vector.

We also rigorously derived the asymptotic expansion formula for the boundary perturbations due to the shape deformation of the crack. This formula enables us to develop two different imaging methods for obtaining a good initial guess and successfully demonstrated by a several numerical simulations.

In this thesis, we have proposed very useful reconstruction algorithms but they still requires some improvements. Finally, we mention some possible further developments.

- Rigorous theoretical development of the location search algorithm for the multiple non-rectangular conductivity cracks is needed.

- Research for the proper choice of testing functions  $b$  and  $c$  for imaging of electromagnetic cracks in chapter 2 is expected. Improvement of imaging algorithm for multiple cracks with different material properties is also.
- In the level set method, we assumed all of material properties and thickness of cracks are known. Development an algorithm which overcomes these assumptions will be the one of the good improvement. Furthermore, extension to the impenetrable cracks is also.
- Estimating the normal direction of screens for imaging of screens in chapter 4 is needed for the fast performance of imaging.
- Implementation of the optimization algorithm introduced in 5 to achieve a better reconstruction with higher resolution would be a challengeable subject.
- We expect that proposed algorithms herein can be extended to the inhomogeneous background. For example, reconstruction of cracks buried in the ground.
- Extension to three-dimensional cracks is expected.

## A Appendix

In this appendix, we introduce some useful facts for the reader's convenience.

### A.1 Neumann function

In this part, we state the Neumann function for Laplace operator. A more detailed description can be found in [12].

**Definition A.1** *Let  $\Omega$  be a bounded Lipschitz domain in  $\mathbb{R}^n$ ,  $n \geq 2$ . Let  $N(x, y)$  be the Neumann function for  $\Delta$  in  $\Omega$  corresponding to a Dirac mass at  $y$ . That is,  $N$  is the solution to*

$$\begin{cases} \Delta_x N(x, y) = -\delta_y & \text{in } \Omega \\ \frac{\partial N(x, y)}{\partial \nu_x} \Big|_{\partial\Omega} = -\frac{1}{|\partial\Omega|} & \text{for } y \in \Omega \\ \int_{\partial\Omega} N(x, y) dS(x) = 0 & \text{for } y \in \Omega. \end{cases}$$

Note that the Neumann function  $N(x, y)$  is defined as a function of  $x \in \bar{\Omega}$  for each fixed  $y \in \Omega$ . The operator defined by  $N(x, y)$  is the solution operator for the Neumann problem

$$\begin{cases} \Delta U = 0 & \text{in } \Omega \\ \frac{\partial U}{\partial \nu} = g & \text{on } \partial\Omega, \end{cases} \quad (\text{A.1})$$

namely, the function  $U$  defined by

$$U(x) := \int_{\partial\Omega} N(x, y) g(y) dS(y)$$

is the solution to (A.1) satisfying

$$\int_{\partial\Omega} U(y) dS(y) = 0.$$

### A.2 Identification of simple poles

Our purpose here is to state a method for identification of simple poles in section 1.6 of chapter 1 introduced in [48]. Let  $f(z)$  be a meromorphic function of the form

$$f(z) = \sum_{j=1}^m \frac{\beta_j}{z - \alpha_j}$$

whose value on the circle  $|z| = R$  is known. Let  $N$  be an upper bound for the number of poles of  $f$ , which is assumed to be known. For  $n = 0, 1, \dots, 2N - 1$ , define

$$c_n := \frac{1}{2\pi i} \int_{|z|=R} z^n f(z) dz = \sum_{j=1}^m \beta_j \alpha_j^n.$$

This  $c_n$  can be computed from  $f(z)$  on  $|z| = R$ . The method of identification of poles from the knowledge of  $c_n$ ,  $n = 0, 1, \dots, 2N - 1$  is based on the following simple observations.

**Lemma A.2** *Suppose that the sequence  $\{c_n\}$  takes the form*

$$c_n = \sum_{j=1}^k \beta_j \alpha_j^n$$

*for  $n = 0, 1, \dots$ . If  $l_1, \dots, l_k$  satisfies the generating equation*

$$c_{n+k} + l_1 c_{n+k-1} + \dots + l_k c_n = 0 \quad \text{for } n = 0, 1, \dots, k-1 \quad (\text{A.2})$$

*then  $\alpha_1, \alpha_2, \dots, \alpha_k$  are solutions of*

$$z^k + l_1 z^{k-1} + \dots + l_k = 0. \quad (\text{A.3})$$

*The converse is also true. Furthermore, if (A.2) holds, then it holds for all  $n$ .*

*Proof.* If  $\alpha_1, \alpha_2, \dots, \alpha_k$  are solutions of (A.3), then for all  $n$ ,

$$\begin{aligned} c_{n+k} + l_1 c_{n+k-1} + \dots + l_k c_n &= \sum_{j=1}^k \beta_j \alpha_j^{n+k} + l_1 \sum_{j=1}^k \beta_j \alpha_j^{n+k-1} + \dots + l_k \sum_{j=1}^k \beta_j \alpha_j^n \\ &= \sum_{j=1}^k \beta_j \alpha_j^n (\alpha_j^k + l_1 \alpha_j^{k-1} + \dots + l_k) = 0. \end{aligned} \quad (\text{A.4})$$

Conversely, since  $c_{n+k} + l_1 c_{n+k-1} + \dots + l_k c_n = 0$  for  $n = 0, 1, \dots, k-1$ , it follows from the identity (A.4) that

$$\sum_{j=1}^k \beta_j \alpha_j^n (\alpha_j^k + l_1 \alpha_j^{k-1} + \dots + l_k) = 0 \quad \text{for } n = 0, 1, \dots, k-1.$$

Since

$$\det \begin{pmatrix} \beta_1 & \beta_2 & \dots & \beta_k \\ \beta_1 \alpha_1 & \beta_2 \alpha_2 & \dots & \beta_k \alpha_k \\ \vdots & \vdots & \ddots & \vdots \\ \beta_1 \alpha_1^{k-1} & \beta_2 \alpha_2^{k-1} & \dots & \beta_k \alpha_k^{k-1} \end{pmatrix} = \beta_1 \beta_2 \dots \beta_k \prod_{1 \leq i, j \leq k} (\alpha_j - \alpha_i) \neq 0,$$

we get

$$\alpha_j^k + l_1 \alpha_j^{k-1} + \dots + l_k = 0$$

for  $j = 1, 2, \dots, k$ . This completes the proof.

### A.3 The Moore–Penrose generalized inverse

Let  $K$  be a bounded operator of a Hilbert space  $H_1$  into the Hilbert space  $H_2$ . Let  $K^*$  denote the adjoint of  $K$ . The Moore–Penrose generalized solution  $f^+$  to  $Kf = g$  is defined as follows:  $f^+$  is the element with the smallest norm in the set of the minimizers of  $\|Kf - g\|$  (if this set is nonempty, i.e., if  $g \in \text{Range}(K) + \text{Range}(K)^\perp$ ). It can be shown that  $f^+$  is the unique solution to the normal equation

$$K^*Kf = K^*g$$

in  $\overline{\text{Range}(K^*)}$ . The linear operator  $K^+$  defined by

$$f^+ = K^+g \quad \text{for } g \in \text{Range}(K) + \text{Range}(K)^\perp$$

is called *the Moore–Penrose generalized inverse*.

### A.4 The singular value decomposition

Let  $K$  be a bounded operator of a Hilbert space  $H_1$  into the Hilbert space  $H_2$ . By the singular value decomposition (SVD) we mean a representation of  $K$  in the form

$$Kf = \sum_j \lambda_j \langle f, f_j \rangle g_j$$

where  $\{f_j\}, \{g_j\}$  are orthonormal systems in  $H_1, H_2$ , respectively, and  $\lambda_j$  are positive numbers, the singular values of  $K$ . The sum may be finite or infinite. The adjoint of  $K$  is given by

$$K^*g = \sum_j \lambda_j \langle g, g_j \rangle f_j$$

and the operators

$$K^*Kf = \sum_j \lambda_j^2 \langle f, f_j \rangle f_j, \quad KK^*g = \sum_j \lambda_j^2 \langle g, g_j \rangle g_j$$

are self-adjoint operators in  $H_1, H_2$ , respectively. The spectrum of  $K^*K, KK^*$  consists of the eigenvalues  $\lambda_j^2$  and possibly the eigenvalue 0, whose multiplicity may be infinite.

The Moore–Penrose generalized inverse is given by

$$K^+g = \sum_j \lambda_j^{-1} \langle g, g_j \rangle f_j.$$

Let us review the basic concepts of singular value decomposition of a matrix. Let  $M_{m,n}(\mathbb{C})$  denote the set of all  $m \times n$  matrices over  $\mathbb{C}$ . The set  $M_{n,n}(\mathbb{C})$  is abbreviated to  $M_n(\mathbb{C})$ . The spectral theorem to the positive semi-definite matrices  $KK^*$  and  $K^*K$  gives the following singular values decomposition of a matrix  $K \in M_{m,n}(\mathbb{C})$ .

**Theorem A.3 (Spectral theorem)** *Let  $K \in M_{m,n}(\mathbb{C})$  be given, and let  $q = \min\{m, n\}$ . There is a matrix  $S = (\lambda_{jl}) \in M_{m,n}(\mathbb{R})$  with  $\lambda_{jl} = 0$  for all  $j \neq l$  and*

$\lambda_{11} \geq \lambda_{22} \geq \cdots \geq \lambda_{qq} \geq 0$ , and there are two unitary matrices  $V \in M_m(\mathbb{C})$  and  $W \in M_n(\mathbb{C})$  such that

$$K = VSW^*.$$

The numbers  $\{\lambda_{jj}\}$  are nonnegative square roots of the eigenvalues of  $KK^*$ , and hence are uniquely determined. The columns of  $V$  are eigenvectors of  $KK^*$  and the columns of  $W$  are eigenvectors of  $K^*K$  (arranged in the same order as the corresponding eigenvalues  $\lambda_{jj}^2$ ).

The diagonal entries  $\lambda_{jj}$ ,  $j = 1, 2, \dots, q = \min\{m, n\}$  of  $S$  are called the *singular values* of  $K$ , and the columns of  $V$  and the columns  $W$  are the (respectively, *left* and *right*) *singular vectors* of  $K$ .

Singular value decomposition has the following desirable computational properties :

- (1) The rank of  $K$  can be easily determined from its singular value decomposition. Specifically,  $\text{rank}(K)$  equals to the number of nonzero singular value of  $K$ .
- (2) The  $L_2$ -norm of  $K$  is given by

$$\|K\|_2 = \left( \sum_{j=1}^q \lambda_{jj}^2 \right)^{1/2}.$$

- (3) Singular value decomposition is an effective computational tool for finding lower-rank approximations to a given matrix. Specifically, let  $p < \text{rank}(K)$ . Then the rank  $p$  matrix  $K_p$  minimizing  $\|K - K_p\|_2$  is given by

$$K_p = VS_pW^*,$$

where the matrix  $S_p$  is obtained from  $S$  after the singular values  $\lambda_{jj}$ ,  $p+1 \leq j \leq q$ , are set to zero.

## A.5 Bessel functions

The Bessel function of the first kind of real order  $\nu$  is defined by

$$J_\nu(x) = \left(\frac{x}{2}\right)^\nu \sum_{s=0}^{+\infty} \frac{(-x^2/4)^s}{s! \Gamma(\nu + s + 1)},$$

where  $\Gamma$  is the gamma function.

For  $n \in \mathbb{Z}$ , we have the following integral representation

$$J_n(x) = \frac{1}{2\pi} \int_{-\pi}^{\pi} e^{ix \sin \theta - in\theta} d\theta,$$

i.e., the functions  $J_n(x)$  are the Fourier coefficients of  $e^{ix \sin \theta}$ . Therefore we can write

$$e^{ix \sin \theta} = \sum_{n \in \mathbb{Z}} J_n(x) e^{in\theta}. \quad (\text{A.5})$$

By the principle of analytic continuation, (A.5) is valid for all complex  $\theta$ , refer to [63].

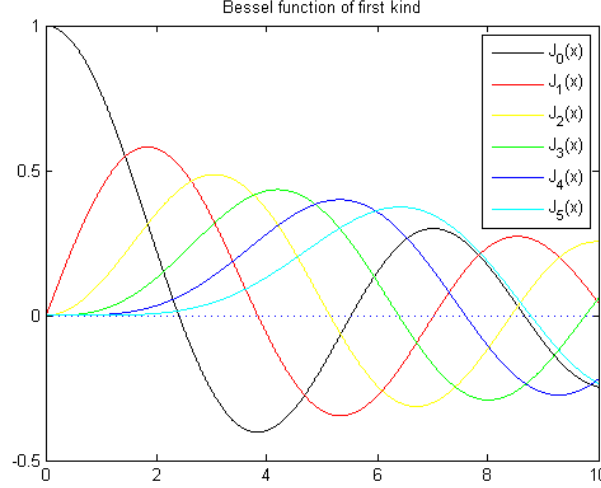


FIG. A.1 – Bessel functions  $J_n(x)$  of the first kind of order  $n$  for  $n = 0, 1, \dots, 5$ .

For arguments  $x < \nu$ , the Bessel function look qualitatively like simple powers law, with the asymptotic form for  $0 < x \ll \nu$

$$J_\nu(x) \sim \frac{1}{\Gamma(\nu + 1)} \left(\frac{x}{2}\right)^\nu.$$

For  $x > \nu$ , the Bessel function look qualitatively like cosine wave whose amplitude decays as  $x^{-1/2}$ . The asymptotic form for  $x \gg \nu$  is

$$J_\nu(x) \sim \sqrt{\frac{2}{\pi x}} \cos\left(x - \frac{\nu\pi}{2} - \frac{\pi}{4}\right).$$

In the transition region where  $x \sim \nu$ , the typical amplitude of the Bessel function is

$$J_\nu(\nu) \sim \frac{2^{1/3}}{3^{2/3}\Gamma(\frac{2}{3})} \nu^{1/3} \sim \frac{0.4473}{\nu^{1/3}},$$

which holds asymptotically for large  $\nu$ .

## A.6 Linear system for numerical simulation

Our purpose here is to sketch a quadrature method for the numerical simulation in section 4.4.2 of chapter 4. Derivation of the linear system for the multiple cracks is similar to the single one introduced in [52, Section 2]. So, we introduce the linear system for the single crack and extend it to multiple ones. We also recommend [60, Chapter 3] for another numerical solution scheme of the multiple crack case.

### A.6.1 Linear system for single crack

In order to establish a quadrature method for numerical simulation of the single-crack case, we start from the integral equation (4.8) in section 4.2 of chapter 4

$$\frac{i}{4} \int_{\Gamma} H_0^1(k|x-y|) \varphi(y) dy = -u_0(x) \quad \text{for } x \in \Gamma.$$

By substituting  $s = \cos t$  for  $t \in [0, \pi]$  into  $\Gamma$ , the formula (4.8) can be transformed into the following parametric form

$$\frac{1}{2\pi} \int_0^\pi H(t, \tau) \psi(\tau) d\tau = g(t) \quad (\text{A.6})$$

where

$$\begin{aligned} \psi(t) &:= |\sin(t)| |z'(\cos t)| \varphi(z(\cos t)) \\ g(t) &:= -2u_0(z(\cos t)) \end{aligned} \quad (\text{A.7})$$

for all  $t \in [0, \pi]$  and the kernel  $H$  is given by

$$H(t, \tau) := \frac{\pi}{i} H_0^1(k|z(\cos t) - z(\cos \tau)|) \quad (\text{A.8})$$

for  $t \neq \tau$ . The author in [52] has transformed the integral equation (A.6) into an equation over the interval  $2\pi$ . From this transformation, (A.6) is equivalent to find an even  $2\pi$ -periodic function  $\psi \in C(\mathbb{R})$  solution of

$$\frac{1}{4\pi} \int_0^{2\pi} H(t, \tau) \psi(\tau) d\tau = g(t) \quad (\text{A.9})$$

for  $t \in [0, 2\pi]$ . From the definition of the Hankel function and the power series of Bessel and Neumann functions of order zero, the kernel  $H$  can be written

$$H(t, \tau) = [1 + H_1(t, \tau)] \ln \left( \frac{4}{e^2} (\cos t - \cos \tau)^2 \right) + H_2(t, \tau) \quad (\text{A.10})$$

where  $H_1$  and  $H_2$  can be written for  $t \neq \tau$ ,

$$\begin{aligned} H_1(t, \tau) &:= J_0(k|z(\cos t) - z(\cos \tau)|) - 1 \\ H_2(t, \tau) &:= H(t, \tau) - [1 + H_1(t, \tau)] \ln \left( \frac{4}{e^2} (\cos t - \cos \tau)^2 \right) \end{aligned} \quad (\text{A.11})$$

and

$$\begin{aligned} H_1(t, t) &= \frac{\partial}{\partial t} H_1(t, t) = 0 \\ H_2(t, t) &= \frac{\pi}{i} + 2 \ln \left( \frac{ke}{4} |z'(\cos t)| \right) + 2C \end{aligned} \quad (\text{A.12})$$

with Euler's constant  $C = 0.57721 \dots$ . By using (A.10), (A.11) and (A.12), integral equation (A.9) turns into

$$\frac{1}{2\pi} \int_0^{2\pi} K(t, \tau) \psi(\tau) d\tau = g(t) \quad (\text{A.13})$$



with the kernel  $K$

$$K(t, \tau) = \left\{ 1 + \sin^2 \left( \frac{t - \tau}{2} \right) K_1(t, \tau) \right\} \ln \left( \frac{4}{e} \sin^2 \left( \frac{t - \tau}{2} \right) \right) + K_2(t, \tau) \quad (\text{A.14})$$

where  $K_1$  and  $K_2$  can be written for  $t \neq \tau$ ,

$$K_1(t, \tau) := \frac{H_1(t, \tau)}{\sin^2 \left( \frac{t - \tau}{2} \right)}, \quad K_2(t, \tau) := \frac{1}{2} H_2(t, \tau) \quad (\text{A.15})$$

and

$$K_1(t, t) = -k^2 \sin^2 t |z'(\cos t)|^2. \quad (\text{A.16})$$

In order to discretize the integral equation (A.13), let us set the equidistant points  $t_j$  for a given number  $n \in \mathbb{N}$  (for a partition of interval  $[0, 2\pi]$ ) as

$$t_j := \frac{j\pi}{n}$$

with  $j = 0, 1, \dots, 2n - 1$ . Then, (A.13) can be approximated to the following linear system

$$\sum_{l=0}^{2n-1} \left\{ R_{|j-l|} + F_{|j-l|} K_1(t_j, t_l) + \frac{1}{2n} K_2(t_j, t_l) \right\} \psi(t_l) = g(t_j) \quad (\text{A.17})$$

where  $K_1$  and  $K_2$  are defined in (A.15) and (A.16) and the coefficients  $R_j$  and  $F_j$  are given

$$\begin{aligned} R_j &:= R_j(0) = \frac{1}{2n} \left\{ c_0 + 2 \sum_{m=1}^{n-1} c_m \cos \left( \frac{mj\pi}{n} \right) + (-1)^j c_n \right\} \\ F_j &:= F_j(0) = \frac{1}{2n} \left\{ \gamma_0 + 2 \sum_{m=1}^{n-1} \gamma_m \cos \left( \frac{mj\pi}{n} \right) + (-1)^j \gamma_n \right\} \end{aligned} \quad (\text{A.18})$$

and the constants  $c_m$  and  $\gamma_m$  are

$$c_m := -\frac{1}{\max(1, |m|)} \quad \text{and} \quad \gamma_m := \frac{1}{4} (2c_m - c_{m+1} - c_{m-1}). \quad (\text{A.19})$$

Note that the linear system (A.17) is expressed as an  $(n+1) \times (n+1)$ -system due to the symmetry property of  $\psi$ , i.e.,  $\psi$  satisfies

$$\psi(t_j) = \psi(t_{2n-j})$$

for  $j = 0, 1, \dots, n$  (see [52]).

By substituting  $s = \cos t$  for  $t \in [0, \pi]$  into  $\Gamma$ , formula (4.11) can be transformed into the following parametric form

$$u_\infty(\hat{x}; \theta) = -\frac{e^{i\frac{\pi}{4}}}{\sqrt{8\pi k}} \int_0^\pi e^{-ik\hat{x} \cdot z(\cos \tau)} \psi(\tau) d\tau, \quad \hat{x} \in S^1. \quad (\text{A.20})$$

Hence, after solving the linear system (A.17), the far-field pattern (A.20) can be obtained by the following trapezoidal rule

$$u_\infty(\hat{x}; \theta) \approx -\frac{e^{i\frac{\pi}{4}}}{\sqrt{8\pi k}} \frac{\pi}{n} \sum_{j=0}^n e^{-ik\hat{x} \cdot z(\cos t_j)} \psi(t_j). \quad (\text{A.21})$$

### A.6.2 Linear system for multiple cracks

Derivation of the linear system for the multiple cracks is similar to the one for the single one. As in the previous section, we start from the integral equation

$$\frac{i}{4} \sum_{j=1}^L \int_{\Gamma} H_0^1(k|x-y|) \varphi_j(y) dy = -u_0(x) \quad \text{for } x \in \Gamma. \quad (\text{A.22})$$

By substituting  $s = \cos t$  for  $t \in [0, \pi]$  into  $\Gamma$  and carrying out the same computation for the single crack case, the formula (A.22) can be rewritten as

$$\begin{aligned} \frac{1}{4\pi} \int_0^{2\pi} [H_{1,1}(t, \tau) \psi_1(\tau) + H_{1,2}(t, \tau) \psi_2(\tau) + \cdots + H_{1,L}(t, \tau) \psi_L(\tau)] d\tau &= g_1(t) \\ \frac{1}{4\pi} \int_0^{2\pi} [H_{2,1}(t, \tau) \psi_1(\tau) + H_{2,2}(t, \tau) \psi_2(\tau) + \cdots + H_{2,L}(t, \tau) \psi_L(\tau)] d\tau &= g_2(t) \\ &\vdots \\ \frac{1}{4\pi} \int_0^{2\pi} [H_{L,1}(t, \tau) \psi_1(\tau) + H_{L,2}(t, \tau) \psi_2(\tau) + \cdots + H_{L,L}(t, \tau) \psi_L(\tau)] d\tau &= g_L(t) \end{aligned} \quad (\text{A.23})$$

Here, the kernel  $H_{j,l}$ ,  $j, l = 1, 2, \dots, L$  is given by

$$H_{j,l}(t, \tau) := \frac{\pi}{i} H_0^1(k|z_j(\cos t) - z_l(\cos \tau)|) \quad (\text{A.24})$$

for  $t \neq \tau$ . For convenience, we change the formula (A.10), (A.11) and (A.12) as follows :

$$H_{j,l}(t, \tau) = [1 + H_1^{(j,l)}(t, \tau)] \ln \left( \frac{4}{e^2} (\cos t - \cos \tau)^2 \right) + H_2^{(j,l)}(t, \tau) \quad (\text{A.25})$$

where  $H_1^{(j,l)}$  and  $H_2^{(j,l)}$  can be written for  $t \neq \tau$ ,

$$\begin{aligned} H_1^{(j,l)}(t, \tau) &:= J_0(k|z_j(\cos t) - z_l(\cos \tau)|) - 1 \\ H_2^{(j,l)}(t, \tau) &:= H_{j,l}(t, \tau) - [1 + H_1^{(j,l)}(t, \tau)] \ln \left( \frac{4}{e^2} (\cos t - \cos \tau)^2 \right) \end{aligned} \quad (\text{A.26})$$

and for  $j = l$ ,

$$\begin{aligned} H_1^{(j,j)}(t, t) &= \frac{\partial}{\partial t} H_1^{(j,j)}(t, t) = 0 \\ H_2^{(j,j)}(t, t) &= \frac{\pi}{i} + 2 \ln \left( \frac{ke}{4} |z'_j(\cos t)| \right) + 2C \end{aligned} \quad (\text{A.27})$$

with Euler's constant  $C = 0.57721 \dots$ . By using (A.25), (A.26) and (A.27), the integral equation (A.23) turns into

$$\begin{aligned} \frac{1}{2\pi} \int_0^{2\pi} [K_{1,1}(t, \tau) \psi_1(\tau) + K_{1,2}(t, \tau) \psi_2(\tau) + \cdots + K_{1,L}(t, \tau) \psi_L(\tau)] d\tau &= g_1(t) \\ \frac{1}{2\pi} \int_0^{2\pi} [K_{2,1}(t, \tau) \psi_1(\tau) + K_{2,2}(t, \tau) \psi_2(\tau) + \cdots + K_{2,L}(t, \tau) \psi_L(\tau)] d\tau &= g_1(t) \\ &\vdots \\ \frac{1}{2\pi} \int_0^{2\pi} [K_{L,1}(t, \tau) \psi_1(\tau) + K_{L,2}(t, \tau) \psi_2(\tau) + \cdots + K_{L,L}(t, \tau) \psi_L(\tau)] d\tau &= g_L(t) \end{aligned} \quad (\text{A.28})$$

with the kernel  $K_{j,l}$

$$K_{j,l}(t, \tau) = \left\{ 1 + \sin^2 \left( \frac{t - \tau}{2} \right) K_1^{(j,l)}(t, \tau) \right\} \ln \left( \frac{4}{e} \sin^2 \left( \frac{t - \tau}{2} \right) \right) + K_2^{(j,l)}(t, \tau) \quad (\text{A.29})$$

where  $K_1^{(j,l)}$  and  $K_2^{(j,l)}$  can be written for  $t \neq \tau$ ,

$$K_1^{(j,l)}(t, \tau) := \frac{H_1^{(j,l)}(t, \tau)}{\sin^2 \left( \frac{t - \tau}{2} \right)}, \quad K_2^{(j,l)}(t, \tau) := \frac{1}{2} H_2^{(j,l)}(t, \tau) \quad (\text{A.30})$$

and for  $j = l$ ,

$$K_1^{(j,j)}(t, t) = -k^2 \sin^2 t \left| z'_j(\cos t) \right|^2. \quad (\text{A.31})$$

In order to discretize the integral equation (A.28), let us set the equidistant points  $t_j$  for a given number  $n \in \mathbb{N}$  (for a partition of interval  $[0, 2\pi]$ ) as

$$t_j := \frac{j\pi}{n}$$

with  $j = 0, 1, \dots, 2n - 1$ . Then, (A.28) can be approximated to the following linear system

$$\begin{aligned} \sum_{l=0}^{2n-1} [A_{1,1}\psi_1(t_l) + A_{1,2}\psi_2(t_l) + \dots + A_{1,L}\psi_L(t_l)] &= g_1(t_j) \\ \sum_{l=0}^{2n-1} [A_{2,1}\psi_1(t_l) + A_{2,2}\psi_2(t_l) + \dots + A_{2,L}\psi_L(t_l)] &= g_2(t_j) \\ &\vdots \\ \sum_{l=0}^{2n-1} [A_{L,1}\psi_1(t_l) + A_{L,2}\psi_2(t_l) + \dots + A_{L,L}\psi_L(t_l)] &= g_L(t_j) \end{aligned} \quad (\text{A.32})$$

here  $A_{j,l}$  for  $j, l = 1, 2, \dots, L$  is defined as

$$A_{j,l} = R_{|j-l|} + F_{|j-l|} K_1^{(j,l)}(t_j, t_l) + \frac{1}{2n} K_2^{(j,l)}(t_j, t_l).$$

Note that the linear system (A.32) is expressed as an  $L(n+1) \times L(n+1)$ -system due to the symmetry property of  $\psi_j$ , i.e.,  $\psi_j$  satisfies

$$\psi_j(t_l) = \psi_j(t_{2n-l})$$

for  $j = 1, 2, \dots, L$  and  $l = 0, 1, \dots, n$  (See [52]).

Similarly with the single-crack case, by substituting  $s = \cos t$  for  $t \in [0, \pi]$  into  $\Gamma$ , the far-field pattern formula can be transformed into the following parametric form

$$u_\infty(\hat{x}; \theta) = -\frac{e^{i\frac{\pi}{4}}}{\sqrt{8\pi k}} \sum_{j=1}^L \int_0^\pi e^{-ik\hat{x} \cdot z_j(\cos \tau)} \psi_j(\tau) d\tau, \quad \hat{x} \in S^1. \quad (\text{A.33})$$

Hence, after solving the linear system (A.32), the far-field pattern for a multiple crack (A.33) can be obtained by the following trapezoidal rule

$$u_\infty(\hat{x}; \theta) \approx -\frac{e^{i\frac{\pi}{4}}}{\sqrt{8\pi k}} \frac{\pi}{n} \sum_{j=1}^L \sum_{l=0}^n e^{-ik\hat{x} \cdot z_j(\cos t_l)} \psi_j(t_l). \quad (\text{A.34})$$

## A.7 Uniqueness result

This is an important result from the theory of the Helmholtz equation. It will help us prove uniqueness for exterior Helmholtz problems. For its proof, we refer to [34, Lemma 2.11].

**Lemma A.4** *Let  $R_0 > 0$  and  $B_R(0) = \{x : |x| < R\}$ . Let  $u$  satisfy the Helmholtz equation*

$$\Delta u(x) + k_0^2 u(x) = 0$$

*for  $|x| > R_0$ . Assume, furthermore, that*

$$\lim_{R \rightarrow +\infty} \int_{\partial B_R(0)} |u(x)|^2 dS(x) = 0.$$

*Then  $u(x) \equiv 0$  for  $|x| > R_0$ .*

Note that, the assertion of this lemma does not hold if  $k_0$  is imaginary or  $k_0 = 0$ .

Now, using Lemma A.4, we can establish the following uniqueness result for the exterior Helmholtz problem.

**Lemma A.5** *Suppose  $n = 2$  or  $3$ . Let  $\Omega$  be a bounded Lipschitz domain in  $\mathbb{R}^n$ . Let  $u \in H_{\text{loc}}^1(\mathbb{R}^n \setminus \overline{\Omega})$  satisfy*

$$\begin{cases} \Delta u(x) + k_0^2 u(x) = 0 & \text{in } \mathbb{R}^n \setminus \overline{\Omega} \\ \left| \frac{\partial u}{\partial r} - ik_0 u \right| = O\left(r^{-\frac{n+1}{2}}\right) & \text{as } r = |x| \rightarrow +\infty \text{ uniformly in } \frac{x}{|x|} \\ u = 0 \text{ or } \frac{\partial u}{\partial \nu} = 0 & \text{on } \partial\Omega. \end{cases} \quad (\text{A.35})$$

*Then  $u \equiv 0$  in  $\mathbb{R}^n \setminus \overline{\Omega}$ .*

*Proof.* Let  $B_R(0) = \{|x| < R\}$ . For  $R$  large enough,  $\Omega \subset B_R(0)$ . Notice first that by multiplying  $\Delta u(x) + k_0^2 u(x) = 0$  by  $\bar{u}$  and integrating by parts over  $B_R(0) \setminus \overline{\Omega}$  we arrive at

$$\text{Im} \int_{\partial B_R(0)} \bar{u} \frac{\partial u}{\partial \nu} dS = 0.$$

But

$$\text{Im} \int_{\partial B_R(0)} \bar{u} \left( \frac{\partial u}{\partial r} - ik_0 u \right) dS = -k_0 \int_{\partial B_R(0)} |u|^2 dx.$$

Applying the Cauchy-Schwarz inequality,

$$\left| \text{Im} \int_{\partial B_R(0)} \bar{u} \left( \frac{\partial u}{\partial r} - ik_0 u \right) dS \right| \leq \left( \int_{\partial B_R(0)} |u|^2 dx \right)^{1/2} \left( \int_{\partial B_R(0)} \left| \frac{\partial u}{\partial r} - ik_0 u \right|^2 dS \right)^{1/2},$$

and using the radiation condition (A.35) we get

$$\left| \text{Im} \int_{\partial B_R(0)} \bar{u} \left( \frac{\partial u}{\partial r} - ik_0 u \right) dS \right| \leq \frac{C}{R} \left( \int_{\partial B_R(0)} |u|^2 dx \right)^{1/2}$$

for some constant  $C$  independent of  $R$ . Consequently, we obtain that

$$\left( \int_{\partial B_R(0)} |u|^2 dx \right)^{1/2} \leq \frac{C}{R},$$

which indicates by Rellich's lemma that  $u \equiv 0$  in  $\mathbb{R}^2 \setminus \overline{B_R(0)}$ . Hence, by the unique continuation property for  $\Delta + k_0^2$ , we can conclude that  $u \equiv 0$  up to the boundary  $\partial\Omega$ . This finishes the proof.



## Références

- [1] J. F. P. J. Abascal, M. Lambert, D. Lesselier and O. Dorn, *3-D Eddy-current imaging of metal tubes by gradient-based, controlled evolution of level sets*, IEEE Trans. Magnetics, to appear.
- [2] D. Álvarez, O. Dorn and M. Moscoso, *Reconstructing thin shapes from boundary electrical measurements with level sets*, Int. J. Inf. Syst. Sci. 2, no. 4, 498–511, 2006.
- [3] H. Ammari, *An introduction to mathematics of emerging biomedical imaging*, Math & Applications, Volume 62, Springer-Verlag, Berlin, 2008.
- [4] H. Ammari, E. Beretta and E. Francini, *Reconstruction of thin conductivity imperfections*, Applicable Analysis, 83, 63–76, 2004.
- [5] H. Ammari, E. Beretta and E. Francini, *Reconstruction of thin conductivity imperfections, II. The case of multiple segments*, Applicable Analysis, 85, 87–105, 2006.
- [6] H. Ammari, E. Bonnetier and Y. Capdeboscq, *Enhanced resolution in structured media*, preprint.
- [7] H. Ammari, P. Garapon, F. Jouve and H. Kang, *A new optimal control approach toward reconstruction of acoustic and elastic inclusions*, preprint.
- [8] H. Ammari, E. Iakovleva and D. Lesselier, *A MUSIC algorithm for locating small inclusions buried in a half-space from the scattering amplitude at a fixed frequency*, SIAM Multiscale Modeling Simul., 3, 597–628, 2005.
- [9] H. Ammari, E. Iakovleva and D. Lesselier, *Two numerical methods for recovering small inclusions from the scattering amplitude at a fixed frequency*, SIAM J. Sci. Comput., 27, 130–158, 2005.
- [10] H. Ammari, E. Iakovleva, D. Lesselier and G. Perrusson, *MUSIC type electromagnetic imaging of a collection of small three-dimensional inclusions*, SIAM J. Scient. Comput., 29, 674–709, 2007.
- [11] H. Ammari and H. Kang, *Polarization and moment tensors : with applications to inverse problems and effective medium theory*, Applied Mathematical Sciences Series, Volume 162, Springer-Verlag, New York, 2007.
- [12] H. Ammari and H. Kang, *Reconstruction of small inhomogeneities from boundary measurements*, Lecture Notes in Mathematics, Volume 1846, Springer-Verlag, Berlin, 2004.
- [13] H. Ammari, H. Kang, E. Kim, K. Louati and M. S. Vogelius, *A MUSIC-type algorithm for detecting internal corrosion from electrostatic boundary measurements*, Numerische Mathematik, 108, 501–528, 2008.
- [14] H. Ammari, H. Kang and H. Lee, *Layer potential techniques in spectral analysis*, Mathematical Surveys and Monographs, Volume 153, American Mathematical Society, Providence RI, 2009.
- [15] H. Ammari, H. Kang, H. Lee and W. K. Park, *Asymptotic imaging of perfectly conducting cracks*, submitted.
- [16] H. Ammari, O. Kwon, J. K. Seo and E. J. Woo, *Anomaly detection in T-Scan trans-admittance imaging system*, SIAM J. Appl. Math., 65, 252–266, 2004.

- [17] H. Ammari, S. Moskow and M. Vogelius, *Boundary integral formulas for the reconstruction of electromagnetic imperfections of small diameter*, ESAIM Control Optim. Calc. Var., 9, 49–66, 2002.
- [18] H. Ammari and J. K. Seo, *An accurate formula for the reconstruction of conductivity inhomogeneities*, Advances Appl. Math., 30, 679–705, 2003.
- [19] S. Andrieux and A. Ben Abda, *Identification of planar cracks by complete overdetermined data : inversion formulae*, Inverse Problems, 12, 553–563, 1996.
- [20] G. Aubert and P. Kornprobst, *Mathematical problems in image processing, partial differential equations and the calculus of variations*, Springer-Verlag, Berlin, Heidelberg, New York, 2002.
- [21] D. Auroux and M. Masmoudi, *Image processing by topological asymptotic analysis*, ESAIM : Proc., to appear.
- [22] Z. Belhachmi and D. Bucur, *Stability and uniqueness for the crack identification problem*, SIAM J. Control Optim., 46, 253–273, 2007.
- [23] C. Berenstein, D. C. Chang and E. Wang, *Determining a surface breaking crack from steady-state electrical boundary measurements reconstruction method*, Rend. Istit. Mat. Univ. Trieste, 29, 63–92, 1997.
- [24] E. Beretta and E. Francini, *Asymptotic formulas for perturbations of the electromagnetic fields in the presence of thin imperfections*, Contemporary Mathematics, Vol. 333, 49–63, 2003.
- [25] E. Beretta, E. Francini and M. Vogelius, *Asymptotic formulas for steady state voltage potentials in the presence of thin inhomogeneities. A rigorous error analysis*, J. Math. Pures Appl., 82, 1277–1301, 2003.
- [26] L. Borcea, *Electrical Impedance Tomography*, Inverse Problems, 18, R99–R136, 2002.
- [27] M. Brühl, M. Hanke and M. Pidcock, *Crack detection using electrostatic measurements*, M2AN Math. Model. Numer. Anal., 35, 595–605, 2001.
- [28] K. Bryan and M. S. Vogelius, *A review of selected works on crack identification*, Geometric Methods in Inverse Problems and PDE Control (IMA Vol. 137), Springer, Berlin, 2004.
- [29] F. Cakoni and D. Colton, *The linear sampling method for cracks*, Inverse Problems, 19, 279–295, 2003.
- [30] F. Cakoni, D. Colton and E. Darrigrand, *The inverse electromagnetic scattering problem for screens*, Inverse Problems, 19, 627–642, 2003.
- [31] Y. Capdeboscq and M. S. Vogelius, *Imagerie électromagnétique de petites inhomogénéités*, ESAIM : Proc. 22, 40–51, 2008.
- [32] M. Cheney, *The linear sampling method and the MUSIC algorithm*, Inverse Problems, 17, 591–595, 2001.
- [33] D. Colton and R. Kress, *Integral equation methods in scattering theory*, John Wiley, New York, 1983.
- [34] D. Colton and R. Kress, *Inverse acoustic and electromagnetic scattering theory*, Applied Math. Sciences 93, Springer-Verlag, New York, 1992.
- [35] D. Colton, H. Haddar and P. Monk, *The linear sampling method for solving the electromagnetic inverse scattering problem*, SIAM J. Scient. Comput., 24, 719–731, 2002.



- [36] R. Courant, K. Friedrichs and H. Lewy, *On the partial differential equations of mathematical physics*, IBM Journal, 215–234, English translation of the 1928 German original.
- [37] O. Dorn, H. Bertete-Aguirre, J. G. Berryman and G. C. Papanicolaou, *A nonlinear inversion method for 3D electromagnetic imaging using adjoint fields*, Inverse Problems, 15, 1523–1558, 1999.
- [38] O. Dorn and D. Lesselier, *Level set methods for inverse scattering*, Inverse Problems, 22, R67–R131, 2006.
- [39] A. R. Elcrat, V. Isakov and O. Neculoiu, *On finding a surface crack from boundary measurements*, Inverse Problems, 11, 343–351, 1995.
- [40] L. C. Evans, *Partial differential equations*, Graduate Studies in Mathematics 19, America mathematical society, 1998.
- [41] G. B. Folland, *Introduction to Partial Differential Equations*, Princeton University Press, Princeton, NJ, 1976.
- [42] S. Gdoura and D. Lesselier, *Incorporation of multiple scattering and MUSIC-type imaging of small spheres*, ESAIM : proc., to appear.
- [43] J. Gomes and O. Faugeras, *Reconciling distance functions and level sets*, Journal of Visual Communication and Image Representation, 11, 209–223, 2000.
- [44] M. T. Heath, *Scientific computing, an introductory survey*, McGraw Hill, 2002.
- [45] S. Hou, K. Solna and H. Zhao, *A direct imaging algorithm for extended targets*, Inverse Problems, 22, 1151–1178, 2006.
- [46] S. Hou, K. Solna and H. Zhao, *A direct imaging method using far-field data*, Inverse Problems, 23, 1533–1546, 2007.
- [47] S. Hou, K. Solna and H. Zhao, *Imaging of location and geometry for extended targets using the response matrix*, J. Comput. Phys., 199, 317–338, 2004.
- [48] H. Kang and H. Lee, *Identification of simple poles via boundary measurements and an application to EIT*, Inverse Problems, 20, 1853–1863, 2004.
- [49] H. Kang, M. Lim and G. Nakamura, *Detection of surface breaking cracks in two dimensions*, Inverse Problems 19, 909–918, 2003.
- [50] A. Kirsch, *The MUSIC-algorithm and the factorization method in inverse scattering theory for inhomogeneous media*, Inverse Problems, 14, 1025–1040, 2002.
- [51] A. Kirsch and S. Ritter, *A linear sampling method for inverse scattering from an open arc*, Inverse problems, 16, 89–105, 2000.
- [52] R. Kress, *Inverse scattering from an open arc*, Math. Methods Appl. Sci., 18, 267–293, 1995.
- [53] O. Kwon, J. K. Seo and J. R. Yoon, *A real-time algorithm for the location search of discontinuous conductivities with one measurement*, Comm. Pure Appl., 55, 1–29, 2002.
- [54] H. Lee and W. K. Park, *Location search algorithm of thin conductivity inclusions via boundary measurements*, ESAIM : proc., to appear.
- [55] A. Litman, D. Lesselier and D. Santosa, *Reconstruction of a two-dimensional binary obstacle by controlled evolution of a level-set*, Inverse Problems, 14, 685–706, 1998.

- [56] D. R. Luke and A. J. Devaney, *Identifying scattering obstacles by the construction of nonscattering waves*, SIAM J. Appl. Math., 68, 271–291, 2007.
- [57] J. E. Marsden and M. J. Hoffman, *Basic complex analysis*, W. H. Freeman, 3 Sub edition, 1998.
- [58] M. McIver, *An inverse problem in electromagnetic crack detection*, IMA J. Appl. Math., 47, 127–145, 1991.
- [59] L. Mönch, *On the numerical solution of the direct scattering problem for an open sound-hard arc*, Computational and Applied Math., 17, 343–356, 1996.
- [60] Z. T. Nazarchuk, *Singular integral equations in diffraction theory*, 210, Karpenko Physicomechanical Institute, Ukrainian Academy of Sciences, Lviv, 1994.
- [61] Z. Nazarchuk and K. Kobayashi, *Mathematical modelling of electromagnetic scattering from a thin penetrable target*, Prog. Electromagn. Research, PIER 55, 95–116, 2005.
- [62] N. Nishimura and S. Kobayashi, *A boundary integral equation method for an inverse problem related to crack detection*, Int. J. Numer. Meth. Eng., 32, 1371–1387, 1991.
- [63] R. G. Novkov and V. B. Uvarov, *Special functions of mathematical physics*, Birkhäuser, Basel, 1988.
- [64] S. Osher and R. Fedkiw, *Level set methods and dynamic implicit surfaces*, Springer-Verlag, New York, 2003.
- [65] S. Osher and J. A. Sethian, *Fronts propagating with curvature-dependent speed : algorithms based on Hamilton-Jacobi formulations*, J. Comput. Phys., 79, 12–49, 1988.
- [66] W. K. Park, H. Ammari and D. Lesselier, *Non-iterative MUSIC-type algorithm for reconstructing two-dimensional thin dielectric inclusions*, 297–305, August, EKC2008 Proceedings of the EU-Korea Conference on Science and Technology, Springer, 2008.
- [67] W. K. Park, H. Ammari and D. Lesselier, *On the imaging of two-dimensional thin inclusions by a MUSIC-type algorithm from boundary measurements*, 13th International Workshop on Electromagnetic Nondestructive Evaluation (ENDE), Seoul, Korea, 2008.
- [68] W. K. Park and D. Lesselier, *MUSIC-type, non-iterative imaging of a thin penetrable inclusion from its far-field multi-static response matrix*, submitted.
- [69] W. K. Park and D. Lesselier, *Reconstruction of thin electromagnetic inclusions by a level set method*, submitted.
- [70] C. Prada and M. Fink, *Eigenmodes of the time-reversal operator : A solution to selective focusing in multiple-target media*, Wave Motion, 20, 151–163, 1994.
- [71] C. Ramananjaona, M. Lambert and D. Lesselier, *Shape inversion from TM and TE real data by controlled evolution of level set*, Inverse Problems, 17, 1585–1595, 2001.
- [72] C. Ramananjaona, M. Lambert, D. Lesselier and J-P. Zolésio, *Shape reconstruction of buried obstacles by controlled evolution of a level set : from a min-max formulation to numerical experimentation*, Inverse Problems, 17, 1087–1111, 2001.

- [73] F. Santosa, *A level set approach for inverse problems involving obstacles*, ESAIM Control Optim. Calc. Var., 1, 17–33, 1996.
- [74] M. Reed and B. Simon, *Methods of Modern Physics, Vol. IV : Analysis of Operators*, Academic Press, New York, 1978.
- [75] L. Rondi, *A variational approach to the reconstruction of cracks by boundary measurements*, J. Math. Pures Appl., 87, 324–342, 2007.
- [76] M. Tanter, J. L. Thomas and M. Fink, *Time reversal and the inverse filter*, J. Acoust. Soc. Am., 34, 108–223, 2000.
- [77] C. W. Therrien, *Discrete random signals and statistical signal processing*, Prentice Hall, Englewood Cliffs, NJ., 1992.
- [78] M. S. Vogelius and D. Volkov, *Asymptotic formulas for perturbations in the electromagnetic fields due to the presence of inhomogeneities of small diameter*, M2AN, 34, 723–748, 2000.